DOCTORAL THESIS

Photovoltaic Microconverter with Universal Compatibility with AC and DC Microgrids

Hossein Afshari

Photovoltaic Microconverter with Universal Compatibility with AC and DC Microgrids

HOSSEIN AFSHARI

TAL
TECH
PRESS

TALLINN UNIVERSITY OF TECHNOLOGY
School of Engineering
Department of Electrical Power Engineering and Mechatronics
This dissertation was accepted for the defence of the degree 21/10/2025

Supervisor: Prof. Dmitri Vinnikov
Department of Electrical Power Engineering and Mechatronics
Tallinn University of Technology
Tallinn, Estonia

Co-supervisor: Ass. Prof. Dr. Oleksandr Husev
Department of Electrical Power Engineering and Mechatronics
Tallinn University of Technology
Tallinn, Estonia

Opponents: Prof. Hani Vahedi
Department of Information Engineering, Computer Science and Mathematics
Delft University of Technology
Delft, Netherland

Prof. Fei Gao
School of Energy and Computer Science
University of Technology of Belfort-Montbeliard
Belfort, France

Defense of the thesis: 11/12/2025, Tallinn

Declaration:
Hereby I declare that this doctoral thesis, my original investigation and achievement, submitted for the doctoral degree at Tallinn University of Technology, has not been submitted for a doctoral or equivalent academic degree.

Hossein Afshari

_____
signature

Universaalne alalis- ja vahelduvvooluvõrkudega ühilduv fotoelektrilise süsteemi mikromuundur

HOSSEIN AFSHARI

Contents

List of Publications

The following is a list of author's publications, on the basis of which the thesis has been prepared:

[PAPER-I]   H. Afshari, O. Husev, O. Matiushkin and D. Vinnikov, "Novel Dual-Purpose Cost-Effective Forward-Based Micro-Converter," *2025 IEEE Seventh International Conference on DC Microgrids (ICDCM)*, Tallinn, Estonia, 2025, pp. 1–5, doi: 10.1109/ICDCM63994.2025.11144743.

[PAPER-II]   H. Afshari, O. Husev, O. Matiushkin, S. Pourjafar, N. V. Kurdkandi and D. Vinnikov, "Comprehensive Comparison of Grid-Connected Flyback-Based Microinverter With Primary and Secondary Side Decoupling Approach," in *IEEE Transactions on Industry Applications*, vol. 60, no. 6, pp. 9080–9089, Nov.-Dec. 2024, doi: 10.1109/TIA.2024.3452069.

[PAPER-III] Afshari, Hossein, Oleksandr Husev, Oleksandr Matiushkin, and Dmitri Vinnikov. 2022. "A Review of Hybrid Converter Topologies", *Energies* 15, no. 24: 9341. https://doi.org/10.3390/en15249341.

[PAPER-IV]   S. Pourjafar, H. Afshari, P. Mohseni, O. Husev, O. Matiushkin and N. Shabbir, "Comprehensive Comparison of Isolated High Step-up DC-DC Converters for Low Power Application," in *IEEE Open Journal of Power Electronics*, vol. 5, pp. 1149–1161, 2024, doi: 10.1109/OJPEL.2024.3433554.

[PAPER-V]   O. Matiushkin, O. Husev, H. Afshari, E. Romero-Cadaval and C. Roncero-Clemente, "Forward-Based DC-DC Converter With Eliminated Leakage Inductance Problem," in *IEEE Trans. on Ind. Electron.*, vol. 72, no. 2, pp. 1638–1648, Feb. 2025, doi: 10.1109/TIE.2024.3429626.

[PAPER-VI]   H. Afshari, O. Husev and D. Vinnikov, "A Novel Isolated Buck-Boost dc-dc Converter with Wide Range of Voltage Regulations," *2023 IEEE 17th International Conference on Compatibility, Power Electronics and Power Engineering (CPE-POWERENG)*, Tallinn, Estonia, 2023, pp. 1–6, doi: 10.1109/CPE-POWERENG58103.2023.10227443.

[PAPER-VII] H. Afshari, D. Vinnikov, O. Matiushkin, O. Husev, and M. Malinowski, "A Cost-Effective Non-Isolated Forward-Based Universal Microconverter for PV: Comparison with Interleaved Single-Stage Flyback Topology," *4th IEEE International Conference on Power Electronics Smart Grid and Renewable Energy December,* 2025, IIT Dharwad, Hubli, Karnataka, India.

Author's Contribution to the Publications

The author's contributions to the papers in this thesis are:

[PAPER-I]   Hossein Afshari as the main author of the paper. He was responsible for the simulation, calculation of the passive elements, PCB Design and development of software for the experimental tests.

[PAPER-II] Hossein Afshari was the main author of the paper and provided experimental results for both types of system. He developed the control and measurement system for the prototype.

[PAPER-III] Hossein Afshari as the main author of the paper was responsible for the literature review, the writing, submission, and the calculation process. He performed comprehensive topological analysis.

[PAPER-IV] Hossein Afshari has co-authored the paper and provided for the experimental validation and contributed to the analysis of the results, writing and editing of the paper.

[PAPER-V]   Hossein Afshari is co-author of the paper. He was responsible for the simulation, design validation and contributed to the analysis of the results.

[PAPER-VI] Hossein Afshari as the main author of the paper was responsible for the literature review, the writing, submission, and the calculation process. He has performed the validation of the calculations in simulation.

[PAPER-VII] Hossein Afshari was the main author of the paper. He has performed a literature review, experimental tests, writing and submission.

Abbreviations

AC	Alternating Current
ADC	Analog to Digital Converter
ASIC	Application Specific Integrated Circuit
BCM	Boundary Conduction Mode
BOM	Bill of Materials
BVSI	Voltage Source Inverter with Boost Cell
CB	Circuit Breaker
CCM	Continuous Conduction Mode
CEC	California Energy Commission
CF	Current-Fed
CI	Current-Injected (as in VF, CI, IS converters)
DC	Direct Current
DCM	Discontinuous Conduction Mode
DCMG	Direct Current Microgrid
EMI	Electromagnetic Interference
ESS	Energy Storage System
HVDC	High-Voltage Direct Current
IS	Impedance Source
MCU	Micro Controller Unit
MOSFET	Metal-Oxide-Semiconductor Field Effect Transistor
MPP	Maximum Power Point
MPPT	Maximum Power Point Tracking
MPC	Model Predictive Control
PCB	Printed Circuit Board
PI	Proportional-Integral
PLL	Phase Locked Loop
PMC	Phase-Modular Converter
PR	Proportional-Resonant
PV	Photovoltaic
PWM	Pulse Width Modulation
RC	Repetitive Controller
RCD	Resistor-Capacitor-Diode (snubber)
RMS	Root Mean Square
SiC	Silicon Carbide
SSA	Steady State Analysis
SSCB	Solid State Circuit Breaker
SSR	Solid State Relay
THD	Total Harmonic Distortion
TRL	Technology Readiness Level
VF	Voltage-Fed
VSI	Voltage Source Inverter
ZVS	Zero Voltage Switching

1 Introduction

1.1 Background

Most modern electronic devices in residential, commercial, and industrial environments ultimately operate on Direct Current (DC). However, because our electricity distribution is predominantly Alternating Current (AC), nearly all devices must include power conversion stages. For instance, a laptop battery requires only 15–22 V DC, while the rectified single-phase AC grid produces around 310–325 V DC. Thus, chargers and adapters must first rectify AC to a constant high-voltage DC through an AC–DC converter and then step it down to the required lower voltage via a DC–DC stage. As shown in Figure 1.1(a), this approach is applied across common devices such as laptops, phones, televisions, personal computers, and lighting systems, reflecting the legacy of AC dominance. Yet it also highlights inefficiency, since most devices and increasingly many sources are fundamentally DC. This raises an important question: is it still reasonable to rely on redundant AC conversion stages, or should direct DC distribution be reconsidered?

This issue is not new but rather a continuation of the historical "war of currents" between Edison, who promoted DC, and Tesla/Westinghouse, who established AC as the global standard. AC prevailed mainly because transformers made it easy to step voltages up and down, enabling long-distance transmission and widespread adoption. For more than a century, this technical advantage has entrenched AC grids. However, the energy landscape is changing [1], [2]. A growing share of renewable energy sources, such as solar panels, batteries, and fuel cells, generate and store electricity in DC. As their deployment expands, the case for DC microgrids (DCMGs) grows stronger. In such systems, devices connect to a common DC bus [3], [4], eliminating unnecessary AC–DC–AC conversions. Compared to traditional AC distribution, DCMGs promise higher efficiency, improved reliability, freedom from harmonics, and simpler control because synchronization is unnecessary. Figure 1.1(b) shows an example of the possible DCMG architecture addressed in [5]–[8].
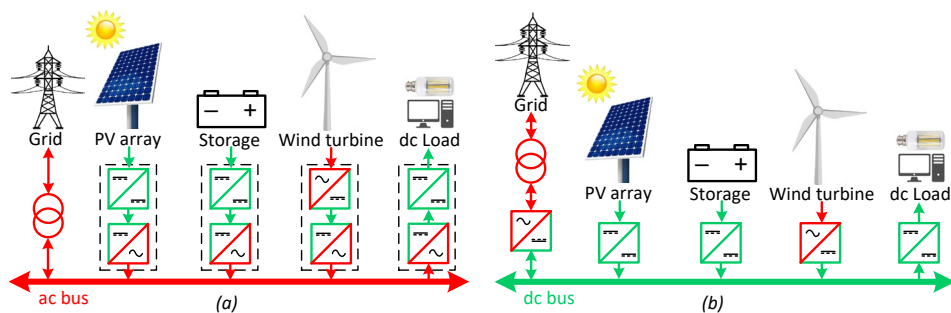
Figure 1.1(a) Traditional AC distribution system, (b) considered energy transmission system based on common DC bus [PAPER-V].

Despite these advantages, AC grids remain dominant largely because no universal standards exist for DC distribution. Researchers and industry stakeholders are actively investigating suitable voltage levels for low-voltage DC systems. A voltage of around 326 V DC is often considered optimal, as it corresponds to the peak of a rectified single-phase AC voltage and can be used with existing cabling infrastructure [9]. Alternative proposals suggest 350 V for low-power systems and up to 700 V for higher-power applications

[10], while some studies recommend a 350–380 V range as a possible standard. The establishment of consistent voltage standards is crucial to enabling DC-ready devices and widespread adoption. Meanwhile, comparisons between AC and DC distribution at higher scales show that High-Voltage DC (HVDC) transmission can outperform high-voltage AC in terms of efficiency and stability, further reinforcing the relevance of DC technologies [11]–[13].

One of the main technical challenges of DC distribution lies in protection. In AC systems, conventional breakers interrupt faults by exploiting current zero-crossings, with clearing times of about 80 ms [14]. In DC systems, however, the voltage does not fall to zero, making fault interruption more difficult. This limitation renders AC breakers unsuitable for DC applications. Alternatives such as solid-state relays (SSRs) or hybrid mechanical breakers [15] are under development, aiming to deliver fast response times, low conduction losses, compact design, high reliability, and affordability [16]. Although several prototypes exist, the lack of mature and cost-effective DC breakers remains a major obstacle to deploying DC grids at scale [17], [18].

Given these challenges, an immediate transition from AC to DC is unlikely. Instead, the near future is expected to feature hybrid systems where AC and DC coexist [19], [20]. Such hybridization could be especially valuable in regions with limited or aging AC infrastructure, where introducing DC from the outset may be more practical, as well as in advanced economies where DC integration can enhance the efficiency of existing systems. A promising enabler of this transition is the concept of dual-purpose converters, devices capable of operating with both AC and DC inputs [21]. These converters provide flexibility to consumers and investors, allowing devices to operate seamlessly during the gradual adoption of DC grids [22]. In this way, dual-purpose converters act as bridging technologies, smoothing the transition from today's AC-dominated landscape toward a more efficient, reliable, and adaptable energy future where DC plays a central role [23].

1.2 Motivation of the Thesis

Hybrid inverters are widely recognized as a flexible solution for combining solar energy, storage, and grid interfaces. Their typical structure, shown in Figure 1.2, includes solar terminals, a grid-connected Voltage Source Inverter (VSI), a buck–boost stage that performs Maximum Power Point Tracking (MPPT), and a common DC link. Commercial designs also feature backup terminals for uninterrupted operation during grid outages. Batteries can be connected either directly to the DC link or through an additional interface converter integrated within the Energy Storage System (ESS). For example, the Huawei SUN2000-5KTL-L1 employs a direct connection, offering simplicity and lower cost, but limiting compatibility to specific battery types and voltages. Conversely, the Fronius SYMO Hybrid 5.0-3-S uses an external ESS with its own interface converter, providing flexibility at the expense of higher cost. Other products, such as the Sungrow SH5K-30, integrate an isolated battery interface converter, allowing higher voltage step-up capability. More complex variants also exist, including structures where the battery interface is tied to the solar panel terminals, extending design versatility [PAPER-III].

In addition to inverters, hybrid microconverters have been developed for lower-voltage applications, typically handling a single solar panel in the 10–60 V range with a low-voltage battery. While hybrid microconverters are attractive for residential use, several studies have reported limitations, particularly battery overheating in tightly coupled designs [24], [25]. Despite these challenges, hybrid topologies demonstrate the adaptability of

power electronics in matching various system requirements and highlight the ongoing effort to balance cost, performance, and reliability across different scales of application [27], [28].
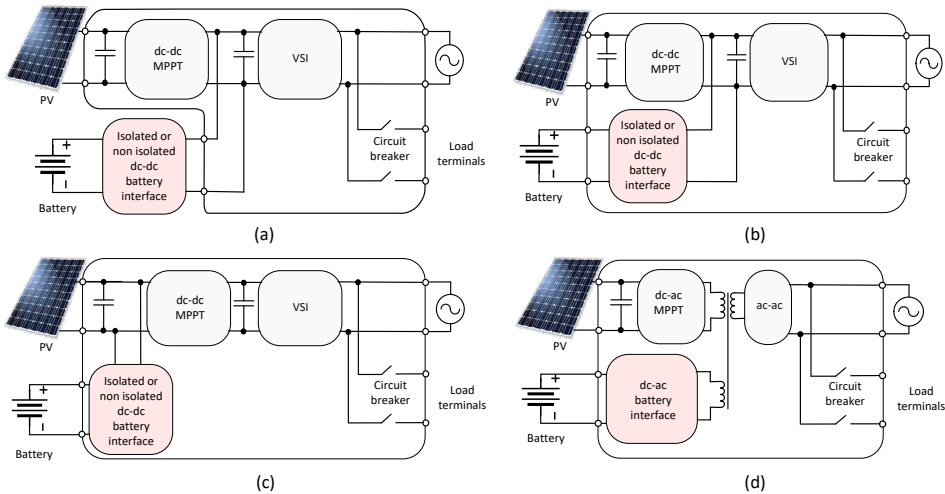
Figure 1.2 Typical structure of the hybrid solar inverter [PAPER-III].

On the other hand, the growing adoption of DC microgrids has accelerated the demand for converters that can seamlessly interface with both AC and DC distribution systems. We expect that many solar converters operating with AC grid will be forced to reconnect to DC grid by economic incentives.

Many hybrid converters are therefore designed with dedicated terminals for each bus [PAPER-III]. However, such designs is not intended for operation with DC microgrid.
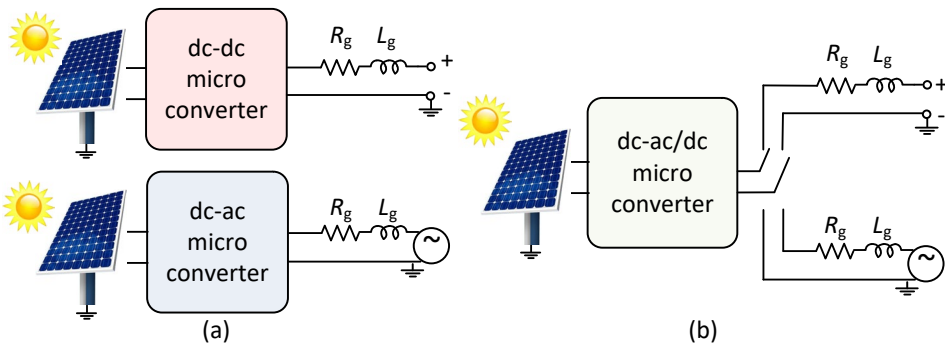
Figure 1.3 Motivation and concept demonstration of the universal solar microconverter: (a) DC–DC microconverter and DC–AC microinverter as independent solutions. (b) Universal single-phase solar DC–DC/AC microconverter [PAPER-I].

To address these limitations, universal converters have been introduced. A universal converter minimizes redundancy by employing a shared control, protection, and conversion unit that automatically detects whether the device is connected to an AC or DC grid depicted in Figure 1.3(a). For instance, in a modern building with DC sockets, the device could operate in DC–DC mode, while in traditional installations it could

12

function as an AC–DC converter. The universal solar converter (Figure 1.3(b)) therefore provides a cost-effective and flexible platform capable of serving both environments with minimal complexity. Moreover, such converters can be designed as bidirectional devices, enabling integration of PV, storage, and grid simultaneously.

This research direction underpins ongoing work at the Power Electronics Group of Tallinn University of Technology, supported by the PRG675 project "New Generation of High-Performance Power Electronic Converters Simultaneously Applicable for DC and AC Grids with Extended Functionalities". The aim is to develop universal solar microconverter that minimizes redundancy, lowers costs, and extends functionality, thereby offering a practical solution for future residential AC/DC systems.

1.3 Concept of a Cost-Effective Universal DC–DC/AC Solar Microconverter

In terms of power processing architecture, microconverter topologies can generally be categorized into single-stage and double-stage configurations. Furthermore, based on the presence or absence of galvanic isolation, they can be classified as either isolated or non-isolated [29], [30]. Single-stage configurations are particularly advantageous as they improve overall conversion efficiency while reducing component count and system cost. Additionally, the integration of an unfolding circuit operating at low switching frequencies significantly reduces switching power losses compared to conventional solutions. Despite these benefits, one of the major challenges in microconverter design is achieving a high voltage gain, which has been the focus of numerous recent studies [31]–[34].

Table 1.1 Microinverter market overview.

Manufacturer	Peak AC Power (VA / W)	MPPT Voltage (V)	Efficiency %		Cost
			Max	EU	
Enphase (IQ7 series)	250	27 - 37	98	97	$$$$
	295	27 - 45			
	320	53 - 67			
Enphase (IQ8 series)	240	27 - 37	98	97	$$$$
	290	29 - 45			
	325	33 - 45			
	349	36 - 45			
	380	38 - 45			
AP systems Dual microinverter (DS3)	625 - 960	28 - 45	96.5	96	$$$
Sungrow (S450S)	450	16 - 60	96.2	95.4	$$$
Hoymiles (HMS series)	450	16 - 60	96.7	96	$$$
ZJ Beny (BYM series)	500 - 700	24 - 50	97.5	97	$$$
Envertech (EVT series)	360	22 - 48	96	95	$$$

Flyback transformer-based topologies are widely adopted by leading manufacturers [35]–[37] due to their simplicity, galvanic isolation, and low component count. However, they typically suffer from leakage inductance in the transformer or coupled inductor, which increases voltage stress on the high-frequency (HF) switch. Mitigating this stress often requires additional circuitry, such as snubber networks, which adds complexity and cost. In contrast, transformerless topologies remove bulky isolation components but create leakage current paths through parasitic capacitance between the PV module and the grid. These paths must be carefully managed to comply with safety standards [38].

The microinverter market features a diverse range of offerings, as shown in Table 1.1, with key players including Enphase, AP Systems, Sungrow, Hoymiles, ZJ Beny, and Envertech [39]. Enphase leads with high-efficiency models reaching up to 98%, while other manufacturers provide more cost-effective alternatives with slightly lower efficiencies. This diversity highlights the trade-offs between efficiency, power output, and cost, underscoring the need for ongoing innovation in microinverter research and commercialisation.

Market efforts have primarily focused on flyback, interleaved flyback, and H-bridge-derived topologies. Consequently, a gap remains in providing a cost-effective, efficient, and flexible solution, one that this research aims to address through a non-isolated, dual-purpose microconverter architecture.

1.4 Aims, Hypothesis, and Research Tasks

The main aim of this PhD research is to develop and experimentally validate universal cost-effective microconverter architecture. The proposed solutions aim to facilitate the global transition from conventional AC-only infrastructures toward hybrid DC/AC microgrids. This work investigates the effectiveness of PV-side passive decoupling techniques, especially using unfolding circuits, as a cost-effective and scalable alternative to traditional DC-link and active decoupling methods. By integrating synergetic closed-loop control strategies with single-stage power conversion, the converter design minimizes circuit complexity and component count while maintaining high conversion efficiency and reliable performance across a wide voltage range (15–70 V input, up to 350 V output).

A key goal is to demonstrate that non-isolated and isolated converter topologies can be designed as a universal microconverter, including a proposed forward-based non-isolated structure, that can deliver competitive efficiency and eliminate leakage current issues often found in conventional flyback-based designs. The final outcome of this research is to develop and test three TRL4 prototypes, including single-stage and double-stage interleaved flyback-based and non-isolated forward-based microconverters, validated under AC grid conditions and a virtual DC grid, proving the system's feasibility, modularity, and readiness for mass production.

Hypotheses:
1. Modified forward-based converter may offer cost effectiveness and acceptable efficiency for applications requiring a wide input range of 15–70 V.
2. The proposed modified forward-based converter can eliminate the Leakage inductance issue of the transformer.
3. The proposed closed-loop synergetic control strategy may provide benefits by utilizing single-stage operation across a wider voltage range.

Research tasks:

1. Overview of the existed solar converters.
2. Design, Simulation and Experimental comparison of new topological DC-DC solutions as an integrated part of the universal solar microconverter.
3. Optimisation of the proposed solution in terms of universal applicability taking into account switches, magnetics and switching frequency.
4. Advanced control method development directed for dual-purpose operation.
5. Design of the experimental setup and experimental verification of the universal microconverter simultaneously applicable for AC and DC grids.

1.5 Research Methods

The research methodology adopted in this thesis combines mathematical analysis, computer-based simulations, and experimental validation. Newly proposed topologies and circuits are examined through Steady-State Analysis (SSA) and transient analysis using functional methods such as Laplace and Fourier transforms. To investigate the performance characteristics of the proposed topologies and control strategies, both dynamic and static models, including versions accounting for component losses, are developed. Simulations and prototype design are conducted primarily using MATLAB, Altium Designer, and PSIM, all accessible at Tallinn University of Technology (TalTech). Experimental validation of theoretical predictions is carried out using small-scale laboratory prototypes of the new topologies, circuits, and unconventional configurations. The Power Electronics Research Laboratory at TalTech provides state-of-the-art facilities including digital oscilloscopes, function generators, solar array simulators, power/efficiency analyzers, microcontroller development platforms, PCB prototyping and assembly tools supporting both hardware and software development.

1.6 Contributions and Disseminations

The results of the research are published via scientific publications, conferences, symposiums, doctoral schools, and presentations. During PhD studies, the author contributed to 11 publications. Among them, five papers were published in peer-reviewed international journals. The remaining papers were reported at international IEEE conferences. The dissertation is based on seven main scientific publications, including four journals and three conference papers presented at three IEEE international conferences.

Scientific novelties:

- Classification of hybrid converter topologies based on functional structure, isolation level, and integration potential for PV-plus-storage systems.
- Design and realization of an isolated buck-boost converter topology capable of ultra-wide voltage regulation for renewable energy integration with galvanic isolation.
- Synthesis of synergetic closed-loop control strategies for single-stage DC–DC/AC microconverter.
- Design and implementation of a non-isolated modified forward-based microconverter that eliminates leakage current in the transformer.
- Comprehensive comparative analysis of PV-side passive decoupling versus conventional DC-link decoupling, including experimental validation, component stress modelling, and system-level cost implications.

Practical novelties:

- Development of a dual-mode microconverter with shared terminals for AC and DC outputs, offering seamless integration into hybrid microgrids with minimal hardware redundancy.
- Reduction of system cost and size by replacing active decoupling and bulky electrolytic DC-link capacitors with PV-side passive decoupling and low-frequency unfolding circuits.
- Experimental validation of synergetic control for ac microgrid toward the limitation of the proposed solution for single-stage operation in ac microgrid.
- Experimental validation of proposed non-isolated forward-based and interleaved flyback-based microconverters.
- Cost-effective design by considering BOM-level cost analysis for the proposed converter families, enabling scalable production for residential and industrial PV systems.

1.7 Experimental Setup and Instruments

The experimental setup was assembled in the Power Electronics Laboratory at Tallinn University of Technology. The laboratory workspace is illustrated in Figure 1.4(a). A Tektronix oscilloscope was employed to capture voltage and current waveforms across the passive components. For precise measurements, Tektronix P5205A and TCP0030A probes were used for voltage and current, respectively. The STM32CubeIDE development environment facilitated programming of the STM32 microcontroller from STMicroelectronics NV.

Figure 1.4(a) Laboratory Workspace, (b) DC and AC Grid Simulators with Supporting Equipment.

For efficiency measurements, a Yokogawa WT1800 power analyzer was utilized, with the WTViewer software enabling remote monitoring and data acquisition. A Chroma 62150H-1000S solar simulator served as the input voltage source for the experimental prototype, while a bidirectional power supply was used to emulate a DC grid. For grid-connected operation, an autotransformer was employed to replicate the AC grid, as shown in Figure 1.4(b). This setup allowed comprehensive testing and validation of the proposed microconverter under realistic operating conditions.

1.8 Thesis Outline

This thesis presents a comprehensive study of a cost-effective, universal DC–DC/AC solar microconverter, addressing design, analysis, control, and experimental validation. Chapter 2 focuses on DC–DC converter topologies suitable for renewable energy applications, including isolated buck–boost and forward-based non-isolated designs. These topologies are analyzed for wide voltage regulation, efficiency, and leakage inductance mitigation, with experimental results demonstrating performance improvements.

Chapter 3 evaluates passive decoupling strategies, comparing PV-side decoupling with conventional DC-link approaches through theoretical modelling, simulations, and experimental validation, providing insights into efficiency, cost, and voltage stability. Chapter 4 develops closed-loop and synergetic control strategies for the universal microconverter, covering both DC and AC microgrid modes. Power loss evaluation, experimental validation, and comparisons with interleaved single-stage flyback topologies demonstrate enhanced efficiency, reduced cost, and operational stability.

Chapter 5 summarizes the main findings, highlighting the versatility, cost-effectiveness, and high performance of the proposed microconverter. The thesis concludes by discussing future research directions, including the integration of wide-bandgap semiconductors, scaling to higher power levels, and potential applications in residential and small-scale renewable energy systems. Overall, the thesis provides a structured exploration of a universal microconverter system from theoretical development to practical implementation and experimental validation.

2 DC–DC Converter Topologies for Renewable Energy Applications

A primary challenge in photovoltaic microconverter design lies in achieving both high step-up conversion ratios and a wide voltage regulation range to accommodate varying MPPT characteristics across different PV panel technologies. Recent advancements in DC-DC converter design have yielded significant progress in attaining high voltage gains through both isolated and non-isolated topologies [40], [29]. For non-isolated configurations, several enhanced conversion techniques have been developed, including coupled inductor implementations, multi-stage cascaded architectures, switched-capacitor networks, switched-inductor circuits, and voltage multiplier configurations [41]–[46]. Among these solutions, galvanically isolated DC–DC converters offer particularly promising advantages by providing essential electrical separation between power source and load while handling substantial voltage fluctuations. These isolated topologies exhibit superior power utilization efficiency, demonstrate robust performance across diverse load conditions, and support operation with wide input voltage ranges, which are critical features for PV applications. The established isolated converter architectures are primarily categorized as either Voltage-Fed (VF) or Current-Fed (CF) topologies.

Current-fed (CF) DC–DC converters present multiple beneficial features, such as diminished input current ripple, decreased transformer turns ratio requirements, enhanced conversion efficiency, reduced voltage stress on rectifier diodes, and elimination of shoot-through issues in power switching devices [47]–[49]. Additionally, another isolated topology exists known as the Impedance Source (IS) converter, which effectively combines attributes of both voltage-fed (VF) and current-fed configurations, enabling it to inherit advantageous characteristics from each type [50]. For clearer comparison, the technical specifications of these three converter categories have been systematically evaluated and presented in Table 2.1.

Isolated high-step-up DC–DC converters include passive and active clamp types. Passive clamp converters use few switches but suffer from hard-switching losses [51]. Active clamp variants (push-pull, half-bridge, full-bridge) enable ZVS turn-on and prevent voltage spikes, yet face efficiency and cost challenges in low-power applications due to complex driving circuits [52], [53]. Resonant bridge converters achieve soft switching via parasitic elements, eliminating clamp circuits, but risk transformer DC-offset currents that increase size.

Table 2.1 Main Features comparison of VF, CI and IS converters.

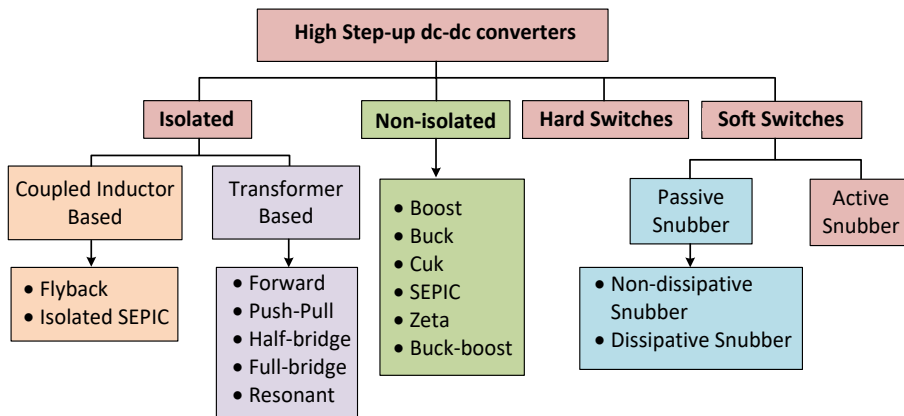| Feature	VF	CI	IS
Voltage step-up	No	Yes	Yes
Voltage step-down	Yes	No	Yes
Short-circuit exemption	No	Yes	Yes
Open-circuit exemption	Yes	No	Yes
Element for storing energy	One capacitor	One inductor	At a minimum, one capacitor and one inductor
Cascading capability of energy elements	No	No	Yes
Simplicity in control	Simple	Complex	Moderate

Figure 2.1 Topological Classification of High Step-Up DC–DC Converters.

Figure 2.1 displays the classification of high step-up DC–DC converters into isolated and non-isolated categories. Non-isolated designs incorporate coupled-inductor topologies (Flyback, isolated SEPIC), while isolated versions employ transformer-based configurations including forward, push-pull, voltage-fed half/full-bridge, current-fed half/full-bridge, and resonant half/full-bridge. Table 2.2 compares advantages and limitations of these conventional isolated high step-up converters.

Table 2.2 Comparison of Conventional Isolated converters.

Topology	Advantages	Disadvantages
Flyback	Simple design and low cost. Suitable for low to moderate power applications	Limited power handling capability High peak currents and voltage stresses
Isolated SEPIC	Dual voltage regulation: step-up and step-down capabilities. Reduced input current ripple	Complex control and higher component count Limited for high power applications
Forward	High efficiency Good for high power applications	Limited voltage regulation range. Requires tight control for reliable operation
Push-pull	High-frequency operation capability Good for high power applications	Complex control and higher component count Transformer design can be challenging
Half-bridge	Moderate complexity. Suitable for a wide range of power applications	Requires careful control to avoid voltage spikes Limited for very low or very high power
Full-bridge	High efficiency. Suitable for high-power applications	Complex control and higher component count Not ideal for low-power applications
Resonant	Reduced electromagnetic interference (EMI) Improved reliability due to soft switching	Complex control and higher cost High current stress through the semiconductor devices

2.1 Comparison Methodology Based on Fundamental Waveform of the Converter

A converter's basic waveforms derive from its modulation scheme rather than component choices or electrical parameters (like switching frequency or semiconductor selection), establishing fundamental design criteria. These universal requirements involve sizing passive components to maintain consistent current ripple through inductors and uniform voltage ripple across capacitors, independent of specific implementation details. The volume of a core of the inductor as well as the volume of capacitor can be estimated based on its maximum accumulated energy:

$$Vol_L \cong \sum_{i=1}^{N_L} L_i \cdot \hat{i}_{Li}^2, \quad Vol_C \cong \sum_{i=1}^{N_C} C_i \cdot \hat{v}_{Ci}^2, \quad (2.1)$$

where L_i and C_i are values of i inductance and capacitor, N_L is number of inductors and N_C is number of capacitors. $\hat{i}_{Li}$ is a peak inductor current and $\hat{v}_{Ci}$ is a peak of capacitor voltage.

Furthermore, semiconductor-independent relative switching and conduction losses can be introduced. The relative conduction losses are proportional to the square of the switch current. As a result, total conduction losses may be expressed to the following scaling relationship:

$$CL \cong \sum_{i=1}^{N_S} \tilde{i}_{Si}^2, \quad (2.2)$$

where $\tilde{i}_{Si}$ is RMS switch current, N_S is a number of switches.

When current ripple is neglected, the hard switching losses depend on both the semiconductor voltage v_{Si} and semiconductor current i_{Si}. The time-averaged product of v_{Si} and i_{Si} across one fundamental period T provides an effective switching loss metric:

$$SL \cong \sum_{i=1}^{N_S} \left\langle \hat{i}_{Si} \cdot \hat{v}_{Si} \right\rangle_T. \quad (2.3)$$

Table 2.3 outlines the comparative design parameters for all converters. The evaluation methodology, applied to the topologies in Figure 2.2, assesses critical metrics including:
- Capacitor Volume
- Magnetic size
- Voltage stress on primary-side switches
- Conduction losses in primary-side semiconductors
- Switching losses

Table 2.3 Key design parameters for converters comparison.

Parameters	Value
Input voltage range (Vin)	20 V – 60 V
Output voltage (Vo)	350 V
Maximum rated power (Po)	400 W
Switching frequency	50 kHz
Maximum input current	10 A
Maximum input current ripple	15 %
Maximum voltage ripple of capacitors	3 %

Figure 2.2 Several isolated high step-up DC–DC converters for DC microgrid applications, (a) Flyback-based converter [54], (b) Forward-based converter [55], (c) Push-pull based converter [56], (d) Half-bridge based converter [57], (e) Current-fed FB with clamp capacitor [58], and (f) Current-fed resonant converter [59] [PAPER-IV].

Figure 2.3 Overall comparison of the isolated converters from each family based on key parameters [PAPER-IV].

The isolated converter topologies shown in Figure 2.2 were systematically compared using the specified comparative methodology, with the comparative analysis results presented in Figure 2.3.

Figure 2.3 presents the individual performance comparison of each converter. This analysis was conducted under specific operating conditions: an output power of 400 W, an input voltage range of 20–50 V, a fixed switching frequency of 50 kHz, and a constant output 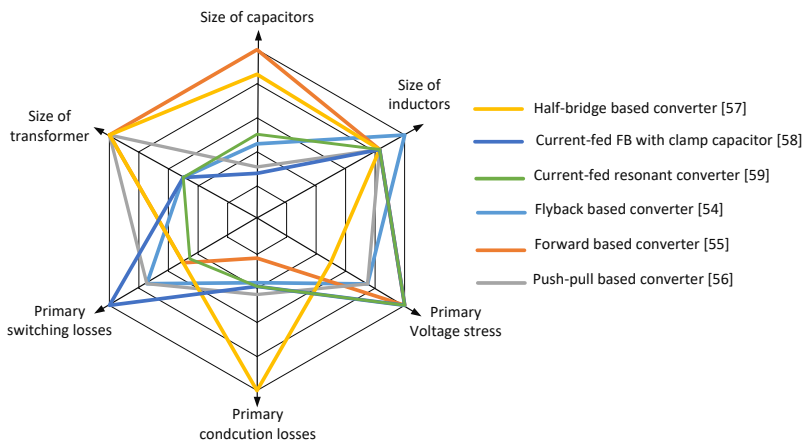voltage of 350 V. To maintain comparability, all converters were evaluated with identical output power and consistent dynamic switch configurations.

2.2 A Novel Isolated Buck-Boost DC–DC Converter with a Wide Range of Voltage Regulations

The conventional current-fed push-pull converter offers advantages including high voltage gain, low input current ripple, and reduced switch conduction losses [60]. However, it suffers from significant drawbacks: voltage spikes caused by transformer leakage inductance, high voltage stress, reverse-recovery issues, limited efficiency, and a narrow input-voltage operating range (requiring duty ratios > 0.5). Recent improvements have addressed these limitations, particularly through ZVS clamping-mode current-fed push-pull converters. These modified topologies employ active-clamp circuits to suppress switch voltage surges and recover leakage inductance energy. Additionally, they operate at duty ratios below 0.5, enabling wider input-voltage ranges. While ZVS operation is achieved, its efficiency improvement is marginal at low input voltages due to insufficient energy storage in switch output capacitances [PAPER-VI].

The developed isolated buck-boost DC–DC converter (Figure 2.4(a)) presents an improved solution featuring three key advantages: (1) zero-voltage-switching operation, (2) complete galvanic isolation between input and output ports, and (3) an exceptionally wide voltage regulation range. This topology achieves unique operational flexibility by functioning in buck, boost, and buck-boost modes through controlled gate signal modulation. Such wide operational capability (0–60 V input to fixed 350 V output) makes it particularly suitable for grid-connected photovoltaic microconverter applications.

As demonstrated in Figure 2.4(b), the converter automatically transitions between operating modes based on input voltage variations while maintaining constant DC-link voltage. The circuit architecture consists of a three-winding transformer (turn ratio *n*) with six power switches and three capacitors on the primary side, combined with two diodes and three capacitors on the secondary side. This configuration preserves the electrical benefits of conventional converters while overcoming their limitations through intelligent mode-switching capability and optimized component arrangement, particularly addressing the requirements of renewable energy systems with wide input voltage variations.
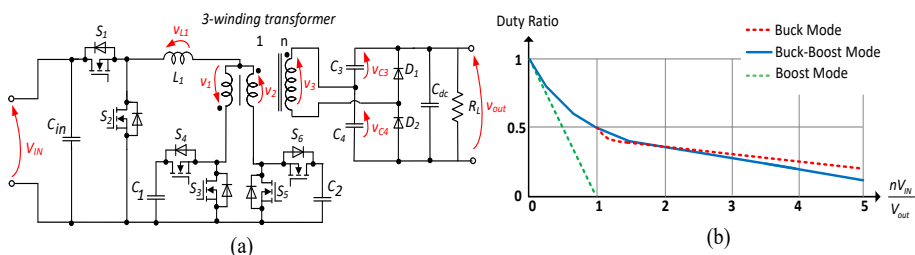

Figure 2.4(a) Circuit topology of the proposed converter, (b) Operation range of the proposed converter [PAPER-VI].

The available operation modes are determined by the switching states of S_1–S_5, where switch pairs (S_1/S_2, S_3/S_4, and S_5/S_6) operate in complementary fashion. Proper switching coordination enables buck, buck-boost, and boost operational capabilities, as detailed in Table 2.4, which also specifies the ZVS conditions. Notably, boost mode operation occurs when gate signal overlapping exists between S_3 and S_5, while ZVS operation is maintained across all modes. This switching strategy ensures soft-switching performance throughout the converter's entire operational range.

Figure 2.5 shows all switching states (Buck, Buck-Boost, Boost) of the proposed converter. A fixed 180° phase shift between S_3/S_4 gate signals ensures consistent switching dynamics. This controlled phase relationship enables full performance evaluation across operational modes while maintaining ZVS conditions.

Table 2.4 Switching table of proposed converter.

Mode	Voltage gain	S_1	S_2	S_3	S_4	S_5	S_6	state	ZVS condition
Buck	$2nD_{Buck}$	ON	OFF	ON	OFF	OFF	ON	c	For D>0.5
		OFF	ON	ON	OFF	OFF	ON	e	
		OFF	ON	OFF	ON	ON	OFF	d	
Buck-Boost	$\dfrac{nD_{BB}}{1-D_{BB}}$	ON	OFF	ON	OFF	OFF	ON	c	For D>0.5
		ON	OFF	ON	OFF	ON	OFF	a	
		OFF	ON	OFF	ON	ON	OFF	d	
Boost	$\dfrac{1}{1-D_{Boost}}$	ON	OFF	ON	OFF	ON	OFF	a	For 0<D<1
		ON	OFF	ON	OFF	OFF	ON	c	
		ON	OFF	OFF	ON	ON	OFF	b	

The proposed converter circuit is simulated in PSIM software incorporating practical models for diodes and MOSFETs. Design parameters calculated from equations in [PAPER-VI]. The converter operates with an input voltage range of 10–60 V, delivering a regulated 350 V output through a 7:1 turn-ratio transformer. Key parameters include: 100 µH inductance, 200 µF output capacitance, and 132.5 Ω load resistance. The 25 kHz switching frequency enables efficient power conversion while maintaining ZVS operation across all modes (buck/boost/buck-boost). Simulation results for the novel isolated buck-boost topology are presented in Figure 2.6, showing operation in (a) Boost, (b) Buck-Boost, and (c) Buck modes.
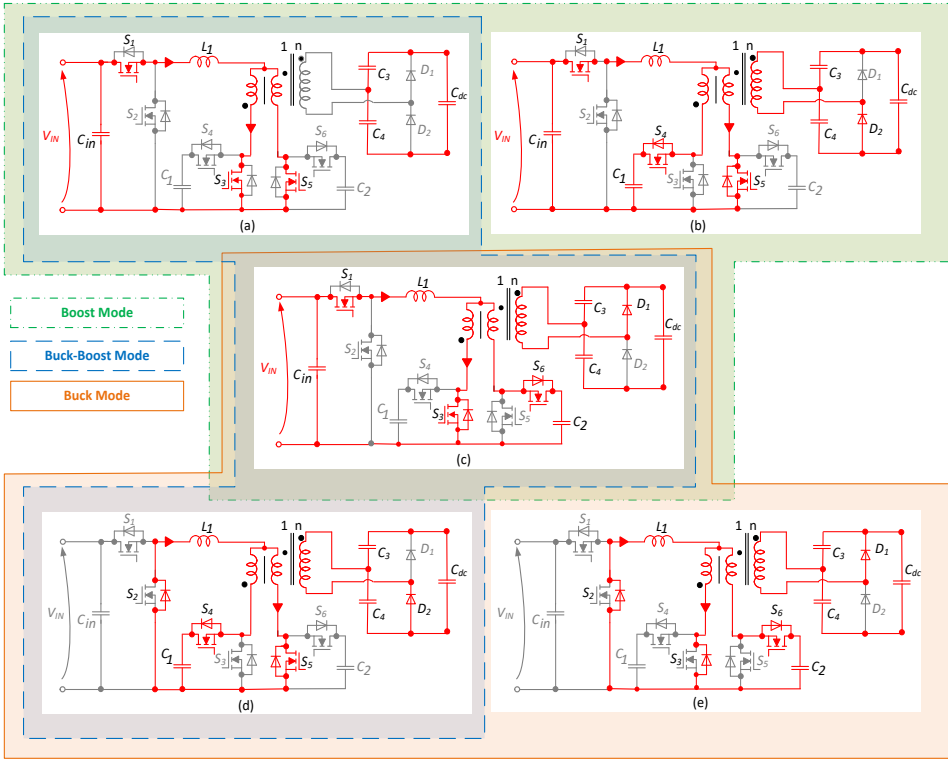
Figure 2.5 Circuit topology of the proposed converter [PAPER-VI].
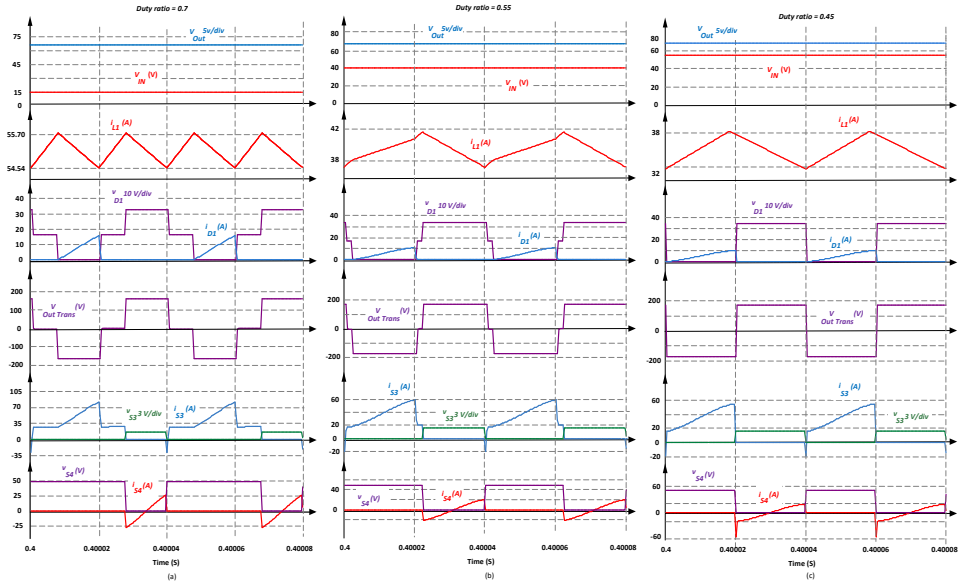

Figure 2.6 Simulation results. (a) Boost mode. (b) Buck-Boost mode. (c) Buck mode [PAPER-VI].

To demonstrate the wide operational range of the proposed topology, the input voltage was varied between 15 V, 40 V, and 55 V while maintaining a constant 350 V output. The required regulation was achieved using duty cycles of 0.7 (Boost), 0.55 (Buck-Boost), and 0.45 (Buck). Figure 2.6 confirms the stable 350 V output across all input voltages. Additionally, the inductor current (L_1) in each mode validates continuous conduction mode (CCM) operation ZVS is achieved for diodes D_1 and D_2 as well as switches S_3 and S_5. The voltage waveform across the tertiary winding of the transformer further corroborates the state equations derived earlier, confirming the theoretical analysis.

2.3 Forward-Based DC–DC Converter with Eliminated Leakage Inductance Problem

The flyback DC–DC converter remains the most prevalent isolated topology due to its structural simplicity, minimal component count, and widespread industrial adoption. Recent advancements in flyback derivatives have enhanced performance characteristics, including hybrid boost-flyback configurations that employ diodes to transfer primary-side magnetizing energy directly to the output enabling step-down voltage conversion. Comparatively, conventional forward converters incorporate additional buck cells and clamp circuits to achieve similar isolation while addressing inherent limitations of flyback architectures. Both topologies serve as foundational solutions, with modern variants progressively improving efficiency and operational flexibility [PAPER-V].

Hybrid forward-flyback converters [61]–[64] present an innovative solution by merging both topologies' advantages, achieving ZVS and reduced input current ripple. This architecture replaces the forward converter's input clamp circuit with a flyback cell, redirecting energy to the output rather than storing it in the input capacitor. Coupled inductor-based topologies offer another promising approach for PV applications, as comprehensively reviewed in [65]. Further developments integrate charge pump functionality through capacitors bridging the transformer windings or coupled inductors [66], [67], enabling energy transfer between primary and secondary sides. Among these, quasi-Z-source converters [50] are particularly suited for PV systems due to their inherent continuous input current characteristic, addressing a critical requirement for solar energy conversion.

2.3.1 Leakage Inductance Issue

The forward DC–DC converter provides key benefits such as single-switch operation, low cost, and high efficiency. Despite its widespread use, this topology suffers from a critical drawback: the transformer core requires reset when the switch turns off. Without proper energy diversion, the stored transformer energy induces damaging voltage spikes across the switch. Furthermore, parasitic components like leakage inductance exacerbate this issue, creating nonlinear behavior during operation.

The leakage inductance's stored energy remains unrecovered during the switch OFF state, causing high-frequency oscillations and severe drain-source voltage spikes. These effects necessitate switches with higher breakdown voltage ratings to withstand the transient overvoltage, ultimately increasing system cost and design complexity.

A three-winding transformer offers one solution for core reset by enabling complete flux dissipation each switching cycle, preventing saturation (Figure 2.7(a)). Alternative approaches to mitigate switch voltage spikes include active clamp circuits (Figure 2.7(b)),

passive clamp topologies, and ZVS techniques, each addressing the reset challenge while optimizing efficiency and switch stress.

However, as demonstrated in [68], leakage inductance directly impacts duty cycle requirements: higher leakage inductance necessitates an increased duty cycle to maintain the same output voltage. When the duty cycle approaches its maximum limit, the transformer's winding ratio must be adjusted. These constraints alongside input voltage and power ranges are critical considerations in transformer design to ensure optimal converter performance.

2.3.2 Proposed Forward-Based Non-Isolated Solution

As illustrated in Figure 2.8, the proposed forward-based DC–DC topologies effectively resolve the transformer core reset issue by redirecting leakage inductance current through diode D_3 to the output capacitor cascade, eliminating primary-side circulation. These non-isolated configurations feature direct input-output ground connection, preventing leakage currents while removing the need for conventional input clamp circuits. Unlike standard forward converters, the additional diode D_3 facilitates magnetizing energy transfer to the output.

Figure 2.7 Forward DC–DC converter: (a) with the third winding, (b) with an active clamp circuit [PAPER-V].

Figure 2.8 Proposed forward-based DC–DC converter as a solution for solar application [PAPER-V].

The forward-based DC–DC converter merges boost-flyback operational principles with forward converter architecture, featuring 4 capacitors, 2 inductors (including output filter L_2), 3 diodes, a single active switch, and a step-up transformer. This minimalist single-switch design simplifies control systems, reduces hardware costs, and streamlines auxiliary circuits while remaining fully compatible with single-PV-panel integration and DC grid interconnection.

The proposed topologies in Figure 2.8 differ primarily in the placement of capacitor C_2. This strategic positioning enables significant system improvements: (1) reduced size and cost of other capacitors through voltage redistribution, (2) faster transient response

at startup by directly transferring input voltage to the output (Figure 2.8(a)), and (3) lower voltage stress on C_2 in the first topology due to its direct input-source connection. These modifications demonstrate how targeted capacitor placement can optimize both performance and cost-effectiveness in DC–DC converter design.

The two topologies were compared using four presented criteria: total capacitor energy (E_C), overall inductance energy (E_L), semiconductor voltage stresses (V_{STR}) and the conduction losses (P_{CL}). Figure 2.9 depicts the total energy of the capacitor with the same ripple factors for both topologies while the input capacitor was neglected. The analysis reveals that increasing C_2 capacitance reduces the system's total capacitive energy. Solution 1 (Figure 2.8(a)) achieves superior performance due to lower voltage stress from its input-source connection. With identical results for other criteria, solution 1 was selected for experimental validation as the optimal capacitor-efficient design.
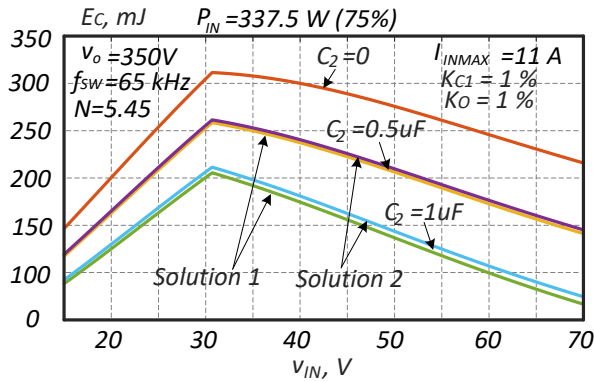

Figure 2.9 Total Capacitor Energy of Two Proposed Topologies for Different C_2 Values vs. Input Voltage [PAPER-V].
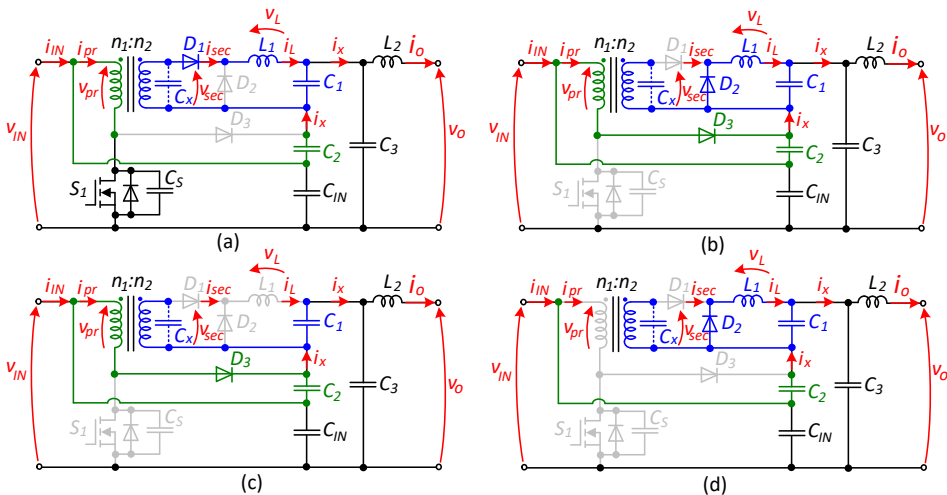

Figure 2.10 Equivalent circuits of the proposed forward-based DC–DC converter: (a) active state, (b) zero state, (c) DCM of inductor current, (d) DCM of the primary current [PAPER-V].

27

This section presents an analytical evaluation of the topology in Figure 2.8(a), with identical methodology applied to Figure 2.8(b). The converter's operation comprises multiple modes: (1) linear Continuous Conduction Mode (CCM), characterized by uninterrupted inductor currents, and (2) Discontinuous Conduction Modes (DCM) for both the magnetizing inductor and forward-cell inductor L_1. Steady State Analysis (SSA) was employed to derive these operational characteristics, with supporting equivalent circuits detailed in Figure 2.10. The SSA approach systematically evaluates each mode's voltage/current relationships while accounting for the converter's unique forward-based architecture.

When the switch S_1 turns ON (Figure 2.10(a)), the transformer energizes the forward cell while the magnetizing inductor stores energy. Diode D_1 conducts during this state, while D_2 and D_3 remain off, enabling capacitor C_1 to charge and C_2 to discharge. At S_1 turn-off, the magnetizing inductor's current requires a conduction path, activating diode D_3. This transition ensures continuous energy transfer while preventing voltage spikes through controlled current diversion.

The forward-based converter goes to a zero state. The diode D_2 is conducted in the zero state, while D_1 is OFF. The capacitor C_1 is discharging and C_2 is charging reversely by the magnetizing current. It is possible to express the output voltage of the proposed solution by analyzing active and zero states and writing Kirchhoff equations. The average value of the output voltage depends on a transformer turns ratio, duty cycle and the input voltage:

$$V_O = \frac{v_{IN} \cdot \left(1 + N \cdot D \cdot \left(1 - D\right)\right)}{1 - D} \tag{2.4}$$

where v_{IN} is the input voltage, N is the step-up ratio of the transformer (n_2/n_1), D is the value of the duty cycle.

The average current of inductor L_1 corresponds to the average output current. The magnetizing current I_M is obtained by considering the input and the output current values:

$$I_{L1} = I_0 \,, I_M = \frac{I_{IN} - I_O}{D} - N \cdot I_O \tag{2.5}$$

where I_O is the average output current and I_{IN} is the average value of the input current.

The output voltage is composed of the voltages across capacitors C_1, C_2, along with the input voltage. The SSA analysis indicated that the average capacitor voltages vary and are influenced by the input voltage, duty cycle, and transformer turns ratio:

$$V_{C1} = V_{IN} \cdot N \cdot D \,, V_{C2} = \frac{V_{IN} \cdot D}{1 - D} \,. \tag{2.6}$$

Figure 2.11 illustrates that semiconductor voltage stresses rise with increasing input voltage, emphasizing the importance of selecting appropriate component voltage ratings. The semiconductor stress values determine the selection of transistors and diodes with the required breakdown voltages. These stresses are defined in eq. (2.6). Nevertheless, the capacitor voltage ripples were not considered:

$$V_{S1} = V_{D3} = V_{IN} + V_{C2} \,, V_{D1} = V_{C2} \cdot N \,, V_{D2} = V_{IN} \cdot N \,. \tag{2.7}$$

Since the proposed DC–DC converter uses a transformer-based topology, the design process may begin with calculating the magnetizing inductor. The inductance value is

defined by transformer parameters such as the number of windings, absolute permeability, and core material; the ripple of the magnetizing inductor current is obtained during the TON interval and depends on the input voltage, duty cycle, switching period, and magnetizing inductance:

$$L_M = \frac{\mu_{ef} \cdot \mu_0 \cdot n_1^2 \cdot A_{ef}}{L_{ef}} \ , \ di_{L_M} = \frac{V_{IN}}{L_M} \cdot D \cdot T \ . \tag{2.8}$$

where μ_{ef} is an effective relative permeability of the material, μ_0 is an absolute permeability of air or vacuum, n_1 is the winding turns number of the primary side of the transformer, A_{ef} is an effective cross-section area of the magnetic core, L_{ef} is the effective magnetic path length, T is the period of switching. The nominal forward inductance value can be obtained by considering the time interval from 0 to DT, which represents the active state. The inductor selection also relies on the operating mode of the proposed converter. The inductance formula is given below:

$$L_1 = \frac{V_{IN} \cdot N - V_{C1}}{di_{L1}} \cdot D \cdot T \ . \tag{2.9}$$

where di_{L1} is the current ripple in the forward cell inductor.

Figure 2.11 Voltage stress across semiconductors.

The determination of the capacitor values is more complex due to their interconnection. From the equivalent circuits, it can be observed that the capacitor ripples are influenced by the current i_x (Figure 2.9(a)) as well as by the output current:

$$C_1 = \frac{I_O - i_x}{dv_{C1}} \cdot D \cdot T \ , C_3 = \frac{i_x - I_O}{dv_{C3}} \cdot D \cdot T \ , C_2 = \frac{-i_x}{dv_{C2}} \cdot D \cdot T \ . \tag{2.10}$$

The capacitor expressions can be derived in terms of the voltage ripples of each capacitor. Capacitor C_2 may take a zero or arbitrary value, while capacitors C_1 and C_3 depend on C_2. The voltage ripple of capacitor C_2 is always equal to the sum of the ripples of the other capacitors:

$$dv_{C2} = dv_{C1} + dv_O \ , \ K_{C1} = \frac{dv_{C1}}{V_{C1}} \ , K_O = \frac{dv_O}{V_O} \ , \tag{2.11}$$

where dv_{C1}, dv_{C2} and dv_O are the ripples of the capacitors C_1, C_2, C_3 correspondingly. K_{C1} and K_O are ripple factors.

An alternative method for calculating the capacitor values is to transform the delta connection of C_1, C_2, C_3 into a star connection. After performing the calculations, the results should be converted back into the delta form, making it possible to determine the required capacitor values. The capacitor formulas are presented below:

$$C_1 = \frac{I_O \cdot D \cdot T + dv_{C1}C_2}{dv_{C1}} \, , C_3 = \frac{I_O \cdot D \cdot T - dv_{C1}C_2}{dv_O} \, , C_2 \in \forall \, . \tag{2.12}$$

The output inductance serves to filter the output current. Its value is proportionally dependent on the voltage ripple of capacitor C_3. The resulting expression for the output inductance is given as follows:

$$\int_{DT/2}^{(1+D)T/2} v_{L2} \cdot dt = \int_{DT/2}^{(1+D)T/2} \left(v_{C3} - V_O \right) \cdot dt \, , \ L_2 = \frac{dv_O \cdot T}{8 \cdot di_O} \, , \tag{2.13}$$

where v_{L2} is a voltage across inductor L_2, v_{C3} is the voltage on the capacitor C_3 with ripples, di_O is the output current ripple.

2.3.3 Experimental Results of Forward-Based Non-Isolated Solution

Figure 2.12(a) and (c) show the experimental prototype of the proposed non-isolated common-grounded forward-based DC–DC converter with a volume of 157 × 112 × 47 mm and maximum input power of 450 W. The prototype consists of power, control, and auxiliary parts, as well as EMI filter, additional output filter, Wi-Fi module, and hardware protection. Main parameters, including passive components, electrical specifications, and transformer data, are listed in Table 2.5. The control unit is based on an STM32H503CBT6 microcontroller, chosen for its low cost and sufficient timers and ADC channels. The converter operates from 15 V to 70 V input, with maximum input current of 11 A and output current of 1.3 A. Figure 2.12(b) shows the test setup used for measurements and debugging. The Tektronix MDO4034B-3 oscilloscope with isolated voltage and current probes was employed for accurate signal acquisition. STLink was used for MCU programming and debugging.
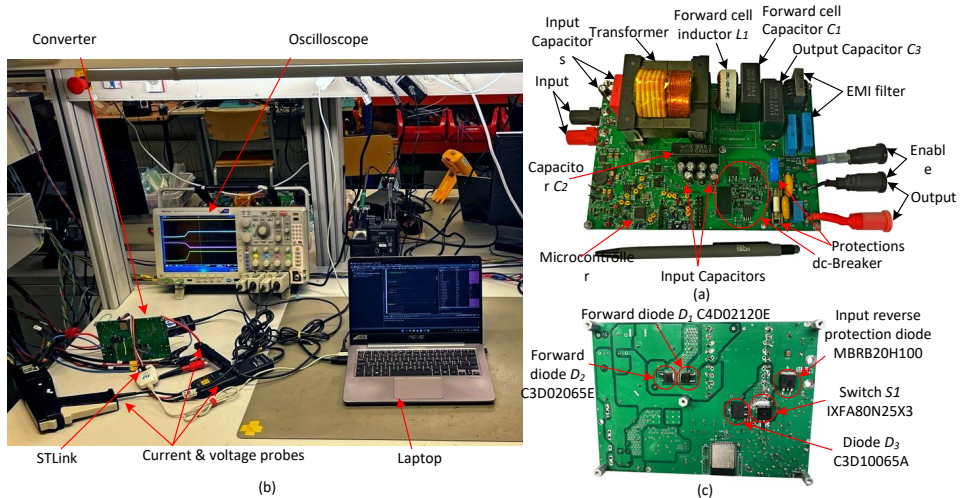

Figure 2.12 Experimental prototype of the proposed forward-based DC–DC converter: (a) top view, (b) experimental setup, (c) bottom view [PAPER-V].

The transformer core is ETD49-3C95 with 18 turns on the primary (0.04 mm × 2000 litz wire) and 98 turns on the secondary (0.1 mm × 45 litz wire). Windings were placed without overlapping to reduce parasitic capacitance, while the primary and secondary magnetizing inductances are 212 µH and 6.36 mH, respectively.

Table 2.5 Parameters of the proposed converter.

Parameter	Value
Input voltage range v_{IN}	15-70 V
Output voltage v_o	350 V
Max input power P_{INMAX}	450 W
Max input current i_{INMAX}	11 A
Max output current i_{OMAX}	1.3 A
Switching frequency f_{SW}	65 kHz
Input capacitor C_{IN}	110 uF
Forward cell capacitor C_1	10 uF
Clamp capacitor C_2	3.3 uF
Output capacitor C_3	10 uF
Secondary side capacitor Cx	2.5 nF
Forward cell inductor L_1	1000 uH
Output inductor L_2	100 uH
Transformer core	ETD49
Core Material Grade	3C95
Magnetizing inductor (pr) L_m	212 uH
Leakage inductance of transformer (pr) L_k	27 uH
Number of turns (pr) n_1	18
Number of turns (sec) n_2	98
Core airgap	400 um

Table 2.6 Possible semiconductors for the proposed solution.

Transistor/Diode Model	Designator	I, A	V_{BR}, V	R_{ON} or V_F	Price, €	Eff., %
IXFA80N25X3	S_1	80	250	16	8.98	95.65
IXFT120N25X3	S_1	120	250	12	13.21	↑0.1
IXFT150N25X3	S_1	150	250	9.0	24.3	↑0.16
UJ3C065030B3	S_1	65	650	35	17.42	↓0.22
IDM02G120C5	D_1, D_2	14	1200	1.65	2.63	95.65
C4D02120E	D_1, D_2	10	1200	1.8	3.03	↓0.05
SBR20A300	D_3	20	300	0.92	1.66	95.65
C3D10065E	D_3	32	650	1.8	6.05	↓0.3
IPD95R450P7	DC-br.	14	950	0.45	2.27	95.65
IPD80R280P7	DC-br.	17	800	0.28	2.64	↑0.05
IPB95R130PFD7	DC-br.	36.5	950	0.13	6.10	↑0.1

Table 2.6 presents possible semiconductor parameters for the proposed converter. Several sets of devices were selected for the experimental prototype, with the first set based on the cheapest available components. For switch S_1, the Si transistor IXFA80N25X3 has 16 mOhms of drain source resistor during the conducting state, and it is suitable for switch S_1. The drain-source breakdown voltage of that transistor is 250 V. For diodes D_1 and D_2, the SiC Schottky diode IDM02G120C5 was used as a low-cost option, while diode SBR20A300 was selected for D3. The DC-breaker is implemented as a four-quadrant switch using two series-connected transistors, with MOSFET IPD95R450P7 selected for cost efficiency. In the second case, the selected semiconductor set was: S_1 – IXFT150N25X3HV, D_1 and D_2 – IDM02G120C5, D_3 – SBR20A300, and the DC-breaker – IPB95R130PFD7 (2 transistors).
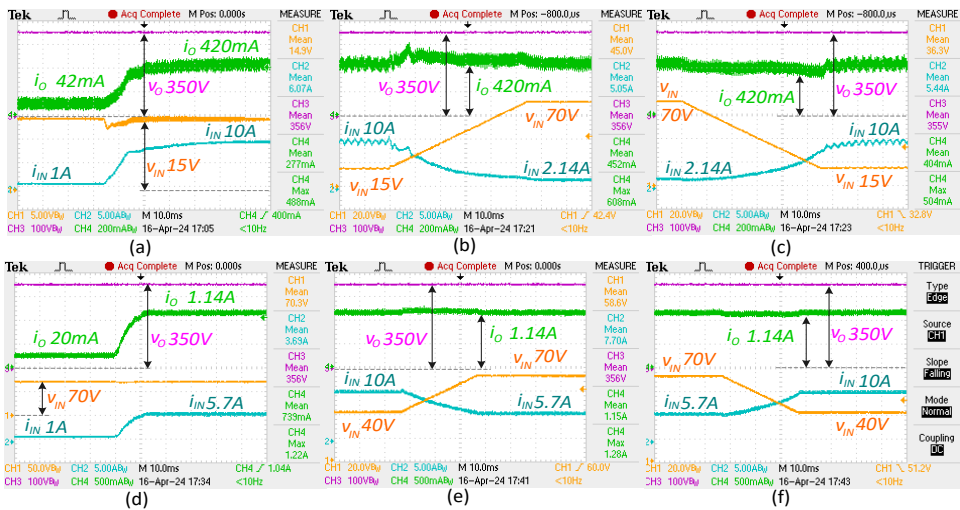

Figure 2.13 Experimental results of the proposed DC–DC converter under different input voltage and current various: (a) step change of the output current when the input voltage is 15V, (b) step change of the input voltage from 15 V to 70V, (c) step change of the input voltage from 70 V to 15 V, (d) step change of the output current when the input voltage is 70V, (e) step change of the input voltage from 40 V to 70V, (f) step change of the input voltage from 70 V to 40 V [PAPER-V].

The proposed converter was experimentally tested under both voltage and load step changes to evaluate its dynamic performance. The voltage steps were applied using a programmable DC power supply, while the load steps were generated through the control system. Figure 2.13 illustrates the corresponding experimental results. In Figure 2.13(a), the output current undergoes a step change from 42 mA to 420 mA with a fixed input voltage of 15 V. Since the input voltage remains constant, the input current changes accordingly from 1 A to 10 A. Figures 2.13(b)–(c) present the results of input voltage steps from 15 V to 70 V and vice versa, while maintaining a constant output current of 420 mA at a regulated output voltage of 350 V. Figures 2.13(d)–(f) show the experimental waveforms under the same test conditions when the input voltage is set to 70 V.
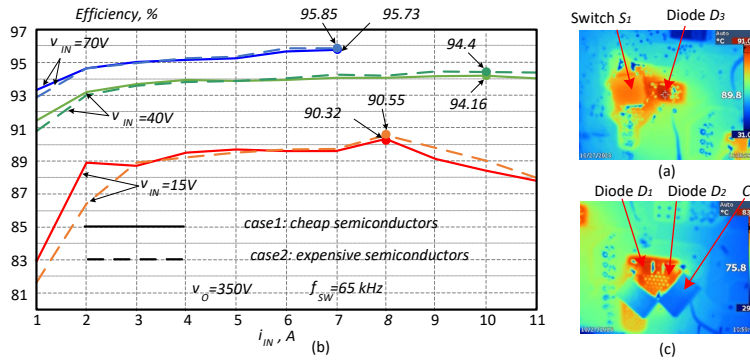
Figure 2.14(a) Thermal image of switch S_1 and diode D_3, (b) Efficiency study versus input current under different input voltages and with different sets of semiconductors, (c) Thermal image of diode D_1 and diode D_2 [PAPER-V].

Figure 2.14(a) and (c) shows thermal images and efficiency results of the proposed converter. Thermal images of switch S_1 and diode D_3 and diodes D_1 and D_2 were obtained using a Fluke Ti10 thermal camera, showing temperatures around 80 °C. The converter's efficiency depicted in Figure 2.14(b) is lower at low input voltages due to high input current and a large duty cycle. At 15 V input, the maximum efficiency is 90.55%, increasing with higher input voltage and reaching 95.85% at 70 V. Auxiliary losses are included in these measurements.

2.4 Summary

A comparative study of DC-DC converter topologies for renewable energy applications was carried out, focusing on performance, efficiency, and design feasibility. Several evaluation criteria were considered, with particular emphasis on the volume of passive elements, as this reflects the stored energies in inductors and capacitors and directly impacts converter cost, size, and dynamic response. A novel isolated buck-boost topology was developed, providing wide voltage regulation capability and achieving ZVS, which minimizes switching losses and improves efficiency. In addition, a forward-based non-isolated solution was proposed, addressing and effectively eliminating the leakage inductance issue typical of transformer-based converters. Both steady-state and transient analyses confirmed the design and stable operation. Experimental validation further demonstrated that the forward-based non-isolated solution is acceptable for low-power renewable applications and represents a strong candidate for practical deployment.

3 Comparative Analysis of Passive Decoupling Strategies

In a single-phase connection, the power delivered to the grid varies over time, while the power drawn from the PV panel must remain constant. Therefore, energy storage elements, typically capacitors, are employed between the input and output to equalize or decouple the mismatch between the instantaneous input DC power and the output AC power [69]. Several power decoupling techniques have been proposed and analyzed, taking into account efficiency, the size of decoupling capacitors, cost, and control complexity [70]. The configurations used to decouple the mismatch power for both single-stage and double-stage systems are shown in Figure 3.1

Based on the microinverter topology, decoupling methods can be either active, using an auxiliary circuit, or passive, and they can be placed on the PV side, DC-link side, or AC side (only active). Active decoupling schemes can extend the lifetime of a microinverter by replacing electrolytic capacitors with film capacitors. However, the auxiliary circuit introduces additional power losses, reducing overall efficiency. At the same time, smaller decoupling capacitors increase stress on the power devices, leading to higher losses and lower efficiency. Most commercial microinverters use electrolytic capacitors as energy storage for power decoupling, chosen for their high capacitance, cost-effectiveness, and ease of implementation. Nevertheless, this choice also limits the lifespan of the microinverter [PAPER-V].

Figure 3.1 Decoupling the mismatch power between DC and AC powers [PAPER-II].

In recent years, numerous studies have focused on flyback-based microinverters due to their low cost, reduced component count, galvanic isolation, high step-up ratio, simple control with a single active switch, and overall reliability. However, a major limitation is the large size of the flyback transformer core for powers exceeding 200 W, which is often addressed using an interleaved approach. Many efforts have aimed to improve flyback microinverter performance through both control and topology modifications. For instance, hybrid boost-flyback or flyback microinverters have been proposed to repurpose leakage energy and mitigate voltage spikes on the main switch. A novel, cost-effective, non-intrusive, isolated method for current sensing in grid-tied flyback-based microinverters was

introduced in [71], while another study proposed a flyback converter with active clamping and an unfolder [72]. Senseless control techniques for flyback microinverters have also been developed, eliminating current sensors to reduce overall cost and measurement noise [73]. Stability analysis of flyback converters has been explored in [74]. Although most research focuses on Discontinuous Conduction Mode (DCM) operation, DCM can lead to higher current stress, lower efficiency, and increased transformer losses [75]. Furthermore, there are increased hysteresis losses on magnetic material devices in addition to the challenges mentioned [76].

In microinverters, passive decoupling can be implemented on either the primary side (PV side) or the secondary side (DC link side). For secondary-side decoupling, two-level H-bridge inverters are commonly used, while for primary-side decoupling, unfolding circuits (pseudo DC link) are often adopted in industrial projects. Therefore, it is crucial to conduct a topological comparison of both configurations, considering energy stored in capacitors and inductors, as well as switching and conduction losses. Power losses associated with the main converter stage, including magnetic components, must also be evaluated for both H-bridge and unfolding-based microinverters. To ensure a fair comparison, an unfolding circuit can be used as a primary decoupling method to equalize the number of passive components between configurations, as illustrated in Figure 3.2. The unfolding bridge operates at line frequency to produce a rectified sinusoidal waveform at the DC link, while the H-bridge operates at high frequency and requires a bulky LCL filter to reduce harmonics and achieve low Total Harmonic Distortion (THD). Similar comparison methodologies between buck–boost and advanced H5, H6, and HERIC inverters are discussed in [77].

The results can be applied to any type of converter to evaluate the advantages of PV-side passive decoupling compared to DC-link-side decoupling. The flyback topology was chosen not for its topology-specific features, but to illustrate the decoupling approach itself. The topology selection is based on its wide applicability and common use. In the design process for both decoupling configurations, a fair comparison was ensured by using nearly identical components and thermal design, the same number of active and passive elements, and maintaining similar output current THD, which is critical for filter design.
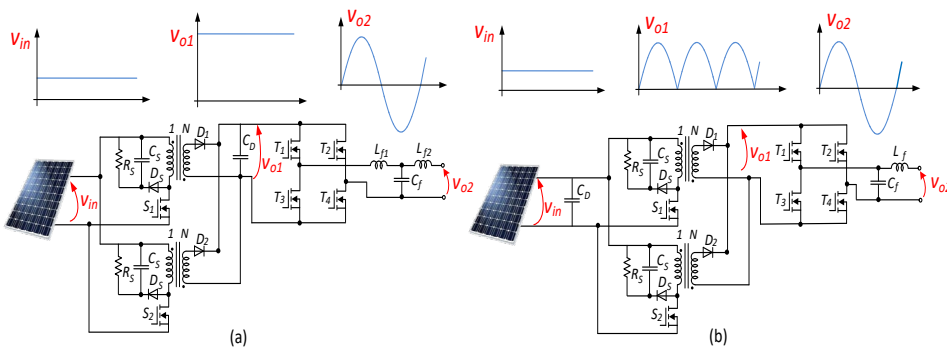

Figure 3.2 Flyback-based microinverter, (a) with a secondary side passive decoupling approach, and (b) with a PV side passive decoupling approach [PAPER-II].

3.1 Design Procedure

The flyback converter can operate in three modes: Continuous Conduction Mode (CCM), Discontinuous Conduction Mode (DCM), and Boundary or Critical Conduction Mode (BCM). Energy conversion is achieved by alternately switching the power transistor on and off, utilizing the transformer's magnetizing inductance (L_M). When the MOSFET switch is on, energy is stored in the magnetizing inductance; when the switch turns off, this energy is transferred to the load. In CCM, the switch is turned on before the secondary current reaches zero. Continuous mode allows higher power capability for a given peak current. For the same output power, peak currents in DCM are significantly higher than in CCM, necessitating a more expensive transistor with a higher current rating. Moreover, the higher secondary peak currents in DCM can produce larger transient voltage spikes during turn-off.

Despite the challenges, the discontinuous mode remains more favored than the continuous mode for two main reasons. Firstly, the inherently smaller magnetizing inductance in DCM results in a faster response and a lower transient output voltage spike when there is a sudden change in load current or input voltage. Secondly, CCM introduces a right-half-plane zero in its transfer function, making the design of the feedback control circuit more complex. Keeping these considerations in mind, the CCM mode is employed for operation due to its higher power capability. The equation (3.1) is derived through the point that in a steady state the average voltage of Inductance in one period is equal to zero. *D* is the duty ratio, and n is the turning ratio of the flyback transformer.

$$\int_0^{DT} (v_{in}) dt + \int_{DT}^{T} (-\frac{v_o}{n}) dt = 0 \rightarrow \frac{v_o}{v_{in}} = n \times \frac{D}{1-D}. \tag{3.1}$$

The operation mode is a boundary for $\Delta I_{Lm}/2 = I_{Lm}$ and is CCM for $\Delta I_{Lm}/2 < I_{Lm}$.

$$I_{Lm} = \frac{P_{in}}{v_{in} D}, \tag{3.2}$$

$$I_{Lm} = \frac{P_{in}}{v_{in} D}, \quad D = \frac{v_{Out}}{n v_{in} + v_{Out}}. \tag{3.3}$$

In CCM operation mode the magnetizing inductance is calculated through replacing equations number (3.2) and (3.3) in $\Delta I_{Lm}/2 < I_{Lm}$.

$$\frac{v_{inMax}^2 \cdot v_{Out}^2}{2 \cdot P_{in} \cdot f_s \cdot (n \cdot v_{inMax} + v_{Out})^2} < L_m. \tag{3.4}$$

The output instantaneous power, shown in Figure 3.1, consists of two components: the average output power ($V_m.I_m$)/2, and the time-varying component, or pulsating power, ($V_m.I_m cos(2\omega t)$)/2, which oscillates at twice the grid frequency. Here, ω is the grid frequency, I_m and V_m are the amplitudes of the grid voltage and current, respectively. The pulsating power must be balanced using a decoupling capacitor. This capacitor is selected through the following equation, where $\Delta V_c \leq 0 \cdot 05 \times V_c$. Through this formula, the difference in voltage results in different decoupling capacitor sizes.

$$P_{out}(t) = \frac{V_m \cdot I_m}{2} + \frac{V_m \cdot I_m}{2} \cos(2\omega t) \rightarrow \frac{P_{dc}}{2\pi \cdot f_{grid} \cdot V_C \cdot \Delta V_C} \leq C_D. \tag{3.5}$$

The output filter is a critical component in pulse-width modulation (PWM) converters. Although the THD level is similar in both topologies, the output filter and other passive components differ, which impacts overall cost and losses. In the H-bridge-based structure, the output filter must be relatively large to achieve an acceptable THD. In contrast, using the unfolding circuit instead of the H-bridge significantly reduces the required output filter size due to the lower harmonic content in the converter's output voltage at the switching frequency. C_f is limited to decrease the capacitive reactive power at a rated load to less than the predetermined relative value Δ.

$$C_f \leq \frac{\Delta \cdot P}{v_g^2 \cdot 2 \cdot \pi \cdot f_{grid}}, \tag{3.6}$$

where P and v_g are output power and voltage, respectively.

In the unfolding case, the grid side inductance is calculated based on equation (3.7).

$$L_f \geq \frac{v_i(h_{sw}) \cdot v_g}{P \cdot THD_V \cdot 2\pi f_{sw}} \cdot , \, v_i(h_{sw}) = \frac{P \cdot (1 - D_{MPPT})}{v_g \cdot C \cdot f_s}. \tag{3.7}$$

where $v_i(h_{sw})$ is the harmonic component of the converter output voltage at the switching frequency (f_{sw}).

In the case of H-bridge inverter, the following equation is used.

$$L = \frac{1}{4 \cdot \pi^2 \cdot C_f \cdot f_{RES}^2}, \tag{3.8}$$

L is weighted inductance value, is equal to $L_{f1}+L_{f2}$. The resonance frequency should be selected based on $10 f_{grid} < f_{RES} < 0.5 f_{sw}$. The design parameters are expressed in Table 3.1.

Table 3.1 Design Target parameters.

Parameter	Value
Input voltage (vin)	Vin=10V – 60V
MPPT voltage (VMPPT)	25V to 60V
Maximum power	600W
Flyback switches Switching frequency (fs)	40kHz
H-bridge switches Switching frequency (fs)	65kHz
Resonance frequency (fRES)	20kHz
Maximum DC-link voltage	400V
Grid frequency (fgrid)	50kHz
Turns ratio (n)	6

Considering the weighted inductance value, the converter side and grid side inductances can be calculated.

$$L_{f1} = \frac{1+r}{r} \times L, \, L_{f2} = r \cdot L_{f1} \tag{3.9}$$

To calculate the relation index between the two inductances the equation (3.10) is used, where r is the relation index and is *0 < r < 1.*

$$r^2(4\pi^2 f_{sw}^2 L^2 C_f - L) - (4\pi^2 f_{sw}^2 L^2 C_f + L) + r(8\pi^2 f_{sw}^2 L^2 C_f - 2L - \frac{v_i(h_{sw}) \cdot v_g}{P \cdot THD_V \cdot 2\pi f_{sw}}) = 0. \qquad (3.10)$$

The snubber circuit components are designed as explained in [PAPER-II].

The spider diagram in Figure 3.3 illustrates the comparison between H-bridge and unfolding-based microinverters across various criteria. Compared to the H-bridge-based flyback microinverter, the unfolding-based flyback microinverter requires a larger decoupling capacitance because the lower primary-side voltage leads to more energy being stored in the capacitor. At the same time, the total energy stored in the inductances remains approximately the same.

The larger coupled inductor required for the solution with the unfolding circuit is compensated by a smaller output filter. Due to the lower peak output voltage on the secondary side of the flyback transformer with the unfolding circuit, the voltage stress across switch S_1 is slightly reduced. Additionally, the drain-source voltage of switches T_1 to T_4 switches equals the maximum grid voltage. In contrast, for the H-bridge configuration, this voltage corresponds to the full DC-link voltage. Additionally, the unfolding-based approach exhibits significantly lower secondary high-voltage stress because the bridge switches operate at a low frequency. Consequently, the secondary-side switching losses are greatly reduced. However, the primary-side switching losses, as well as conduction losses on both the primary and secondary sides, are higher.
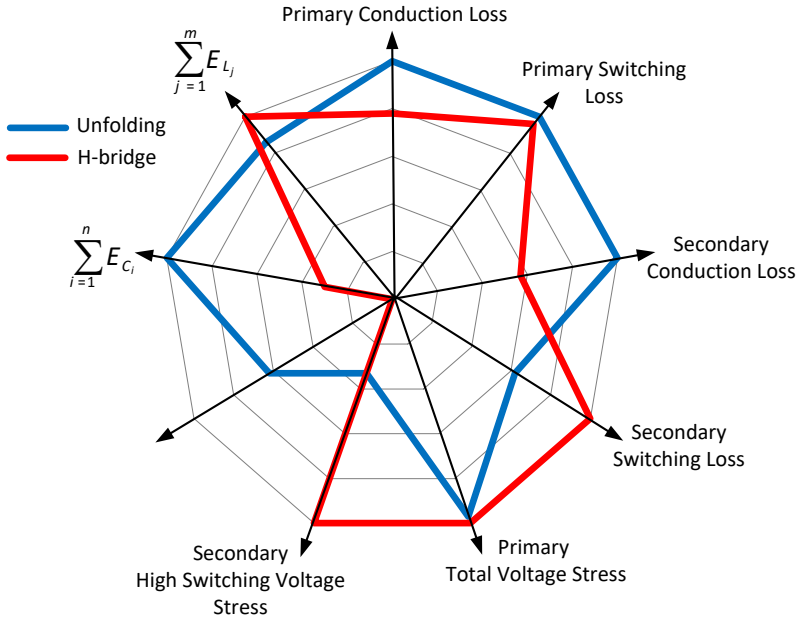

Figure 3.3 Comparison of H-bridge-based and unfolding-based flyback microinverters based on theoretical analysis [PAPER-II].
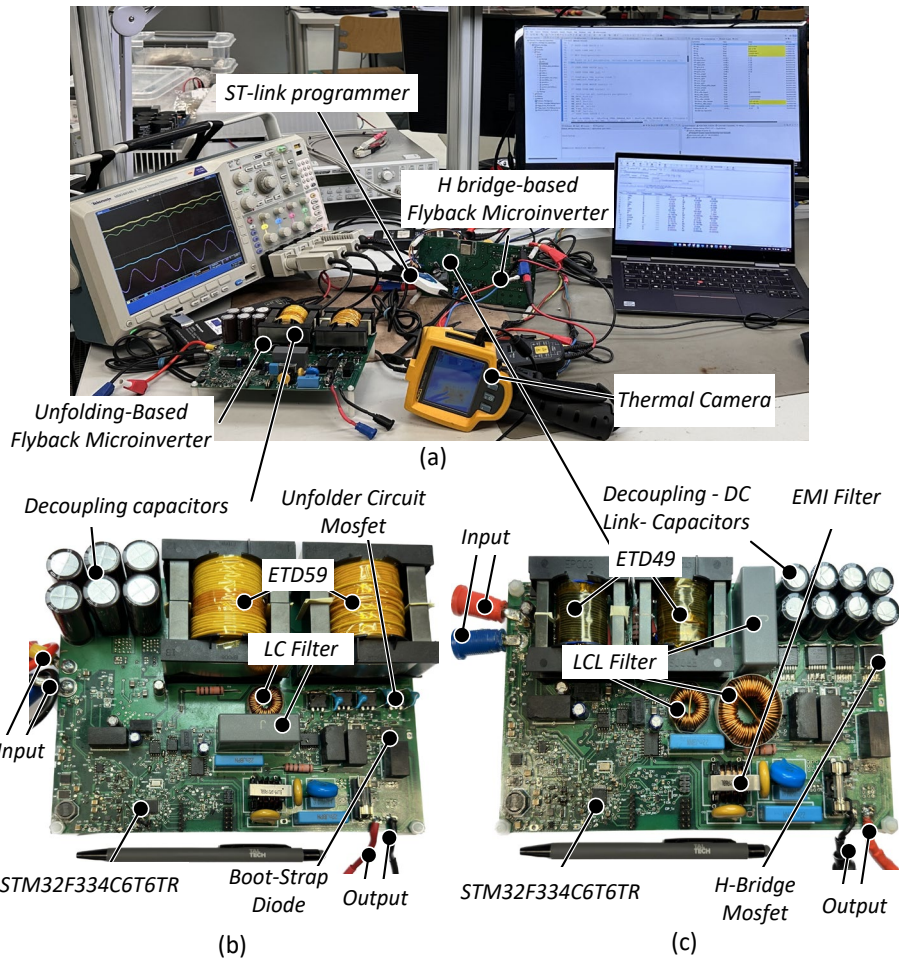
(a)

(b) **(c)**

Figure 3.4(a) laboratory-developed environment, (b) the unfolding-based flyback microinverter prototype, and (c) the prototype of the H-bridge-based flyback microinverter.

3.2 Experimental Verification

The unfolding-based flyback microinverter prototype, the laboratory test setup, and the H-bridge-based flyback microinverter prototype are shown in Figure 3.4(a), (b), and (c), respectively. Each prototype is implemented on a four-layer printed circuit board, incorporating the power stage, auxiliary circuitry, and control components. ETD59 and ETD49 cores are used for the interleaved flyback transformers in the primary and secondary side decoupling solutions, respectively.

Passive RCD snubbers are employed to reduce the voltage stress on the primary-side switches of the flyback converters, which arises from the resonance between the MOSFET's output capacitance, the leakage inductance, and the winding capacitance. Electrolytic capacitors are used as decoupling elements.

Table 3.2 contains electrical specifications, the physical size of the prototypes and values of the passive components, as well as core materials and electrical details of the transformers used in the experimental setups.

Table 3.2 Electrical specification.

Parameter / Specification	Value / Type		
	Primary side decoupling	Secondary side decoupling	
Converter volume (mm^3)	197.48*152.29*31.2	187.92*111.45*24.9	
Transformer Core/ normalized core volume (mm^3)	ETD59 / 100	ETD49 / 40	
Magnetic inductance (uH)	60		
Leakage inductance (nH)	370	450	
Decoupling capacitor (uF)	6 * 2200	8 * 22	
Output filter Capacitance (uF)	1		
Output filter inductance (uH)	Lf =220	Lf 1=680	Lf2 =180
Secondary diode	IDM05G120C5XTMA1		
Microcontroller	STM32F334C6T6TR		
Flyback switches	IPB044N15N5ATMA1		
Bridge switches	STB28N65M2	C3M0120065J	
Snubber capacitor (nF)	10		
Snubber Diode	MBR20H100CT		
Snubber Resistor (kΩ)	2.35		

Due to the line-frequency switching in the unfolding topology, conduction losses and the low turn-on resistance become key factors when selecting switches. The low RMS current allows for the use of a less expensive silicon-based switch, with only a minor reduction in the converter's efficiency. This represents a trade-off between cost and efficiency. Additionally, because dynamic performance requirements are minimal, these transistors have a low overall figure of merit, making them relatively inexpensive.

The control unit incorporates an ST microcontroller, STM32F334C6T6TR, which provides sufficient peripherals, including high-resolution timers and analog-to-digital converters A bootstrap circuit is implemented to reduce the number of power supplies required for the dual-output isolated drivers used in the bridge switches. However, this bootstrap cannot be used for a DC connection and low-side driver of the bridge must be supplied separately in such cases [78].
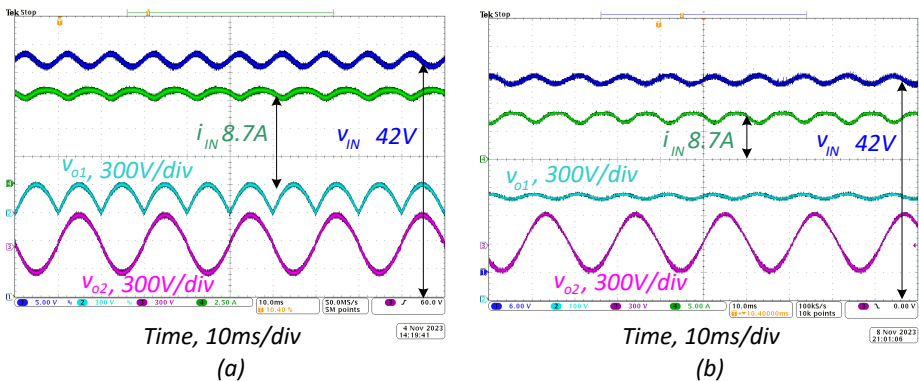

Figure 3.5(a) The unfolding-based flyback microinverter prototype. (b) Laboratory-developed environment. (c) The prototype of the H-bridge-based flyback microinverter [PAPER-II].

3.2.1 Efficiency Study

Both converters operate over an open-circuit voltage range of 25 V to 75 V and an MPPT voltage range of 25 V to 60 V. Figure 3.5(a) and (b) illustrate the desired operation of the primary-side and secondary-side decoupling-based flyback microinverters at an MPPT voltage point of 42 V and 8.7 A.

The DC-link and input voltage oscillations are presented to illustrate the decoupling process and validate the control methods discussed in the previous section. Additionally, the grid voltage and the output of the flyback converter are plotted to highlight the differences between H-bridge and unfolding operations. In the primary-side decoupling approach, the flyback converter produces a rectified sinusoidal waveform, which is then shaped into a near-ideal sinusoid by the unfolding bridge operation. This unfolding circuit offers a practical advantage, as it operates at grid frequency, allowing for a significantly smaller output filter compared to the H-bridge configuration.

Figure 3.6(a) and (c) show the thermal images of the unfolding-based and H-bridge-based solutions, respectively, highlighting the hottest points during operation at a maximum output power of 600 W. Figure 3.6(b) presents the efficiency curves for varying input voltages at a constant input current of 9 A, measured using the Yokogawa WT1800E high-performance power analyzer. As expected, the efficiency of both solutions decreases at lower input voltages due to the higher input current and larger duty cycle. The maximum efficiency at an input voltage of 54 V reaches 91% for the secondary-side decoupling approach and 94.4% for the primary-side decoupling approach, with auxiliary losses included.
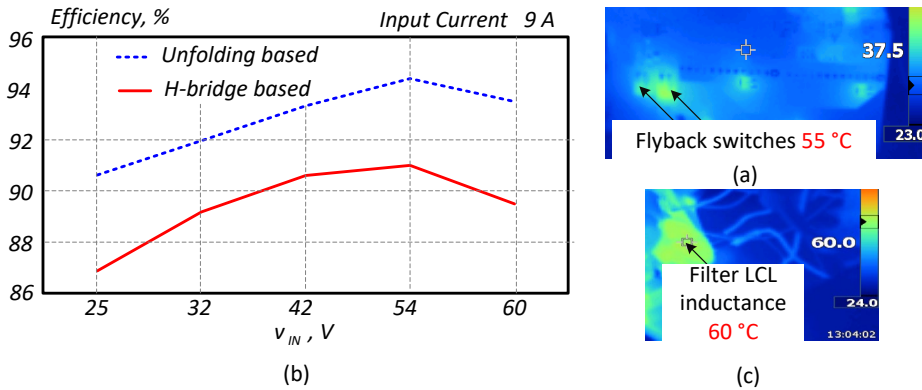

Figure 3.6(a) Thermal image depicting the hottest points during operation in the maximum 600 W output power in unfolding case,(b)Efficiency study versus different input voltages under constant input current, and (c) Thermal image depicting the hottest points during operation in the maximum 600 W output power in H bridge case [PAPER-II].

3.2.2 Cost Comparison

Figure 3.7 presents a comprehensive comparison of component costs for different production quantities between H-bridge-based and unfolding-based flyback microinverters. For a more detailed cost breakdown, the individual component costs are provided in Table 3.3.

The information presented in Table 3.3 and Figure 3.7 provides a detailed breakdown of the cost analysis, focusing on the number of semiconductor elements in the power circuit, including switches and diodes, as well as the quantity of capacitors, inductors,

and auxiliary components. It is important to note that auxiliary components such as those on driver boards, control circuits, auxiliary power supplies, and protective elements—contribute a consistent cost across both converters. Additionally, the data in this figure is based on current component prices obtained from distributor webpages.

As a classical cost function, the grid current serves as the main parameter for regulation. Simple differential equations can be employed to predict its behavior. A specific adjustment of the duty cycle is defined, where the new duty cycle value can be selected within a range of 0.5% to 3% around the open-loop voltage ratio.

Upon examination of Figure 3.7, it is evident that the costs of capacitors, PCBs, and inductive elements in the H-bridge-based microinverter are relatively lower than in the Unfolding-based microinverter. Consequently, for a smaller number of assemblies, the overall cost of the H-bridge-based microinverter is somewhat more economical compared to its Unfolding-based counterpart.
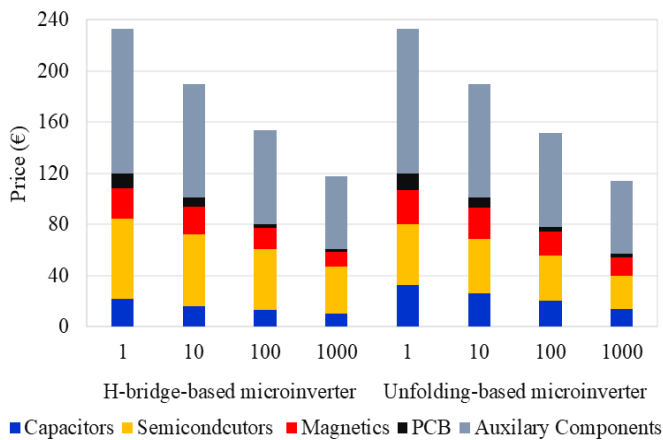

Figure 3.7 The cost graph of the H-bridge and Unfolding-based flyback microinverters for different numbers of assemblies [PAPER-II].

Table 3.3 Cost comparison of the Unfolding-based and H-bridge-based microinverters.

Characteristic	All components of the power circuit							
	Price (€)				Price (€)			
	H-bridge-based				Unfolding-based			
No. assembly	1	10	100	1000	1	10	100	1000
Capacitors	21	16	13	10	32	26	20	14
Semiconductors	63	57	48	37	48	43	36	26
Magnetics	24	22	17	12	27	24	19	14
PCB	11	7	3	2	13	8	4	3
Auxiliary Components	113	89	74	57	113	89	74	57
Total Price	233	190	153	118	233	190	152	114

It is essential to recognize that, although the total cost of the H-bridge-based microinverter may be lower for small production volumes, the cost of semiconductors which constitutes a substantial portion of the overall expense is reduced in the Unfolding-based microinverter. Moreover, at higher production volumes, the overall cost of the Unfolding-based microinverter becomes lower than that of the H-bridge-based design. By optimizing components such as PCBs and magnetic elements in future

iterations, the Unfolding-based microinverter has the potential to achieve a more cost-effective design. Coupled with reduced semiconductor expenses, this positions the Unfolding-based microinverter for a competitive pricing advantage.

The chart in Figure 3.8 compares flyback-based microinverters employing primary- and secondary-side fundamental power decoupling approaches across key factors, including efficiency, size, and cost. Notably, the Unfolding-based approach demonstrates higher efficiency while maintaining nearly identical costs, making it particularly advantageous for large-scale production scenarios

In terms of size, the use of a larger transformer and a relatively higher-capacitance decoupling capacitor in the unfolding-based microinverter results in a slightly increased physical footprint. Despite this, the primary-side decoupling approach offers a significant advantage: by employing low-voltage, high-capacity decoupling capacitors, it enhances both the lifetime and reliability of the microinverter.
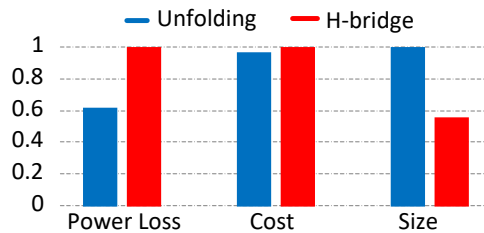

Figure 3.8 Comparison between the flyback-based microinverter using primary and secondary side decoupling approaches in terms of cost, size and efficiency [PAPER-II].

3.3 Summary

This chapter analyses flyback-based microinverters, comparing primary-side (PV) and secondary-side (DC-link) power decoupling. A fair comparative framework evaluated efficiency, cost, size, and performance. Experimental validation confirmed that primary-side decoupling enables a significant reduction in passive component size and cost while maintaining stability, making it ideal for compact, cost-sensitive designs. Secondary-side decoupling offers greater robustness across wider operating variations but requires larger, more expensive components. The study concludes that primary-side decoupling presents a superior trade-off for modern solar applications, favouring large-scale production. The presented design guidelines and comparative methodology are also applicable to other converter topologies for renewable energy integration.

4 Closed-Loop Control, Synergetic Control, and Experimental Validation of the Proposed Universal Microconverter

This section presents a control concept for a universal solar microconverter capable of operating with either DC or single-phase AC grids using the same power terminals. The proposed microconverter solution is based on an advanced non-isolated forward DC–DC converter, which offers a wide input voltage regulation range and a low component count. A novel synergetic control strategy, a combination of high-frequency and low-frequency operation, is employed in the inverter stage, where the control of the inverter bridge is optimized for improved performance and efficiency. A synergetic control strategy is introduced for the forward-based microinverter operating in AC mode, enabling a cost-effective single-stage architecture across a broad range of operations.

To validate the concept, power loss evaluation under synergetic control is carried out, followed by experimental testing of a laboratory prototype. The results confirm high performance with reliable control of both input and output variables. A comparative analysis with the interleaved single-stage flyback topology further highlights the advantages of the proposed design. While both topologies achieve practical performance, the forward-based universal microconverter demonstrates superior efficiency, competitive cost distribution, and industrial scalability. By reducing semiconductor and auxiliary costs and optimising the use of magnetic and PCB elements, it positions itself as a practical alternative for large-scale, cost-effective deployment.

4.1 Operation of Proposed Universal DC–DC/AC Microconverter Solution

A forward-based non-isolated microconverter topology, as shown in Figure 4.1, is proposed. The DC–DC part is presented in Chapter 2. This configuration achieves high voltage gain while overcoming the drawbacks of both flyback and transformerless designs. The modification in the forward converter eliminates issues related to leakage inductance and voltage overshoots without requiring snubber circuits. Moreover, its common-grounded, non-isolated structure removes the leakage current path typically seen in transformerless systems.

The proposed topology belongs to the single-stage, wide-operation-range, non-isolated category, offering significant advantages in cost and efficiency, particularly for large-scale manufacturing. While it incorporates more semiconductor devices, it requires only a single active switch, ensuring conduction losses remain comparable to those of flyback converters. Importantly, the secondary-side inductance does not increase the total stored magnetic energy, and the cascaded output capacitors do not add to the total capacitive energy relative to conventional designs. The proposed design reduces galvanic isolation to only the high-side gate drivers and current sensors, ensuring compactness, efficiency, and cost-effectiveness.

Figure 4.1 Proposed dual-purpose forward-based microconverter [PAPER-I].
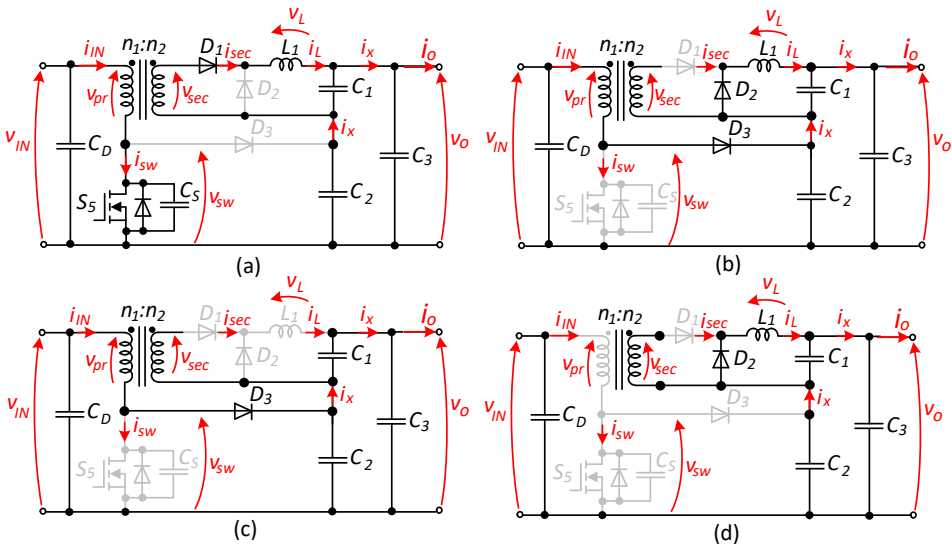
Figure 4.2 Operation modes of forward-based stage in the proposed microconverter: (a) active state, (b) zero state, (c) DCM of inductor current, (d) DCM of the primary current.
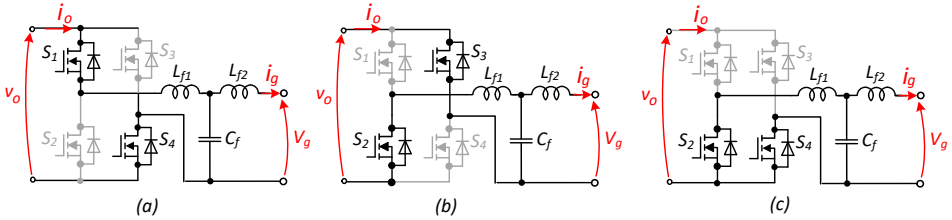

Figure 4.3 Operation modes of the bridge stage in the proposed microconverter. Connection to (a) DC or positive half cycle of AC, (b) negative half cycle of AC, and (c) zero level in unipolar PWM mode for AC.

Due to the presence of diode D_1, the proposed topology employs a hybrid control strategy that integrates high-frequency and low-frequency operation, thereby exploiting the advantages of both modes. The system is evaluated through Steady-State Analysis (SSA), with its operating modes depicted in Figure 4.2 and Figure 4.3.

Figure 4.2 illustrates the operating modes of the forward-based stage, which functions primarily as a DC–DC or DC-to-rectified-AC converter. In this process, energy transfer and storage are managed by the transformer and the magnetizing inductor. The specific operating states are described below.

• Active State (Figure 4.2(a)): When the primary switch S_5 is turned ON, energy flows from the input to the secondary winding of the transformer. The magnetizing inductance simultaneously begins storing energy. Diode D_1 conducts current to the output, while diodes D_2 and D_3 remain reverse-biased (OFF). Capacitor C_1 charges, and C_2 supplies the load.

• Zero State (Figure 4.2(b)): When S_5 switches OFF, the energy stored in the magnetizing inductor needs a path to discharge. Diode D_3 becomes forward biased and carries the magnetizing current. At the same time, D_2 conducts while D_1 turns OFF. Capacitor C_1 discharges, and C_2 is recharged by the reverse-flowing magnetizing current.

45

• Discontinuous Conduction Mode (DCM) of the Inductor (Figure 4.2(c)): Once the energy in the inductors is fully delivered, the inductor current drops to zero, signaling entry into Discontinuous Conduction Mode (DCM). This mode generally happens under light load conditions.

• DCM of Primary Current (Figure 4.2(d)): Similarly, the primary current transitions into discontinuous mode during light load or certain modulation conditions, which lowers conduction losses while adding complexity to the control.

The bridge stage operation in the proposed microconverter depends on the desired output polarity. For DC output or the positive AC half-cycle (Figure 4.3(a)), switches S_2 and S_3 turn ON, directing energy from the forward stage to the load with proper polarity. During the negative AC half-cycle (Figure 4.3(b)), switches S_4 and S_5 conduct, reversing the output polarity and completing the full waveform.

To produce a zero-voltage interval needed for unipolar PWM modulation (Figure 4.3(c)), all switches are turned OFF, temporarily disconnecting the output. This approach enables efficient AC output generation while minimizing harmonic distortion.

4.2 Closed-Loop Control Strategy for Universal Microconverter

Figure 4.4 depicts the control flowchart implemented in the proposed universal solar microconverter, which enables automatic selection between AC and DC grid operation. The process begins with a software-based protection routine that checks whether measured parameters—including voltage, current, and temperature—remain within predetermined safe limits. This safeguard ensures reliable operation and prevents potential damage during startup or transient conditions. Once the protection verification is successfully completed, the controller examines the output voltage to determine whether it is suitable for connection to a 230 V, 50 Hz AC grid or a 350 V nominal DC microgrid. These voltage thresholds correspond to standard residential distribution levels and align with the converter's rated maximum output of 450 W, associated with input voltage and current limits of 75 V and 13 A, respectively. If the output voltage falls within acceptable bounds for both grid types, the control system then evaluates the synchronization status of the grid to ensure safe and efficient power injection.
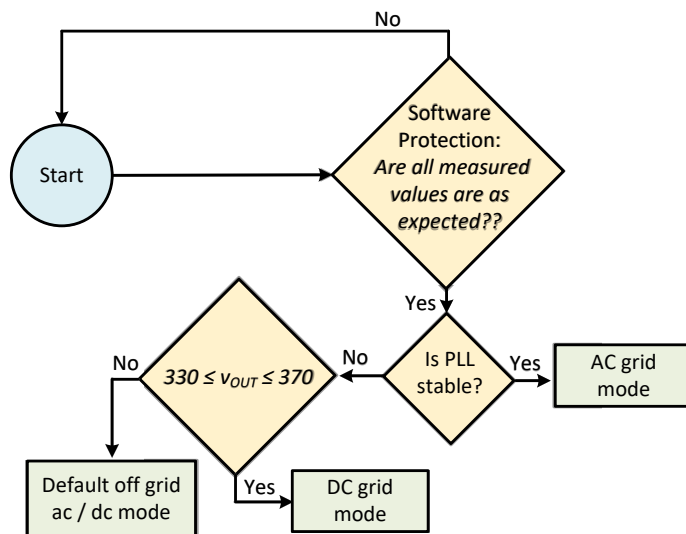

Figure 4.4 Control concept of universal microconverter.

The Phase-Locked Loop (PLL) monitors the AC grid to detect a valid and stable reference. When the PLL is synchronized and stable, the system automatically switches to AC grid-connected operation. If the PLL cannot establish a stable grid due to frequency instability, absence of a voltage reference, or voltage levels outside acceptable AC limits the controller then verifies the presence of a DC grid. A DC grid is considered valid when the output voltage falls within 320 V to 370 V. Upon meeting this criterion, the converter operates in DC grid-connected mode, ensuring proper functionality under either grid type.

If neither a valid AC nor DC grid is detected, the system switches to an autonomous off-grid mode. In this mode, a voltage-mode control scheme is employed to maintain the output voltage independently of external grid conditions. This guarantees uninterrupted operation for connected loads even when no grid reference is available. The control strategy, illustrated in Figure 4.5(a) and (b), allows smooth transitions and seamless adaptation between AC and DC operation within a unified microconverter architecture.

$$D = \frac{N \cdot v_{IN} + |v_M| - \sqrt{(N \cdot v_{IN} - |v_M|)^2 + 4 \cdot N \cdot v_{IN}^2}}{2 \cdot N \cdot v_{IN}}$$

(a)

(c)

Figure 4.5(a) Control methodology for a DC microgrid, (b) Synergetic control methodology for an AC microgrid.

4.2.1 Control Strategy for a DC Microgrid Mode

Figure 4.5(a) shows the control framework for DC-grid operation. This structure resembles the AC-grid configuration, especially in the unfolding control, which relies on zero-crossing detection. A Proportional-Integral (PI) controller manages the forward-stage output voltage, which sets the reference current for power delivery to the grid. The reference current is continuously adjusted by a Maximum Power Point Tracking (MPPT) module using the hill-climbing algorithm, ensuring the photovoltaic system operates near its peak power under varying solar irradiation. The forward-based DC–DC converter uses a single switch, requiring only one Pulse Width Modulation (PWM) signal. Furthermore, a DC breaker is employed to support the current control system.
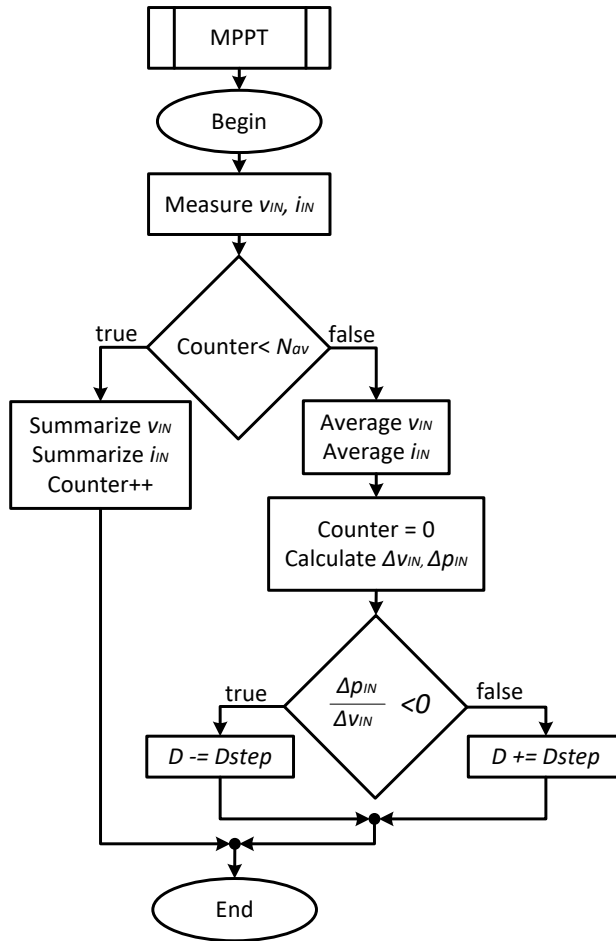
Figure 4.6 Flowchart diagram of the MPPT hill climbing technique for the forward based DC–DC converter [79].

The MPPT directly adjusts the duty cycle *D* of the control signal for switch S_5. The control system considers both the current and previously measured input voltage and current values. The converter's output is connected to the DC grid, while diodes on the secondary side prevent reverse current flow from the grid, eliminating the need for explicit output current control. Nonetheless, measuring the output voltage and current remains necessary for verifying DC grid availability, implementing droop control, and supporting the software protection system. This protection system monitors input and output voltages and currents to detect overvoltage and overcurrent conditions.

The flowchart of the MPPT algorithm is depicted in Figure. 4.6. The algorithm starts with a measurement of the input voltage and current. These values are averaging by software to avoid noise and ripples of measurements. That is why there is the counter which counts until some number N_{av} that regards to the averaging period. When the counter reaches the N_{av} value the system calculates the deviations of the input voltage and input power. Similar to P&O technique the HC algorithm computes the ratio of the change in input power to the change in input voltage ($\Delta p_{IN}/\Delta v_{IN}$).

There are 4 zones of working MPPT: zone 1- $\Delta v_{IN}\downarrow$, $\Delta p_{IN}\uparrow$, zone 2- $\Delta v_{IN}\uparrow$, $\Delta p_{IN}\downarrow$, zone 3- $\Delta v_{IN}\uparrow$, $\Delta p_{IN}\uparrow$, zone 4- $\Delta v_{IN}\downarrow$, $\Delta p_{IN}\downarrow$. When ratio $\Delta p_{IN}/\Delta v_{IN}$ is less than zero, it corresponded to the right side of the PV characteristic according to the MPP (zone 1 and zone 2). The current duty cycle D should be decreased on D_{step}. In another case, the ratio is positive. This case corresponded to zone 3 and zone 4. The duty cycle D should be increased on D_{step} in this case. The changing of the duty cycle can be increased or decreased with different steps [79].

The PI-controlled output capacitor voltage establishes a stable reference for regulating the output current, ensuring efficient and consistent power transfer to the DC grid. A soft-start procedure precharges the output capacitor to the 350 V grid level before closing the circuit breaker, preventing inrush currents and enabling smooth grid connection.

4.2.2 Synergistic Control in an AC Microgrid Mode

The proposed universal solar microconverter supports both double-stage and a combination of single-stage and double-stage configurations for AC microgrid interfacing. Although the double-stage design is possible, it requires larger energy storage components, namely capacitors C_1, C_2, and C_3. These larger capacitors increase both the cost and size of the system, making this configuration less attractive for cost-sensitive or space-constrained applications.

The single-stage configuration provides notable efficiency gains and cost savings, especially for large-scale production. Additionally, integrating low-frequency unfolding circuits in single-stage designs reduces switching losses, enhancing thermal performance and system reliability. However, continuous single-stage operation is limited by diode D1, which transfers the input voltage to the output in the forward-based non-isolated topology, preventing full single-stage operation with an AC load. To address this, the proposed microconverter employs a synergetic control method, dynamically switching between single- and double-stage modes according to real-time operating conditions.
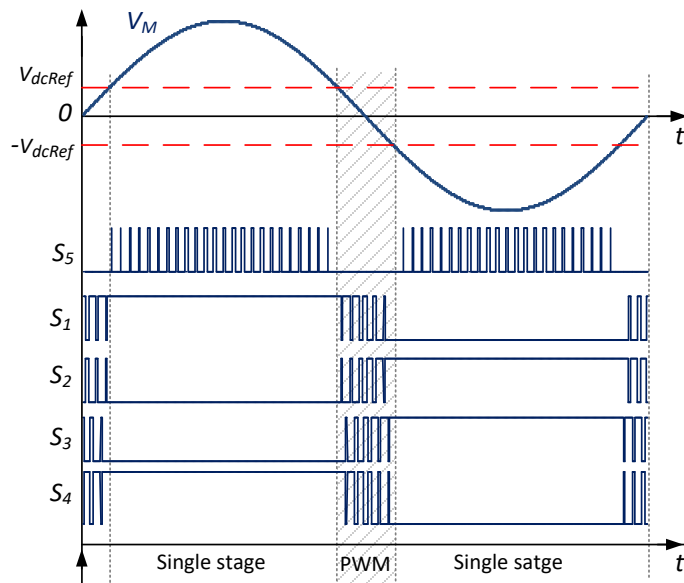

Figure 4.7 Switches signal considering synergetic control for AC mode.

The dual-mode operation combines a high-frequency unipolar pulse modulation with a low-frequency (100 Hz) unfolding method, as shown in Figure 4.7. This setup allows the forward-based microinverter to operate efficiently on AC grids by switching modes according to the real-time ratio of the forward stage output voltage to the input voltage. In high-frequency mode, when the controller output V_M is below the desired DC-link voltage (V_{dcRef}), a three-level unipolar PWM is applied to produce a rectified sinusoidal waveform, minimizing switching losses and enhancing efficiency. When V_M surpasses V_{dcRef}, the system shifts to low-frequency operation using a simplified two-level switching approach through the unfolding circuit, reducing switching frequency and losses while maintaining effective power delivery.

The proposed synergetic control framework, shown in Figure 4.5(b), is an adaptation of the strategy introduced in [80]. It incorporates a PLL block for grid phase synchronization and precise angle detection, ensuring the inverter output remains aligned with the grid voltage. The combined operation of the Proportional Resonance (PR) and Repetitive Controller (RC) enhances current tracking and reduces V_{dcRef} – crossing distortions, which are typical in PR-only designs. Additionally, a Proposition (P) block is integrated into the double-stage control to stabilize the DC-link voltage around the reference V_{dcRef}, which is selected near the maximum open-circuit voltage of each panel.

4.3 Power Loss Evaluation of Proposed Microconverter Using Synergetic Control Methodology

The theoretical analysis considers only the ideal scenario, ignoring parasitic effects from passive components and the transformer. The total converter losses can then be determined using the following equation:

$$P_{Total} = P_{CL} + P_{DL} + P_{cu} + P_{core} \tag{4.1}$$

where P_{CL} is a total conduction loss which includes the semiconductor's static loss and inductance ESR loss, P_{DL} is a dynamic loss which includes the semiconductor's dynamic loss, P_{cu} is copper loss of transformer, and P_{coper} is loss of the core of the transformer. The duty cycle value is obtained by using steady-state analysis:

$$D = \frac{N \cdot v_{IN} + V_O - \sqrt{\left(N \cdot v_{IN} - V_O\right)^2 + 4 \cdot N \cdot v_{IN}^2}}{2 \cdot N \cdot v_{IN}} \tag{4.2}$$

where v_{IN} is the input voltage, N is the step-up ratio of the transformer (n_2/n_1), and D is the value of the duty cycle.

According to the control methodology illustrated in Figure 4.5, the output voltage of the forward stage is 350 V in DC mode and can be expressed for AC mode as follows:

$$V_O = \begin{cases} \left|V_M \sin(\omega t)\right| & \left|V_M \sin(\omega t)\right| > V_{dcRef} \\ V_{dcRef} & \left|V_M \sin(\omega t)\right| \le V_{dcRef} \end{cases} \tag{4.3}$$

V_M is the peak ac grid voltage and ω is the angular grid frequency.

Magnetic losses can be determined by following the approach: First, the flux density must be defined. Its calculation should account for the maximum area (λ_1) of the transformer's primary voltage, corresponding to the peak input voltage of 70 V. The number of primary windings is then derived from the flux density equation:

$$\Delta B = \frac{\lambda_1}{2 \cdot n_1 \cdot A_e} = \frac{v_{IN} \cdot D \cdot T}{2 \cdot n_1 \cdot A_e} \, , \, n_1 = \frac{v_{IN} \cdot D \cdot T}{2 \cdot \Delta B \cdot A_e} \, , \tag{4.4}$$

The time-average power loss per unit volume for non-sinusoidal voltage across the transformer depends on the frequency, constants found by curve fitting (α and β), number of turns and the cross-sectional core area and flux density. Therefore, the core loss of the transformer can be found by multiple time-average power loss and an effective magnetic volume:

$$\overline{P_v} = k_i \cdot \frac{\Delta B^{\beta - \alpha}}{T} \cdot \left(\frac{v_{IN}}{n_1 \cdot A_e} \right)^\alpha \cdot D \cdot T + k_i \cdot \frac{\Delta B^{\beta - \alpha}}{T} \cdot \left(\frac{v_{C2}}{n_1 \cdot A_e} \right)^\alpha \cdot T \cdot (1 - D) \, , \, P_{CORE} = \overline{P_v} \cdot V_e \, ,$$

$$k_i = \frac{C_M \cdot \left(C_{t2} \cdot T_C^2 - C_{t1} \cdot T_C + C_t \right)}{2^{\beta + 1} \cdot \pi^{\alpha - 1} \cdot \left(0.2761 + \dfrac{1.7061}{\alpha + 1.354} \right)} \, , \tag{4.5}$$

where T_c is the temperature of the core, C_M, C_{t1}, C_{t2}, and C_t are temperature Steinmetz coefficients.

The copper loss of the transformer is possible to calculate by using the below equation:

$$P_{CU} = \left(\frac{\rho \cdot \lambda_1^2 \cdot I_{tot}^2}{4 \cdot K_U} \right) \cdot \left(\frac{MLT}{W_A \cdot A_e^2} \right) \cdot \left(\frac{1}{\Delta B} \right)^2 \tag{4.6}$$

where ρ is wire effective resistivity, *Itot* is the total *RMS* winding currents, *MLT* is the mean length per turn, W_A is a core window area, and K_U is a winding fill factor.

Semiconductor losses are divided into conduction losses and switching (dynamic) losses. Diode conduction losses depend on the forward voltage and average current. Switch conduction losses are determined by the ON-state resistance of the transistor and its RMS current, with *i* representing the switch number. Additionally, the conduction losses of the inductor ESRs are included:

$$P_{CL} = \sum_{i=1}^{7} I_{sw_i RMS}^2 \cdot R_{ONsw_i} + I_{LRMS}^2 \cdot R_L + I_{ORMS}^2 \cdot R_O + I_{D1} \cdot V_{D1} + I_{D2} \cdot V_{D2} + I_{D3} \cdot V_{D3} \tag{4.7}$$

The dynamic losses of switches and diodes can be calculated by using the next equations:

$$P_{DL} = \sum_{i=1}^{5} \frac{1}{T} \cdot \left(\frac{t_{DONsw_i} + t_{rsw_i} + T_{DOFFsw_i} + t_{fsw_i}}{2} \cdot I_{P\_AVGsw_i} \cdot V_{P\_AVGsw_i} \right) + \underbrace{\frac{5}{4} \cdot Q_{rrD1} \cdot V_{P\_AVGD1}}_{P_{D1DYN}} +$$

$$+ \underbrace{\frac{5}{4} \cdot Q_{rrD2} \cdot V_{P\_AVGD2}}_{P_{D2DYN}} + \underbrace{\frac{5}{4} \cdot Q_{rrD3} \cdot V_{P\_AVGD3}}_{P_{D3DYN}} \, , \tag{4.8}$$

where t_{DON} is the turn on the delay time, t_r is the rise time of the transistor, t_{DOFF} is the turn-off delay time, t_f is the fall time, I_{P_AVG} equals an average value of transistor current spikes during the grid period, V_{P_AVG} is the average value of the transistor drain source stress during the sine period, Q_{rr} is the reverse recovery charge of the diode.

All the previously described equations can be directly used to estimate power losses during DC operation. In contrast, for AC mode, the voltages and currents in both semiconductor and passive components fluctuate continuously because of the instantaneous variations in the duty cycle.
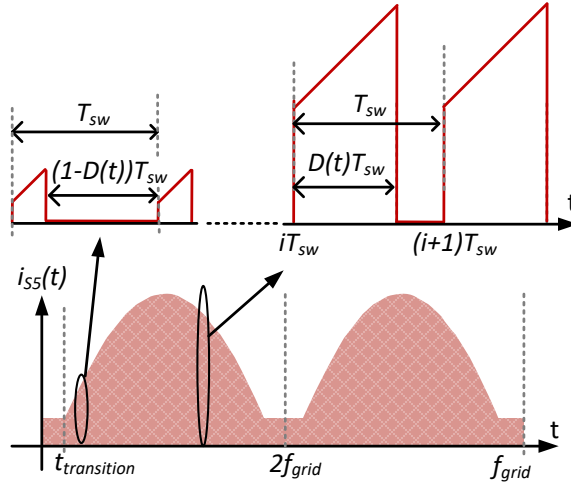
Figure 4.8 Forward Switch current with duty cycle variation.

When operating in AC mode, as illustrated by the forward switch current in Figure 4.8, even the peak values vary over time. To accurately assess power losses under these conditions, the following equations are applied to calculate the RMS and average current values.

$$F_{rms} = \sqrt{2 \cdot f_{grid} \cdot \sum_{i=0}^{m} (\int_{iT_{sw}}^{(i+d(i))T_{sw}} F(i)^2 dt + \int_{(i+d(i))T_{sw}}^{(i+1)T_{sw}} F(i)^2 dt)} ,$$

$$F_{ave} = 2 \cdot f_{grid} \cdot \sum_{i=0}^{m} (\int_{iT_{sw}}^{(i+d(i))T_{sw}} F(i) dt + \int_{(i+d(i))T_{sw}}^{(i+1)T_{sw}} F(i) dt). \quad (4.9)$$

where F_{rms} and F_{ave} are the RMS and average value of desired function for the grid period respectively. T_{sw} is the switching period, and "i" is the current number of high-switching period. m is the total number of high switching period in the fundamental period, which is equal to $2T_{grid}/T_{sw}$ which is 500 for 50 Hz grid with 50 KHz switching frequency. Moreover, any power signal or other variables are calculated as functions of the current switching period.

$$\varphi \rightarrow \varphi(i) = \omega_0 \cdot i \cdot T_{sw} . \quad (4.10)$$

To determine the bridge power losses, it is essential to identify the transition time ($t_{transition}$) from unfolder operation to unipolar PWM mode.

$$t_{transition} = \frac{\arcsin(V_{dcRef}/V_M)}{\omega_0} . \quad (4.11)$$

The input current of the transformer, calculated as:

$$i_{IN} = \frac{2P_{PV}}{V_{IN}} \cdot \sin^2(\omega t) , \quad (4.12)$$

where the P_{PV} and V_{IN} are input power and voltage.

As shown in Figure 4.9, the converter's performance was assessed using analytical methods. Figure 4.9(a) depicts the calculated efficiency for a 230 V, 50 Hz AC output across varying input voltages, while Figure 4.9(b) illustrates the power loss distribution at 40 V input as a function of input current. This analysis enables estimation of the converter's power losses, and experimental verification provides the confirmed efficiency curve.
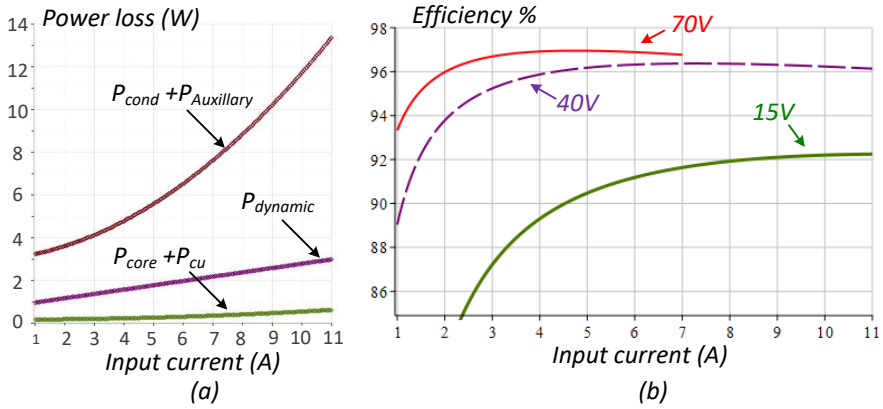
Figure 4.9(a) Analytical efficiency for AC 230 V 50Hz output with Input power changing for different input voltage. (b) Power loss distribution for input 40 V vs input current variation.

4.4 Experimental Validation

To experimentally verify the proposed non-isolated DC–DC/AC microconverter, a complete hardware prototype was built. As shown in Figure 4.10, the prototype incorporates the full power and control systems, including protection, switching devices, auxiliary supply, and logic circuits. An STM32H503RBT6 microcontroller acts as the central controller, handling PWM generation, sensor data processing, and control decisions. The auxiliary circuitry is powered directly from the PV input, providing low-voltage DC rails for the microcontroller, sensor interfaces, and ESP32 communication module, enabling fully autonomous and responsive operation.

The power stage consists of a high-frequency ETD49 transformer, forward converter MOSFETs, bridge switches, output rectifiers, and passive filtering components. An LC filter mitigates output voltage ripple, while an EMI filter ensures electromagnetic compatibility compliance. A DC circuit breaker provides additional output protection. High-speed SiC Schottky diodes (C4D02120, C3D02065E, and C3D10065A) are employed for D_1, D_2, and D_3 to enable fast switching and minimal reverse recovery losses, improving efficiency and thermal performance. For the single-stage design, STF28N65M2 MOSFETs are selected to reduce conduction losses, with dynamic losses being negligible due to low-frequency operation. The IPD95R450P7ATMA1 MOSFET is used as a cost-effective option for the breaker.
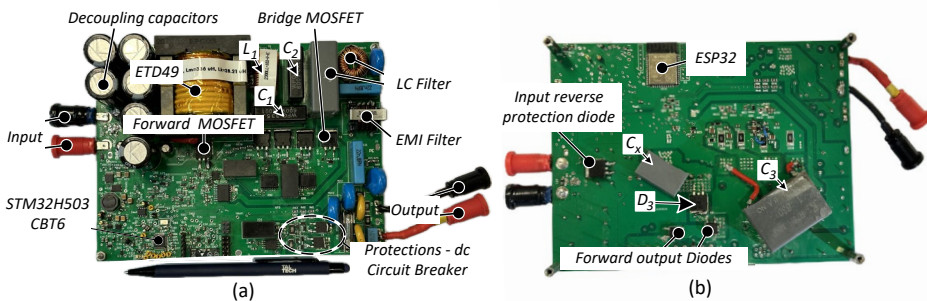
Figure 4.10 Experimental prototype of the proposed universal forward-based microconverter: (a) top view, (b) bottom view [PAPER-I].

Table 4.1 Design parameters of the proposed universal microconverter.

Parameter	Value
Input voltage range v_{IN}	15-70 V
Output voltage vo	350 V
Max input power P_{INMAX}	540 W
Max input current i_{INMAX}	11 A
Max output current i_{OMAX}	1.3 A
Switching frequency of switches f_{SW}	50 kHz
Input decoupling capacitor C_{IN}	15.3 mF
Forward cell capacitor C_1	3.3 uF
Clamp capacitor C_2	3.3 uF
Output capacitor C_3	1 uF
Secondary side capacitor Cx	2.2 nF
Forward cell inductor L_1	1000 uH
LCL filter inductance L_{f1}	620 uH
LCL filter inductance L_{f2}	180 uH
LCL filter capacitance C_f	1 uF
Transformer core	ETD49
Core Material Grade	3C95
Magnetising inductance (pr) L_m	100 uH
Leakage inductance of transformer (pr) L_k	28 uH
Number of turns (pr) n_1	18
Number of turns (sec) n_2	98
Core airgap	700 um

Table 4.1 summarizes the main electrical specifications of the passive components and transformer employed in the prototype. The converter's overall design prioritizes cost-effectiveness by restricting galvanic isolation to critical sections only. Specifically, isolation is applied to the high-side gate drivers of the full-bridge stage and the output current sensor, ensuring adherence to safety requirements while minimizing system costs.

The input stage incorporates a 15.3 mF decoupling capacitor to stabilize the PV bus voltage. The transformer core is an ETD49-3C95, with the primary wound using 18 turns of 0.04 mm × 2000-strand litz wire and the secondary with 98 turns of 0.1 mm × 2000-strand litz wire. To minimize interwinding capacitance and parasitic effects, the windings are spaced deliberately without overlapping layers. Although this slightly increases leakage inductance, it reduces voltage stress on the switches, enhancing reliability under full-load operation.

Figure 4.11(a) and (b) demonstrate the dual-mode functionality of the proposed forward-based microconverter under DC and AC grid configurations.

4.4.1 DC–AC Mode

Figure 4.11(b) depicts AC grid operation, highlighting the input behavior, forward-stage output voltage, and load current. The control strategy adaptively switches modes based on the relative levels of input and output voltages. If the output drops below the input, the system engages conventional unipolar PWM inverter control.
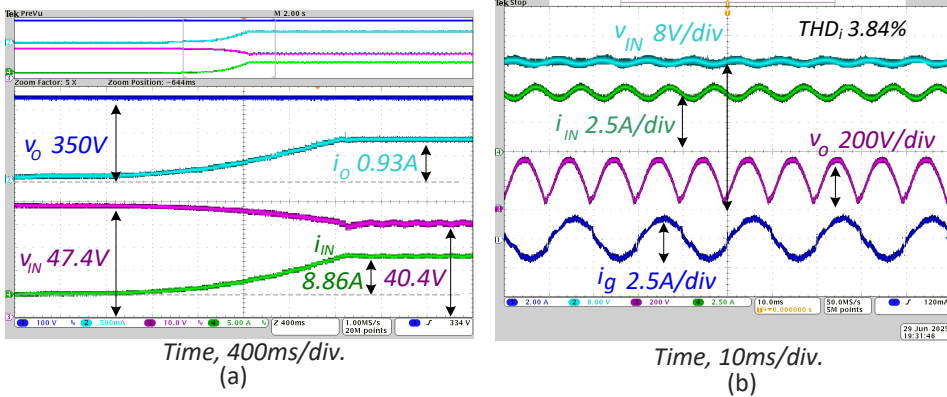

Figure 4.11 Experimental Results of the proposed universal forward-based dc ready microconverter connected to(a) dc grid, (b) AC grid.

When the output exceeds the input, it transitions to the unfolder mode, regulating power via the forward-stage switch. This dynamic approach maintains efficient performance under varying operating conditions.

4.4.2 DC–DC Mode

In Figure 4.11(a), DC operation is validated with input and output voltage/current measured at a nominal 350 V output Table 4.2 contains commercial solar panels which were considered for the experimental validation of the proposed forward-based DC–DC converter. The solar panels have different voltages and currents, and they were selected to demonstrate a wide voltage and power range of operation of the proposed converter. A programmable PV simulator Keysight E4360A emulates parameters of a real PV panel and acts as an input source for the proposed converter.

The bidirectional power supply Itech IT6006-800-25 is used as an emulated grid side, where the voltage is 350 V. All the efficiency measurements were done by using precision power analyzer Yokogawa WT1800. Figure. 4.12 shows the experimental results of the proposed converter for a single panel ED160-6M and 355R-AC. ED160-6M panel has the Maximum Power Point (MPPT) current is 8.79 A and the MPP voltage is 18.2 V. However, if set datasheet specifications for power supply, the PV simulator changes a little bit those parameters (V_{MPP} = 18.6 V, I_{MPP} = 8.659 A, P_{MPP} = 161.06 W).

Table 4.2 Commercial solar panel parameters available on the market and the efficiency results of the proposed converter in DC–DC mode.

Solar panel	P_{MPP}, W	V_{OC}, V	V_{MPP}, V	I_{SC}, A	I_{MPP}, A	η_{MPP} case 1, %	η_{Con} case 1, %	η_{Total} case 1, %	η_{MPP} case 2, %	η_{Con} case 2, %	η_{Total} case 2, %
ED90-6P	90	22.6	17.8	5.36	5.06	99.84	90.24	90.1	99.84	90.17	90.03
ED160-6M	160	22.2	18.2	9.32	8.79	99.93	90.83	90.77	99.93	91.1	91.04
355R-AC	355	47.4	39.1	9.53	9.09	99.95	93.81	93.76	99.95	94.16	94.11
SPR-X22-370	370	69.5	59.1	6.66	6.26	99.48	93.96	94.47	99.48	95.05	94.55

Figure 4.12 The experimental results of the proposed converter with different PV panels. PV and grid currents and voltages for: (a) solar panel ED160-6M, (d) solar panel 355R-AC; PV current and voltage and voltage stresses on switch S1 and diode D1 for: (b) solar panel ED160-6M, (e) solar panel 355R-AC; PV current and voltage and voltages across diodes D2 and D3 for: (c) solar panel ED160-6M, (f) solar panel 355R-AC [PAPER-V].

As a result, the MPPT algorithm identified the MPP with a current of 8.672 A and a voltage of 18.56 V (η_{MPPT} = 99.93%). The overall efficiency reached 90.83% using the cost-effective semiconductor set listed in Table 2.6. The MPPT required 1.8 s to reach the MPP (Figure 4.12(a)), while the semiconductor voltage stresses are presented in Figures 4.12(b)–(c).

The diodes D_1 and D_2 experience high voltage stresses due to the transformer turns ratio and a fading-resonance interaction between the primary magnetizing inductor and parasitic capacitances. Adding a secondary-side capacitor, C_x, can reduce the diode voltage stress but simultaneously raises the voltage stress on the main switch and diode D_3. During experiments, C_x was set to 2.5 nF.

The experimental results for the PV panel 355R-AC are presented in Figure 4.12(d–f). The PV simulator defines the real parameters as V_{MPP} = 40.034 V, I_{MPP} = 8.961 A, and P_{MPP} = 358.75 W. The controller identified a power point at V_{MPP} = 39.94 V and I_{MPP} = 8.98 A, yielding an MPPT efficiency of 99.95% and a total efficiency of 93.76 % with low-cost semiconductors. Using a more expensive semiconductor set slightly increased total efficiency, as reported in Table 4.2, by 0.35%, since the transistors share the same dynamic characteristics, an important factor for the proposed converter. Theoretically, diode D1 voltage stress could reach 1.4 kV at high boost, but experimental measurements showed a maximum of 1.19 kV.

The experimental results confirm that the proposed forward-based microconverter does not suffer from voltage spike issues across the semiconductors. These findings demonstrate that the leakage inductance problem has been effectively mitigated, validating the robustness and reliability of the proposed design.

Under conditions of rapid input or output changes, the system is generally robust because such variations are usually gradual. PV voltage and current can fluctuate due to shadowing, high temperatures, or low solar irradiance. Sudden load or voltage changes may occur during line interruptions or short-circuit faults. To handle these situations, the control system incorporates both software and hardware protections, including current and voltage limits, a reverse-protection diode on the PV side, fuses, a varistor, and a DC breaker. In the event of a fault, the protection system immediately halts duty-cycle generation, stopping the converter to ensure safe operation.

4.4.3 Efficiency Study

Figure 4.13(a) evaluates system efficiency for AC and DC loads at input voltages of 40 V and 60 V over a current range of 1–10 A, using a Yokogawa WT1800E analyzer. Higher input voltage and lower current levels yield greater efficiency due to minimized conduction losses and favorable duty cycle operation. Peak DC efficiency reaches 94.2% at 60 V and 6 A, while AC efficiency peaks at 94.4% at 4 A. DC loads benefit from constant duty cycles, especially at 350 V output, while AC efficiency benefits from sinusoidal modulation under lighter loads. Beyond 5 A, AC efficiency declines faster due to cumulative switching and conduction losses.

Figure 4.13(b) and (c) present thermal images of critical semiconductors during AC grid operation at 450 W with 60 V input, recorded using a Fluke Ti10 camera. The switch and diodes D1, D2, and D3 reached about 80 °C, whereas the transformer stayed near 50 °C.
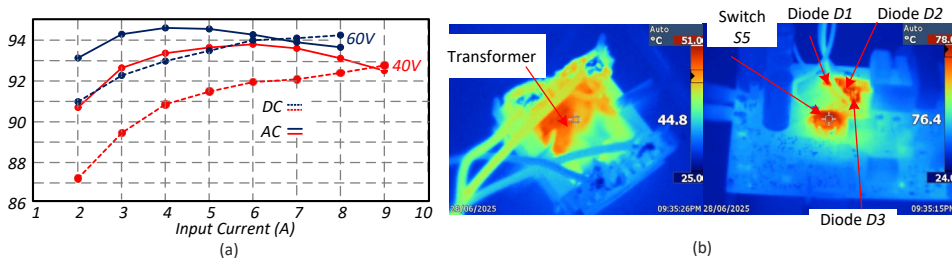

Figure 4.13 (a) Efficiency comparison of AC and DC loads across input voltages (40V and 60V) at varying current levels, (b) Thermal pictures of the semiconductors and forward transformer in maximum AC power at input voltage of 60 V.

4.5 Comparison of Non-Isolated Forward-Based Universal Microconverter with Interleaved Single-Stage Flyback Topology

The proposed dual-purpose forward-based microconverter in Figure 4.1 is compared with a dual-purpose flyback topology with primary-side passive decoupling, shown in Figure 3.2(b), which represents a cost-effective industrial solution. The forward non-isolated microinverter outperforms conventional single-stage flyback designs by removing isolation components, such as transformers and optocouplers, while using shared auxiliary circuits for both DC and AC operation.

Unlike flyback designs, this topology uses a simplified magnetic structure. The term "non-isolated" indicates the removal of galvanic isolation between primary and secondary circuits, while retaining a magnetic element for voltage step-up and passive filtering.

To objectively evaluate the proposed design, two TRL4 universal prototypes—one flyback-based and one non-isolated forward-based—were developed using identical components, differing only in their core topologies, as shown in Figure 3.4(a) and Figure 4.1.

Cost savings stem from simplified magnetics and removal of isolation components in the gate driver and sensor circuits. The additional inductance L_{f1} in the forward-based converter, compared to the flyback design, is included to meet the zero-level requirement of the unipolar PWM scheme, not to improve THD.

4.5.1 Theoretical Comparison of Flyback and Forward-Based Non-Isolated Solutions

With the single-stage configuration, the converters generate a pulsating AC output that is directly rectified. Steady-state analysis was performed for both the forward-based and flyback DC–DC converters. Ripple values of passive components were kept the same for both topologies to ensure a fair comparison, and transformer design maintained identical deviation and maximum flux density (240 mT).

The turn ratio was similarly selected to emphasize topological differences while and maintained identical ripple factors for the capacitors (K_c = 5%) and inductances (K_L = 20%). Table 4.3 summarizes mathematical expressions for both converters, including passive components, magnetizing current, and semiconductor voltage stresses, with the comparison illustrated in Figure 4.14.

Table 4.3 Comparison table of the passive components and voltage stress.

Parameter	Flyback DC-DC converter	Proposed Forward-based DC-DC converter
Gain, $G=V_o/V_{IN}$	$N\cdot D\big/(1-D)$	$\big(1+N\cdot D\cdot(1-D)\big)\big/(1-D)$
Duty cycle, D	$V_O\big/(V_O+N\cdot V_{IN})$	$\Big(N\cdot V_{IN}+V_O+\sqrt{4\cdot N\cdot V_{IN}^2+(N\cdot V_{IN}-V_O)^2}\Big)\big/(2\cdot N\cdot V_{IN})$
Average magnetizing current, I_M	I_{IN}/D	$\big(I_{IN}-I_O(1+N\cdot D)\big)\big/D$
Capacitor, C_O	$I_O\cdot D\cdot T\big/(K_o\cdot V_O)$	$\big(I_O\cdot D\cdot T-(K_{C1}\cdot V_{C1}+K_O\cdot V_O)\cdot C_2\big)\big/(K_O\cdot V_O)$
Capacitor, C_1	–	$\big(I_O\cdot D\cdot T-(K_{C1}\cdot V_{C1}+K_O\cdot V_O)\cdot C_2\big)\big/(K_{C1}\cdot V_{C1})$
Inductance, L_1	–	$N\cdot V_{IN}\cdot(1-D)\cdot D\cdot T\big/(1-D)$
Inductance, L_M	$\mu_{ef}\cdot\mu_0\cdot\big(V_{IN}\cdot D\cdot T\big)^2_{MAX}\big/\big(L_{ef}\cdot A_{ef}\cdot 4\cdot\Delta B^2\big)$	
Voltage stress across switch S_1, v_{S1}	$\big(v_{IN}\cdot N+v_o\big)/N$	$v_{IN}/(1-D)$
Voltage stress across diode D_1, v_{D1}	$v_O+v_{IN}\cdot N$	$\big(v_{IN}\cdot N\cdot D\big)\big/(1-D)$
Voltage stress across diode D_2, v_{D2}	–	$v_{IN}\cdot N$
Voltage stress across diode D_3, v_{D3}	–	$v_{IN}\big/(1-D)$

Figure 4.14 The comparison between the flyback and proposed forward-based DC–DC converters: (a) input voltage is 15 V and input current is 10 A, (b) input voltage is 40 V and input current is 10 A, (c) input voltage is 70 V and input current is 6.43 A. (d) Total power loss with input voltage variation.

Figure 4.14 compares the two topologies across varying input voltages and power levels. Red areas denote the forward-based DC–DC converter, while blue areas indicate the flyback DC–DC converter. At 15 V input and 10 A (Figure 4.14(a)), the forward-based converter shows higher semiconductor stress, with other metrics similar. For 40 V and 70 V inputs (Figure 4.14(b)–(c)), although semiconductor voltage stress remains higher for the forward-based design, the flyback converter has greater total inductive energy due to its higher magnetizing current, balancing the overall comparison. Figure 4.14(d) shows the theoretical comparison of losses between Flyback and Forward based DC–DC converter.

The proposed forward-based DC–DC converter provides key advantages: it is non-isolated and shares a common ground, reducing costs and eliminating leakage currents. Although it uses more semiconductors, only one active switch is required, and total conduction losses remain comparable to conventional designs, making it a cost-effective alternative for specific applications.

4.5.2 Efficiency Comparison

This subchapter presents the experimental results comparing a dual-purpose microconverter based on the proposed non-isolated forward topology (Figure 4.10) with a widely used conventional single-stage flyback topology (Figure 3.4(b)) under both AC and DC load conditions.

Figure 4.15 shows the efficiency curve for varying input voltages at a constant 9 A input current, measured using the high-performance Yokogawa WT1800E power analyser.
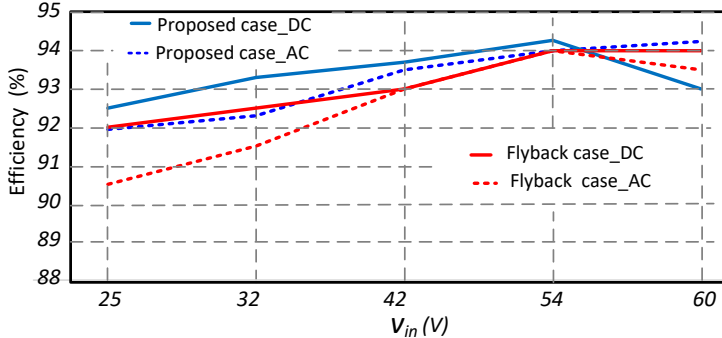

Figure 4.15 Efficiency study versus different input voltages under constant input current.

4.5.3 Cost Comparison

The cost comparison is based on current component prices obtained from the same supplier's website, highlighting the cost savings achieved with the proposed converter design relative to the conventional single-stage flyback solution, which is widely recognized in the industry as a cost-effective option for power levels up to 450 watts.

As illustrated in Figure 4.16, the forward-based topology demonstrates a 28.5% reduction in total costs based on the number of components required at different production levels (1, 10, 100, and 1000 units). The cost analysis is divided into several parts, such as the total cost of capacitors, semiconductors, Magnetics, Integrated Circuits (IC), resistors/varistors for protection, as well as printed circuit boards. In terms of semiconductors, PCB, resistors/ protection, as well as capacitor costs, both topologies have almost similar costs. However, the cost of magnetics and ICs used for drivers and sensors is higher in the flyback-based solution compared to the proposed.
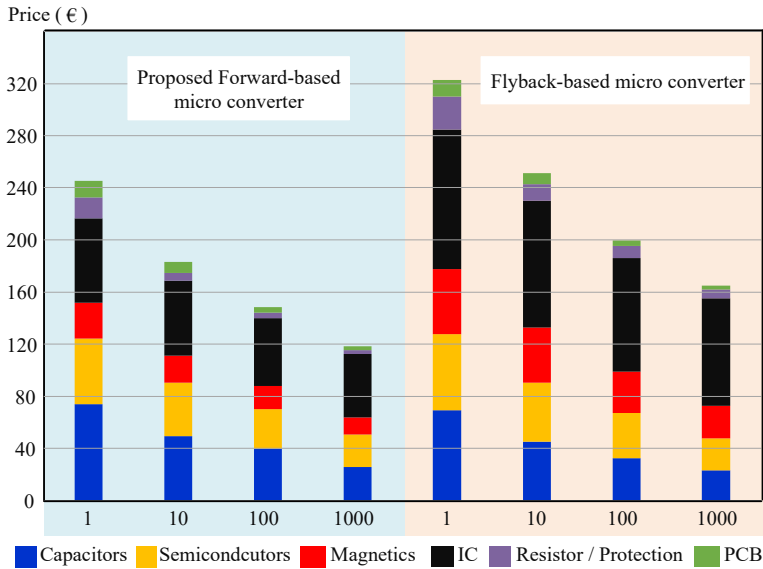
Figure 4.16 Cost benchmarking of proposed non-isolated forward and interleaved flyback-based microconverters.

As illustrated in Figure 4.16, the forward-based topology achieves a 28.5% reduction in total cost by optimizing the number of components required across different production volumes (1, 10, 100, and 1000 units). The cost analysis is divided into several categories, including capacitors, semiconductors, magnetics, integrated circuits (ICs), resistors/varistors for protection, PCBs. For semiconductors, PCBs, resistors/protection components, and capacitors, both topologies exhibit nearly identical costs. However, the flyback-based solution incurs higher costs for magnetics and ICs used for drivers and sensors. This is primarily due to the non-isolated nature of the proposed topology, which eliminates the need for isolated sensors, isolated drivers, and, in general, additional ICs.

Meanwhile, the control part, which includes current and voltage sensors, control and communication circuits, and auxiliary supplies, exhibits significant cost reductions due to the non-isolated architecture. By eliminating the need for costly isolation components, the design is streamlined and more efficient. These savings make the forward-based topology particularly well-suited for mid-power systems (300–500 W), ensuring both cost-effectiveness and universal compatibility with DC and AC microgrids.

Table 4.4 Cost comparison of the control part and the power part, considering the current market price.

Topology	Control Part Cost (€) by Volume				Power Part Cost (€) by Volume			
	1	10	100	1000	1	10	100	1000
Proposed forward-based	49	34	27	23	178	134	114	90
Flyback based	85	64	52	44	218	171	140	115

To further enhance cost efficiency, the adoption of Application-Specific Integrated Circuit (ASIC) technology can be considered. In large-scale production, an ASIC-based design minimizes component count, reduces manufacturing costs, and improves performance. By integrating multiple control and sensing functions into a single chip, ASICs streamline circuit complexity, enhance reliability, and lower overall production costs, thereby making the forward-based topology even more competitive for photovoltaic (PV) module applications.

4.6 Summary

This chapter presents the design, implementation, and experimental validation of a closed-loop synergetic control system engineered for a universal DC-DC/AC microconverter. The proposed control framework enables robust and stable dual-mode operation, seamlessly transitioning between DC and AC microgrid applications. For DC operation, the system employs precisely tuned PI-based voltage and current regulators, while AC operation utilizes a combined PR (Proportional-Resonant) and RC (Repetitive Controller) strategy with phase-locked loop (PLL) synchronization for grid interconnection. A thorough power loss analysis confirms the control system's effectiveness in optimizing the balance between conduction and switching losses, thereby maintaining high efficiency across both operational modes. Experimental validation through laboratory prototypes verifies theoretical models, demonstrating reliable performance in DC–DC conversion with buck/boost capabilities and high-quality sinusoidal output in DC–AC inversion mode. The measured efficiency exceeds 95% under optimal conditions, confirming the design's practical viability. The chapter concludes with a comprehensive comparative analysis against interleaved flyback topologies, highlighting the proposed converter's superior cost-effectiveness with a 28% reduction in component costs while maintaining competitive efficiency. The successful integration of advanced control strategies with the forward-based non-isolated architecture represents a significant advancement in universal microconverter technology, offering improved economic viability and operational flexibility for modern renewable energy systems.

5 Summary and Conclusions

This thesis has presented a comprehensive study of cost-effective power electronic converter solutions for dual-purpose operation in both DC and AC microgrids. The research addressed the growing demand for universal, compact, and efficient interfaces in renewable energy systems, with an emphasis on minimizing redundancy while maintaining robust performance, guided by core hypotheses on topology and control.

A comparative evaluation of DC–DC converter topologies was carried out, focusing on both isolated and non-isolated solutions. This investigation confirmed that a modified forward-based converter offers cost-effectiveness and high efficiency for applications requiring a wide input range of 15–70 V, validating the first hypothesis. Furthermore, it was demonstrated that this proposed non-isolated forward-based solution effectively eliminates the leakage inductance issue typically observed in transformer-based converters, thus confirming the second hypothesis. In parallel, a novel isolated buck-boost topology with wide voltage regulation and ZVS was also proposed, offering reduced switching losses. Theoretical analysis, simulations, and experimental validation confirmed that both approaches achieve compact design and reliable operation.

The investigation into passive decoupling methods demonstrated that PV-side decoupling, compared to conventional DC-link capacitor approaches, reduces bulky energy storage requirements, improves efficiency, and lowers cost without sacrificing reliability. This makes it particularly attractive for the proposed cost-sensitive systems where minimizing capacitor volume is a critical factor.

A synergetic closed-loop control strategy was developed to enable universal DC–DC/AC microconverter operation across wide input and output ranges. The proposed control scheme was experimentally validated under both steady-state and dynamic conditions. The results confirmed that this strategy provides significant benefits by utilizing single-stage operation across a wider voltage range, delivering fast transient response, stable regulation, and improved efficiency compared to conventional designs, thereby validating the third hypothesis. The use of a multicore controller allowed computationally intensive tasks, such as predictive control, to be distributed efficiently, further enhancing system performance.

Overall, the thesis demonstrates that the proposed universal microconverter achieves compactness, high efficiency, reduced internal redundancy, and cost-effectiveness. As the primary outcomes, the author can claim the following:

- The modified forward-based converter offers a cost-effective and efficient solution for a wide input range of 15–70 V.
- The proposed forward-based converter topology effectively eliminates the leakage inductance issue of the transformer.
- The proposed synergetic closed-loop control strategy successfully enables stable and efficient single-stage operation across a wide voltage range.
- The universal microconverter is a competitive candidate for renewable energy integration in residential and microgrid applications.

Future work is directed toward further TRL-6 development and a long-term testing process. Efforts will focus on the further optimization of the control strategies, and magnetic component designs, as well as reduction of number of components.

List of Figures

List of Tables

References

[1] L. Zhang, K. Sun, Y. Xing, L. Feng, and H. Ge, "A modular grid connected photovoltaic generation system based on DC bus," *IEEE Trans. Power Electron*., vol. 26, no. 2, pp. 523–531, Feb. 2011.

[2] J. Nan, W. Yao, and J. Wen, "Energy storage-based control of multiterminal DC grid to eliminate the fluctuations of renewable energy," *J. Eng*., vol. 16, no. 3, pp. 991–995, Mar. 2019.

[3] T. Dragicevic, X. Lu, J. C. Vasquez, and J. M. Guerrero, "DC microgridspart I: A review of control strategies and stabilization techniques," *IEEE Trans. Power Electron.*, vol. 31, no. 7, pp. 4876–4891, Jul. 2016.

[4] T. Dragicevic, X. Lu, J. C. Vasquez, and J. M. Guerrero, "DC microgridspart II: A review of power architectures, applications, and standardization issues," *IEEE Trans. Power Electron.*, vol. 31, no. 5, pp. 3528–3549, May 2016.

[5] R. H. Lasseter, "MicroGrids," in proc. of 2002 IEEE Power Engineering Society Winter Meeting. Conference Proceedings (Cat. No.02CH37309), New York, NY, USA, Jan. 2002.

[6] J. M. Guerrero, M. Chandorkar, T.-L. Lee; P. C. Loh, "Advanced Control Architectures for Intelligent Microgrids—Part I: Decentralized and Hierarchical Control," *IEEE Trans. Ind. Electron.*, vol. 60, no. 4, pp. 1254–1262, Apr. 2013.

[7] J. Lee, B. Han, and N. Choi, "DC micro-grid operational analysis with detailed simulation model for distributed generation," *in Proc. Energy Convers. Congr. Expo.*, 2010, pp. 3153–3160.

[8] D. L. Gerber, V. Vossos, W. Feng, C. Marnay, B. Nordman, R. Brown, "A simulation-based efficiency comparison of AC and DC power distribution networks in commercial buildings," *Applied Energy*, vol. 210, pp. 1167–1187, Jan. 2018.

[9] A. Sannino, G. Postiglione, and M. H. J. Bollen, "Feasibility of a DC network for commercial facilities*," IEEE Trans. Ind. Appl.*, vol. 39, no. 5, pp. 1499–1507, Sep./Oct. 2003.

[10] [Online]. Available: https://www.dc.systems/company/articles/current-os-on-350v-or-700v-lvdc.

[11] J. Arrillaga, Y. H. Liu, and N. R. Watson, *Flexible Power Transmission*. *The HVDC Options*. Hoboken, NJ, USA: Wiley, 2007.

[12] L. Mackay, N. H. van der Blij, L. Ramirez-Elizondo & P. Bauer, "Toward the Universal DC Distribution System," *Electric Power Components and Systems*, pp.1032-1042, 2017, 45:10, 1032-1042, DOI: 10.1080/15325008.2017.1318977.

[13] L. Mackay, T. Gebremedhin Hailu, G. Chandra Mouli, L. Ramírez-Elizondo, J.A. Ferreira, P. Bauer, "From DC nano- and microgrids towards the universal DC distribution system - a plea to think further into the future," *in proc. of 2015 IEEE Power & Energy Society General Meeting*, Denver, CO, USA, 26-30 July, 2015.

[14] G. Ziegler, Numerical Distance Protection: Principles and Applications. *Hoboken*, NJ, USA: Wiley, 2011.

[15] S. Sen, S. Mehraeen, "Improving Low-Voltage DC Circuit Breaker Performance Through an Alternate Commutating Circuit," *IEEE Trans. Ind. Appl.,* Vol. 55, no. 6, pp. 6127–6136, Nov.-Dec. 2019.

[16] S. Beheshtaein, R. M. Cuzner, M. Forouzesh, M. Savaghebi, and J. M. Guerrero, "DC microgrid protection: A comprehensive review," *IEEE J. Emerg. Sel. Topics Power Electron*.

[17] E. Kontos, T. Schultz, L. Mackay, L. M. Ramirez-Elizondo, C. M. Franck, P. Bauer, "Multiline Breaker for HVdc Applications," *IEEE Trans. Pow. Deliv*., vol. 33, no. 3, pp. 1469–1478, Jun. 2018.

[18] J. Shen, G. Sabui, Z. Miao, and Z. Shuai, "Wide-bandgap solid-state circuit breakers for DC power systems device and circuit considerations," *IEEE Trans. Electron Devices*, vol. 62, no. 2, pp. 294–300, Feb. 2015.

[19] X. Liu, P. Wang, P. Chiang Loh, "A Hybrid AC/DC Microgrid and Its Coordination Control," *IEEE Trans. on Smart Grid*, vol. 2, no. 2, pp. 278–286, Jun. 2011.

[20] R. Zeng, L. Xu, L. Yao, "DC/DC Converters Based on Hybrid MMC for HVDC Grid Interconnection," *in proc. of 11th IET International Conference on AC and DC Power Transmission,* Birmingham, Feb. 10-12, 2015.

[21] O. Husev, D. Vinnikov, S. Kouro, F. Blaabjerg, C. Roncero-Clemente, "Dual-Purpose Converters for DC or AC Grid as Energy Transition Solution: Perspectives and Challenges*," IEEE Industrial Electron. Magazine*, Early access, 2023.

[22] O. Matiushkin, O. Husev, D. Vinnikov and J. Kurnitski, "DC-Ready Photovoltaic Solar Converter," PCIM Europe 2023; International Exhibition and Conference for Power Electronics, Intelligent Motion, Renewable Energy and Energy Management, Nuremberg, Germany, 2023, pp. 1–7.

[23] O. Husev, O. Matiushkin, D. Vinnikov, C. Roncero-Clemente and S. Kouro, "Novel Concept of Solar Converter With Universal Applicability for DC and AC Microgrids," in *IEEE Transactions on Industrial Electronics*, vol. 69, no. 5, pp. 4329–4341, May 2022.

[24] Vega Garita, V.; Garg, S.; Narayan, N.; Ramirez Elizondo, L.; Bauer, P. Testing a PV-battery Integrated Module Prototype. In Proceedings of the 2018 IEEE 7th World Conference on Photovoltaic Energy Conversion (WCPEC) (A Joint Conference of 45th IEEE PVSC, 28th PVSEC & 34th EU PVSEC), Waikoloa, HI, USA, 10–15 June 2018.

[25] Vega Garita, Victor.; Garg, Sh.; Narayan, N.; Ramirez Elizondo, L.; Bauer, P. PV-battery integrated module as a solution for off-grid applications in the developing world. *In Proceedings of the 2018 IEEE International Energy Conference (ENERGYCON)*, Limassol, Cyprus, 3–7 June 2018.

[26] W. Jiang, B. Fahimi, "Multiport Power Electronic Interface—Concept, Modelling, and Design," *IEEE Trans. Pow. Electron*., vol. 26, no. 7, pp. 1890–1900, July 2011.

[27] M. Amirabadi, "A new class of high-power-density universal power converters," *in proc. of 2015 IEEE Energy Conversion Congress and Exposition (ECCE)*, Sept. 20-24, 2015.

[28] S. Falcones, R. Ayyanar, X. Mao, "A DC–DC Multiport-Converter-Based Solid-State Transformer Integrating Distributed Generation and Storage," *IEEE Trans. Pow. Electron.*, vol. 28, no. 5, May 2013.

[29] J. Yuan, F. Blaabjerg, Y. Yang, A. Sangwongwanich and Y. Shen, "An Overview of Photovoltaic Microinverters: Topology, Efficiency, and Reliability," *2019 IEEE 13th International Conference on Compatibility, Power Electronics and Power Engineering (CPE-POWERENG)*, 2019, pp. 1–6.

[30] Dominic, J, "Comparison and design of high efficiency microinverters for photovoltaic applications," *M.S. thesis*, Virginia Tech, 2014.

[31] C. Xiao et al., "A Novel Single-Phase Nonisolated Dual-Input Microinverter With Active Power Decoupling," in *IEEE Transactions on Power Electronics*, vol. 40, no. 3, pp. 4437–4448, March 2025.

[32] D. Sha, J. Zhang and J. Wu, "A GaN-Based Microconverter Utilizing Fixed-Frequency BCM Control Method for PV Applications," in *IEEE Transactions on Industrial Electronics*, vol. 65, no. 6, pp. 4771–4780, June 2018.

[33] W. -J. Cha, Y. -W. Cho, J. -M. Kwon and B. -H. Kwon, "Highly Efficient Microinverter With Soft-Switching Step-Up Converter and Single-Switch-Modulation Inverter," in *IEEE Transactions on Industrial Electronics*, vol. 62, no. 6, pp. 3516–3523, June 2015.

[34] A. R. Paul, A. Bhattacharya and K. Chatterjee, "A Novel SEPIC-Ćuk-Based High Gain Solar PV Microinverter for Grid Integration," in *IEEE Transactions on Industrial Electronics*, vol. 70, no. 12, pp. 12365–12375, Dec. 2023.

[35] R. Heidari, M. A. Ghanbari, E. Adib and M. Rivera, "Coupled Inductor-Based Soft-Switched Boost-Ćuk Converter for Microinverter Applications," in *IEEE Transactions on Power Electronics*, vol. 40, no. 7, pp. 9543–9555, July 2025.

[36] V. Gautam and P. Sensarma, "Enhancing the Voltage Gain of a Flyback Converter Using Leakage Energy," in *IEEE Transactions on Industry Applications*, vol. 54, no. 5, pp. 4717-4727, Sept.-Oct. 2018.

[37] F. Zhang, Y. Xie, Y. Hu, G. Chen and X. Wang, "A Hybrid Boost–Flyback/Flyback Microinverter for Photovoltaic Applications," in *IEEE Transactions on Industrial Electronics*, vol. 67, no. 1, pp. 308–318, Jan. 2020, doi: 10.1109/TIE.2019.2897543.

[38] L. Wang and X. Yang, "A Single-Stage Common-Ground Inverter With High-Voltage-Gain Ability," in *IEEE Transactions on Power Electronics*, vol. 40, no. 5, pp. 7058–7069, May 2025.

[39] [Online]. Available: https://www.cleanenergyreviews.info/microinverter-comparison.

[40] O. Matiushkin, O. Husev, H. Afshari, D. Vinnikov, R. Strzelecki, "Cost-effective piggyback forward based DC-DC converter," *2024 IEEE Applied Power Electronics Conference and Exposition (APEC), 2024.*

[41] M. Forouzesh, Y. P. Siwakoti, S. A. Gorji, F. Blaabjerg and B. Lehman, "Step-up DC–DC converters: a comprehensive review of voltage-boosting techniques, topologies, and applications," *IEEE Transactions on Power Electronics*, vol. 32, no. 12, pp. 9143–9178, Dec. 2017.

[42] Y. Koç, Y. Birbir, and H. Bodur, "Non-isolated high step-up DC-DC converters–An overview," *Alexandria Engineering Journal*, vol. 61, no. 2, pp. 1091–1132, Feb. 2022.

[43] O. Husev, L. Liivik, F. Blaabjerg, A. Chub, D. Vinnikov and I. Roasto, "Galvanically isolated quasi-z-source DC–DC converter with a novel ZVS and ZCS technique," *IEEE Transactions on Industrial Electronics*, vol. 62, no. 12, pp. 7547–7556, Dec. 2015.

[44] E. S. Oluwasogo and H. Cha, "A quadratic quasi-z-source full-bridge isolated DC–DC converter with high reliability for wide input applications," *IEEE Transactions on Industrial Electronics*, vol. 69, no. 10, pp. 10090–10100, Oct. 2022.

[45] J. Lee, M. Kim, S. Kim and S. Choi, "An isolated single-switch ZCS resonant converter with high step-up ratio," *IEEE Transactions on Power Electronics*, vol. 36, no. 10, pp. 11555-11564, Oct. 2021Y. Ma, X. Wang, X. Zhou, Z. Gao, "An overview of energy routers," *in proc. of 2017 29th Chinese Control And Decision Conference (CCDC)*, Chongqing, China, May 28-30, 2017.

[46] Zhang, Z., et al., "High efficiency step-up DC–DC converter for grid-connected photovoltaic microinverter applications", *IET Renewable Power Generation*, vol. 16, no. 6, pp. 1159–1169, April 2022.

[47] N. Yang, J. Zeng, R. Hu and J. Liu, "Analysis and design of an isolated high step-up converter without voltage-drop," *IEEE Transactions on Power Electronics*, vol. 37, no. 6, pp. 6939–6950, June 2022.

[48] M. -K. Nguyen, Y. -C. Lim, J. -H. Choi and G. -B. Cho, "Isolated high step-up DC–DC converter based on quasi-switched-boost network," *IEEE Transactions on Industrial Electronics*, vol. 63, no. 12, pp. 7553–7562, Dec. 2016.

[49] A. Chub, O. Husev and D. Vinnikov, "Input-parallel output-series connection of isolated quasi-Z-source DC-DC converters," *2014 Electric Power Quality and Supply Reliability Conference (PQ)*, Rakvere, Estonia, 2014, pp. 277–284.

[50] A. Chub, D. Vinnikov, F. Blaabjerg and F. Z. Peng, "A review of galvanically isolated impedance-source DC–DC converters," *IEEE Transactions on Power Electronics*, vol. 31, no. 4, pp. 2808–2828, April. 2016.

[51] Q. Wu, Q. Wang, J. Xu and L. Xiao, "A wide load range ZVS push–pull DC-DC converter with active clamped," *IEEE Transactions on Power Electronics*, vol. 32, no. 4, pp. 2865–2875, April 2017.

[52] H. Kim, C. Yoon and S. Choi, "An improved current-fed ZVS isolated boost converter for fuel cell applications," *IEEE Transactions on Power Electronics*, vol. 25, no. 9, pp. 2357–2364, Sept. 2010.

[53] K. Kanathipan, R. Emamalipour and J. Lam, "A single-switch high-gain PV microconverter with low-switch-voltage-to-high-voltage-bus ratio," *IEEE Transactions on Power Electronics*, vol. 35, no. 9, pp. 9530–9540, Sept. 2020.

[54] W. Li, J. Liu, J. Wu and X. He, "Design and analysis of isolated ZVT boost converters for high-efficiency and high-step-up applications," *IEEE Transactions on Power Electronics*, vol. 22, no. 6, pp. 2363–2374, Nov. 2007.

[55] T. Qian and Q. Wu, "A boost type resonant forward converter with topology combination," *IEEE Transactions on Circuits and Systems II: Express Briefs*, vol. 65, no. 12, pp. 2008–2011, Dec. 2018.

[56] Q. Wu, Q. Wang, J. Xu, H. Li and L. Xiao, "A high-efficiency step-up current-fed push–pull quasi-resonant converter with fewer components for fuel cell application," *IEEE Transactions on Industrial Electronics*, vol. 64, no. 8, pp. 6639–6648, Aug. 2017.

[57] H. -S. Lee and J. -J. Yun, "Quasi-resonant voltage doubler with snubber capacitor for boost half-bridge DC–DC Converter in Photovoltaic Microinverter," *IEEE Transactions on Power Electronics*, vol. 34, no. 9, pp. 8377–8388, Sept. 2019.

[58] S. Pourjafar, P. Mohseni, O. Husev, O. Matiushkin and D. Vinnikov. "Novel isolated high step-up DC-DC converter with wide input voltage regulation range," *2023 IEEE 64the International Scientific Conference on Power and Electrical Engineering of Riga Technical University (RTUCON)*.

[59] H. Seok, B. Han, B. -H. Kwon and M. Kim, "High step-up resonant DC–DC converter with ripple-free input current for renewable energy systems," *IEEE Transactions on Industrial Electronics*, vol. 65, no. 11, pp. 8543–8552, Nov. 2018.

[60] A. L. Rabello, M. A. Co, D. S. L. Simonetti and J. L. F. Vieira, "An isolated DC-DC boost converter using two cascade control loops," *in proc. of ISIE*, Guimaraes, Portugal, 1997, pp. 452–456, vol. 2.

[61] W. Li, L. Fan, Y. Zhao, X. He, D. Xu, B. Wu, "High-Step-Up and High-Efficiency Fuel-Cell Power-Generation System With Active-Clamp Flyback–Forward Converter," *IEEE Trans. on Ind. Electron.*, vol. 59, no. 1, pp. 599–610, Jan. 2012.

[62] F. Zhang, Y. Yan, "Novel Forward–Flyback Hybrid Bidirectional DC–DC Converter," *IEEE Trans. on Ind. Electron.*, vol. 56, no. 5, pp. 1578–1584, May 2009.

[63] R.-L. Lin, Y.-H. Huang, "Forward-flyback converter with snubber-feedback network for contactless power supply applications," *in proc. of IEEE Energy Conversion Congress and Exposition*, Atlanta, GA, USA, Sep. 12-16, 2010.

[64] K.-C. Tseng, J.-Z. Chen, J.-T. Lin, C.-C. Huang, T.-H. Yen, "High Step-Up Interleaved Forward-Flyback Boost Converter With Three-Winding Coupled Inductors," *IEEE Trans. Power Electron.*, vol. 30, no. 9, pp. 4696–4703, Sep. 2015.

[65] H. Liu, H. Hu, H. Wu, Y. Xing, I. Batarseh, "Overview of High-Step-Up Coupled-Inductor Boost Converters," *IEEE Journ. of Emerg. and Select. Topics in Power Electron.*, vol. 4, no. 2, pp. 689–704, Jun. 2016.

[66] W. Yu, C. Hutchens, J.-S. Lai, J. Zhang, G. Lisi, A. Djabbari, G. Smith, T. Hegarty, "High efficiency converter with charge pump and coupled inductor for wide input photovoltaic AC module applications," *in proc. of 2009 IEEE Energy Conversion Congress and Exposition,* San Jose, CA, USA, Sep. 20-24, 2009.

[67] Y. Tang, D. Fu, J. Kan, T. Wang, "Dual Switches DC/DC Converter With Three-Winding-Coupled Inductor and Charge Pump," *IEEE Trans. Power Electron.*, vol. 31, no. 1, Jan. 2016.

[68] R. Nur Hasanah, T. Taufik, O. Setyawatia, "Impact of transformer's leakage inductance on duty cycle in isolated dc-dc converters," *International Journal of Smart Grid and Clean Energy*, vol. 9, no. 1, Jan. 2020, pp. 61–68.

[69] H. Hu, S. Harb, N. Kutkut, I. Batarseh and Z. J. Shen, "A Review of Power Decoupling Techniques for Microinverters With Three Different Decoupling Capacitor Locations in PV Systems," in *IEEE Transactions on Power Electronics*, vol. 28, no. 6, pp. 2711–2726, June 2013.

[70] A. R. Paul, A. Bhattacharya and K. Chatterjee, "A Novel Single Phase Grid Connected Transformer-Less Solar Microinverter Topology With Power Decoupling Capability," in *IEEE Transactions on Industry Applications*, vol. 59, no. 1, pp. 949–958, Jan.-Feb. 2023.

[71] R. Za'im, J. Jamaludin and N. A. Rahim, "Photovoltaic Flyback Microinverter With Tertiary Winding Current Sensing," *in IEEE Trans. on Power Electron.*, vol. 34, no. 8, pp. 7588–7602, Aug. 2019, doi: 10.1109/TPEL.2018.2881283.

[72] M. A. Rezaei, K. -J. Lee and A. Q. Huang, "A High-Efficiency Flyback Microinverter With a New Adaptive Snubber for Photovoltaic Applications," *in IEEE Trans. on Power Electron.*, vol. 31, no. 1, pp. 318–327, Jan. 2016.

[73] N. Falconar, D. S. Beyragh and M. Pahlevani, "An Adaptive Sensorless Control Technique for a Flyback-Type Solar Tile Microinverter," *in IEEE Trans. on Power Electron.*, vol. 35, no. 12, pp. 13554–13562, Dec. 2020.

[74] T. Nhien Huynh and J. Khazaei, "Stability Analysis of Grid-Connected Flyback Converter for PV Power Applications," *2020 52nd North American Power Symposium (NAPS)*, 2021, pp. 1–6.

[75] A. Bhattacharya, A. R. Paul and K. Chatterjee, "A Coupled Inductor Based Ćuk Microinverter for Single Phase Grid Connected PV Applications," *in IEEE Trans. on Industry Appl.*, vol. 59, no. 1, pp. 981–993, Jan.-Feb. 2023.

[76] T. V. Thang, N. M. Thao, Do-Hyun Kim and Joung-Hu Park, "Analysis and design of a single-phase Flyback microinverter on CCM operation," *Proceedings of The 7th International Power Electronics and Motion Control Conference*, 2012, pp. 1229-1234.

[77] O. Matiushkin, O. Husev, D. Vinnikov and N. V. Kurdkandi, "Comparative Analysis of Buck-Boost Inverters Based on Unfolding Circuit Versus H5, H6, HERIC Topologies," *2022 International Symposium on Power Electronics, Electrical Drives, Automation and Motion (SPEEDAM)*, 2022, pp. 547–552.

[78] H. Afshari, O. Husev, O. Matiushkin, D. Vinnikov and C. Roncero-Clemente, "DC-Ready Flyback-Based Microconverter," *2024 IEEE 18th International Conference on Compatibility, Power Electronics and Power Engineering (CPE-POWERENG)*, Gdynia, Poland, 2024, pp. 1–6.

[79] O. Matiushkin, O. Husev, E. Romero-Cadaval and C. Roncero-Clemente, "Implementation of MPPT Hill Climbing Technique for Forward Based DC-DC Converter," *2024 IEEE 18th International Conference on Compatibility, Power Electronics and Power Engineering (CPE-POWERENG)*, Gdynia, Poland, 2024, pp. 1–6.

[80] D. Zhang, C. Leontaris, J. Huber and J. W. Kolar, "Optimal Synergetic Control of Three-Phase/Level Boost–Buck Voltage DC-Link AC/DC Converter for Very-Wide Output Voltage Range High-Efficiency EV Charger," in *IEEE Journal of Emerging and Selected Topics in Power Electronics*, vol. 12, no. 1, pp. 28–42, Feb. 2024.

Acknowledgements

First and foremost, I would like to express my deepest gratitude to my supervisors from Tallinn University of Technology, Associate Professor Dr. Oleksandr Husev and Professor Dmitri Vinnikov, for their invaluable supervision, continuous motivation, and unwavering support. Thank you for providing me with the exceptional opportunity to conduct my PhD research as a member of the Power Electronics Research Group.

I extend my sincere thanks to Dr. Oleksandr Matiushkin for his help and collaboration on the experimental work. I am also profoundly grateful to all the members of the Power Electronics Group for their shared knowledge and the supportive environment they fostered in the laboratory.

I would also like to extend my heartfelt thanks to my friends for their friendship, encouragement, and the memorable moments we shared throughout this journey. Your companionship made this experience truly special.

Finally, I wish to express my deepest personal gratitude to my family. Their unwavering support, constant motivation, and steadfast belief in me were fundamental throughout this journey. My heartfelt thanks go to my father, my mother, and my brother for their immense understanding and unconditional love.

Abstract

Photovoltaic Microconverter with Universal Compatibility with AC and DC Microgrids

This work presents a novel universal solar microconverter capable of interfacing with both DC and single-phase AC grids through the same hardware. The key innovation is the dual-purpose use of its power semiconductors, significantly reducing component redundancy and cost. The core topology is a non-isolated forward converter, chosen for its wide input voltage range (15–70 V), low component count, and inherent mitigation of leakage inductance effects.

A synergetic control strategy is introduced to manage both high-frequency regulation and low-frequency grid synchronization, enabling efficient single-stage power conversion across all operating modes. In AC operation, a passive unfolding circuit with zero switching losses is employed to construct the output waveform, further enhancing efficiency.

An experimental prototype was developed and tested, validating reliable performance in both DC and AC environments under various steady-state and dynamic conditions. The results demonstrate that the proposed universal microconverter achieves a compact, cost-effective, and efficient solution for renewable energy integration, making it a competitive candidate for residential and microgrid applications.

This work has substantial practical value:

- The proposed non-isolated forward converter topology provides a proven, cost-effective hardware foundation for universal power conversion.
- The synergetic control strategy offers a flexible software framework for managing dual-mode operation and optimizing performance.

The theoretical and practical results established in this thesis serve as a direct foundation for further development towards a TRL-6 prototype. The proposed synergetic control strategy can be improved upon, particularly by integrating more advanced modulation techniques to achieve further reduction in output current and voltage THD.

Lühikokkuvõte

Universaalne alalis- ja vahelduvvooluvõrkudega ühilduv fotoelektrilise süsteemi mikromuundur

Käesolev töö esitleb uudset universaalset fotoelektrilise süsteemi mikromuundurit, mis suudab riistvara muutmata ühilduda nii alalisvoolu (DC) kui ka ühefaasilise vahelduvvoolu (AC) mikrovõrkudega. Põhiinnovatsiooniks on pooljuhtlülitite kahetine kasutamine, mis vähendab oluliselt komponentide liiasust ja kulusid. Keskseks topoloogiaks on galvaanilise isolatsioonita pärilülitusmuundur (ingl forward converter), mis on valitud laia sisendpinge vahemiku (15–70 V), väikese komponentide arvu ja omaduse tõttu vähendada lekkeinduktiivsuse negatiivset mõju.

Sünergiline juhtimisstrateegia on kasutusele võetud nii kõrgsageduslikuks reguleerimiseks kui ka madalsageduslikuks võrguga sünkroniseerimiseks, võimaldades tõhusat üheastmelist võimsuse muundamist kõikides töörežiimides. Vahelduvpinge režiimis väljundsignaali kujundamiseks rakendatakse passiivset pinge formeerimisahelat koos transistoride pehmelülitusega, mis parendab muunduri energiatõhusust.

Arendati ja testiti katseprototüüp, mis kinnitas usaldusväärset toimimist nii alalis- kui ka vahelduvvoolu mikrovõrgus erinevates staatilistes ja dünaamilistes tööpunktides. Tulemused tõestavad, et pakutud universaalne muundur võimaldab integreerida päikesepaneele kompaktselt, efektiivselt ja kulutõhusalt, muutes selle konkurentsivõimeliseks kandidaadiks eramute mikrovõrkude rakendustele.

Sellel tööl on oluline praktiline väärtus:

- Universaalne galvaanilise isolatsioonita pärilülitusmuundur pakub kulutõhusat riistvaralist baasi erinevatele muundurite rakendustele.
- Sünergiline juhtimisstrateegia pakub paindlikku tarkvararaamistiku kahe-režiimilise töö haldamiseks ja jõudluse optimeerimiseks.

Käesolevas doktoritöös saavutatud teoreetilised ja praktilised tulemused annavad hea aluse edasiseks arendustööks TRL-6 prototüübi suunal. Pakutud sünergilist juhtimisstrateegiat on võimalik täiustada integreerides täiustatud modulatsioonitehnikaid väljundvoolu ja -pinge moonutuse edasiseks vähendamiseks.

Appendix

PAPER I

H. Afshari, O. Husev, O. Matiushkin and D. Vinnikov, "Novel Dual-Purpose Cost-Effective Forward-Based Micro-Converter," 2025 IEEE Seventh International Conference on DC Microgrids (ICDCM), Tallinn, Estonia, 2025, pp. 1–5, doi: 10.1109/ICDCM63994.2025.11144743.

Novel Dual-Purpose Cost-effective Forward-Based Micro-Converter

Hossein Afshari
Department of Electrical Power Engineering and Mechatronics.
Tallinn University of Technology
Tallinn, Estonia
hossein.afshari@taltech.ee

Oleksandr Husev
Department of Electrical Power Engineering and Mechatronics
Gdansk University of Technology
Gdansk, Poland
oleksandr.husev@pg.edu.pl

Oleksandr Matiushkin
Department of Electrical Power Engineering and Mechatronics
Tallinn University of Technology
Tallinn, Estonia
oleksandr.matiushkin@taltech.ee

Dmitri Vinnikov
Department of Electrical Power Engineering and Mechatronics
Tallinn University of Technology
Tallinn, Estonia
Dmitri.vinnikov@taltech.ee

Abstract— This article presents an innovative universal non-isolated forward-based micro-converter, designed for seamless integration into both dc and single-phase ac grids through shared terminals. It features a wide input voltage regulation range and minimizes the use of components, isolated drivers and sensors to achieve cost efficiency. The proposed solution advances the conventional forward dc-dc converter by incorporating an additional clamp output capacitor circuit. Its core innovation lies in channeling the transformer's magnetizing energy directly to the output side. The article provides design guidelines for passive components and control methodologies tailored to this approach. Experimental prototypes of the dual-purpose solar micro-converter were developed and tested to validate their efficient and reliable performance.

Keywords—dc Microgrid, Dual Purpose, Micro-inverter, Forward, Common Ground.

I.   INTRODUCTION

As global electrical energy consumption surges and fossil fuels deplete, renewable sources like solar power are becoming increasingly vital. Solar photovoltaic (PV) capacity is projected to reach approximately 160 billion watts, with significant national initiatives underway to expand PV integration [1]. Micro-inverter technology, which eliminates bulky low-frequency transformers and supports "plug-and-play" setups, is gaining prominence. It offers advantages such as localised Maximum Power Point Tracking (MPPT) for optimizing performance despite module mismatches and partial shading, and it enhances safety by enabling fast shutdown features at the module level [2]-[10]. Micro-inverters enable real-time module-level monitoring, providing users with enhanced control and insights.

The micro-inverter market, as shown in Table I, includes key players like Enphase, AP Systems, Sungrow, Hoymiles, ZJ Beny, and Envertech, offering a range of products with varying power outputs, MPPT voltage ranges, and efficiencies [11]. Enphase leads with high-efficiency models (up to 98%), while others provide cost-effective alternatives with slightly lower efficiency. This diversity highlights the trade-offs between efficiency, power output, and cost, underscoring the need for innovative solutions like the proposed non-isolated, dual-purpose micro-inverter to bridge the gap in the market. micro-inverter research and commercialization have largely focused on flyback, interleaved flyback, and H-bridge-derived topologies. Flyback converters dominate the market (e.g., Enphase, APS Systems) due to their simplicity, galvanic isolation, and low component count Recent advancements in micro-inverter technology have led to improved efficiency and reduced costs, largely due to developments in semiconductor technology and power electronics. Innovations in manufacturing processes and materials are expected to further decrease the cost [12].

TABLE I – MICRO-INVERTER MARKET OVERVIEW.

Manufacturer	Peak AC Power (VA / W)	MPPT Voltage (V)	Efficiency %		Cost
			Max	EU	
Enphase (IQ7 series)	250	27 - 37	98	97	$$$$
	295	27 - 45			
	320	53 - 67			
Enphase (IQ8 series)	240	27 - 37	98	97	$$$$
	290	29 - 45			
	325	33 - 45			
	349	36 - 45			
	380	38 - 45			
AP systems Dual Micro-inverter (DS3)	625 - 960	28 - 45	96.5	96	$$$
Sungrow (S450S)	450	16 - 60	96.2	95.4	$$$
Hoymiles (HMS series)	450	16 - 60	96.7	96	$$$
ZJ Beny (BYM series)	500-700	24 - 50	97.5	97	$$$
Envertech (EVT series)	360	22 - 48	96	95	$$$

The micro-inverter market is growing rapidly, with its value expected to surpass USD 6.48 million by 2032, driven by factors such as improved energy harvesting efficiency and real-time monitoring capabilities. The shift towards solar energy's benefits is fostering the industry landscape, making micro-inverters a more cost-effective choice for solar power systems. Among the various micro-inverter solutions, the forward-based non-isolated converter stands out for its cost-effectiveness, especially in the context of power ranges around
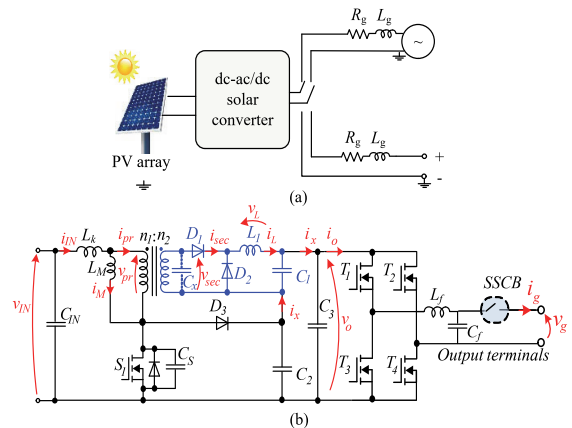

Fig. 1. (a) Concept of dual-purpose converter, (b) Proposed forward-based micro-converter.

450 W. Unlike flyback converters, which often require interleaving for higher power applications forward-based converters utilize a transformer rather than a choke, which can significantly reduce component costs and losses [13].

The main advantage of a forward-based dc-dc converter is a single switch solution, low cost and high efficiency. Despite the popularity of forward dc-dc converter, it has a disadvantage that it requires a core "reset": when the switch is turning OFF, the storage energy in the transformer should be transferred somewhere, otherwise it causes a big voltage spike on the switch [14]. On the other hand, if considering the parasitic parameters of the transformer, such as leakage inductance, the nonlinear processes appear during the operation of the converter, resulting in a spike and high-frequency oscillation of the drain-source voltage of the switch. There are several solutions to solve a spike problem across the switch [13].

DC provides several advantages over ac, making it a viable alternative as modern power systems increasingly incorporate variable renewable energy sources, which often require costly adaptations in ac infrastructure [15]. However, the widespread adoption of dc grids faces a key challenge: the limited availability of dc-compatible devices[16]-[21]. Developing hybrid equipment capable of operating on both ac and dc could enable a smoother transition, particularly in applications where dc offers the greatest benefits [22]. This is especially relevant for new installations in regions with underdeveloped ac grids, as well as for upgrading existing ac cables to enhance power capacity. To bridge the gap between ac and dc systems, we propose dual-purpose converters (Fig. 1) that function in both grid types, facilitating a flexible transition to dc while supporting LVDC investments and meeting the needs of dc consumers [23], [24].

The forward-based dual-purpose non-isolated micro-converter, as illustrated in Fig. 1, represents an efficient and cost-effective solution for solar power systems. It solves the "reset" core problem of the transformer and instead of circulating the leakage inductance current in the primary side of the transformer, it flows to the output capacitor cascade and to the output. The ideal configuration in terms of efficiency and cost is to incorporate primary side passive decoupling in conjunction with an unfolding stage with the advantage of zero dynamic loss. However, the presence of diode D1 necessitates a hybrid approach that combines both high-frequency and low-frequency operations. This combination effectively leverages the benefits of each method.

Section II provides a general description of the proposed topology. Section III presents control methodology and experimental results, including efficiency curves, thermal performance, and Bill of Materials (BOM) comparisons. Section IV concludes the study.

II. DESCRIPTION OF THE PROPOSED STRUCTURE

A. General Overview

Fig. 1(a) shows the general concept of the solar dc-ac/dc micro-converter. The developed converter can be connected to both types of grids by the same terminals and at the same time, has minimal internal redundancy. The proposed solution has the same protection system and control unit for both types of grids. The structure of the universal solar (dc-dc/ac) converter contains a semiconductor part, an output filter, an Electromagnetic Interference (EMI) filter, and protection circuits.

The forward-based micro-converter is designed to offer a cost-effective solution for integrating PV systems into the grid. Unlike traditional flyback converters, the forward-based proposed configuration benefits from a transformer rather than a choke, which helps reduce component costs and minimize energy losses. Also as it is the non-isolated solution the non-isolated sensors and drivers can be used to reduce overall costs additionally. The core architecture includes a primary side decoupling stage combined with an unfolding circuit. This design optimizes efficiency and reduces component stress by leveraging the transformer's ability to manage power transfer effectively.

The proposed forward-based micro-converter offers several advantages over conventional solutions. As a non-isolated common-grounded system, it significantly reduces costs while effectively eliminating leakage currents between grounds. Despite incorporating a higher number of semiconductors, it operates with only one active switch, ensuring that conduction losses remain comparable to those of a flyback converter. Additionally, the extra inductance on the transformer's secondary side does not increase the total stored inductive energy, making the design more efficient than a conventional flyback converter. Furthermore, while the output stage includes an additional capacitor cascade, the total capacitance energy remains unchanged compared to the flyback topology. A key advantage of this design is its ability to prevent voltage spikes on the switch, even in cases of high leakage inductance, which is a common issue in flyback converters. These features make the proposed micro-converter an efficient and cost-effective alternative for photovoltaic applications, ensuring stable performance while minimizing material and costs.

As depicted in fig. 1b, when the switch S_1 is turned ON the transformer gives energy to the forward cell and the magnetizing inductor starts to keep energy . Diode D_1 also starts to conduct, but D_2 and D_3 are OFF. Capacitor C_1 is charging while capacitor C_2 is discharging. When switch S_1 is turning OFF, the current of the magnetizing inductor should flow with some path, therefore diode D_3 starts to conduct. The forward-based converter goes to a zero state. The diode D_2 is conducting in the zero state, while D_1 is OFF. The capacitor C_1 is discharging and C_2 reversely is charging by the magnetizing current. It is possible to express the output voltage of the proposed solution by analyzing active and zero states and writing Kirchhoff equations. The average value of the output voltage depends on a transformer turns ratio, duty cycle and the input voltage:

$$V_O = \frac{v_{IN} \cdot \left(1 + N \cdot D \cdot \left(1 - D\right)\right)}{1 - D},$$ (1)

where v_{IN} is the input voltage, N is the step-up ratio of the transformer (n_2/n_1), D is the value of the duty cycle.

B. Control System

The presence of diode D_1 makes it impossible for the proposed solution to operate as a single stage when connected to an ac load. To overcome this limitation, the bridge operates with a combination of 62.5 kHz PWM and 100 Hz unfolding. This approach allows the solution to function efficiently with AC load. The forward-based micro-inverter employs a sophisticated control strategy that integrates both high-frequency and low-frequency operation modes to achieve optimal performance.

The control approach enables dual-purpose operation for

ac or dc loads, are depicted in fig. 2 (a), (b), and (c), respectively. The forward-based micro-converter employs an advanced dual-mode control strategy (Fig. 2. (a) and (b)) for controlling the ac power that optimally balances high-frequency and low-frequency operations to enhance power conversion efficiency and adaptability. The system architecture is designed to maximize power transfer by integrating primary-side decoupling with an unfolding circuit, effectively achieving near-zero dynamic loss.

As shown in fig.3 , during high-frequency operation, when the forward stage output remains below input voltage, a three-level unipolar Pulse-Width Modulation bridge converts dc into a rectified ac waveform with minimal energy dissipation, reducing switching losses and improving overall efficiency. However, as output voltage falls below the modulation index threshold, the system seamlessly transitions to a dual-stage operation mode. In this mode, MPPT is managed by the dc-dc stage, while the unfolding circuit ensures efficient ac power injection, maintaining stable operation across a wide range of input voltages. This adaptive control strategy prevents efficiency degradation under fluctuating solar conditions, making the converter well-suited for PV applications.

To further enhance grid compliance and dynamic response, the control methodology incorporates a Proportional-Resonant (PR) controller for precise current regulation, a Phase-Locked Loop (PLL) for accurate grid synchronization, and PWM techniques for optimized switching sequences. The unfolding circuit, in coordination with these control elements, refines the ac output waveform while maintaining grid compatibility with minimal harmonic distortion. The proposed forward-based topology, with its ability to operate seamlessly across various input conditions, offers a cost-effective and space-efficient alternative for next-generation solar energy systems, making it an attractive solution for residential and commercial PV applications.

Fig. 3. Proposed synergetic control strategy.

The system employs dual high-frequency and low-frequency operation modes to achieve optimal performance. During high-frequency operation, a high-frequency bridge configuration is activated when the output voltage of the forward stage ranges between 0 and the input voltage (Vin). This mode employs techniques akin to conventional 3-level unipolar PWM to efficiently convert dc into a rectified ac signal. Conversely, in low-frequency operation—triggered when the output voltage exceeds Vin—the system shifts to a simplified 2-level switching strategy to minimize switching losses and enhance efficiency under high-voltage conditions. This low-frequency mode corresponds to the activation of the unfolder circuit, which processes the rectified ac signal by unfolding it into a sinusoidal ac waveform at line frequency.
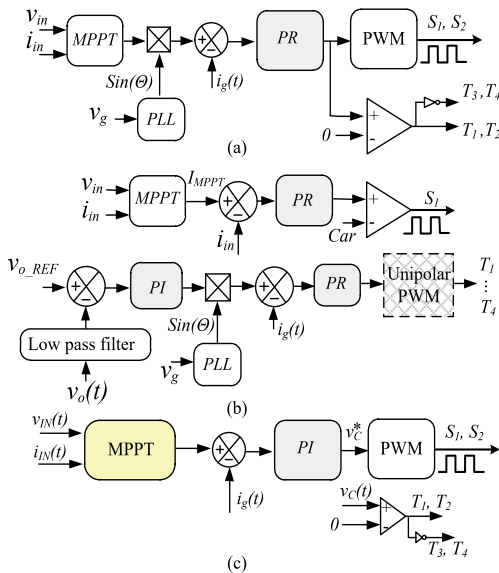

Fig. 2. Control methodology: (a) AC load connection when output voltage is lower than input voltage, (b) AC load connection when output voltage exceeds input voltage, (c) DC load connection.
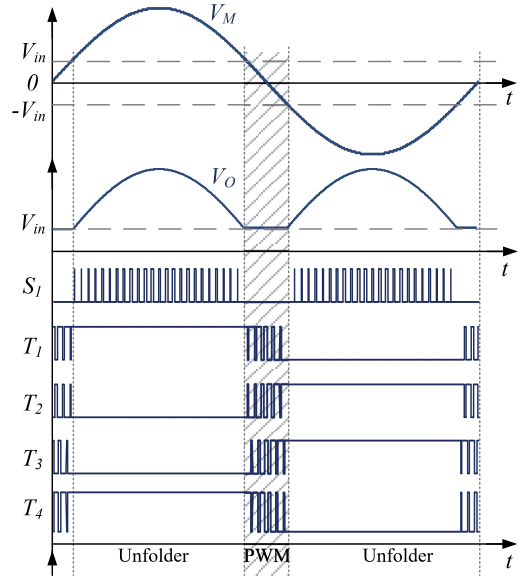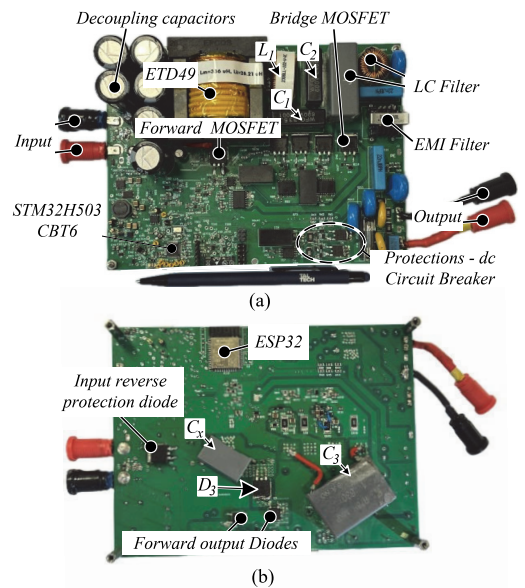

Fig. 4. Experimental prototype of the proposed forward-based dc ready micro-converter: (a) top view, (b) bottom view.

III. EXPERIMENTAL RESULTS

To validate the operation and performance of the proposed non-isolated dc-dc micro-converter, a comprehensive experimental prototype was developed and tested. The physical prototype, as shown in Fig. 4, integrates both power and control stages, including the auxiliary power supply, control logic, switching components, and protection features. The converter is designed around an STM32H503RBT6 microcontroller, which acts as the central control unit, handling PWM generation, sensor feedback, and system logic. The auxiliary circuit, powered directly from the input PV source, provides the required low-voltage dc rails to supply the microcontroller, sensors, and ESP32 communication module.

The power stage consists of a high-frequency ETD49 transformer, forward and bridge MOSFETs, output diodes, and passive filtering elements. The output stage incorporates an LC filter to minimize voltage ripple, and a dedicated EMI filter is added at the output to meet electromagnetic compatibility (EMC) requirements. For additional protection, a dc circuit breaker is integrated on the output side. High-speed SiC Schottky diodes (C4D02120, C3D02065E, and C3D10065A) were selected for D_1, D_2, and D_3 respectively to ensure fast switching, low reverse recovery losses, and high thermal reliability. These diodes facilitate efficient power transfer and robust reverse polarity protection.

Table II summarizes the electrical characteristics of the passive components and transformer. The design follows a cost-effective approach by minimizing isolation components. Only the high-side gate drivers of the bridge configuration and the output current sensor are galvanically isolated, aligning with safety requirements while optimizing system cost. Figs. 5(a), and 5(b) illustrate the desired dual-purpose operation of the forward-based micro-converter showcasing the performance for both ac and dc load connection.

TABLE II – DESIGN PARAMETERS.

Parameter	Value
Input voltage range v_{IN}	15-70 V
Output voltage v_o	350 V
Max input power P_{INMAX}	540 W
Max input current i_{INMAX}	11 A
Max output current i_{OMAX}	1.3 A
Switching frequency f_{SW}	62.5 kHz
Input decoupling capacitor C_{IN}	15.3 mF
Forward cell capacitor C_1	3.3 uF
Clamp capacitor C_2	3.3 uF
Output capacitor C_3	1 uF
Secondary side capacitor C_x	2.2 nF
Forward cell inductor L_1	1000 uH
LCL filter inductance L_{f1}	620 uH
LCL filter inductance L_{f2}	180 uH
LCL filter capacitance C_f	1 uF
Transformer core	ETD49
Core Material Grade	3C95
Magnetising inductance (pr) L_m	220 uH
Leakage inductance of transformer (pr) L_k	28.2 uH
Number of turns (pr) n_1	18
Number of turns (sec) n_2	98
Core airgap	400 um
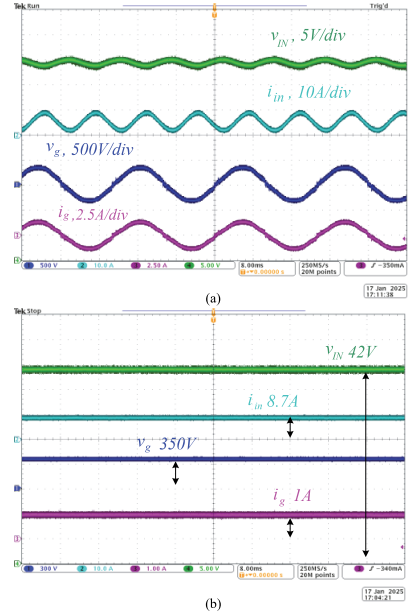
Fig. 5. Experimental results of dual propose forward-based micro-converter when the input voltage is 45 V for AC (a), DC(b).

The input stage incorporates a 15.3 mF decoupling capacitance, designed using the methodology outlined in [12] to maintain stable bus voltage regulation. The transformer is built around an ETD49-3C95 ferrite core, with the primary winding consisting of 18 turns of 0.04mm × 2000 litz wire and the secondary winding featuring 98 turns of 0.1mm × 2000 litz wire. To minimize interwinding capacitance, the windings are wound without layer overlap. While this design choice slightly increases leakage inductance, it prevents excessive stress on semiconductor devices, ensuring reliable operation.

Fig. 5 (a) demonstrates the input voltage and current of the proposed solution, along with the output voltage of the forward-based stage and the load current when connected to ac loads. The control methodology is validated by analyzing the output current and voltage. When the output voltage falls below the input level, the system switches to conventional unipolar PWM inverter control mode. Conversely, if the output voltage exceeds the input, the control shifts to unfolder mode, where output power is regulated by gating the forward-based switch. This adaptive control ensures efficient operation across varying conditions.

For dc load applications, as illustrated in Fig. 5 (b), the input voltage and current are presented alongside the output voltage and current at a standard 350V level. These measurements provide insight into the system's performance under different operational scenarios, highlighting its versatility in handling both ac and dc loads. The waveforms confirm stable regulation and effective power delivery, reinforcing the robustness of the proposed design.

Fig. 6 compares the efficiency of AC and DC loads under 40V and 60V input voltages across 1–10A current levels, measured using a Yokogawa WT1800E power analyzer. Efficiency increases at higher input voltages and lower currents due to reduced conduction losses and optimized duty cycles. Peak efficiency occurs at 60V, reaching 94.2% for DC loads at 6A and 94.4% for AC loads at 4A. While DC loads typically operate with near-constant duty cycles (especially
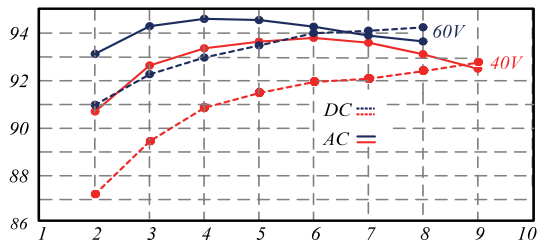
Fig. 6. Efficiency comparison of AC and DC loads across input voltages (40V and 60V) at varying current levels.

evident at 350V), AC loads benefit from a sinusoidal duty cycle at lower currents. However, beyond 5A, cumulative losses cause AC efficiency to drop below DC.

IV. CONCLUSION

This paper presented a novel dual-purpose, non-isolated forward-based micro-converter capable of seamless integration into both dc and single-phase ac grids. The proposed topology addresses key challenges in renewable energy systems by offering a cost-effective, high-efficiency solution with minimal component redundancy. By leveraging a transformer-based design with an innovative clamp capacitor circuit, the converter efficiently channels magnetizing energy to the output side, eliminating voltage spikes and reducing switching losses. The dual-mode control strategy ensures adaptive operation, switching between high-frequency PWM and low-frequency unfolding modes to optimize performance across varying load conditions. Experimental validation confirmed peak efficiencies of 94.4% for ac and 94.2% for dc loads, along with stable operation under a wide input voltage range (15–70 V). These results demonstrate the converter's potential as a versatile and economical solution for next-generation photovoltaic systems, particularly in applications requiring flexible grid compatibility. Future work could explore scalability for higher power ranges and further optimization of passive components to enhance efficiency at lower input voltages.

REFERENCES

[1] Ali O M Maka, Jamal M Alabid, Solar energy technology and its roles in sustainable development, Clean Energy, Volume 6, Issue 3, June 2022, Pages 476–483.

[2] K. Alluhaybi, I. Batarseh and H. Hu, "Comprehensive Review and Comparison of Single-Phase Grid-Tied Photovoltaic Microinverters," in *IEEE Journal of Emerging and Selected Topics in Power Electronics*, vol. 8, no. 2, pp. 1310-1329, June 2020.

[3] Dominic, J, "Comparison and design of high-efficiency microinverters for photovoltaic applications," M.S. thesis, Virginia Tech, 2014.

[4] M. Forouzesh, Y. P. Siwakoti, S. A. Gorji, F. Blaabjerg and B. Lehman, "Step-Up DC–DC Converters: A Comprehensive Review of Voltage-Boosting Techniques, Topologies, and Applications," in *IEEE Transactions on Power Electronics*, vol. 32, no. 12, pp. 9143-9178, Dec. 2017.

[5] X. Li, J. Liu, X. Zhou and J. Liu, "A High-Frequency-Link Split-phase Voltage-Source Microinverter Based on Buck-Boost AC Chopper for High Efficiency and Low Voltage Stress," in *IEEE Transactions on Power Electronics*. (Early Access)

[6] H. Afshari, O. Husev, O. Matiushkin, D. Vinnikov and C. Roncero-Clemente, "DC-Ready Flyback-Based Micro-Converter," *2024 IEEE 18th International Conference on Compatibility, Power Electronics*

and Power Engineering (CPE-POWERENG), Gdynia, Poland, 2024, pp.

[7] R. Heidari, M. A. Ghanbari, E. Adib and M. Rivera, "Coupled Inductor-Based Soft-Switched Boost-Ćuk Converter for Microinverter Applications," in *IEEE Transactions on Power Electronics*, vol. 40, no. 7, pp. 9543-9555, July 2025

[8] X. Xue, Z. Liu, W. Li and H. Su, "Design of a Single-Stage Dual Active Bridge Microinverter With Wide Load Adaptability Based on Loss Optimization," in *IEEE Transactions on Power Electronics*, vol. 40, no. 6, pp. 7919-7935, June 2025.

[9] C. Xiao *et al*., "A Novel Single-Phase Nonisolated Dual-Input Microinverter With Active Power Decoupling," in *IEEE Transactions on Power Electronics*, vol. 40, no. 3, pp. 4437-4448, March 2025.

[10] H. Wu, X. Tang, J. Zhao and Y. Xing, "An Isolated Bidirectional Microinverter Based on Voltage-in-Phase PWM-Controlled Resonant Converter," in *IEEE Transactions on Power Electronics*, vol. 36, no. 1, pp. 562-570, Jan. 2021

[11] MicroInverter Comparison Chart 2024. Available online: https://www.cleanenergyreviews.info/microinverter-comparison (accessed on 24 March 2025).

[12] H. Afshari, O. Husev, O. Matiushkin, S. Pourjafar, N. V. Kurdkandi and D. Vinnikov, "Comprehensive Comparison of Grid-Connected Flyback-Based Microinverter With Primary and Secondary Side Decoupling Approach," in *IEEE Transactions on Industry Applications*, vol. 60, no. 6, pp. 9080-9089, Nov.-Dec. 2024.

[13] C.-S. Leu, "Improved Forward Topologies for DC-DC applications with Built-in Input Filter," Ph.D dissertation, Virginia Polytechnic Institute and State University, Blacksburg, Virginia, 2006.

[14] O. Matiushkin, O. Husev, H. Afshari, E. Romero-Cadaval and C. Roncero-Clemente, "Forward-Based DC-DC Converter With Eliminated Leakage Inductance Problem," in *IEEE Transactions on Industrial Electronics*, vol. 72, no. 2, pp. 1638-1648, Feb. 2025.

[15] Mackay, L., Blij, N. H. van der, Ramirez-Elizondo, L., & Bauer, P. (2017). Toward the Universal DC Distribution System. *Electric Power Components and Systems*, 45(10), 1032–1042.

[16] P. Mohseni, S. Pourjafar, O. Matiushkin, O. Husev and D. Vinnikov, "Isolated High Step-Up Current-Fed DC-DC Converter With Low Input Current Ripple and Wide Full-Soft-Switching Capability," in *IEEE Transactions on Industry Applications*.

[17] S. Pourjafar, H. Afshari, P. Mohseni, O. Husev, O. Matiushkin and N. Shabbir, "Comprehensive Comparison of Isolated High Step-up DC-DC Converters for Low Power Application," in *IEEE Open Journal of Power Electronics*, vol. 5, pp. 1149-1161, 2024.

[18] H. Afshari, O. Husev and D. Vinnikov, "A Novel Isolated Buck-Boost dc-dc Converter with Wide Range of Voltage Regulations," *2023 IEEE 17th International Conference on Compatibility, Power Electronics and Power Engineering (CPE-POWERENG)*, Tallinn, Estonia, 2023, pp. 1-6.

[19] V. Sidorov, A. Chub and D. Vinnikov, "Bidirectional Isolated Hexamode DC–DC Converter," *IEEE Trans. on Power Electron.*, vol. 37, no. 10, pp. 12264-12278, Oct. 2022.

[20] S. Khan, A. Chub and D. Vinnikov, "An Overview of Wide-Voltage Range Isolated DC-DC Converters," *2023 IEEE 64th International Scientific Conference on Power and Electrical Engineering of Riga Technical University (RTUCON)*, Riga, Latvia, 2023, pp. 1-6.

[21] N. Yadav, A. Chub, N. Hassanpour, A. Blinov and D. Vinnikov, "Protection and Control Implementation for Bidirectional Step-Up/Down Partial Power Converter for Droop-Controlled DC Microgrids," in *IEEE Transactions on Industry Applications*, doi: 10.1109/TIA.2025.3561767

[22] O. Matiushkin, O. Husev, D. Vinnikov and J. Kurnitski, "DC-Ready Photovoltaic Solar Converter," *PCIM Europe 2023; International Exhibition and Conference for Power Electronics, Intelligent Motion, Renewable Energy and Energy Management*, Nuremberg, Germany, 2023, pp. 1-7.

[23] O. Husev, O. Matiushkin, T. Jalakas, D. Vinnikov and N. V. Kurdkandi, "Comparative Evaluation of Dual-Purpose Converters Suitable for Application in DC and AC Grids," in *IEEE Journal of Emerging and Selected Topics in Power Electronics*, vol. 12, no. 2, pp. 1337-1347, April 2024.

[24] O. Husev, D. Vinnikov, S. Kouro, F. Blaabjerg, C. Roncero-Clemente, "Dual-Purpose Converters for DC or AC Grid as Energy Transition Solution: Perspectives and Challenges," *IEEE Industrial Electron. Magazine*,vol. 18, no. 1, pp. 46-57, March 2024.

PAPER II

Comprehensive Comparison of Grid-Connected Flyback-Based Microinverter With Primary and Secondary Side Decoupling Approach

Hossein Afshari [ID], *Graduate Student Member, IEEE*, Oleksandr Husev [ID], *Senior Member, IEEE*,
Oleksandr Matiushkin [ID], *Member, IEEE*, Saeed Pourjafar [ID], *Member, IEEE*, Naser Vosoughi Kurdkandi [ID],
and Dmitri Vinnikov [ID], *Fellow, IEEE*

Abstract—This paper compares grid-connected flyback-based microinverters employing primary and secondary side fundamental power ripple decoupling approaches. The passive decoupling techniques involve the use of the unfolding circuit on the primary side and an H-bridge inverter on the secondary side to achieve the same number of passive components. The unfolding circuit operates at the grid frequency, unfolding/folding the rectified sinusoidal waveform and providing a current pathway to the grid. Comparative assessments encompass energy accumulation in inductances and capacitors, conduction and switching losses, and voltage stress across semiconductors. Proportional Resonant controllers govern grid current. The theoretical evaluation is complemented by cost analysis using existing component prices, and experimental setups utilizing four-layer printed circuit boards for primary and secondary side decoupling. The results provide a comprehensive comparison, and conclusions offer valuable recommendations based on both theoretical and experimental insights.

Index Terms—Comparison, cost, decoupling approach, H-bridge, microinverter, renewable energy, unfolding circuit.

I. INTRODUCTION

ELECTRICAL energy consumption all over the world is growing rapidly. Because traditional fossil fuels are running out, and there is a risk of climate change happening, finding alternative energy sources is crucial. Different limitations are anticipated to boost the use of renewable energy, like solar and wind power. About 60% of new renewable energy sources will be from solar energy. The global addition of solar photovoltaic capacity is estimated to reach around 160 billion watts so far [1]. Current reports clearly indicate this pattern, and many nations have ambitious plans for the coming decades to integrate widely used PV systems into their renewable energy setups [2].

Typically, with advanced technologies, either centralized or string inverters are employed to feed PV power into the grid. Microinverter technology has garnered significant research attention because it eliminates the requirement for low-frequency power transformers, which are both bulky and costly, and supports "plug-and-play" applications [3], [4]. Key features of the individual Maximum Power Point Tracking (MPPT) algorithm include local optimization and the minimization of power losses arising from mismatched PV modules and partial shading [5]. Microinverter technology can also facilitate the implementation of a fast shutdown function at the module level, addressing specific concern of firefighter safety in rooftop and building-integrated PV installations [6].

The main functions carried out by the grid-connected microinverter involve taking dc power from the panel, implementing MPPT, boosting voltage to meet grid requirements, and injecting ac power into the grid. In terms of the number of power processing stages, inverter topologies can be categorized into single-stage and double-stage configurations [7]. Furthermore, based on the existence of galvanic isolation, microinverters can be classified into isolated and non-isolated structures. An assessment of industrial microinverters considering efficiency, reliability, and topology is provided in Ref. [8].

In a single-phase connection, the power supplied to the grid fluctuates over time, but the power drawn from the PV panel needs to remain constant. Consequently, energy storage elements, typically a capacitor, are employed between the input and output to equalize (or decouple the imbalance - a mismatch between the input DC and the output AC powers) the varying

Fig. 1.   Decoupling the mismatch power between dc and ac powers.

Fig. 2.   Flyback based microinverter, (a) H-bridge-based grid-connected flyback microinverter, and (b) unfolding-based grid-connected flyback microinverter.
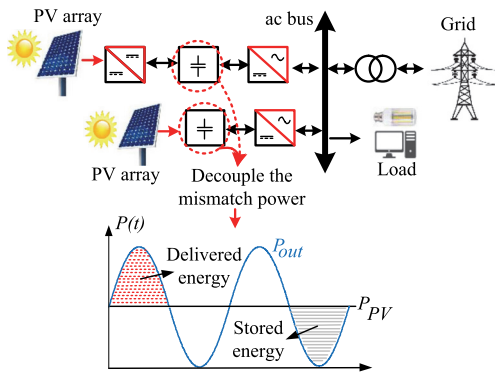
instantaneous input and output power [9], [10]. Several power decoupling techniques have been suggested and evaluated based on efficiency, the size of decoupling capacitors, cost, and control complexity [11], [12]. The configuration for decoupling the mismatch power between dc and ac powers for single-stage and double-stage configurations has been indicated in Fig. 1.

Based on the microinverter topology, the decoupling methods either active, which uses an axillary circuit or passive, can be placed on the PV side, dc link side, and ac side (only active) [13], [14]. Using an active decoupling scheme may extend the lifetime of the microinverter because of the replacement of electrolyte capacitors with film capacitors [15], [16]. However, the power losses corresponding to using an axillary circuit will reduce the overall efficiency. Meanwhile, the power devices have higher stress because of the smaller decoupling capacitor, which causes more losses and lower efficiency. Most commercial microinverters utilize electrolytic capacitors as power decoupling storage elements [17], [18]. This choice is driven by their significant capacitance, cost-effectiveness, and ease of implementation. However, it is important to note that this selection also imposes limitations on the lifespan of the microinverter [19].

In recent years, a quite number of papers have been devoted to using the flyback-based microinverter because of its low cost, low component counts, galvanic isolation, high step-up ratio, simple control due to the existence of one active switch, reliability, etc [20]. However, its main deficiency is the large size of the flyback transformer core with a power of more than 200 W. The interleaved approach is used to overcome this drawback [21]. Numerous efforts have been made to enhance the performance of the flyback microinverter through adjustments to both control and topology. One example is the introduction of a hybrid boost–flyback/flyback microinverter, aiming to repurpose leakage and mitigate the voltage spike of the main switch [22], [23]. A novel, affordable, non-intrusive, and isolated method for sensing current in the grid-tied photovoltaic flyback-based microinverter is introduced in [24]. A flyback converter with active clamping and an unfolder was suggested in [25]. A novel sensorless control system for a microinverter utilizing the flyback topology is put forward. This system eliminates the need for current sensors in the circuit, resulting in a reduction
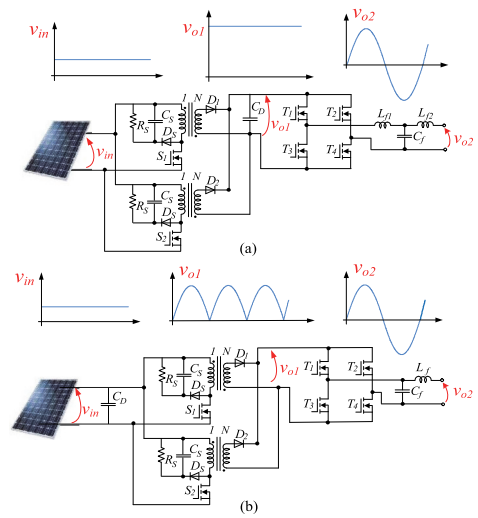
in both overall cost and measurement noise [26]. In [27], an exploration into the stability analysis of the flyback converter is conducted. While most research studies on the flyback focus on its Discontinuous Conduction Mode (DCM) during operation, it is worth noting that DCM can lead to elevated current stress and decreased efficiencies. Additionally, the flyback transformer experiences a relatively higher number of losses in DCM [28]. Furthermore, there are increased hysteresis losses on magnetic material devices in addition to the challenges mentioned [29].

In the flyback-based microinverter, passive decoupling can be done on either the primary side (PV side) or the secondary side (dc link side). Two-level H-bridge inverter is a common topology for the secondary side decoupling approach, while for decoupling on the primary side, the unfolding circuit, which is named a pseudo dc link, is used in most industry lead projects [17]. Hence, it is crucial to conduct a topological comparison of both configurations, considering parameters like energy stored across capacitors and inductances, as well as assessing switching and conduction power losses within the same unit. Additionally, the power loss originating from the flyback transformer core, identified as a significant source [30], is evaluated in both H-bridge-based and Unfolding-based microinverters. To ensure a fair comparison, an unfolding circuit is introduced as a primary decoupling method to equalize the number of passive components in both configurations, as illustrated in Fig. 2. The unfolding bridge is switched at line frequency, generating a rectified sinusoidal waveform at the dc-link between the flyback converter and unfolding bridge. Meanwhile, H-Bridge (HB) operates in high frequency and needs the bulky *LCL* filter-to-filter harmonics and reach output low Total Harmonic Distortion (THD) [31]. In [32] the same methodology of comparison between buck-boost inverters based on the unfolding circuit and H5, H6, HERIC inverters are discussed.

This paper builds upon the results of the conference paper [33], and has been written to distinguish the practical impact of passive decoupling industry-lead approaches in primary as well as secondary sides of flyback-based microinverters. The result itself can be used in any type of converter to figure out the advantage of the PV-side passive decoupling approach versus the DC-link-side decoupling ones. The same flyback topology was selected to stress the decoupling approach, not the topology itself. Topology itself is selected based on the most useable topology. In the design process for both topologies, a fair comparison is proved by almost the same type of components and thermal design, the same number of active and passive components, and output current THD, which is critical while designing the filter. In this regard, both converters are designed and tested in the laboratory. Various analyses such as cost, size, as well as efficiency were done. Considering that contemporary photovoltaic panels can operate within a maximum power output up to 600 W, the designed converters are structured to span a varied power range, catering to MPPT voltages ranging from 25 V to 60 V.

The article is organized as follows. Section II is devoted to the designing of passive components, the CCM mode flyback, Filter design as well as control. Section III outlines the comparison methodology, presenting the results through a spider diagram that combines simulation and theoretical analysis. Section IV denoted the experimental validation, including assessments of size, cost, and efficiency. Finally, Section V is devoted to the recommendations and conclusions of this article.

II. METHODOLOGY OF COMPARISON

To ensure a fair discussion, both topologies are assessed under identical input voltage and power ranges. Additionally, both configurations share the same number of passive components. The comparative analysis involves several criteria, with the first criterion being the assessment of the energy stored across inductances. This criterion aids in predicting the values of the inductors.

This parameter takes into account the maximum currents across inductances with the nominal values of components. The second criterion involves evaluating the energy stored across capacitors $\sum E_C$, which directly affects the size requirements of the capacitors.

To calculate the total energy accumulated in inductances as well as capacitors, and the total conduction power loss the following equations are used:

$$\sum_{i=1}^{n} E_{C_i} = \frac{1}{2} C_i V_{Peak_i}{}^2, \tag{1}$$

$$\sum_{j=1}^{m} E_{L_j} = \frac{1}{2} L_j I_{Peak_j}{}^2, \tag{2}$$

where n and m are the number of capacitors and inductances, respectively. Another important criterion is a total voltage stress across semiconductors, which defines the necessary parameters of switches.

Next criterion is the semiconductor power losses, and switching power loss, which is consists of switching as well as conduction power losses, and has direct impact on the size and efficiency of the system. The fundamental waveforms of a converter are independent of the selection of components and electric parameters (e.g., switching frequency, selected semiconductors) and result from the basic modulation scheme, yielding some general requirements for the dimensioning of the components. Considering this statement, the simplified equations can be used:

$$P_{\text{conduction}} \cong \sum_{i=1}^{N_S} R_{DS} I_{RMSi}^2, \tag{3}$$

where I_{RMSi} is RMS switch current, N_S is the number of switches. To calculate the conduction loss of switches we need R_{DS}, drain-source resistor, which is described in datasheet. This value is chosen 2.6 mΩ, for the primary side switch, and 0.38 Ω for the secondary side switches. Switching loss of semiconductors is derived by (4). V_s and I_s are maximum voltage and current of switch in off as well as on states respectively. t_r is rise time.

$$P_{\text{switching}} \cong t_r f_s \sum_{i=1}^{N_S} \left\langle \hat{i}_{Si} \cdot \hat{v}_{Si} \right\rangle_T. \tag{4}$$

The main idea is to compare topologies from a topological point of view. With this mind, the comparison has been implemented based on assuming the constant value for semiconductor dependent values such as rise time. The passive component is designed in the next section.

III. DESIGN PROCEDURE

A. Passive Component Designation

The fundamental concept of a flyback current source inverter is to adapt the current source with its voltage linked to the grid voltage. The PV panel functions as the current source. In an unfolding-based application, the flyback is managed to extract maximum power from the PV module and deliver a semi-sinusoidal current to the grid output.

The flyback converter can function in three operation modes: CCM, DCM, and Boundary or Critical Current Mode (BCM). Energy conversion in the flyback converter is achieved by alternately turning the power transistor on and off, utilizing the transformer's magnetizing inductance (L_M). When the MOSFET switch is turned on, energy is stored in the magnetizing inductance. Subsequently, the energy is transferred to the load when the switching power transistor turns off. The operation modes of the flyback converter are illustrated in Fig. 3. In a continuous mode of operation, switch S_1 is turned on before the secondary current falls to zero. Continuous mode offers a greater power capability for an equivalent peak current value. This implies that, for the same output power, the peak currents in DCM are significantly higher than those in CCM). Consequently, a more expensive power transistor with a higher current rating is required. Additionally, the higher secondary peak currents in the DCM mode can lead to a larger transient spike at the moment of turn-off.
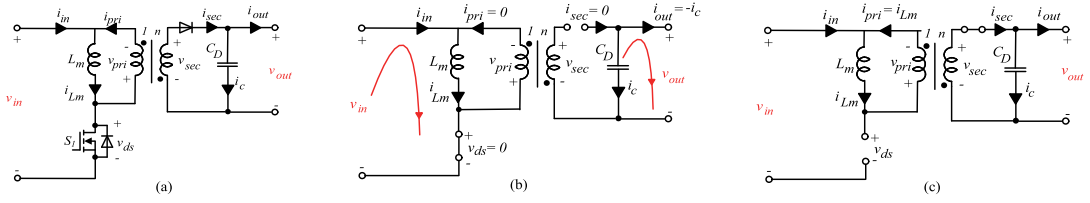
Fig. 3. Operation mode of the flyback converter, (a) Flyback converter (b) operation mode 1, and (c) operation mode 2.
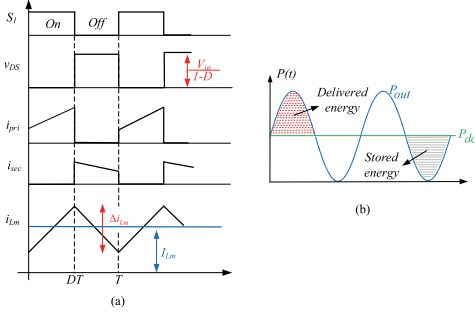
Fig. 4. Current and voltage shapes in CCM operation mode (a) and output power pulsation and decoupling capacitor power process (b).

Despite the challenges, the discontinuous mode remains more favored than the continuous mode for two main reasons. Firstly, the inherently smaller magnetizing inductance in DCM results in a faster response and a lower transient output voltage spike when there is a sudden change in load current or input voltage. Secondly, CCM introduces a right-half-plane zero in its transfer function, making the design of the feedback control circuit more complex. Keeping these considerations in mind, the CCM mode is employed for operation due to its higher power capability. The (5) is derived through the point that in a steady state the average voltage of Inductance in one period is equal to zero ($<V_L>T = 0$). D is the duty ratio, and n is the turning ratio of the flyback transformer.

$$\int_0^{DT} (v_{in})dt + \int_{DT}^T \left(-\frac{v_{out-flyback}}{n} \right) dt = 0$$
$$\rightarrow \frac{v_{out-flyback}}{v_{in}} = n \times \frac{D}{1-D}. \tag{5}$$

Fig. 4(a) illustrates the current and voltage shapes in CCM. Through the magnetizing inductance current shape in Fig. 4(a), and regarding calculated space for both the average and instant value of the magnetizing inductance current and time zone between zero to switching time. It can be derived that the operation mode is a boundary for $\Delta I_{Lm}/2 = I_{Lm}$ and is CCM for $\Delta I_{Lm}/2<I_{Lm}$.

$$I_{Lm} = \frac{P_{in}}{v_{in}D}, \tag{6}$$

$$D = \frac{v_{Out}}{nv_{in} + v_{Out}}. \tag{7}$$

In CCM operation mode the magnetizing inductance is calculated through replacing equation number (6) and (7) in $\Delta I_{Lm}/2<I_{Lm}$.

$$\frac{v_{inMax}^2 \cdot v_{Out}^2}{2 \cdot P_{in} \cdot f_s \cdot (n \cdot v_{inMax} + v_{Out})^2} < L_m. \tag{8}$$

The output instantaneous power, illustrated in Fig. 4(b), consists of two terms: the average output power ($V_m.I_m$)/2, and the time varying term (pulsating power) ($V_m.I_m\cos(2\omega t)$)/2, which oscillates at twice the line frequency. The symbol ω is the grid frequency, I_m and V_m are the amplitudes of the grid voltage and grid current, respectively:

$$P_{out}(t) = \frac{V_m \cdot I_m}{2} + \frac{V_m \cdot I_m}{2} \cos(2\omega t). \tag{9}$$

To maintain power balance, the pulsating power should be balanced with a decoupling capacitor. This capacitor is selected through the following equation, where $\Delta V_C \leq 0 \cdot 05 \times V_C$. Through this formula, the difference in voltage results in different decoupling capacitor sizes.

$$\frac{P_{dc}}{2\pi \cdot f_{grid} \cdot V_C \cdot \Delta V_C} \leq C_D. \tag{10}$$

The output filter is a substantial component of pulse width modulation (PWM) converters. The THD level is very similar in both cases, but the output filter and other passive components are different. It highlights the difference between solutions and contribution to cost and losses. The size of output filter in HB-based structure should be high to reach an acceptable THD. However, by using the unfolding circuit instead of H-bridge topology the required output filter size significantly reduces due to the lower harmonic component of the converter output voltage at the switching frequency. The output filter is designed based on the equations presented in [31].

C_f is limited to decrease the capacitive reactive power at a rated load to less than the predetermined relative value Δ.

$$C_f \leq \frac{\Delta \cdot P}{v_g^2 \cdot 2 \cdot \pi \cdot f_{grid}}, \tag{11}$$

where P and v_g are output power and voltage, respectively.

In the unfolding case, the grid side inductance is calculated based on (12).

$$L_f \geq \frac{v_i(h_{sw}) \cdot v_g}{P \cdot THD_V \cdot 2\pi f_{sw}}. \tag{12}$$

TABLE I
DESIGN TARGET PARAMETERS

Input voltage (v_{in})	10 V to 75 V
MPPT voltage (V_{MPPT})	25 V to 60 V
Maximum power	600 W
Flyback switches Switching frequency (f_s)	40 kHz
H-bridge switches Switching frequency (f_s)	65 kHz
Resonance frequency (f_{RES})	20 kHz
Maximum DC-link voltage	400 V
Grid frequency (f_{grid})	50 Hz
Turns ratio (n)	6

Fig. 5. Comparison of H-bridge-based and unfolding-based flyback microinverters based on theoretical analysis.

In the above equation, $v_i(h_{sw})$ is the harmonic component of the converter output voltage at the switching frequency (f_{sw}).

$$v_i(h_{sw}) = \frac{P \cdot (1 - D_{MPPT})}{v_g \cdot C \cdot f_s}. \tag{13}$$

In the case of H-bridge inverter, the following equation is used.

$$L = \frac{1}{4 \cdot \pi^2 \cdot C_f \cdot f_{RES}^2}, \tag{14}$$

L is weighted inductance value, is equal to $L_{f1} + L_{f2}$. Resonance frequency should select based on $10 f_{grid} < f_{RES} < 0.5 f_{sw}$. The design parameters are expressed in Table I.

Considering the weighted inductance value, the converter side and grid side inductances can be calculated.

$$L_{f1} = \frac{1+r}{r} \times L, \quad L_{f2} = r \cdot L_{f1} \tag{15}$$

To calculate the relation index between the two inductances the (15) is used, where r is the relation index and is $0 < r < 1$.

$$r^2 \left(4\pi^2 f_{sw}^2 L^2 C_f - L \right) - \left(4\pi^2 f_{sw}^2 L^2 C_f + L \right)$$
$$+ r \left(8\pi^2 f_{sw}^2 L^2 C_f - 2L - \frac{v_i(h_{sw}) \cdot v_g}{P \cdot THD_V \cdot 2\pi f_{sw}} \right) = 0. \tag{16}$$

The snubber circuit components are designed as explained in [34]. Therefore, the following equations can be written for snubber circuit components:

$$P_{sn} = V_{sn} \frac{i_{peak} t_s}{2} f_s, \tag{17}$$

$$R_{sn} = \frac{V_{sn}^2}{\frac{1}{2} L_{nk} i_{peak}^2 \frac{V_{sn}}{V_{sn} - n V_{out}} f_s}, \tag{18}$$

$$C_{sn} = \frac{V_{sn}}{\Delta V_{sn} R_{sn} f_s}. \tag{19}$$

In (17)–(19), V_{sn} is the voltage of the snubber capacitors which needs to be established under conditions of minimum input voltage and full load. f_s denotes the switching frequency
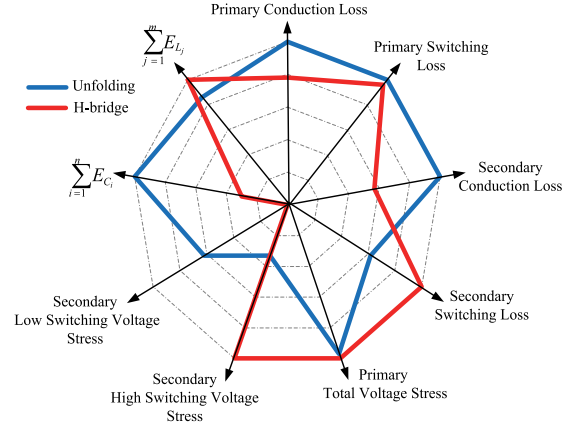
of the flyback converter. R_{sn} is the snubber resistance. Moreover, i_{peak} is the primary current peak. L_{nk} is the leakage inductance of the transformers. P_{sn} is dissipated power in snubber circuit. Besides, 5–10% ΔV_{sn} ripple for is acceptable.

B. Comparison Results

In previous sections, passive components for both case of h-bridge and unfolding circuit are designed. Furthermore, four criteria are chosen to use in comparison. The spider diagram in Fig. 5 depicts the comparison between the h-bridge and unfolding-based microinverter.

The mentioned criteria are shown in this picture. In comparison with H-bridge based flyback microinverter, the unfolding based flyback microinverter has bigger value of decoupling capacitance due to lower voltage in primary side results in the more energy accumulated in this capacitor. At the same time, the total energy accumulated in inductances is approximately the same. The larger coupled inductor required for solution with unfolding circuit is compensated by smaller output filter. Due to the lower peak output voltage in the secondary side of flyback transformer with unfolding circuit, the voltage stress across the switch S_1 is slightly lower. Also, the drain-source voltage of T_1 to T_4 switches is equal to the maximum grid voltage. Meanwhile, in the h-bridge case, this voltage is equal to the DC-link voltage.

Also, a solution based on unfolding approach has significantly lower secondary high switching voltage stress due to the low frequency operation of bridge switches. As a result, the secondary side switching losses are significantly lower as well. While primary switching as well as conduction losses in primary and secondary sides are higher.

C. Control Scheme

To obtain a high-quality sinusoidal output current on the grid side, direct control of the output current is essential through a closed-loop controller. Various control methods can

Fig. 6. Control block diagram. (a) Unfolding-based flyback microinverter. (b) h-bridge-based flyback microinverter.

TABLE II
ELECTRICAL SPECIFICATIONS

Parameter / Specification	Value / Type	
	Primary side decoupling	Secondary side decoupling
Converter volume (mm^3)	197.48*152.29*31.2	187.92*111.45*24.9
Transformer Core/ normalized core volume (mm^3)	ETD59 / 100	ETD49 / 40
Magnetic inductance (uH)	60	60
Leakage inductance (nH)	370	450
Decoupling capacitor (uF)	6 * 2200	8 * 22
Output filter Capacitance (uF)	1	1
Output filter inductance (uH)	$L_f = 220$	$L_{f1} = 680$ / $L_{f2} = 180$
Secondary diode	IDM05G120C5XTMA1	IDM05G120C5XTMA1
Microcontroller	STM32F334C6T6TR	STM32F334C6T6TR
Flyback switches	IPB044N15N5ATMA1	IPB044N15N5ATMA1
Bridge switches	STB28N65M2	C3M0120065J
Snubber capacitor (nF)	10	10
Snubber Diode	MBR20H100CT	MBR20H100CT
Snubber Resistor (kΩ)	2.35	2.35

be employed for managing the inverter connected to the grid, with the most prevalent ones being PID (Proportional-Integral-Derivative) and Proportional-Resonant (PR) controllers.

In an unfolding-based flyback microinverter, all control dynamics are managed by controlling the gate signal of the switch on the primary side of the flyback converter. Essentially, both Maximum Power Point Tracking (MPPT) and grid current control are accomplished by manipulating the gated signal of $S1$.

In an H-bridge-based flyback microinverter, power control for injection is achieved in the inverter section, while MPPT is attained by controlling the dc-dc stage. Control block diagrams for the two topologies are sequentially depicted in Fig. 6(a) and (b). In both instances, the overall control systems comprise a few distinct blocks, including a Phase-Locked-Loop (PLL) and an MPPT algorithm.

The control system in unfolding-based microinverter requires measuring some parameters such as solar panel voltage and current, as well as grid voltage, and current. These parameters are necessary to reach MPPT, which generates the amplitude value of the grid current I_{REF}. Furthermore, PLL generates a signal, which is in phase with the grid voltage. The PR controller is used to obtain rectified sinusoidal current at the output of the dc-dc stage.

IV. EXPERIMENTAL VERIFICATION

A. Experimental Results

The unfolding-based flyback microinverter prototype, laboratory-developed environment, and the prototype of the h-bridge-based flyback microinverter are illustrated in Fig. 7(a), (b), and (c), respectively. Each prototype is a four-layer printed circuit board that includes a power stage, auxiliary and control

parts. Cores ETD59 and ETD49 are used for interleaved flyback transformers in the primary and secondary side decoupling-based solutions sequentially. Passive RCD snubbers are used to surplus the voltage stress across the primary side switches of the flyback converters caused by the resonance of the output capacitance of the MOSFET in combination with the leakage inductance and the winding capacitance. Electrolyte capacitors are used as decoupling capacitors. The electromagnetic interference (EMI) section is placed after the filter on the output side to effectively address any EMI in the output signal.

The E4360A PV area simulator is employed to accurately replicate various photovoltaic conditions, ensuring a thorough assessment of our system's performance. This choice not only enhanced result reliability but also contributed to the reproducibility of findings in real-world photovoltaic applications.

Table II contains electrical specifications, the physical size of the prototypes and values of the passive components, as well as core materials and electrical details of the transformers used in the experimental setups. All passive components were chosen according to the calculations in Section II. Because of line frequency switching in unfolding topology, the conduction losses, and lower turn-on resistor come into consideration while choosing the switches. Due to the low RMS current, another cheaper silicon-based switch can be used with a small reduction in the efficiency of the converter. It is a matter of trade of between cost and efficiency. However, due to the lack of dynamic features requirement, these transistors have a low overall figure of merit and are relatively cheap.
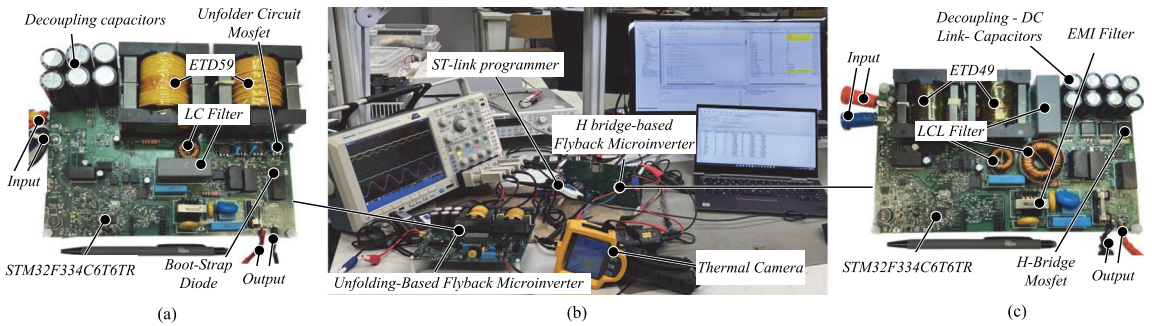
Fig. 7.   (a) The unfolding-based flyback microinverter prototype. (b) Laboratory-developed environment. (c) The prototype of h-bridge-based flyback microinverter.
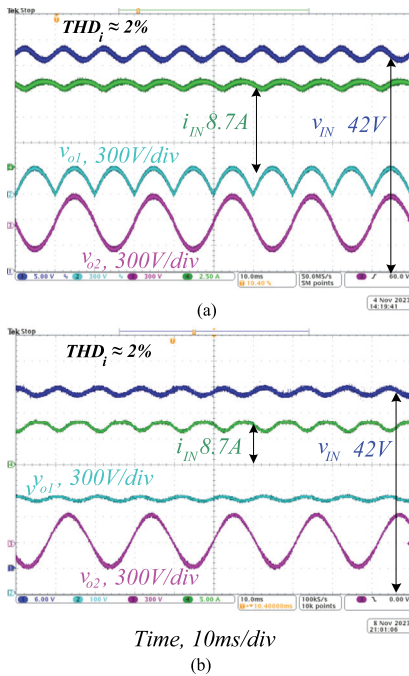

Fig. 8.   Experimental results of flyback-based microinverter when the input voltage is 42 V and the input current 8.7 A. (a) With a primary side decoupling method. (b) With a secondary side decoupling approach.

Fig. 9.   Efficiency study versus different input voltages under input constant current.

The control unit includes an ST microcontroller STM32F334C6T6TR, which has enough peripherals such as high-resolution timers, analogue to digital converters, etc. The bootstrap circuit is designed to reduce the number of power supplies for dual-output isolated drivers in bridge switches. The input current and voltage sensors are non-isolated, while the output sensors are isolated ones.

Both converters work from 25 V to 75 V open circuit voltages and 25 V to 60 V MPPT voltage ranges. Fig. 8(a) and (b) show the desired operation for the secondary side and primary side decoupling-based flyback microinverters for MPPT Voltage
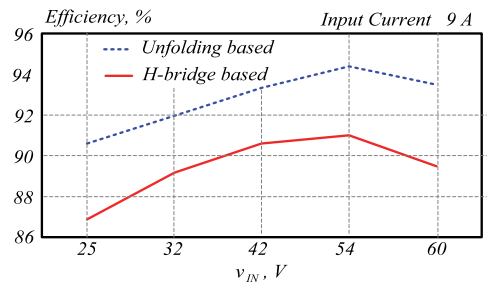
points 42 V and 8.7 A. The dc-link and input voltage oscillation are shown to visualize the decoupling procedure and to verify the control methods, which are described in the previous section. Furthermore, the grid voltage as well as the output of the flyback converter also plotted to distinguish between h-bridge and unfolding operations. In the primary side decoupling approach, the flyback converter produces a rectified sinusoidal waveform, and the unfolding bridge's role is to further shape this signal into a sinusoidal wave within the circuit. The unfolding circuit is very attractive for practical applications considering that the unfolding circuit works with the grid frequency and needs the incredibly lower size of the filter in the output of the unfolding bridge.

Fig. 9 contains the efficiency curve versus different variations of the input voltage with 9 A constant input current, which is conducted using the Yokogawa WT1800E high-performance power analyzer. Logically efficiency of the proposed solutions is lower under lower input voltages, because of the high input current and big duty cycle. The maximum points of efficiency in a case of 54 V are 91 % and 94.4 % for solutions with secondary and primary side decoupling approaches respectively, which included auxiliary losses as well.

Fig. 10(a) and (b) depict the thermal image of the unfolding and h-bridge-based solution consequently, which indicates the hottest points during operation in the maximum 600 W output power.
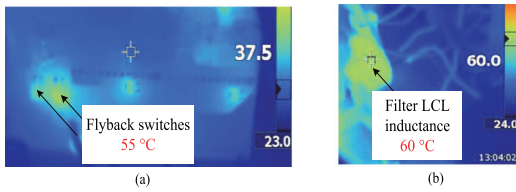
Fig. 10. Thermal image captured by a thermal camera depicting the hottest points during operation in the maximum 600 W output power. (a) Unfolding case. (b) H-bridge case.

Fig. 12. Comparison between the flyback-based microinverter using primary and secondary side decoupling approaches in terms of cost, size and efficiency.
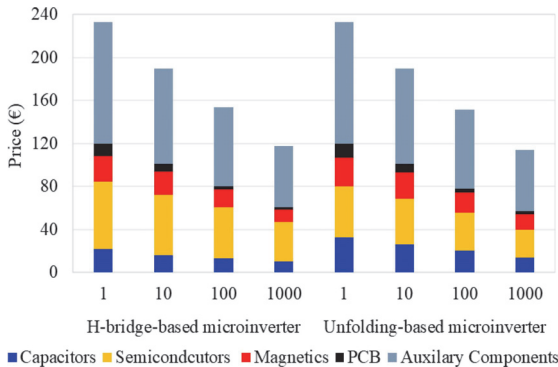

Fig. 11. The cost graph of the H-bridge and Unfolding-based flyback microinverters for different numbers of assemblies.

TABLE III
Cost Comparison of the Unfolding-Based and H-Bridge-Based Microinverters

Characteristic	All components of the power circuit							
	Price (€)				Price (€)			
	H-bridge-based				Unfolding-based			
No. assembly	1	10	100	1000	1	10	100	1000
Capacitors	21	16	13	10	32	26	20	14
Semiconductors	63	57	48	37	48	43	36	26
Magnetics	24	22	17	12	27	24	19	14
PCB	11	7	3	2	13	8	4	3
Auxiliary Components	113	89	74	57	113	89	74	57
Total Price	233	190	153	118	233	190	152	114

B. Cost Comparison

Fig. 11 illustrates a comprehensive comparison of component costs across varying assembly quantities for both H-bridge-based and Unfolding-based flyback microinverters. To provide a deeper insight into the cost analysis, the cost data for each individual component has been detailed in Table III. The information presented in Table III and Fig. 11 offers a precise breakdown of the cost analysis, focusing on the number of semiconductor elements in the power circuit, including switches and diodes, as well as the count of capacitors, induction elements, and auxiliary components. It is important to note that auxiliary components, such as those found on driver boards, control circuits, auxiliary supplies, and protective parts, maintain a consistent cost across
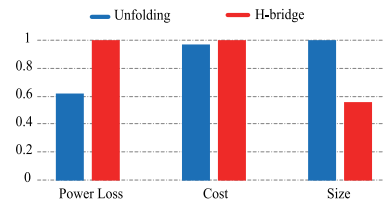
both converters, as visualized in Fig. 12. It is worth highlighting that the data in this figure is based on current component prices available from component distributor webpage.

Upon examination of Fig. 11, it becomes evident that the cost of capacitors, printed circuit boards (PCB), and inductive elements in the H-bridge-based microinverter is relatively lower compared to the Unfolding-based microinverter. This results in the overall cost of the H-bridge-based microinverter being somewhat more economical than its Unfolding-based counterpart for less number of assemblies. However, it is essential to recognize that although the total cost of the H-bridge-based microinverter may be lower than that of the Unfolding-based microinverter, the cost of semiconductors, which plays a substantial role in determining the overall cost, has decreased in the Unfolding-based microinverter. In addition, the overall cost of the Unfolding-based microinverter in high quantities is cheaper than H-bridge-based. Therefore, the Unfolding-based microinverter has the potential to achieve a more cost-effective design compared to the H-bridge-based alternative by optimizing components like PCB and magnetic elements in future iterations. This, coupled with the reduced semiconductor expenses, positions the unfolding-based microinverter for a competitive pricing advantage.

The drawn chart in Fig. 12. Compares the flyback-based microinverter using primary and secondary side fundamental power decoupling approaches in terms of key factors including cost, size and cost. Notably, the unfolding-based approach demonstrates enhanced efficiency at nearly identical costs, making it particularly advantageous for large-scale production scenarios.

In the context of size, the utilization of a larger transformer and a relatively higher capacitor in the unfolding-based microinverter design contributes to a slightly increased physical footprint. Despite this size difference, a notable advantage arises from the primary side decoupling approach. This involves the strategic use of low-voltage and high-capacity decoupling capacitors, which can increase the lifetime and the reliability of the microinverter.

V. Conclusion

This paper meticulously analyzes grid-connected industry lead flyback-based microinverters, comparing their low-frequency power ripple decoupling methods on both the primary and secondary sides. It provides comprehensive design guidelines for key components like the decoupling capacitor, flyback

converter, snubber circuit, and output filter. The closed-loop control is achieved by properly tuning both PI and PR controllers. The result itself can be used in any type of converter to figure out the advantage of the PV-side passive decoupling approach versus the DC-link-side decoupling ones.

The comparative analysis introduces multiple criteria, encompassing power losses, voltage stress, and energy accumulation in capacitors and inductances. Experimental setups are designed and tested in the laboratory to validate theoretical results. Crucial factors such as efficiency/power loss, cost, and size are comprehensively compared. The design strives for fairness and considers advancements in the design of flyback transformers and semiconductor technology for an equitable evaluation. A detailed cost analysis breaks down semiconductor and power circuit elements, capacitors, induction elements, and auxiliary components based on component distributor website prices.

The secondary side decoupling approach stands out for its smaller decoupling capacitor size, potentially reducing conduction losses. Primary side decoupling is highlighted for its efficiency enhancement at lower costs, especially advantageous for large-scale production. Moreover, the utilization of unfolding circuits results in significantly reduced switching power losses owing to their low-frequency switching characteristics. The paper emphasizes a holistic approach to comparison, acknowledging that while efficiency is crucial the price is also given for reference and can be considered in relative units because the components available for companies are significantly cheaper.

REFERENCES

[1] M. Malinowski, J. I. Leon, and H. Abu-Rub, "Solar photovoltaic and thermal energy systems: Current technology and future trends," *Proc. IEEE*, vol. 105, no. 11, pp. 2132–2146, Nov. 2017.

[2] N. Shabbir et al., "Techno-economic analysis and energy forecasting study of domestic and commercial photovoltaic system installations in Estonia," *Energy*, vol. 153, 2022, Art. no. 124156.

[3] Z. Zhang et al., "High efficiency step-up DC–DC converter for grid-connected photovoltaic microinverter applications," *IET Renewable Power Gener.*, vol. 16, pp. 1159–1169, 2022.

[4] K. Alluhaybi, I. Batarseh, and H. Hu, "Comprehensive review and comparison of single-phase grid-tied photovoltaic microinverters," *IEEE J. Emerg. Sel. Top. Power Electron.*, vol. 8, no. 2, pp. 1310–1329, Jun. 2020.

[5] V. Sidorov, A. Chub, and D. Vinnikov, "High-efficiency quad-mode parallel PV power optimizer for DC microgrids," *IEEE Trans. Ind. Appl.*, vol. 59, no. 1, pp. 1002–1012, Jan./Feb. 2023.

[6] H. M. Maheri, D. Vinnikov, A. Chub, V. Sidorov, and I. Galkin, "Application of cycle skipping modulation in buck–boost photovoltaic microconverters," *IEEE Trans. Ind. Appl.*, vol. 58, no. 4, pp. 4804–4815, Jul./Aug. 2022.

[7] Y. Yang et al., *Advances in Grid-Connected Photovoltaic Power Conversion Systems*. Sawston, U.K.: Woodhead Publishing, 2018.

[8] A. Lunardi, L. F. N. Lourenço, E. Munkhchuluun, L. Meegahapola, and A. J. S. Filho, "Grid-connected power converters: An overview of control strategies for renewable energy," *Energies*, vol. 15, no. 11, 2022, Art. No. 4151.

[9] J. Dominic, "Comparison and design of high efficiency microinverters for photovoltaic applications," M.S. thesis, Virginia Tech, Blacksburg, VA, USA, 2014.

[10] H. Hu, S. Harb, N. Kutkut, I. Batarseh, and Z. J. Shen, "A review of power decoupling techniques for microinverters with three different decoupling capacitor locations in PV systems," *IEEE Trans. Power Electron.*, vol. 28, no. 6, pp. 2711–2726, Jun. 2013.

[11] Z. Yang, J. Zeng, Q. Zhang, Z. Zhang, V. Winstead, and D. Yu, "A composite power decoupling method for a pv inverter with optimized energy buffer," *IEEE Trans. Ind. Appl.*, vol. 57, no. 4, pp. 3877–3887, Jul./Aug. 2021.

[12] A. R. Paul, A. Bhattacharya, and K. Chatterjee, "A novel single phase grid connected transformer-less solar micro-inverter topology with power decoupling capability," *IEEE Trans. Ind. Appl.*, vol. 59, no. 1, pp. 949–958, Jan./Feb. 2023.

[13] Y. Ohnuma, K. Orikawa, and J. -i. Itoh, "A single-phase current-source PV inverter with power decoupling capability using an active buffer," *IEEE Trans. Ind. Appl.*, vol. 51, no. 1, pp. 531–538, Jan./Feb. 2015.

[14] K.-P. Huang, Y. Wang, and R.-J. Wai, "Design of power decoupling strategy for single-phase grid-connected inverter under nonideal power grid," *IEEE Trans. Power Electron.*, vol. 34, no. 3, pp. 2938–2955, Mar. 2019.

[15] Y. Xia, J. Roy, and R. Ayyanar, "A capacitance-minimized, doubly grounded transformer less photovoltaic inverter with inherent active-power decoupling," *IEEE Trans. Power Electron.*, vol. 32, no. 7, pp. 5188–5201, Jul. 2017.

[16] E. Heydari, A. Y. Varjani, and D. Diallo, "A dual-function power decoupling circuit for single-stage grid-connected PV inverter," *IEEE Trans. Power Electron.*, vol. 37, no. 6, pp. 7422–7431, Jun. 2022.

[17] J. Yuan, F. Blaabjerg, Y. Yang, A. Sangwongwanich, and Y. Shen, "An overview of photovoltaic microinverters: Topology, efficiency, and reliability," in *2019 IEEE 13th Int. Conf. Compat., Power Electron. Power Eng.*, 2019, pp. 1–6.

[18] A. Jamatia, V. Gautam, and P. Sensarma, "Power decoupling for single-phase PV system using C´uk derived microinverter," *IEEE Trans. Ind. Appl.*, vol. 54, no. 4, pp. 3586–3595, Jul./Aug. 2018.

[19] Y. Liu, W. Zhang, Y. Sun, M. Su, G. Xu, and H. Dan, "Review and comparison of control strategies in active power decoupling," *IEEE Trans. Power Electron.*, vol. 36, no. 12, pp. 14436–14455, Dec. 2021.

[20] V. Gautam and P. Sensarma, "Enhancing the voltage gain of a flyback converter using leakage energy," *IEEE Trans. Ind. Appl.*, vol. 54, no. 5, pp. 4717–4727, Sep./Oct. 2018.

[21] T. Lodh, N. Pragallapati, and V. Agarwal, "Novel control scheme for an interleaved flyback converter based solar PV microinverter to achieve high efficiency," *IEEE Trans. Ind. Appl.*, vol. 54, no. 4, pp. 3473–3482, Jul./Aug. 2018.

[22] A. B. Shitole, S. Sathyan, H. M. Suryawanshi, G. G. Talapur, and P. Chaturvedi, "Soft-switched high voltage gain boost-integrated flyback converter interfaced single-phase grid-tied inverter for SPV integration," *IEEE Trans. Ind. Appl.*, vol. 54, no. 1, pp. 482–493, Jan./Feb. 2018.

[23] F. Zhang, Y. Xie, Y. Hu, G. Chen, and X. Wang, "A hybrid boost–flyback/flyback microinverter for photovoltaic applications," *IEEE Trans. Ind. Electron.*, vol. 67, no. 1, pp. 308–318, Jan. 2020, doi: 10.1109/TIE.2019.2897543.

[24] R. Za'im, J. Jamaludin, and N. A. Rahim, "Photovoltaic flyback microinverter with tertiary winding current sensing," *IEEE Trans. Power Electron.*, vol. 34, no. 8, pp. 7588–7602, Aug. 2019, doi: 10.1109/TPEL.2018.2881283.

[25] M. A. Rezaei, K.-J. Lee, and A. Q. Huang, "A high-efficiency flyback micro-inverter with a new adaptive snubber for photovoltaic applications," *IEEE Trans. Power Electron.*, vol. 31, no. 1, pp. 318–327, Jan. 2016.

[26] N. Falconar, D. S. Beyragh, and M. Pahlevani, "An adaptive sensorless control technique for a flyback-type solar tile microinverter," *IEEE Trans. Power Electron.*, vol. 35, no. 12, pp. 13554–13562, Dec. 2020, doi: 10.1109/TPEL.2020.2992779.

[27] T. N. Huynh and J. Khazaei, "Stability analysis of grid-connected flyback converter for PV power applications," in *2020 IEEE 52nd North Amer. Power Symp.*, 2021, pp. 1–6.

[28] A. Bhattacharya, A. R. Paul, and K. Chatterjee, "A coupled inductor based ćuk microinverter for single phase grid connected PV applications," *IEEE Trans. Ind. Appl.*, vol. 59, no. 1, pp. 981–993, Jan./Feb. 2023.

[29] T. V. Thang, N. M. Thao, D.-H. Kim, and J.-H. Park, "Analysis and design of a single-phase Flyback microinverter on CCM operation," in *Proc. IEEE 7th Int. Power Electron. Motion Control Conf.*, 2012, pp. 1229–1234.

[30] T. Instruments, "Flyback transformer design considerations for efficiency and EMI," Power Supply Design Seminar, Texas Instrum., Dallas, TX, USA, Tech. Rep. 2016/17, 2016.

[31] A. C. Husev, E. Romero-Cadaval, C. Roncero-Clemente, and D. Vinnikov, "Voltage distortion approach for output filter design for off-grid and grid-connected PWM inverters," *J. Power Electron.*, vol. 15, no. 1, pp. 278–287, Jan. 2015.

[32] O. Matiushkin, O. Husev, D. Vinnikov, and N. V. Kurdkandi, "Comparative analysis of buck-boost inverters based on unfolding circuit versus H5, H6, HERIC topologies," in *2022 IEEE Int. Symp. Power Electron., Elect. Drives, Automat. Motion*, 2022, pp. 547–552.

[33] H. Afshari, O. Husev, D. Vinnikov, O. Matiushkin, and N. V. Kurdkandi, "Comparison of grid-connected flyback-based microinverter with primary and secondary side decoupling approach," in *2022 IEEE 63th Int. Sci. Conf. Power Elect. Eng. Riga Tech. Univ.*, Riga, Latvia, 2022, pp. 1–6.

[34] G.-B. Koo, "Application note AN-4147: Design guidelines for RCD snubber of flyback converters," *Fairchild Semicond. Corp.*, 2006.

Hossein Afshari (Graduate Student Member, IEEE) was born in Zanjan, Iran, in 1997. He received the B.S. degree in electrical engineering from Semnan University, Semnan, Iran, in 2019, and the M.S. degree in electrical Railway engineering from Iran University of Science and Technology, Tehran, Iran, in 2022. He is currently working toward the Ph.D. degree in power electronics with the Tallinn University of Technology (Taltech), Tallinn, Estonia. His research interests include modeling, control, and design of power electronic converters, power electronic transformer, grid-connected solar converters, and modular multilevel converters.

Oleksandr Husev (Senior Member, IEEE) received the B.Sc. and M.Sc. degrees in industrial electronics from Chernihiv State Technological University, Chernihiv, Ukraine, in 2007 and 2008 respectively. He defended Ph.D. thesis with the Institute of Electrodynamics of the National Academy of Science of Ukraine, Kyiv, Ukraine, in 2012. He is currently a Senior Researcher and projects Leader of the Department of Electrical Power Engineering and Mechatronics, Tallinn University of Technology (TalTech), Tallinn, Estonia, and is an Associate Professor with his home University (Chernihiv National Polytechnic University), Chernihiv, Ukraine. He has more than 200 publications and is the holder of several patents (including European patents). He is recognized as a Best Young Scientist in both Taltech and home Universities. His research interests include power electronics systems, design of novel topologies, and control systems based on a wide range of algorithms, including modeling, design, and simulation, applied design of power converters and control systems and application. He was the recipient of the Estonian National Research Award in Technical Sciences in 2024.

Oleksandr Matiushkin (Member, IEEE) received the B.Sc. and M.Sc. degrees in industrial electronics from the Chernihiv National University of Technology, Chernihiv, Ukraine, in 2016 and 2018, respectively, and the Ph.D. degree in power electronics from the Tallinn University of Technology, Tallinn, Estonia, in 2022. He is currently a Researcher with the Department of Electrical Engineering at the same university. He is also a Postdoctoral Researcher with the University of Extremadura, Badajoz, Spain. His research interests include power electronics, new topology design, microcontroller and FPGA programming, modeling, filter calculations, and control techniques for power electronics converters.

Saeed Pourjafar (Member, IEEE) was born in Ardabil, Iran. He received the B.Sc. degree in electrical engineering from Azerbaijan Shahid Madani University, Tabriz, Iran, in 2015, and the M.Sc. degree in power electronics and drives from the Sahand University of Technology, Faculty of Electrical and Computer Engineering, Tabriz, Iran, in 2017, and the Ph.D. degree in power electronics and drives from the Energy Management Research Center, University of Mohaghegh Ardabili, Ardabil, Iran, in 2021. He is currently a Postdoctoral Researcher with the Tallinn University of Technology, Tallinn, Estonia, focusing on DC-DC converters, and the application of power electronics in renewable systems.

Naser Vosoughi Kurdkandi (Member, IEEE) was born in Bostanabad, East Azerbaijan Province, Iran, in 1989. He received the B.Sc. degree in electrical engineering from Islamic Azad University, South Tehran Branch, Tehran, Iran, in 2011, and the M.Sc. and Ph.D. degrees in electrical engineering and power electronics from the University of Tabriz, Tabriz, Iran, in 2014 and 2019, respectively. From 2019 to 2020, he was a Postdoctoral Researcher with the University of Tabriz, Tabriz, Iran. In 2020, he joined the Tallinn University of Technology, Tallinn, Estonia, as a Postdoctoral Researcher. Since 2022, he has been a Postdoctoral Research-Fellow with San Diego State University, San Diego, CA, USA. His research interests include multilevel inverters, grid-connected PV inverters, DC-DC switched-capacitor and switched-inductor converters, fast charging stations for electric vehicles, battery-based energy storage systems, and induction motor drives.

Dmitri Vinnikov (Fellow, IEEE) received the Dipl.Eng., M.Sc., and Dr.Sc.techn. degrees in electrical engineering from the Tallinn University of Technology, Tallinn, Estonia, in 1999, 2001, and 2005, respectively. He is currently the Head of the Power Electronics Group, Department of Electrical Power Engineering and Mechatronics, Tallinn University of Technology. Moreover, he is one of the founders and leading researchers of ZEBE—Estonian Centre of Excellence for zero energy and resource efficient smart buildings and districts. He has authored or coauthored two books, five monographs, and one book chapter as well as more than 400 published articles on power converter design and development, and he is the holder of numerous patents and utility models in this field. His research interests include the applied design of power electronic converters and control systems, renewable energy conversion systems (photovoltaic and wind), impedance-source power converters, and the implementation of wide bandgap power semiconductors. Dr. Vinnikov is the Chair of the IEEE Estonia Section.

PAPER III

Afshari, Hossein, Oleksandr Husev, Oleksandr Matiushkin, and Dmitri Vinnikov. 2022. "A Review of Hybrid Converter Topologies", *Energies* 15, no. 24: 9341. https://doi.org/10.3390/en15249341.

Review

A Review of Hybrid Converter Topologies

Hossein Afshari *, Oleksandr Husev, Oleksandr Matiushkin and Dmitri Vinnikov [ID]

Department of Electrical Power Engineering and Mechatronics, Tallinn University of Technology, 12616 Tallinn, Estonia
* Correspondence: hoafsh@ttu.ee

Abstract: There is a growing interest in solar energy systems with storage battery assistance. There is a corresponding growing interest in hybrid converters. This paper provides a comprehensive review of hybrid converter topologies. The concept of a hybrid inverter is introduced and then classified into isolated and non-isolated structures based on using a galvanic transformer. The classification and description of each type are presented based on the features and applications. Furthermore, the most popular commercial solutions are investigated in terms of their simplicity, flexibility, efficiency, and battery technology. The summarizing features are presented through tables, and future trends for researchers to follow to develop efficient hybrid converters are discussed. This review paper is intended as a convenient reference for hybrid converter users.

Keywords: dc-dc/ac converter; hybrid converter; buck-boost converter; derived converter

1. Introduction

Electrical energy consumption over the whole world is rapidly growing. There is a consistent increase in the demands on power capacity and the efficient production, distribution, and utilization of energy. The general power generation capacity must be increased to meet dynamic load variations [1]. A decrease in the accessibility of conventional energy resources has prompted power engineers and researchers around the globe to look for better and more productive means of the utilization of renewable energy sources (RES).

Power electronic converters play a crucial role in the usage of RES [2]. Power electronic converters are increasingly used in various applications including electric cars, ships, and photovoltaic (PV) panels. An independent power system can be formed by combining renewable energy with local loads. This approach is widely incorporated into modern power systems [3,4]. In this system, dc and ac loads are provided by different types of energy sources using efficient power electronic converters.

Figure 1a shows a simple example of a solar energy system in which a single dc source supplies an ac grid or load. Figure 1b shows the same system with battery assistance. Hybrid converters as multi-output converters are used to provide simultaneous dc and ac outputs for systems, delivering better power density and improved reliability [5,6]. Researchers have been focused on improving the performance of hybrid converters through topological innovations and control methods [7–9].

As a result of the limited amount of power that can be injected into the grid by renewable energy produced by local households, the feed-in energy costs of solar systems are decreasing and are expected to be zero in the current decade [10]. With this in mind, the use of battery storage systems along with renewable energy sources has great importance.

Some review papers have been published in the literature [11–14]. However, this paper focuses on the existing solutions on the market in terms of structure (simplicity), rating powers, and insulation, as well as high efficiency. The main goal of this paper is to propose a general classification of hybrid converters, as well as a brief overview of their state in the marketplace. In this regard, Section 2 presents the ancillary services of converters. Section 3 describes the various functions of the Hybrid converter. The existing solutions for hybrid

converters are analyzed in Section 4. A research overview of isolated and non-isolated hybrid converters is presented in Sections 5 and 6 respectively. Finally, the conclusion is presented in Section 7.
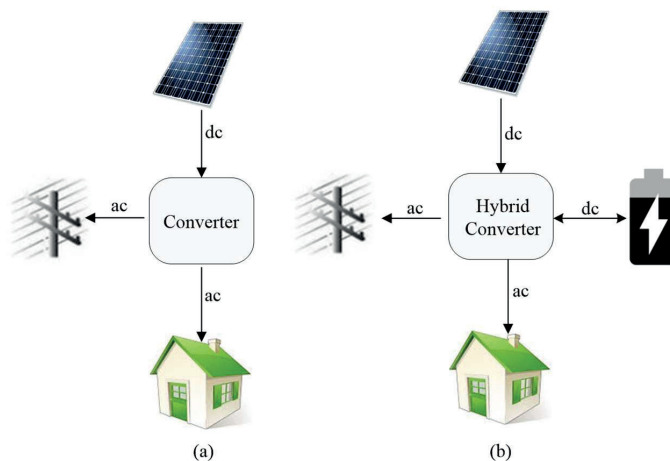

Figure 1. Schematic diagram of a solar energy system: without (**a**) and with (**b**) battery storage assistance.

2. Ancillary Services of Converters

The Federal Energy Regulatory Commission (FERC) defines ancillary services as "those services necessary to support the transmission of electric power from seller to purchaser given the obligations of control areas and transmitting utilities within those control areas to maintain reliable operations of the interconnected transmission system". They are needed for grid reliability [15]. FERC identified six ancillary services including reactive power and voltage control, loss compensation, scheduling and dispatch, load following, system protection, and energy imbalance [16]. Among these services, the power electronics converters seem to be best suited for providing reactive power and voltage control. Voltage regulation has traditionally been done on transmission lines because distribution networks are passive networks. The diffusion of RES directly connected to the distribution networks gave rise to the problem of voltage regulation on these networks. Voltage regulation can be achieved by compensating the reactive power required by the users and aims primarily to maintain voltages within certain ranges, but it is also concerned with minimizing temporal variations in voltage and harmonic distortion. The voltage that is traditionally controlled is that acting on the ratio-changing devices (e.g., transformer taps and voltage regulators), reactive-power-control devices (e.g., capacitors, static-var compensators, and occasionally synchronous condensers), and harmonic-control devices (active power filters). The system operator must monitor and control these voltages and compensate for the reactive power of the grid. Sometimes the network management may find it more economical to purchase reactive power from a customer than to directly compensate the customer for the same reactive power. In this case, some customers can provide this ancillary service to the network [17,18].

When the electrical energy conversion is made with photovoltaic (PV) arrays, an intermediate converter is needed for the connection to the grid. This converter can be either single-stage or dual-stage [19]: the first stage is a dc-dc converter, whereas the second is an inverter synchronized with the utility grid. The dc-dc converter boosts the voltage of the PV arrays up to values suitable for the PWM modulation of the inverter. Maximum Power Point Tracking control (MPPT) is usually implemented on the boost converter to extract the maximum power available from the solar source. Finally, the inverter supplies the power generated by the PV array with the desired power factor to the grid.

When PV systems are used to perform ancillary services to improve grid power quality, they pose several control challenges. For example, in harmonic compensation, it is important to detect the current or voltage harmonic information.

Reference [20] proposed a method based on conservative power theory to detect the harmonic current of the load. In [21], the Point of Common Coupling (PCC) voltage information for harmonic compensation is used through a voltage control loop. In addition, reactive power compensation methods are discussed in [22].

3. Functionalities of Hybrid Converters

An intelligent hybrid converter is a trending type of converter for solar applications using renewable energy for home consumption, especially for solar photovoltaic installations. Some see this as a new technology, however, in some parts of the world such products have been around since the 1990s. In solar systems, power generation fluctuates and may not be synchronized with a load's electricity consumption since solar panels generate electricity only during the day. To fill the gap between what is produced and what is consumed during the evening when solar electricity is not produced, it is necessary to store energy for later use and to manage energy storage as well as consumption with a hybrid converter.

Hybrid converters enable the selection and orientation of renewable energy, grid energy, and energy storage based on consumption. Unlike conventional converters, which systematically store energy in batteries, hybrid converters only store energy when it is needed. This system also allows a choice between whether electricity from photovoltaic panels should be stored or consumed through an internal intelligent apparatus control unit. Hybrid converters can operate in different modes: on-grid, off-grid, hybrid (both on-grid and off-grid at the same time), and backup (in case of a black-out) as described in the following subsections.

3.1. On-Grid General Mode (Hybrid)

As illustrated in Figure 2a,b respectively, if PV has sufficient power to inject the required power of the load, the surplus power of PV is used to charge the battery and feed into the grid. Conversely, when PV has insufficient power, batteries and the grid have the responsibility to supply the load.

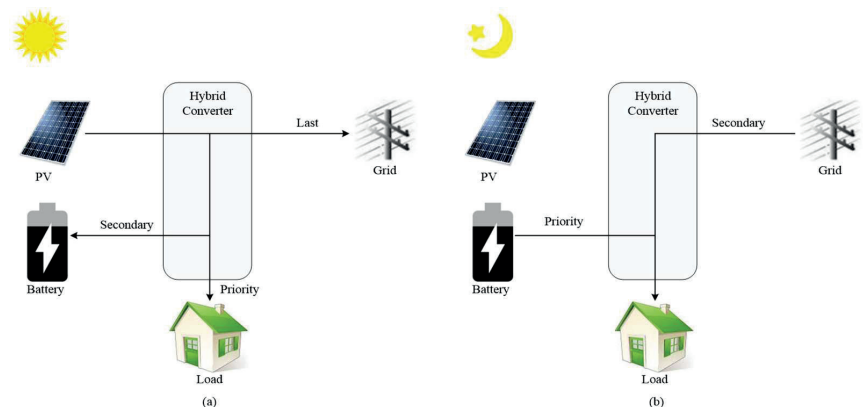**Figure 2.** On-grid general mode: PV power is sufficient (**a**), PV power is insufficient (**b**).

3.2. On-Grid with Battery Backup Mode

PV and the grid both supply the load and charge the batteries (Figure 3a). When the grid is working smoothly, the battery's State of Charge (SOC) is always in full state as depicted in Figure 3b. Batteries discharge only when a grid faults occur (Figure 3c).
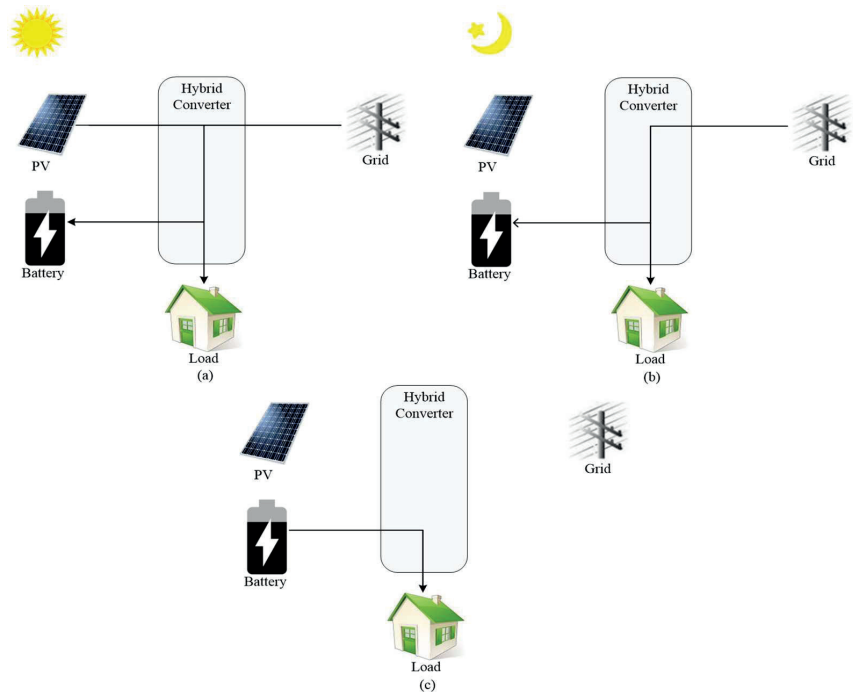
Figure 3. On-grid with battery backup mode: PV power is sufficient (**a**), PV power is insufficient (**b**), when a grid fault occurs (**c**).

3.3. Off-Grid Mode

PV and battery constitute an off-grid system. If PV can supply the required power of the load, the priority is to supply the required power to the load. Any surplus power is used to charge the battery, as shown in Figure 4a. When PV has insufficient power, the battery is used to supply power to the load (Figure 4b).

Figure 4. Off-grid mode: PV power is sufficient (**a**), PV power is insufficient (**b**).

4. Analysis of Hybrid Inverters Available on the Market

The purpose of this section is to provide a comparative analysis of hybrid solar inverters on the market. Several of the most popular commercial hybrid inverters have been chosen for comparison [23]. The select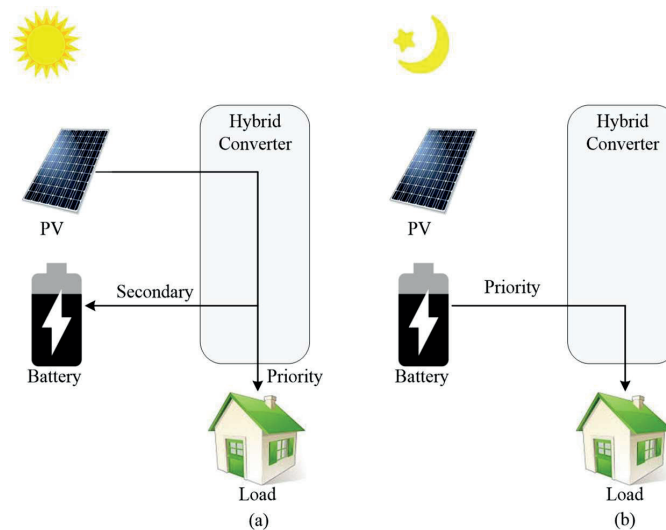ed power range is from 3 kW to 5 kW, which is the typical PV power range for residential applications. All characteristics of the commercial hybrid inverters have been obtained from open sources and are shown in Table 1 [24–35]. These inverters illustrate a variety of solutions that are available on the market currently. The most popular manufacturers were selected for analysis. Most of the inverters are single-phase with an average maximum efficiency of about 97%.

Table 1. Table of commercial hybrid inverters.

№	Device	Nominal AC Power, W	Max. Efficiency, %	Number of Phases	Battery Type	Battery Voltage Range, V	Max. Battery Power, W	Battery Communication	Comments
1	Huawei SUN2000 -5KTL-L1 [27]	5000	97.8	1	Li-ion	350–450	5000	RS485	Battery is connected to dc-link
2	Fronius SYMO Hybrid 5.0-3-S [26]	5000	96	3	LiFePO$_4$	240–345	4800	RS485	Different battery packs can be used (BATTERY 9.0 is shown)
3	Sungrow SH5K-30 [28]	5000	97.1	1	Li-ion	32–70	4500	CAN/ RS485	
4	Redback SH5000 [31]	5000	97	1	Li-ion	42–60	4600	CAN	
5	ABB REACT2- UNO-5.0-TL [30]	5000	96.6	1	Li-ion	170–575	5000	RS485	
6	Solis RHI-1P5K- HVES-5G [32]	5000	97.5	1	Li-ion	120–500	7000	CAN/ RS485	Continuous maximum battery power is 6 kW
7	Imeon 3.6 [33]	3000	94.5	1	Li-ion	42–62	3840	RS485	
8	SolaX X3 Hybrid 5.0 T [34]	5000	97	3	Li-ion	200–500	5000	CAN/ RS485	
9	Sunny Boy Storage 5.0 [35]	5000	97.5	1	Li-ion	100–550	5000	CAN/ RS485	

As Table 1 shows, there are two types of inverters. The first type is those with a low battery voltage range such as the Sungrow SH5K-30, Redback SH5000, and Imeon 3.6. A low voltage range (42–58.8 V) leads to high charging/discharging currents. In the case of the Redback SH5000 inverter, these are 85 A/100 A, respectively. The second type is inverter is those with a high battery voltage. For example, the Solis RHI-1P5K-HVES-5G. The battery voltage of the latter varies from 120 V to 500 V. However, the charging and discharging current in this system is only 20 A. Compatible batteries for inverters are mostly Li-ion. However, according to its datasheet, the 3-phase Fronius SYMO Hybrid uses the LiFePO$_4$-type battery technology, which guarantees a long service life, short charging times, and high depth of discharge. Furthermore, the storage capacity of the Fronius Solar Battery can be adapted to meet individual customer needs. All the selected inverters use the same standard communications—an RS485 connection or a CAN Bus.

The possible structure of the hybrid inverters is illustrated in Figure 5. They consist of solar terminals, a grid-connected Voltage Source Inverter (VSI), a buck-boost cell, which realizes the Maximum Power Point Tracking (MPPT) function, and a common dc-link. In addition, most commercially available inverters have terminals for backup operation.

In the case of string solar hybrid inverters, the battery can be connected directly to the dc-link, or with an additional interface converter, which is integrated into the Energy Storage Systems (ESS), as shown in Figure 5a,b, respectively.

An example of an inverter with a structure without an additional interface converter is the Huawei SUN2000-5KTL-L1. It is evident that simplicity and low cost are the main advantages, while limited battery types and voltage are the main drawbacks. An example

of an inverter with an external ESS with an additional interface converter, as in Figure 5a, is the Fronius SYMO Hybrid 5.0-3-S. In this case, the company provides the ESS system as an additional feature, while the inverter has dc-link terminals for connection. Other hybrid solar inverters, such as the Sungrow SH5K-30, have an isolated integrated battery interface converter. This corresponds to the structure illustrated in Figure 5b. A high step-up of the battery voltage can be realized through this topology. In addition, Figure 5c shows the internal structure of a hybrid inverter where the internal interface battery converter can be connected to the solar panel terminals.
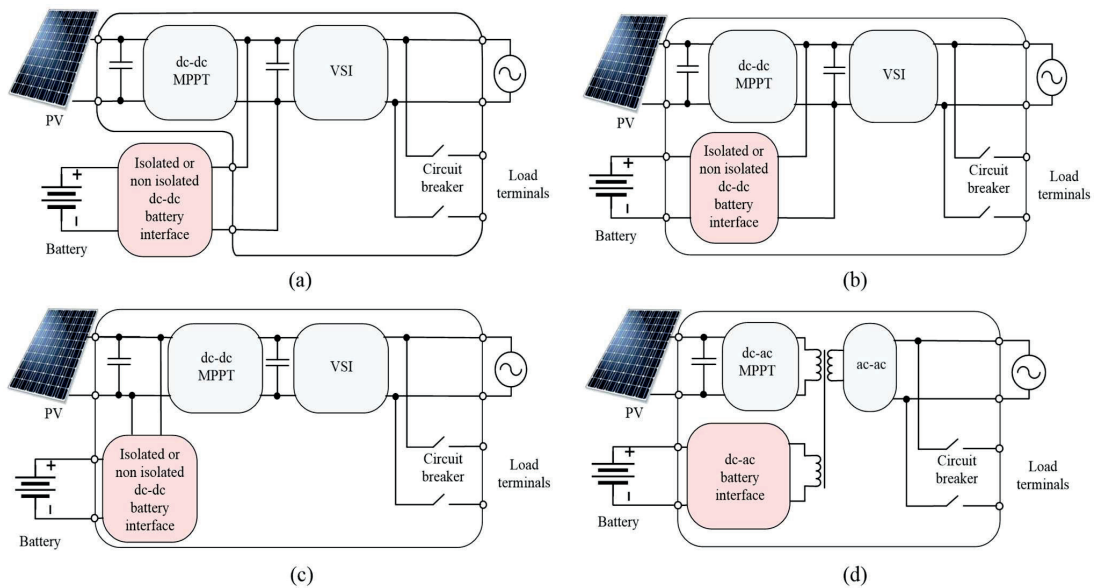

Figure 5. Typical structures of hybrid solar inverters. The battery connected directly to the dc-link (**a**), The battery integrated into the Energy Storage Systems and connected to dc-link (ESS) (**b**), the integrated battery interface connected to the dc low voltage (**c**), the integrated battery interface connected to the ac voltage (**d**).

There are several examples of hybrid microconverters. The concept of hybrid microconverters is the same as that of hybrid converters. The difference consists of the power and voltage levels. Usually, microconverters are intended for connecting to a single solar panel in a range from 10 V to 60 V and a low-voltage battery. Due to the significant voltage difference between the input side and the grid, a step-up transformer is utilized [36]. This concept is illustrated in Figure 5d. Despite being an interesting idea, which seems to be suitable for residential use, some difficulties are reported in [37,38]. The main constraints are related to the battery overheating in the case of tied coupling with a solar panel.

The structure of the hybrid inverter can be much more complex. There are many studies dedicated to alternative solutions. The next part of this work is devoted to the detailed analysis of possible solutions.

5. Overview of the Non-Isolated Multi-Port Converters

As was mentioned above, hybrid inverters can be realized with and without an isolation stage. This chapter is devoted to an overview of different structures of the non-isolated Multi-Port Converters (MPC) reported in the research literature that are considered suitable candidates for hybrid inverters [39–47].

5.1. Battery Connected to the DC Bus

A simple example of the battery connected directly to the dc-link is shown in [48]. This system consists of a PV array, a dc-dc converter, and a single-phase battery energy storage system that is formed by a bidirectional converter, and connects in parallel with the batteries, the load, and the grid. The power of the PV is controlled by a dc-dc converter to track the MPPT point. The generated power is stored in a battery connected to the dc-link, as illustrated in Figure 6.
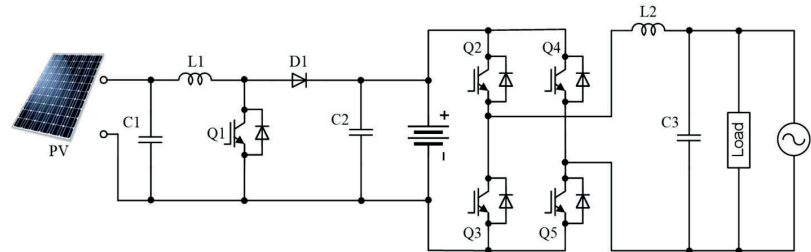

Figure 6. Battery link MPC with PV boost converter [48].

5.2. DC Bus Multi-Port Converter

In the more general case, an electrolytic capacitor is used as a dc-link, while the multiple dc sources are connected through non-isolated power electronics interfaces. An ac inverter links the dc sources and the ac grid. In [49], a commonly used topology of dc bus MPCs is discussed, as shown in Figure 7. The PV array is connected to the dc bus via a boost converter, the battery is connected to the dc bus through a bi-directional boost dc-dc converter, and the dc bus is integrated into the ac utility grid by a three-phase VSI.
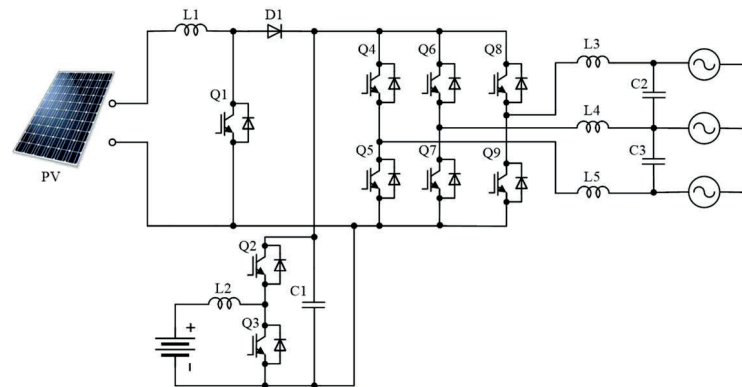
Figure 7. Dc bus MPC with boost-boost converters [49].

In [50], the proposed topology consists of a PV array connected directly to the dc bus, a battery with a bi-directional dc-dc converter, and a dc-ac single-phase inverter, as shown in Figure 8.

5.3. Diode-Clamped Multi-Port Converter

Based on a three-level diode-clamped converter, a topology is presented in [51] using a battery and a supercapacitor instead of the standard two dc-link capacitors, as shown in Figure 9. A new space vector modulation method is used for diode-clamped three-level converters with variable dc-link voltages. The authors tested the system experimentally.

Figure 8. DC Bus MPC with battery boost converter [50].

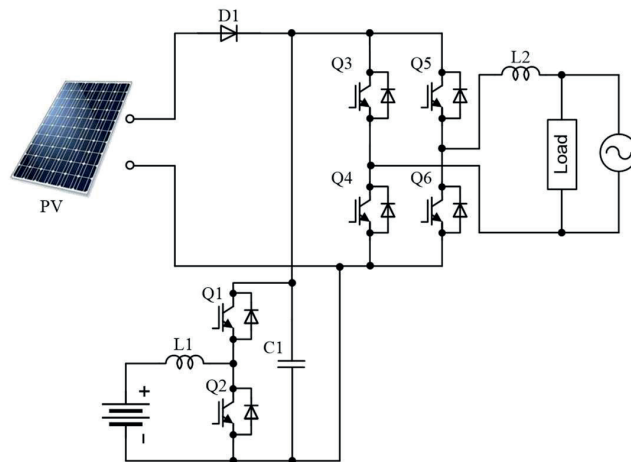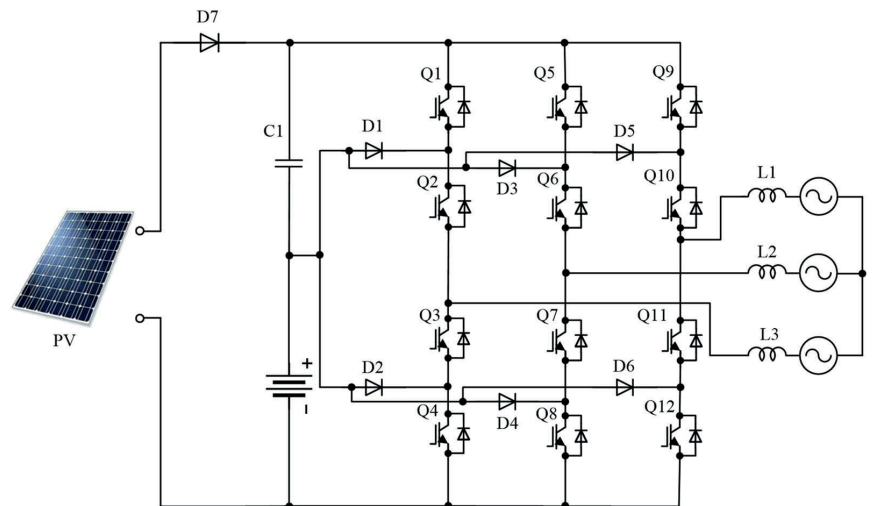**Figure 9.** Diode-Clamped Multi-Port Converter [51].

5.4. Z-Source Based Multi-Port Converters (ZS-MPC)

The Z-Source Converter (ZSC) is a single-stage buck-boost converter with two independent control freedoms, a modulation index that controls the output of the ZSC, and a shoot-through to boost the dc-link voltage [52,53]. The quasi-Z-Source Converter (qZSC) is created from the Z-source converter and, as well as all the benefits of the ZSC for application in a RES system, it has continuous input current. Many different solutions were proposed based on a Z-source network [54,55].

Similarly, several solutions based on ZSC were proposed with battery integration [56–58]. To create a ZS-MPC, one of the capacitors is replaced by a battery. This solution is studied in [56] and is shown in Figure 10. In the study, the SOC of the battery is simulated and experimentally tested.

A single switch quasi-Z-Source MPC with a PV power generation system and battery connected to the upper capacitor of the qZSC, as shown in Figure 11, is analyzed and simulated in [57,58].
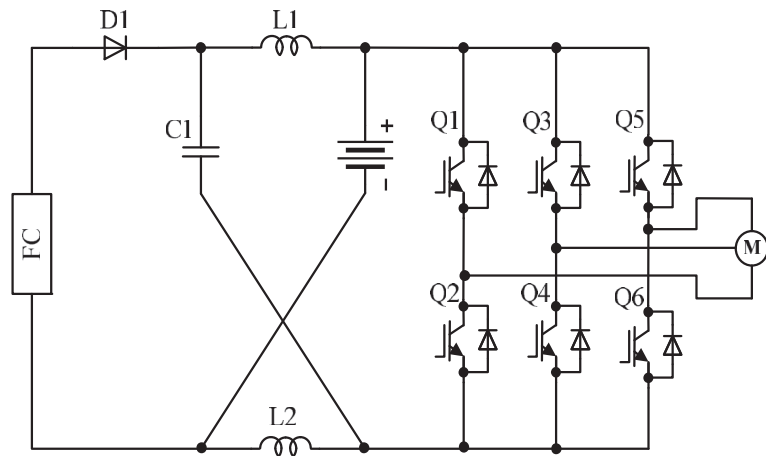
Figure 10. ZS-MPC [56].
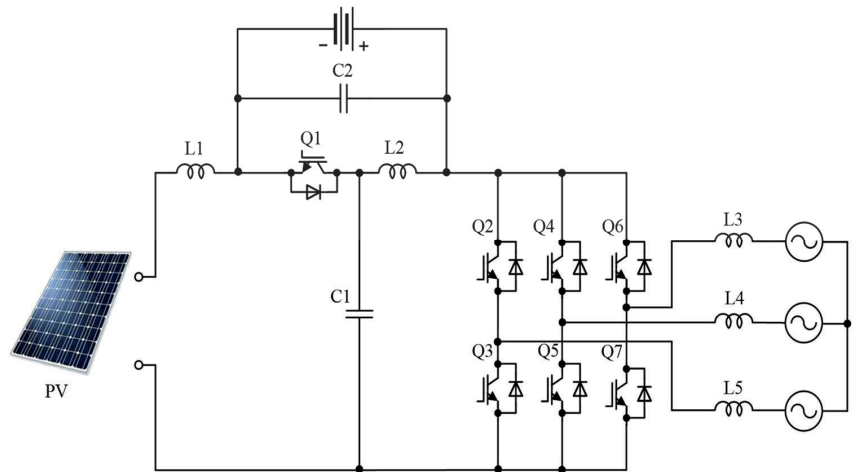
Figure 11. qZS-MPC with Battery Storage Paralleling an Upper Capacitor [57].

Despite several solutions based on qZS networks being reported as pre-industrialization prototypes [59,60] that show acceptable efficiency, it is reported that qZS-based solutions may have a problem with power and volume density compared to comparable designs [61–63]. Moreover, the solution reported in [57] is not feasible for hybrid inverter applications because the battery is not usable during the night when power from solar panels is not available [64].

5.5. Hybrid Transformerless PV Converter

The hybrid transformerless PV converter is discussed in [65]. This system has one ac and two dc outputs. In this case, the inductor of the conventional boost converter is split into two symmetrical ones placed at the positive and negative dc rails, as shown in Figure 12. In addition, the switch of the conventional boost converter is replaced with a transformerless VSI.

Figure 12. Hybrid Transformerless PV Converter [65].

6. Overview of the Isolated Multi-Port Converters

In this section, isolated converter topologies are discussed. Isolated multiport converters involving galvanic isolation between different ports have been introduced in several papers [66–71]. The use of a high-frequency transformer ensures isolation. Most of the topologies have been derived from conventional full-bridge or half-bridge dc-dc converters.
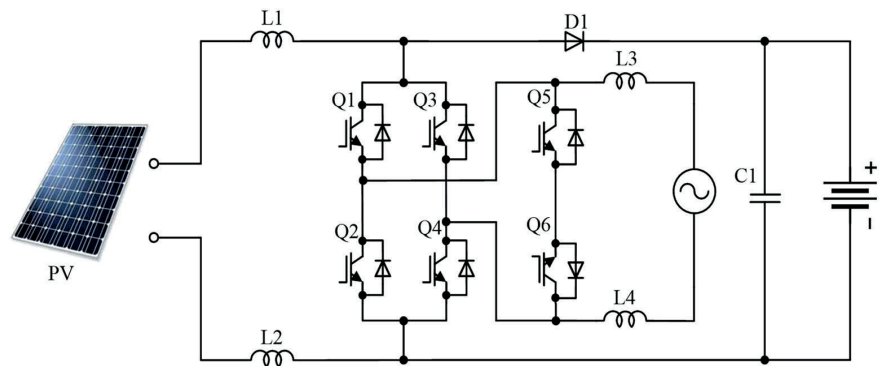
6.1. Symmetric Boost Integrated Phase Shift Converter

The topology of a three-port partially isolated converter is shown in Figure 13 and discussed in [72]. Ports 1 and 2 are inherently bidirectional. This means that each port can source or sink average power depending on the state of the converter and connected devices. Port 0 is unidirectional due to the use of diode rectifiers. The main power source is connected to port 0, and the battery is connected to port 2. Switch Q2 is driven complimentary to Q1 and switch Q4 is driven complimentary to Q3 with a short dead time in between. The power delivered to the load is controlled by controlling the phase shift between the gating signals of switches Q1 and Q3, and by controlling the duty ratio of the switches Q1 and Q3, which are required to be the same.
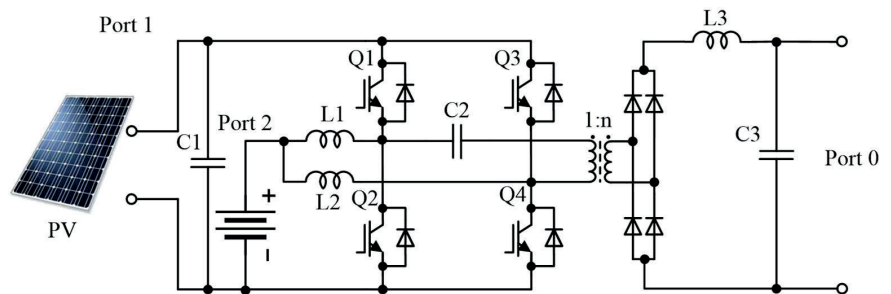
Figure 13. Symmetric Boost Integrated Phase Shift Converter [72].

6.2. PV-Partially Isolated Three-Port Converter

A three-port partially isolated converter is shown in Figure 14 and discussed in [73]. The PV array is connected to port 1, the battery is connected to port 2, and port 0 is the load port. This converter has three operational modes: single input, dual output mode (PV to dc bus and battery), dual input, single output mode (PV and battery to dc bus), and single input, single output mode (battery to dc bus).
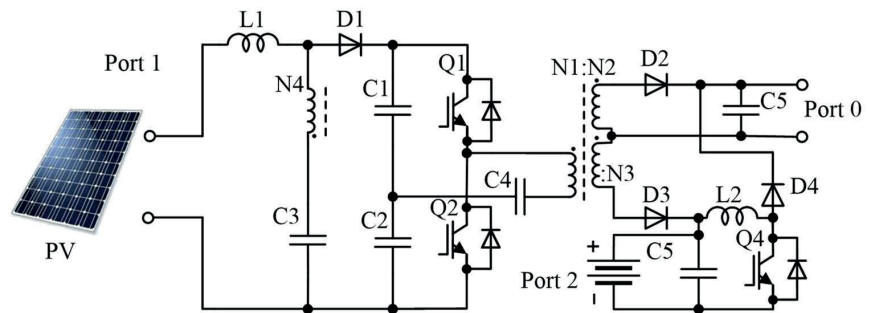
Figure 14. PV-Partially Isolated Three-Port Converter [73].

6.3. Fully Isolated Three-Port Converter

A three-port fully isolated converter is shown in Figure 15 and discussed in [73]. These modular systems have multiple modules. Each module has three ports, one fuel cell port, one energy storage port, and one load port, and all of these ports are bidirectional. The fuel cell port should be protected from reverse current, and diode D1 is used in this case for that purpose. Inductor L1 is used to mitigate current ripples. The phase shift between the active bridge interfacing port 1 and the active bridge interfacing port 0 is used to control the power flow.
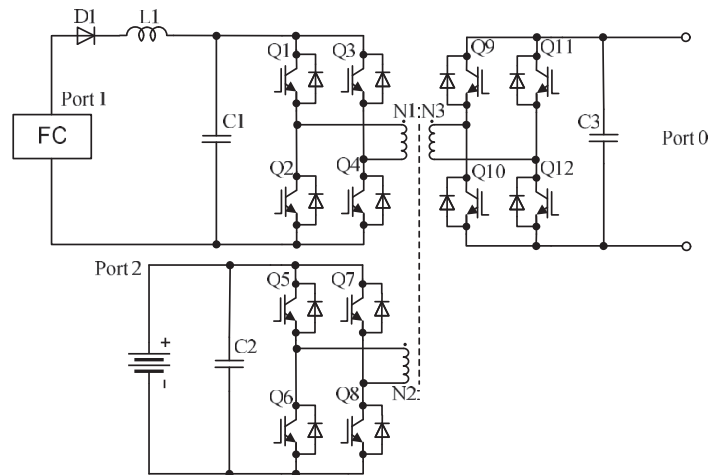
Figure 15. Isolated Three-Port Bi-Directional DC-DC Converter [74].

6.4. Multiport CLL-Resonant Converter

A three-port fully isolated converter is shown in Figure 16 and discussed in [75]. Port 1 is the main input port, port 2 is an auxiliary input port, and port 0 is the load port. The phase shift between the two input ports is used to control the output voltage.

The phase shift between the two input ports is maintained at 90°. In the paper, this converter is modeled as a square wave voltage source and the transformer is modeled with its equivalent T model.

A summary of the hybrid solutions discussed above is presented in Table 2. The table illustrates the number of components, power rating, and insulation, as well as electrical features. L and C represent the number of inductors and capacitors, respectively.
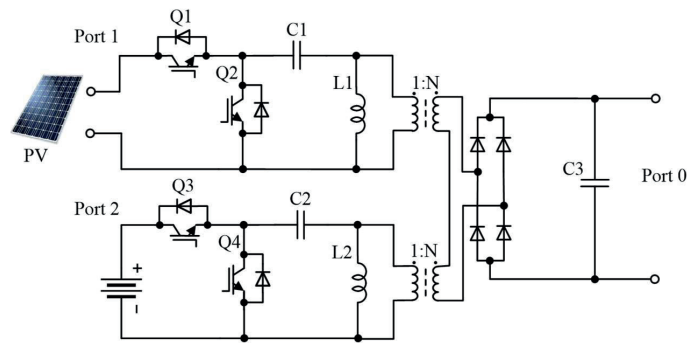
Figure 16. Isolated Three-Port CLL- Resonant Converter [75].

Table 2. Summary of hybrid solutions.

References	Number of Components			Power Ratings	Isolation	Pros	Cons
	Switch & Diode	L	C				
Ref [48]	6	2	3	600 W	No	• Conventional solution, low cost.	• Limited range of battery voltage
Ref [50]	7	2	1	5 kW	No	• Conventional solution, low cost.	• Limited range of photovoltaic voltage
Ref [51]	19	3	1	10 kW	No	• Possible improved power density	• The inverter complexity, losses, limited range of photovoltaic voltage
Ref [57]	7	5	2	10 kW	NO	• Greater reliability	• Complexity of the control and limited range of battery voltage, cannot work without photovoltaic input
Ref [65]	7	4	1	4.5 kW	No	• Low leakage current • High efficiency	• Limited range of battery and photovoltaic voltage, range
Ref [72]	8	3	3	5 kW	Yes	• High-efficiency, isolated solution	• Voltage Limitation
Ref [74]	13	1	2	1 kW	Yes	• Isolated solution	• Voltage Limitation, not high efficiency
Ref [75]	8	2	3	1 kW	Yes	• Isolated solution • Simplicity, high efficiency	• Voltage Limitation

Despite the many benefits provided by hybrid converters, there are some technical challenges that still need to be resolved to accelerate their practical feasibility. Future trends that should be followed by researchers in order to develop efficient hybrid converters are as follows:

- Derived hybrid converters can be further improved to reduce the number and size of electrical components such as semiconductors, passive elements, etc. This will result in a reduction in the cost of manufacturing converters as well as their size.
- Derived hybrid converters can be improved to reduce power conversion stages, which will reduce the total loss of the system.

- Improved controllers can be designed in order to reduce switching complexity.
- The power quality factors create a major problem when integrating the renewable energy system with the grid. Therefore, hybrid converters should be developed to take care of these power quality issues.
- In order to enhance the performance of the power electronics converters, various improved switches should be developed, such as GaN-based switches. Therefore, while designing new hybrid converters, improved semiconductor devices must be employed to augment the performance of the system.

7. Conclusions

This paper presents a review of hybrid converter topologies. It is intended as a convenient reference for engineers. The main goal of this work was to analyze possible internal power electronics configurations that can be utilized inside commercial solutions.

The paper presents a review of significant commercially available single-phase and three-phase hybrid solar inverters. The review shows that the maximum input voltage range differs between different manufacturers and starts from 480 V and goes up to 1000 V. The MPPT voltage range also varies depending on the manufacturer. At the same time, the battery input voltage range is significantly smaller as is battery power.

The review also shows that most solutions are built based on a configuration consisting of a boost converter and VSI, while a bidirectional dc-dc converter provides power exchange between the battery and a common dc-link. Furthermore, solutions can be divided into isolated (have an isolated battery and/or load) and non-isolated. In addition, many different and more complex solutions have been proposed that are doubtful for practical utilization.

Author Contributions: Conceptualization, H.A. and O.H.; methodology investigation, and writing, H.A. and O.H.; validation, H.A., O.H., O.M. and D.V.; formal analysis, H.A., O.H. and O.M.; investigation, H.A.; resources, H.A. and O.H.; writing—original draft preparation, O.H. and H.A.; writing—review and editing, H.A.; visualization, H.A.; supervision, O.H. and D.V. All authors have read and agreed to the published version of the manuscript.

Data Availability Statement: The data used in this study is publicly available and sources are referred.

Conflicts of Interest: The authors declare no conflict of interest related to the study.

References

1. Ilić, M.D.; Zaborszky, J. Electric power systems engineering. In *Encyclopedia of Energy*; Elsevier: Amsterdam, The Netherlands; Academic Press: Boston, MA, USA, 2004; Volume 2, pp. 267–287.
2. Blaabjerg, F.; Chen, Z.; Kjaer, S.B. Power electronics as efficient interface in dispersed power generation systems. *IEEE Trans. Power Electron.* **2004**, *19*, 1184–1194. [CrossRef]
3. Lai, J.S.H.; Nelson, D.J. Energy Management Power Converters in Hybrid Electric and Fuel Cell Vehicles. *Proc. IEEE* **2007**, *95*, 766–777. [CrossRef]
4. Boroyevich, D.; Cvefkovic, L.; Dong, D.; Burgos, R.; Wang, F.; Lee, F. Future electronic power distribution systems-A contemplative view. In Proceedings of the 12th International conference OPTIM Electrical and Electronic Equipment, Brasov, Romania, 20–22 May 2010; pp. 1369–1380.
5. Adda, R.; Ray, O.; Mishra, S.K.; Joshi, A. Synchronous-Reference-Frame-Based Control of Switched Boost Inverter for Standalone DC Nanogrid Applications. *IEEE Trans. Power Electron.* **2013**, *28*, 1219–1233. [CrossRef]
6. Nag, S.S.; Adda, R.; Ray, O.; Mishra, S.K. Current-Fed Switched Inverter based hybrid topology for DC Nanogrid application. In Proceedings of the IEEE 39th Annual Conference of the Industrial Electronics Society, Vienna, Austria, 10–13 November 2013; pp. 7146–7151.
7. Ravindranath, A.; Mishra, S.K.; Joshi, A. Analysis and PWM Control of Switched Boost Inverter. *IEEE Trans. Ind. Electron.* **2013**, *60*, 5593–5602. [CrossRef]
8. Ray, O.; Mishra, S. Boost-Derived Hybrid Converter with simultaneous DC and AC outputs. *IEEE Trans. Ind. Appl.* **2014**, *50*, 1082–1093. [CrossRef]

9. Ray, O.; Mishra, S. Constant-frequency shoot-through sine pulse-width-modulation scheme for three-phase single-input–hybrid-output converter. *IET Power Electron.* **2016**, *9*, 1819–1827. [CrossRef]
10. Sharma, A.; Pramod, B.; Singh, R.K.; Mahanty, R. Interleaved hybrid boost converter with simultaneous DC and AC outputs for micro-source applications. In Proceedings of the IEEE Energy Conversion Congress and Exposition (ECCE), Milwaukee, WI, USA, 18–22 September 2016; pp. 1–8.
11. Bhattacharjee, A.K.; Kutkut, N.; Batarseh, I. Review of Multiport Converters for Solar and Energy Storage Integration. *IEEE Trans. Power Electron.* **2019**, *34*, 1431–1445. [CrossRef]
12. Affam, A.; Buswig, Y.M.; Othman, A.K.B.H.; Julai, N.B.; Qays, O. A review of multiple input DC-DC converter topologies linked with hybrid electric vehicles and renewable energy systems. *Renew. Sustain. Energy Rev.* **2021**, *135*, 110186. [CrossRef]
13. Raju, N.; Mohan, N.M.; Kumar, V. A Review of Extended Voltage Range DC-DC Converter Topologies. In *Intelligent Computing & Optimization. Lecture Notes in Networks and Systems*; Vasant, P., Weber, G.W., Marmolejo-Saucedo, J.A., Munapo, E., Thomas, J.J., Eds.; Springer: Cham, NY, USA, 2022; Volume 569.
14. Sonia, B.; Venkata Lakshmi, V.; Varas Prasad, M.V.G. Boost Derived Multi Level Hybrid Converters in Micro Grid. In *Smart Energy and Advancement in Power Technologies. Lecture Notes in Electrical Engineering*; Namrata, K., Priyadarshi, N., Bansal, R.C., Kumar, J., Eds.; Springer: Singapore, 2023; Volume 927.
15. Edson, H.W.; Gilson, S., Jr. Flexible AC Transmission Systems. In *Power Electronics Handbook: Devices, Circuits and Applications (Engineering)*; Academic Press: Cambridge, MA, USA, 2018.
16. Hirst, E.; Kirby, B. *Electric-Power Ancillary Services. ORNL/CON-426*; Oak Ridge National Laboratory: Oak Ridge, TN, USA, 1996.
17. Pagano, E.; Piegari, L.; Tricoli, P. Approaches to analytical analysis of active filter behaviour. In Proceedings of the 29th Annual Conference of the IEEE Industrial Electronics Society IECON'03, Roanoke, VA, USA, 2–6 November 2003; Volume 3, pp. 2003–2022.
18. D'Arco, S.; Iannuzzi, D.; Pagano, E.; Tricoli, P. Analysis of active filter behaviour by means of modified z-transform method. *IEE Proc. Electric Power Applications.* **2005**, *152*, 695–702. [CrossRef]
19. Yang, B.; Li, W.; Zhao, Y.; He, X. Design and Analysis of a Grid-Connected Photovoltaic Power System. *IEEE Trans. Power Electron.* **2010**, *25*, 992–1000. [CrossRef]
20. Pereira, H.; Domingos, R.; Xavier, L.; Cupertino, A.; Mendes, V.; Paulino, J. Adaptive saturation for a multifunctional three-phase photovoltaic inverter. In Proceedings of the 17th European Conference on Power Electronics and Applications, Geneva, Switzerland, 29 October 2015; pp. 1–10.
21. He, J.; Li, Y.W.; Munir, M.S. A flexible harmonic control approach through voltage-controlled DG–Grid interfacing converters. *IEEE Trans. Ind. Electron.* **2012**, *59*, 444–455. [CrossRef]
22. Narinder, K.; Trehan, P.E. Ancillary Services- Reactive and Voltage Control. *Power Eng. Soc. Winter Meet.* **2001**, *3*, 1341–1346.
23. Svarc, J. Hybrid Inverter Comparison Chart. Available online: https://www.cleanenergyreviews.info/hybrid-solar-inverter-comparison (accessed on 26 November 2022).
24. Ev Charching Single Phase Inverter. Available online: https://www.europe-solarstore.com/download/solaredge/solaredge_3680-6000h_hd-wave_setapp_integrated_ev_charger_en.pdf (accessed on 26 November 2022).
25. LG Energy Solutions. Available online: https://www.europe-solarstore.com/download/lgchem/LG_Chem_RESU_datasheet.pdf (accessed on 26 November 2022).
26. FRONIUS SYMO HYBRID. Available online: https://www.europe-solarstore.com/download/fronius/solarbattery/DS_Fronius_Energy_Package_EN_386411_snapshot.pdf (accessed on 26 November 2022).
27. Smart Energy Controller. Available online: https://solar.huawei.com/en-GB/download?p=%2F%2Fmedia%2FSolar%2Fattachment%2Fpdf%2Feu%2Fdatasheet%2FSUN2000-2-6KTL-L1.pdf (accessed on 26 November 2022).
28. Power Conversion System/Hybrid Inverter. Available online: https://uk.sungrowpower.com/upload/file/20210723/EN%20DS%20SH5.0RT%206.0RT%208.0RT%2010RT%20Datasheet.pdf (accessed on 26 November 2022).
29. Power Conversion System/Hybrid Inverter. Available online: https://www.sungrowpower.com/sites/default/files/SBP4K8-UEN-Ver14-201807.pdf (accessed on 10 June 2021).
30. ABB PV + Storage. Available online: https://www.rectifier.co.za/wp-content/uploads/2019/08/REACT2-3.6-5.0-TL_BCD.00688_EN_RevD.pdf (accessed on 26 November 2022).
31. Redback SH5000 Hybrid Solar-Battery Inverter-Charger Inverter. Available online: https://www.ecocool.com.au/products/inverters/redback-sh5000-hybrid-solar-battery-inverter-charger-inverter (accessed on 26 November 2022).
32. Solis High Voltage Energy Storage Inverters. Available online: https://www.invertersupply.com/media/data/Datasheet_RHI-1P5K-HVES-5G.pdf (accessed on 26 November 2022).
33. Self Consumption Solar Hybrid Inverters. Available online: https://imeon-energy.com/wp-content/uploads/datasheet-imeon-hybrid-solar-inverter.pdf (accessed on 26 November 2022).
34. X1-HYBRID HV/X3-HYBRID HV. Available online: https://www.solaxpower.com/wp-content/uploads/2017/01/X-Hybrid-SingleThree-Phase-Datasheet.pdf (accessed on 26 November 2022).
35. Hybrid Converter. Available online: https://files.sma.de/downloads/SBS37-60-DAU1902-V21web.pdf (accessed on 10 June 2021).
36. Afshari, H.; Husev, O.; Vinnikov, D.; Matiushkin, O.; Vosoughi KurdKandi, N. Comparison of Grid-Connected Flyback-based Microinverter with Primary and Secondary Side Decoupling Approach. In Proceedings of the IEEE 63rd International Scientific Conference on Power and Electrical Engineering of Riga Technical University (RTUCON), Riga, Latvia, 10 October 2022.

37. Vega Garita, V.; Garg, S.; Narayan, N.; Ramirez Elizondo, L.; Bauer, P. Testing a PV-battery Integrated Module Prototype. In Proceedings of the 2018 IEEE 7th World Conference on Photovoltaic Energy Conversion (WCPEC) (A Joint Conference of 45th IEEE PVSC, 28th PVSEC & 34th EU PVSEC), Waikoloa, HI, USA, 10–15 June 2018.

38. Vega Garita, V.; Garg, S.; Narayan, N.; Ramirez Elizondo, L.; Bauer, P. PV-battery integrated module as a solution for off-grid applications in the developing world. In Proceedings of the 2018 IEEE International Energy Conference (ENERGYCON), Limassol, Cyprus, 3–7 June 2018.

39. Nahavandi, A.; Hagh, M.T.; Sharifian, M.B.; Danyali, S. A nonisolated multiinput multioutput dc–dc boostconverter for electric vehicle applications. *IEEE Trans. Power Electron.* **2015**, *30*, 1818–1835. [CrossRef]

40. Gummi, K.; Ferdowsi, M. Double-Input DC–DC Power Electronic Converters for Electric-Drive Vehicles—Topology Exploration and Synthesis Using a Single-Pole Triple-Throw Switch. *IEEE Trans. Ind. Electron.* **2010**, *57*, 617–623. [CrossRef]

41. Solero, L.; Lidozzi, A.; Pomilio, J.A. Design of multiple-input power converter for hybrid vehicles. *IEEE Trans. Power Electron.* **2005**, *20*, 1007–1016. [CrossRef]

42. Hintz, A.; Prasanna, U.R.; Rajashekara, K. Novel Modular Multiple-Input Bidirectional DC–DC Power Converter (MIPC) for HEV/FCV Application. *IEEE Trans. Ind. Electron.* **2015**, *62*, 3163–3172. [CrossRef]

43. Yang, P.; Tse, C.K.; Xu, J.; Zhou, G. Synthesis and Analysis of Double-Input Single-Output DC/DC Converters. *IEEE Trans. Ind. Electron.* **2015**, *62*, 6284–6295. [CrossRef]

44. Nagata, H.; Uno, M. Multi-port converter integrating two PWM converters for multi-power-source systems. In Proceedings of the IEEE 3rd International Future Energy Electronics Conference and ECCE, Taiwan, China, 3–7 June 2017; pp. 1833–1838.

45. Zhu, H.; Zhang, D.; Zhang, B.; Zhou, Z. A Non-Isolated Three-Port DC–DC Converter and Three-Domain Control Method for PV-Battery Power Systems. *IEEE Trans. Ind. Electron.* **2015**, *62*, 4937–4947. [CrossRef]

46. Marchesoni, M.; Vacca, C. New DC–DC Converter for Energy Storage System Interfacing in Fuel Cell Hybrid Electric Vehicles. *IEEE Trans. Power Electron.* **2007**, *22*, 301–308. [CrossRef]

47. Zhu, H.; Zhang, D.; Liu, Q.; Zhou, Z. Three-Port DC/DC Converter with All Ports Current Ripple Cancellation Using Integrated Magnetic Technique. *IEEE Trans. Power Electron.* **2016**, *31*, 2174–2186. [CrossRef]

48. Chiang, S.J.; Chang, K.T.; Yen, C.Y. Residential photovoltaic energy storage system. *IEEE Trans. Ind. Electron.* **1998**, *45*, 385–394. [CrossRef]

49. Ding, F.; Li, P.; Huang, B.; Gao, F.; Ding, C.; Wang, C. Modeling, and simulation of grid-connected hybrid photovoltaic/battery distributed generation system. In Proceedings of the CICED 2010 Proceedings, Nanjing, China, 13–16 September 2010; pp. 1–10.

50. Gurkaynak, Y.; Li, Z.; Khaligh, A. A novel grid-tied, solar powered residential home with plug-in hybrid electric vehicle (PHEV) loads. In Proceedings of the IEEE Vehicle Power and Propulsion Conference, Dearborn, MI, USA, 7–11 September 2009; pp. 813–816.

51. Jayasinghe, S.D.G.; Vilathgamuwa, D.M.; Madawala, U.K. Diode-Clamped Three-Level Inverter-Based Battery/Supercapacitor Direct Integration Scheme for Renewable Energy Systems. *IEEE Trans. Power Electron.* **2011**, *26*, 3720–3729. [CrossRef]

52. Stepenko, S.; Husev, O.; Pimentel, S.P.; Makovenko, E.; Vinnikov, D. Small Signal Modeling of Interleaved Quasi-Z-Source Inverter with Active Power Decoupling Circuit. In Proceedings of the IEEE 59th International Scientific Conference on Power and Electrical Engineering of Riga Technical University (RTUCON), Riga, Latvia, 12–14 November 2018; pp. 1–6.

53. Zheng Peng, F. Z-source inverter. *IEEE Trans. Ind. Electron.* **2003**, *39*, 504–510. [CrossRef]

54. Liu, Y.; Abu Rub, H.; Ge, B. Z-Source/Quasi-Z-Source Inverters: Derived Networks, Modulations, Controls, and Emerging Applications to Photovoltaic Conversion. *IEEE Ind. Electron. Mag.* **2014**, *8*, 32–44. [CrossRef]

55. Ellabban, O.; Abu-Rub, H. Z-Source Inverter: Topology Improvements Review. *IEEE Ind. Electron. Mag.* **2016**, *10*, 6–24. [CrossRef]

56. Holland, K.; Shen, M.; Peng, F.Z. Z-source inverter control for traction drive of fuel cell—Battery hybrid vehicles. In Proceedings of the Fourtieth IAS Annual Meeting. Conference Record of the 2005 Industry Applications Conference, Hong Kong, China, 2–6 October 2005; Volume 3, pp. 1651–1656.

57. Sun, D.; Ge, B.; Peng, F.Z.; Abu Rub, H.; De Almeida, A.T. Power flow control for quasi-Z source inverter with battery-based PV power generation system. In Proceedings of the IEEE Energy Conversion Congress and Exposition, Phoenix, AZ, USA, 17–22 September 2011; pp. 1051–1056.

58. Khajesalehi, J.; Sheshyekani, K.; Hamzeh, M.; Afjei, E. High-performance hybrid photovoltaic-battery system based on quasi-Z-source inverter: Application in microgrids. *IET Gener. Transm. Distrib.* **2015**, *9*, 895–902. [CrossRef]

59. Vinnikov, D.; Chub, A.; Liivik, E.; Kosenko, R.; Korkh, O. Solar Optiverter—A Novel Hybrid Approach to the Photovoltaic Module Level Power Electronics. *IEEE Trans. Ind. Electron.* **2019**, *66*, 3869–3880. [CrossRef]

60. Husev, O.; Vinnikov, D.; Roncero-Clemente, C.; Chub, A.; Romero-Cadaval, E. Single-Phase String Solar qZS-based Inverter: Example of Multi-Objective Optimization Design. *IEEE Trans. Ind. Appl.* **2021**, *57*, 3120–3130. [CrossRef]

61. Husev, O.; Shults, T.; Vinnikov, D.; Roncero-Clemente, C.; Romero-Cadaval, E.; Chub, A. Comprehensive Comparative Analysis of Impedance-Source Networks for DC and AC Application. *Electronics* **2019**, *8*, 405. [CrossRef]

62. Panfilov, D.; Husev, O.; Blaabjerg, F.; Zakis, J.; Khandakji, K. Comparison of three-phase three-level voltage source inverter with intermediate dc–dc boost converter and quasi-Z-source inverter. *IET Power Electron.* **2016**, *9*, 1238–1248. [CrossRef]

63. Wolski, K.; Zdanowski, M.; Rabkowski, J. High-Frequency SiC-Based Inverters with Input Stages Based on Quasi-Z-Source and Boost Topologies—Experimental Comparison. *IEEE Trans. Power Electron.* **2019**, *34*, 9471–9478. [CrossRef]

64. Kroics, K.; Zakis, J.; Suzdalenko, A.; Husev, O.; Tytelmaier, K.; Khandakji, K. Operation possibility of grid connected Quasi-Z-Source Inverter with energy storage and renewable energy generation in wide power range. In Proceedings of the IEEE First Ukraine Conference on Electrical and Computer Engineering (UKRCON), Kyiv, Ukraine, 29 May–2 June 2017; pp. 564–569.
65. Zhongting, T.; Yang, Y.; Wan, J.; Blaabjerg, F. Hybrid transformerless PV converters with low leakage currents: Analysis and configuration. *IET Renew. Power Gener.* **2021**, *15*, 368–381.
66. Y-S, L.; Y-P, K. Switched-capacitor bi-directional converter performance comparison with and without quasi-resonant zero-current switching. *IET Power Electron.* **2010**, *3*, 269–278.
67. Zhao, C.; Round, S.D.; Kolar, J.W. An Isolated Three-Port Bidirectional DC-DC Converter with Decoupled Power Flow Management. *IEEE Trans. Power Electron.* **2008**, *23*, 2443–2453. [CrossRef]
68. Tao, H.; Kotsopoulos, A.; Duarte, J.L.; Hendrix, M.A.M. Transformer-Coupled Multiport ZVS Bidirectional DC–DC Converter with Wide Input Range. *IEEE Trans. Power Electron.* **2008**, *23*, 771–781. [CrossRef]
69. Das, P.; Laan, B.; Mousavi, S.A.; Moschopoulos, G. A Nonisolated Bidirectional ZVS-PWM Active Clamped DC–DC Converter. *IEEE Trans. Power Electron.* **2009**, *24*, 553–558.
70. Duan, R.Y.; Lee, J.D. High-efficiency bidirectional DC-DC converter with coupled inductor. *IET Power Electron.* **2012**, *5*, 115–123. [CrossRef]
71. Ahmadi, M.; Mohammadi, M.R.; Adib, E.; Farzanehfard, H. Family of non-isolated zero current transition bi-directional converters with one auxiliary switch. *IET Power Electron.* **2012**, *5*, 158–165. [CrossRef]
72. Al-Atrash, H.; Batarseh, I. Boost-Integrated Phase-Shift Full-Bridge Converter for Three-Port Interface. In Proceedings of the IEEE Power Electronics Specialists Conference, Orlando, FL, USA, 17–21 June 2007; pp. 2313–2321.
73. Zhu, H.; Zhang, D.; Athab, H.S.; Wu, B.; Gu, Y. PV Isolated Three-Port Converter and Energy-Balancing Control Method for PV-Battery Power Supply Applications. *IEEE Trans. Ind. Electron.* **2015**, *62*, 3595–3606. [CrossRef]
74. Phattanasak, M.; Gavagsaz Ghoachani, R.; Martin, J.P.; Nahid Mobarakeh, B.; Pierfederici, S.; Davat, B. Control of a Hybrid Energy Source Comprising a Fuel Cell and Two Storage Devices Using Isolated Three-Port Bidirectional DC–DC Converters. *IEEE Trans. Ind. Appl.* **2015**, *51*, 491–497. [CrossRef]
75. Asa, E.; Colak, K.; Bojarski, M.; Czarkowski, D. Asymmetrical Duty-Cycle and Phase-Shift Control of a Novel Multiport CLL Resonant Converter. *IEEE J. Emerg. Sel. Top. Power Electron.* **2015**, *3*, 1122–1131. [CrossRef]

PAPER IV

S. Pourjafar, **H. Afshari**, P. Mohseni, O. Husev, O. Matiushkin and N. Shabbir, "Comprehensive Comparison of Isolated High Step-up DC-DC Converters for Low Power Application," in *IEEE Open Journal of Power Electronics*, vol. 5, pp. 1149–1161, 2024, doi: 10.1109/OJPEL.2024.3433554.

Comprehensive Comparison of Isolated High Step-up DC-DC Converters for Low Power Application

SAEED POURJAFAR [1] **(Member, IEEE), HOSSEIN AFSHARI** [1] **(Student Member, IEEE),
PARHAM MOHSENI** [1] **(Student Member, IEEE), OLEKSANDR HUSEV** [1] **(Senior Member, IEEE),
OLEKSANDR MATIUSHKIN** [2] **(Member, IEEE), AND NOMAN SHABBIR** [1] **(Senior Member, IEEE)**

[1]Tallinn University of Technology, 12616 Tallinn, Estonia
[2]Tallinn University of Technology and University of Extremadura, 06006 Badajoz, Spain

CORRESPONDING AUTHOR: SAEED POURJAFAR (e-mail: sapour@taltech.ee).

ABSTRACT In this paper comprehensive evaluations of isolated high step-up dc-dc topologies have been investigated. These converters are especially well suited for distributed generation systems utilizing renewable or alternative energy sources that need a wide input voltage range with load regulation. With this in mind, this work primarily concentrates on comparative analysis of various isolated configurations employed in possible industry applications. Consequently, several isolated structures, including flyback, forward, push-pull, and full bridge and other similar solutions have been carried out in the literature. For the purpose of comparative and theoretical analysis, some of the circuit parameters are considered, which include voltage conversion ratio, semiconductor element voltage stress, component size, and conduction and switching losses. Furthermore, the selected configurations have been discussed in terms of cost estimation and financial feasibility. In addition, the design procedure and experimental prototypes of the available solutions with the main results are presented. Derived from this investigation, the authors provide a guide to help researchers to identify different isolated topologies with wide input voltage range and galvanic isolation for prospective research directions within this area.

INDEX TERMS Isolated high step-up converter, distributed generation systems, wide input voltage range.

I. INTRODUCTION

Environmental concerns, including issues like global warming, the limited availability of fossil fuels, and the need to decrease carbon dioxide emissions, have motivated the research for cleaner and more sustainable energy sources [1]. Simultaneously, there has been a growing demand for renewable energy systems such as solar panels, fuel cells, and wind turbines in recent years. This increased demand for cleaner energy options has led to a shift in thinking about operating grid-connected systems, necessitating the development of innovative strategies [2], [3]. In essence, the challenges posed by environmental issues and the push for renewable energy are reshaping the energy landscape and how power is generated and distributed [4], [5].

In recent times, microgrids have gained considerable attention due to the substantial benefits they offer to both electricity consumers and power grid operators. Microgrid deployments are seen as a means to enhance power quality, lower emissions, ease network congestion, reduce power losses, improve energy efficiency, and potentially enhance the overall economic performance of the system [6]. Furthermore, over the past decade, dc microgrids have garnered significant interest from both academia and industry. These dc microgrids have proven to be superior to ac microgrids in terms of reliability, efficiency, ease of control, integration of renewable energy sources, and connecting dc loads [7]. The architecture of a simple dc microgrid with a various power conversion section is depicted in Fig. 1.
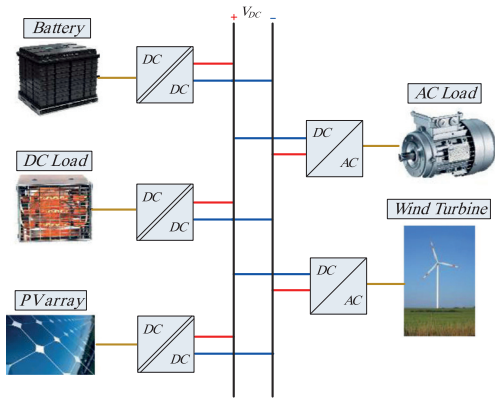
TABLE 1. Main Features Comparison of VF, CI and IS Converters

Feature	VF	CF	IS
Voltage step-up	No	Yes	Yes
Voltage step-down	Yes	No	Yes
Short-circuit exemption	No	Yes	Yes
Open-circuit exemption	Yes	No	Yes
Element for storing energy	One capacitor	One inductor	At a minimum, one capacitor and one inductor.
Cascading capability of energy elements	No	No	Yes
Simplicity in control	Simple	Complex	Moderate

The primary challenge in implementing a dc grid is the lack of a viable business model. Hence, the power electronic converters need to be versatile and compatible with both dc and ac applications [8], [9]. Power electronic structures play a crucial role in incorporating renewable energy generation into the power grid, meanwhile their usage is widespread and expanding rapidly [10].

Solar Photovoltaic (PV) energy is a highly significant global energy source and is projected to be the leading contributor to electricity generation among all renewable options by 2040. This is due to its renewable nature, absence of harmful emissions, and high efficiency. PV power plants are an effective means of harnessing energy from the sun and directly converting it into electricity [11] and [12]. However, PV panels produce very low voltage, and for applications requiring high voltage, these panels must be connected in series and parallel configurations. Unfortunately, this approach increases the overall cost of PV power systems. To address the issue of low voltage output from PV panels, a high step-up dc-dc converter is needed to boost the low voltages (typically 20–30 V) to align with the voltage level for distribution of a dc microgrid (usually 350–400 V) [13], [14].

Lately, there have been numerous advancements in high step-up dc-dc converters designed to achieve high voltage gains in both isolated and non-isolated configurations [15], [16]. In non-isolated setups, where galvanic isolation is not present, various methods have been employed to enhance the dc-dc conversion process. These methods include using coupled inductors, cascading techniques, switched capacitors, switched inductors, and voltage multiplier cells [17]. They are used to achieve a substantial voltage boost in a cascade setup without the need for a transformer, all while maintaining high efficiency and high-power density [18]. To link energy sources with lower input voltages to a higher-voltage dc bus, galvanically isolated dc-dc converters are among the most promising solutions.

These converters provide isolation to shield the energy source from significant voltage fluctuations at the load. They are efficient in utilizing the energy source, offer more flexibility in handling varying load conditions, and are capable of working with a wider range of input voltages [19], [20], [21], [22], [23]. Various established isolated dc-dc converters can be broadly categorized as Voltage-Fed (VF) and Current-Fed (CF) converters. Current-fed converters primarily function by reducing the input voltage through the adjustment of switch duty cycles [24], [25]. They typically incorporate an output LC filter, which smoothens the pulsating voltage. To operate as boost isolated dc-dc converters, current-fed dc-dc converters offer several advantages, including reduced input current ripple, a lower transformer turns ratio, improved efficiency, lower voltage requirements for rectifier diodes, and the absence of shoot-through faults in power switches [26]. Moreover, there is another isolated converter called Impedance Source (IS) converter, which is a combination of VF and CF converters, and it can have the characteristics of both of them [19], [27], [28], [29]. To better understanding, the specifications of these three types of converters been compared with each other and illustrated in Table 1 [30]. Alternatively, in different scenarios, isolated converters can be classified into three primary types: those based on full or half-bridge switching (BS), single or two-switch PWM, and resonant designs. Full-BS converters offer high voltage step-up ratios and efficiency but are better suited for high-power applications due to their numerous switches [31]. For low-power applications PWM, half-BS, and resonant converters are more practical [32]. In PWM DC-DC converters, standard configurations such as Cuk, SEPIC, and Zeta, incorporating galvanic isolation, as well as Forward, Flyback, and Push-Pull designs, are simple yet may exhibit certain constraints such as reduced static voltage step-up ratios, high input current ripple, and the need for high-breakdown voltage diodes [33]. Isolated High step-up dc-dc converters also can be divided into two types: passive clamp and active clamp converters.

Passive clamp converters have a simple structure and few switches but suffer from power losses due to hard switching of the main switch [34]. Active clamp converters, based on push-pull, half-bridge, and full-bridge topologies, achieve zero-voltage switching (ZVS) for switch turn-on and eliminate voltage spikes. However, they may not be highly efficient or cost-effective in low-power applications due to increased switch count and complex driving circuits [35].

Resonant bridge isolated high step-up dc-dc converters address issues with soft switching, using parasitic elements for resonance and featuring a simple structure without clamp circuits. However, they may cause a significant dc-offset current in the transformer, increasing its size [36].

This paper presents a comprehensive evaluation of isolated high step-up DC-DC converter topologies for distributed generation systems using renewable energy sources. Unlike existing reviews that focus on individual converter types, this paper conducts a thorough comparative analysis across multiple configurations, including flyback, forward, push-pull, and full-bridge converters. The evaluation considers critical parameters such as capacitor and magnetic sizes, primary side switch voltage stress, semiconductor conduction losses, and switching losses, standardized for a fair comparison under identical conditions of 400 W output power, 20–50 V input voltage range, and 50 kHz switching frequency, maintaining a constant 350 V output voltage. The main contributions of the paper include:

1) *Component Sizing Analysis:* Introducing a quantitative approach to compare capacitor and magnetic sizes based on accumulated energy calculations, aiding in optimizing component selection.

2) *Voltage Stress and Losses Comparison:* Utilizing normalized parameters like Voltage Stress Ratio (VSR) and Conduction Loss Ratio (CLR) to evaluate primary side switch voltage stress and semiconductor conduction losses.

3) *Switching Losses Assessment:* Employing a Switching Loss Ratio (SLR) to assess the efficiency of switching losses management across different converter types.

To validate the comparative methodology, a series of experiments were conducted under controlled laboratory conditions. Representative converters, one using coupled inductors (flyback) and another using a transformer (full-bridge), were selected for direct performance comparison. This setup ensured a fair and equitable comparison of efficiency, losses, thermal characteristics, and cost-effectiveness under similar operating conditions.

By evaluating key performance indicators crucial for real-world applications, such as efficiency under varying loads, detailed losses analysis, thermal behavior, and cost considerations, this paper provides practical insights into the strengths and weaknesses of each converter type. Unlike many theoretical studies, this paper bridges theory with practice by incorporating experimental validation. The classification of converters into coupled inductor-based and transformer-based categories, based on their operational principles, aligns with the distinctions made in the introduction and the main body of the paper. This classification is essential for understanding the different converter types and their applications in renewable energy systems. The paper is structured as follows:

1) Section II provides an overview of the competitive solutions.

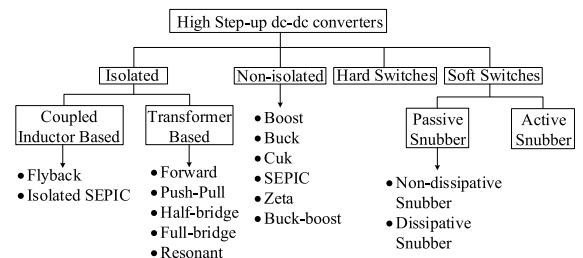2) Section III delves into the methodology for comparative evaluation and offers guidelines for component design.

FIGURE. 2. Classification of high step-up DC-DC converters.

3) Section IV offers experimental evaluation of the proposed solutions.

4) Finally, Section V presents the conclusions drawn from this study.

Overall, this paper aims to guide engineers and researchers in selecting optimal DC-DC converter topologies for diverse renewable energy applications, contributing significantly to the field by combining theoretical insights with practical validation.

II. OVERVIEW OF COMPETITIVE SOLUTIONS

The concise summary of the categorization of high step-up DC-DC converters for both isolated and non-isolated types is illustrated in Fig. 2. This paper primarily concentrates on isolated dc-dc converter topologies. Several isolated high step-up dc-dc converters have gained prominence in the industry due to their efficiency, capability, and suitability for applications such as single-phase PV application. The conventional isolated converters, as shown in Fig. 2, include coupled-inductor based converters like Flyback, isolated SEPIC, and transformer-based converters consisting of various topologies such as forward, Push-pull, voltage-fed half-bridge, voltage-fed full-bridge, current-fed half-bridge, current-fed full-bridge, resonant half-bridge, and resonant full-bridge. These converters are widely used based on their inherent characteristics, performance metrics, and suitability for specific applications. Table 2 provides a concise merits and demerits of main features among the conventional isolated high step-up dc-dc converters. In next sub-sections, a set of these solutions has been explained and discussed.

A. COUPLED INDUCTOR BASED ISOLATED SOLUTIONS

The isolated SEPIC, is one of the coupled inductor based isolated converter, commonly used in renewable application, which has advantages like low-input current ripples, minimal EMI, and versatile outputs. These converters possess a fundamental flaw, experiencing notable voltage stress on switch devices that is on par with the combined magnitude of both output and input voltages [37], [38], [39].

Flyback based converter, with its coupled-inductor based isolation, is known for its simplicity and cost-effectiveness. It is suitable for low to moderate power applications [40],
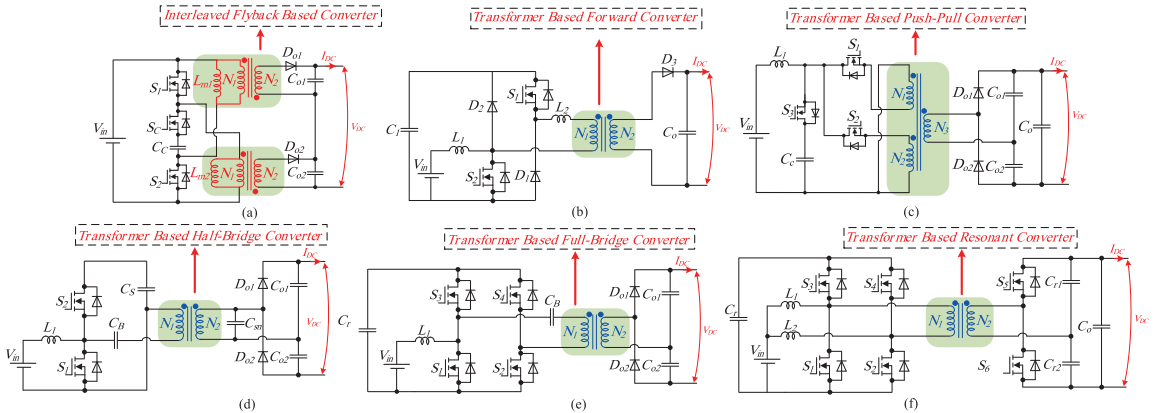
FIGURE. 3. Several isolated high step-up DC-DC converters for dc-microgrid applications, (a) Flyback based converter [47], (b) Forward based converter [52], (c) Push-pull based converter [54], (d) Half-bridge based converter [56], (e) Current-fed FB with clamp capacitor [58], and (f) Current-fed resonant converter [67].

TABLE 2. Comparison of Conventional Isolated Converters

Topology	Advantages	Disadvantages
Flyback	• Simple design and low cost. • Suitable for low to moderate power applications	• Limited power handling capability • High peak currents and voltage stresses
Isolated SEPIC	• Dual voltage regulation: step-up and step-down capabilities. • Reduced input current ripple	• Complex control and higher component count • Limited for high power applications.
Forward	• High efficiency • Good for high power applications	• Limited voltage regulation range. • Requires tight control for reliable operation
Push-pull	• High-frequency operation capability • Good for high power applications.	• Complex control and higher component count • Transformer design can be challenging
Half-bridge	• Moderate complexity. • Suitable for a wide range of power applications.	• Requires careful control to avoid voltage spikes • Limited for very low or very high power
Full-bridge	• High efficiency. • Suitable for high-power applications	• Complex control and higher component count • Not ideal for low-power applications.
Resonant	• Reduced electromagnetic interference (EMI) • Improved reliability due to soft switching	• Complex control and higher cost • High current stress through the semiconductor devices

[41], [42], [43], [44], [45]. The conventional flyback converter topology has drawbacks that limit its performance in some applications. Some issues include high voltage spikes and oscillations caused by leakage inductance in the main transformer, reducing efficiency and risking switch and diode damage. Furthermore, the main switch requires a high voltage rating due to the summation of input and reflected output voltages [46]. Fig. 3(a) depicts a two-switch flyback PWM dc–dc converter with active snubber [47]. The proposed converter introduces a dual-flyback high step-up, enhancing voltage gain while minimizing turn ratios. Increasing voltage gain and

reducing switching losses are achieved by coupling two series secondary inductors.

To minimize input current ripple, the two primary sides are interconnected in a parallel configuration.

B. TRANSFORMER BASED ISOLATED SOLUTIONS

The forward converter is one of transformer based isolated solutions that extensively employed in applications requiring low to medium power supplies, primarily owing to its straightforward design and cost-effectiveness. Nonetheless, it possesses two primary disadvantages: When the switch is deactivated, the energy confined in the magnetizing inductance within the core results in transformer saturation, and the transformer's leakage inductance subjects the switch to substantial voltage stress [48], [49], [50], [51]. Ref. [52] introduces an innovative Active-Clamp Forward Converter (ACFC) incorporating a lossless snubber on the secondary side to mitigate voltage spikes on the free-wheeling diode and forward-rectifier diode. Fig. 3(b) depicts the circuit configuration of the suggested converter.

The Push-Pull based converter is other transformer based isolated solution, which utilized in single phase PV applications. This converter is known for its simplicity and reduced component count, is often chosen for applications where isolation and high step-up ratios are essential. While cost-effective and efficient, it may face challenges in EMI [53]. One push pull based converter with Three Winding Transformer (3WT) has been illustrated in Fig. 3(c) [54]. This configuration's primary benefit lies in its capacity for achieving a high voltage gain, operating with ZVS, and offering a wide operational range suitable for applications like PV microconverters.

A half-bridge converter finds wide application in motor drives, power supplies, battery chargers, and renewable energy systems. Similar to forward and push-pull converters, it can generate variable output voltages and offer electrical isolation. Despite its more intricate design compared to

forward or push-pull converters, the half-bridge converter delivers greater output power using fewer and cost-effective components [55]. Ref. [56] (Fig. 3(d)) explored an efficient quasi-resonant boost half-bridge dc–dc converter for PV micro-inverters, with a wide input voltage range. The design optimized conversion using a voltage doubler and snubber capacitor, eliminating DC-magnetizing currents in transformers. Employing quasi-resonance in switches and diodes achieved ZVS, minimizing turn-off losses.

The isolated Full-Bridge (FB) converters, which is another transformer based solution, offers improved efficiency and reduced stress on components compared to its half-bridge counterpart. Its full-bridge configuration allows bidirectional power flow, making it suitable for applications demanding higher power density [57]. In [58], which demonstrated in Fig. 3(e), a current fed FB with wide input voltage range has been presented. The voltage spike throughout this converter has been decreased because of using clamp capacitor.

Resonant converters, notably the LLC type, are gaining attention for their outstanding performance [59], [60], [61], [62], [63], [64]. Their benefits and drawbacks vary based on application needs like power density, efficiency, cost, complexity, and reliability [65]. The LLC converter, with low EMI, high power density, and ZVS capability in switches, is particularly favored. In high-step-up PV applications, LLC resonant converters operating at resonant frequencies are preferred for efficient power conversion [66]. Nevertheless, integrating additional components leads to increased magnetic loss, costs, and complexity within these converters. In [67] (Fig. 3(f)), a resonant dc-dc converter was created with the aim of attaining input currents devoid of ripples. Through the maintenance of a consistent duty cycle and the incorporation of a resonant circuit on the secondary side, this converter reduces turn-off currents and minimizes switching losses, ultimately enhancing efficiency.

III. COMPARISON METHODOLOGY OF ISOLATED SOLUTIONS

In this section, a comprehensive comparison of solutions depicted in Fig. 2 is conducted using a methodology that considers key parameters such as follows:

1) Capacitor size
2) Magnetic size
3) Primary side switch voltage stress
4) Primary side semiconductor conduction losses
5) Switching losses

The design parameter of comparison for all converters has been indicated in Table 3.

Capacitor size impacts energy efficiency, inductor size influences energy transfer, and high frequency transformer dimensions, which are magnetic elements, affect overall system size and efficiency. Analysis of relative conduction and switching losses of semiconductors provides insights into system efficiency and control mechanisms. Additionally, evaluating primary side switch voltage stress informs about component reliability. In a very general case, the fundamental

TABLE 3. Design Parameter of Comparison for All Converters

Parameters	Value
Input voltage range (V_{in})	20 V – 60 V
Output voltage (V_o)	350 V
Maximum rated power (P_o)	400 W
Switching frequency	50 kHz
Maximum input current	10 A
Maximum input current ripple	15 %
Maximum voltage ripple of capacitors	3 %

waveforms of a converter are independent of the selection of components and electric parameters (e.g., switching frequency, selected semiconductors) and result from the basic modulation scheme, yielding some general requirements for the dimensioning of the components [68]. This approach offers a nuanced understanding of the strengths and weaknesses of each solution, aiding engineers and researchers in optimizing these converters for diverse applications. It was applied in some other research works [69], [70].

A. MAGNETIC AND CAPACITORS SIZE COMPARISON

For comparing capacitor and magnetic sizes among the solutions, a methodology relies on calculating the total accumulated energy in these elements. This quantitative approach evaluates their energy storage capacities, providing insights into efficiency. The analysis also considers total conduction power loss, offering a holistic perspective on how effectively each solution manages power flow through these components. Therefore, the following equations has been utilized:

$$\sum_{i=1}^{n} E_{C_i} = \frac{1}{2} C_i V_{C_i}^2, \tag{1}$$

$$\sum_{j=1}^{m} E_{L_j} = \frac{1}{2} L_j I_{L_j}^2. \tag{2}$$

In the above equations, E_C, E_L, V_C, I_L, n and m are respectively the accumulated energy in capacitors and inductors, the voltage across the capacitors, the current through the inductors, number of capacitors and number of inductors.

B. PRIMARY SIDE SWITCH VOLTAGE STRESS COMPARISON

To compare the primary side switch voltage stress (V_{stress}) of switches, a normalized parameter called the Voltage Stress Ratio (*VSR*) can be used as follows:

$$VSR = \frac{V_{stress}}{V_{out}}. \tag{3}$$

This ratio provides a comparative measure that considers the impact of the voltage stress relative to the output voltage. A lower *VSR* indicates that the primary side switch voltage stress is a smaller proportion of the output voltage, which can be useful for evaluating the stress level on the switch in relation to the desired output voltage.

C. PRIMARY SIDE SEMICONDUCTOR CONDUCTION LOSSES COMPARISON

The primary side semiconductor conduction losses in mentioned converters are compared based on normalized parameter known as the Conduction Loss Ratio (*CLR*). The CLR is expressed as the ratio of the conduction losses to the total power:

$$CLR = \frac{P_{Condcution}}{P_{out}}. \tag{4}$$

In (4) P_{out} is the total power of the converter and $P_{conduction}$ represents the total conduction losses in the primary side semiconductor devices that define as follows:

$$P_{conduction} = \sum_{i=1}^{N} R_{on} I_{RMSi}^2. \tag{5}$$

I_{RMS} is the Root Mean Square (RMS) current flowing through the semiconductor device during conduction, and R_{on} is the ON-state resistance of the semiconductor device.

D. SWITCHING LOSSES COMPARISON

The switching loss ratio (*SLR*) is defined as the ratio of the switching losses to the total power for this comparison as follows:

$$SLR = \frac{P_{switching}}{P_{out}}. \tag{6}$$

The switching losses ($P_{switching}$) occur during both turn-on and turn-off events are influenced by semiconductor parameters such as the switching frequency, device capacitances that we assume to be similar to all compared solutions, while the voltage and current waveforms during switching are define by the selected topology and are expressed as follows:

$$SL \cong \sum_{i=1}^{N_S} \left\langle \hat{i}_{Si} \cdot \hat{v}_{Si} \right\rangle_T. \tag{7}$$

In (7), the average of the product v_{Si} and i_{Si} throughout a fundamental period T serves as an appropriate indicator for assessing switching losses. Besides, *SLR* provides a comparative measure for evaluating how efficiently the converter handles switching losses relative to the total power. Based on the mentioned specification for methodology of comparison, the converters presented in Fig. 3 from each family of isolated converter has been compared with each other that is indicated in Fig. 4.

The comparison performance of each converter separately has been illustrated in Fig. 5. It is essential to emphasize that this comparative analysis is specifically implemented with an output power set at 400 W. The input voltage ranges between 20 V and 50 V, with a consistent switching frequency of 50 kHz, while the output voltage is maintained at a constant 350 V. To ensure a comprehensive and fair comparison, not only is the output power standardized, but the duty cycle and other dynamic switch configurations are also kept consistent
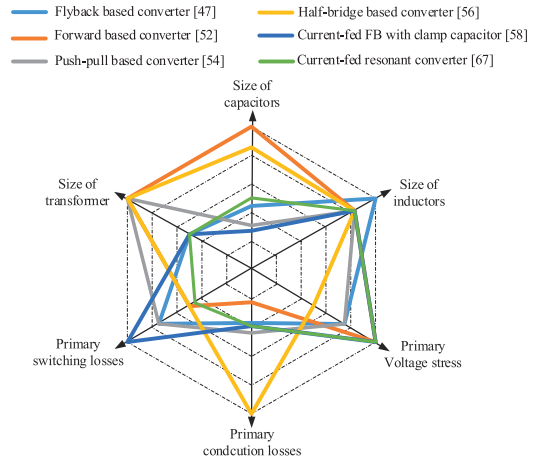

FIGURE. 4. Overall comparison of the isolated converters form each family based on key parameters.

across all converters. It's worth noting that isolated high-step-up converters typically incorporate a voltage multiplier rectifier on their secondary side, a common feature among most isolated converters.

As a result, specifications related to the secondary side, such as the voltage stress of diodes and conduction losses, have been omitted from this comparison. This intentional exclusion allows us to focus specifically on the primary aspects influencing performance, providing a standardized basis for evaluating the efficiency and effectiveness of the converters. This meticulous approach ensures that the comparison is not only fair but also comprehensive, enabling a detailed examination of the converters' performance under consistent conditions.

In general isolated converters have been extensively employed across different power levels, frequently as adaptations of non-isolated converters [71] and [72]. As previously noted, DC-DC converters featuring galvanic isolation can be classified based on the energy transmission element as either transformers or coupled inductors [26]. Even though both transformers and coupled inductors share the commonality of having multiple windings on a magnetic core, their operational principles and roles in switching converters exhibit significant variations [73]. Transformers are the favored option for achieving galvanic isolation due to their noteworthy power density, making them a popular choice for high-power applications. Conversely, converters based on coupled inductors present a more efficient solution characterized by a smaller size and weight. Moreover, they find common use in applications with lower power requirements [74].

IV. EXPERIMENTAL EXAMPLE OF ISOLATED DC-DC CONVERTERS

To validate the comparison methodology, a series of experiments with various configurations was conducted in the
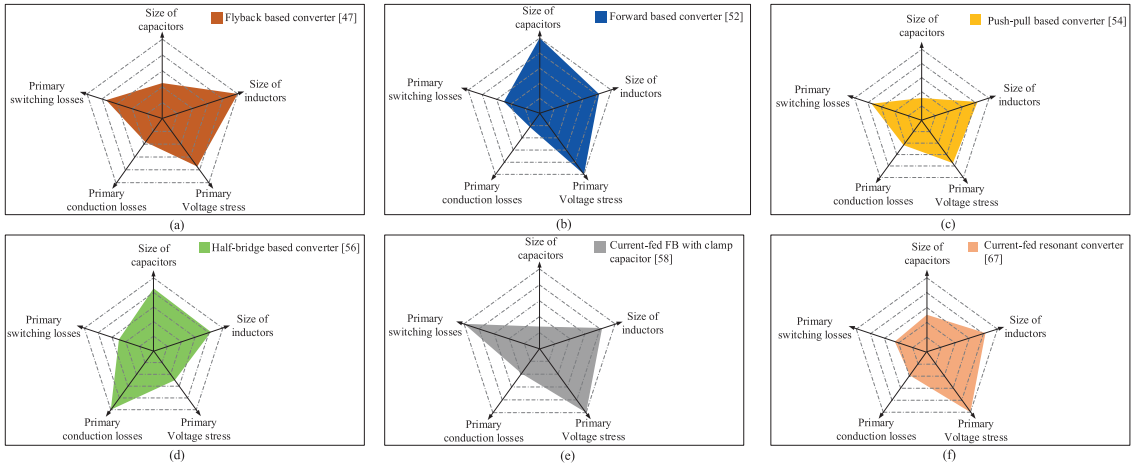
FIGURE. 5. Performance Comparison of the isolated converters, (a) Flyback based converter [47], (b) Forward based converter [52], (c) Push-pull based converter [54], (d) Half-bridge based converter [56], (e) Current-fed FB with clamp capacitor [58], and (f) Current-fed resonant converter [67].
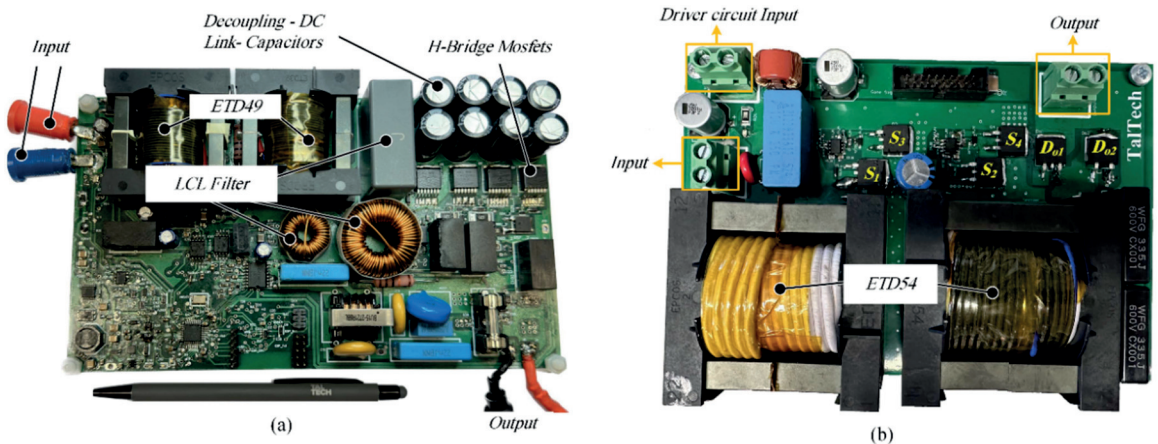

FIGURE. 6. The experimental prototype of the isolated converters, (a) Flyback based converter, (b) FB based converter.

laboratory. In this specific comparison, the flyback converter was chosen from the family of isolated converters due to its reliance on the coupling inductor. Similarly, the full-bridge converter, selected from the same family of isolated converters, was chosen based on its use of a transformer. Moreover, Fig. 6 illustrates the experimental prototypes of each converter.

It's crucial to emphasize that the flyback converter showcased in this study was meticulously designed for PV microinverter applications and includes additional components because of its performance [45]. However, for a fair and focused comparison, only the DC portion of the flyback converter was considered. This deliberate choice enables a comprehensive and equitable evaluation of the essential

aspects pertinent to the comparison. The parameter specifications for both converters are provided in Table 4. Both converters underwent testing with an input voltage range of 20–60 V and a power rating of 400 W. The experimental waveforms for both the flyback-based high step-up converter and the full-bridge (FB) based converter are presented in Fig. 6. It is crucial to note that these waveforms were obtained with an input voltage fixed at 40 V and a constant output voltage of 350 V. In Fig. 7(a), the waveforms for input voltage (V_{in}), output voltage (V_{out}), and input current of the FB-based converter are displayed. Notably, the input current ripple content is approximately 20 %, indicating an acceptable level for this type of converter. Fig. 7(b) depicts the voltage and current waveforms of the main switches of the FB-based
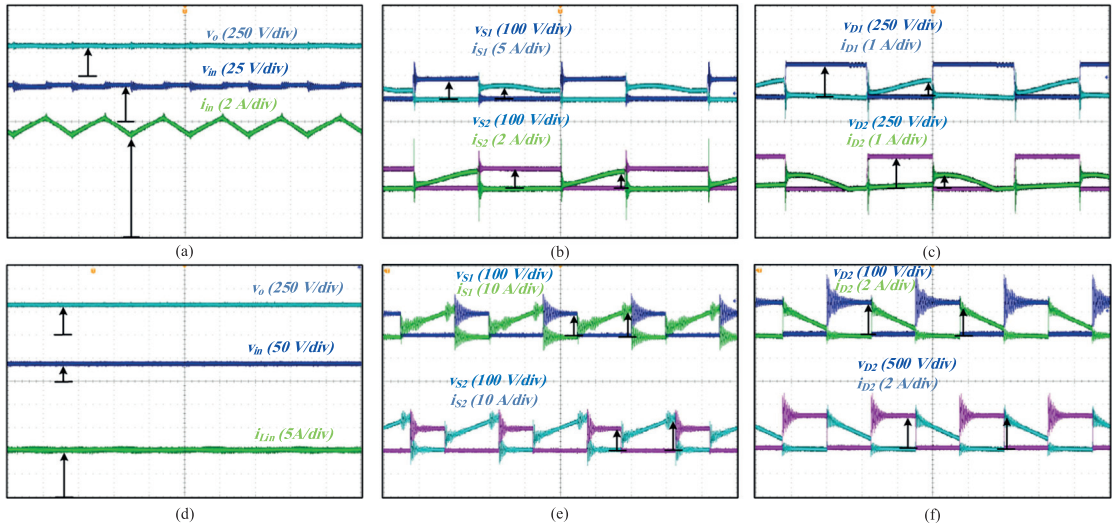
FIGURE. 7. Experimental measurement of the isolated dc-dc converters, (a) Input voltage (V_{in}), output voltage (V_{out}) and input current of FB based converter, (i_{in}) waveforms, (b) current and voltage waveforms of switches S_1 and S_2 of FB based converter, (c) current and voltage waveforms of diode D_1 and D_2 of FB based converter, (d) Input voltage (V_{in}), output voltage (V_{out}) and input current (i_{in}) of flyback based converter, (e) current and voltage waveforms of switches S_1 and S_2 of flyback based converter, (f) current and voltage waveforms diodes D_1 and D_2 of flyback based converter.

**TABLE 4.** Specification of the Isolated Converters

Parameters	Value/Type	
	Flyback based	FB based
Transformer core	ETD49	ETD54
Input inductor	-	220 µH
Magnetic inductance	60 µH	870 µH
Leakage inductance	450 nH	1.7 µH
Decoupling capacitor	8 × 22 µF	-
Capacitors C_b, C_r	-	22 µF, 10 µF
Semiconductor elements		
Switches $S_1..S_4$	-	IPB048N15N5LFATMA1
Diodes D_{o1}, D_{o2}	IDM05G120C5XTMA1	C6D08065G
Flyback switches	IPB044N15N5ATMA1	IPB044N15N5ATMA1
Operating point		
Input voltage range (V_{in})	20 V – 60 V	20 V – 60 V
Output voltage (V_o)	350 V	350 V
Maximum rated power (P_o)	400 W	400 W
Switching frequency	60 kHz	60 kHz

converter. From this figure, it is observed that the voltage stress on the two main switches is around 90 V, which is four times smaller than the output voltage. Moving to Fig. 7(c), the voltage and current waveforms of the voltage multiplier rectifier diodes (D_1 and D_2) are illustrated. The voltage stress on the output diode matches the output voltage, a typical characteristic in converters of this kind. Switching our attention to the isolated flyback converter, Fig. 7(d) showcases the input voltage, output voltage, and magnetizing current waveforms. A comparison with the FB-based converter reveals that the input current ripple of the flyback-based converter is generally higher. In Fig. 7(e), the voltage and current of switches S_1

and S_2 are presented, indicating a maximum switch voltage of around 120 V. In terms of voltage stress evaluation, although each switch's voltage stress in the FB-based converter is lower than that of the flyback-based converter, the total voltage stress in the FB-based converter is higher when compared to the flyback-based converter. Finally, Fig. 7(f) exhibits the voltage and current waveforms of the output diodes, revealing that their voltage stress is twice as high as the output voltage. While this may suggest high stress on the output diodes, it is noteworthy that there are also flyback-based converters mentioned in previous studies [45], where the output diode voltage stress aligns with the output voltage. In summary, the waveforms analysis indicates distinct performance characteristics between the flyback-based high step-up converter and the FB-based converter. The FB-based converter demonstrates lower voltage stress on individual switches but higher total voltage stress. The output diodes in the FB-based converter exhibit higher stress, yet it's important to recognize that similar stress levels have been reported in certain flyback-based converters according to prior studies [45]. Choosing between the two converters depends on the specific application requirements and observed waveform characteristics

In order to provide a thorough comparison between coupled inductor-based and transformer-based structures, various key performance aspects have been analyzed and presented in Fig. 8(a)–(e) for both converters. These figures offer insights into the efficiency curve, losses breakdown of the power circuit, and thermal characteristics of the main switches for both FB based and flyback based converters.

In Fig. 8(a), the efficiency curve shows the performance of the proposed converters across a range of output power

(a)
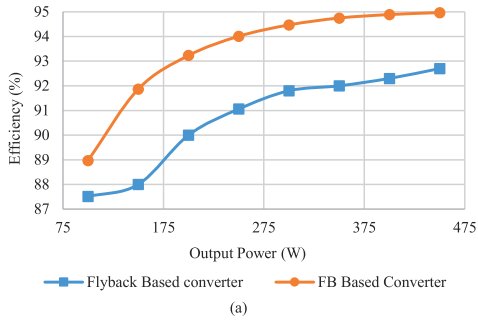
Power Losses Breakdown of FB Based Converter

(b)
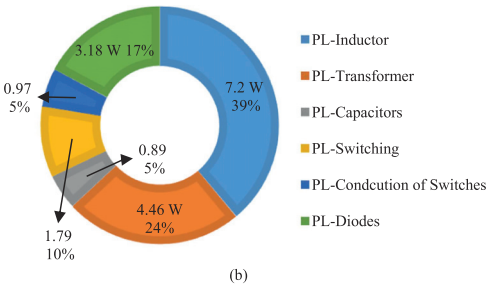
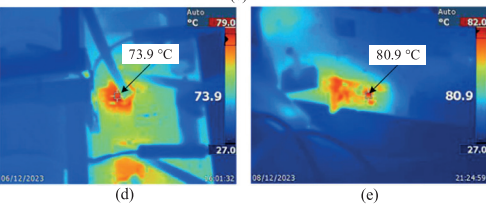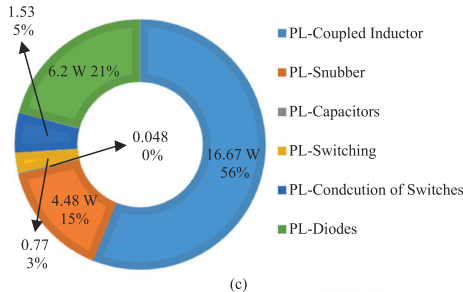Power Losses Breakdown of Flyback Based Converter

(c)

(d)　　　　　(e)

FIGURE. 8. Efficiency, power loss curve and thermal image flyback based and FB based converters, (a) Efficiency curve versus output power, (b) Total losses breakdown of the components in FB based converter, (c) Total losses breakdown of the components in flyback based converter, (d) Thermal image of the main switch in FB based converter, (e) Thermal image of the main switch in flyback based converter.

levels, differing from light load to full load conditions. It is evident from this figure that the FB based converter exhibits a notably higher efficiency when compared to the flyback based converter. Fig. 8(b) and (c) present a detailed breakdown of losses within the power circuit for both converter types. The analysis reveals that the predominant source of losses in both converters is attributed to magnetic elements.
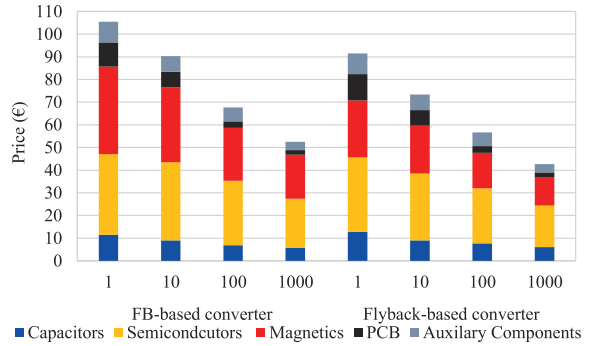

FIGURE. 9. The cost graph of the image flyback based and FB based converters for different numbers of assemblies.

This commonality underscores the intrinsic nature of losses associated with these components. Notably, the Flyback converter introduces additional losses in the form of snubber circuit losses, which are conspicuously significant.

This observation raises considerations for optimizing the snubber circuit design to mitigate its impact on overall efficiency. Furthermore, the temperature curves of the main switches for each converter, as depicted in Fig. 8(d) and (e), highlight the thermal characteristics under the specified operating conditions. Based on this Figs, both converters demonstrate satisfactory thermal performance in this scenario, indicating that neither converter is adversely affected by excessive heating issues. In Fig. 9, the cost comparison between full-bridge and flyback converters reveals an interesting insight. Despite the full-bridge converter showing higher efficiency, the overall cost of the flyback converter is significantly lower. In essence, while efficiency is undoubtedly a critical factor in converter selection, the general consideration of cost-effectiveness, proves the practical appeal and widespread utilization of flyback-based converters across various industrial sectors.

This cost advantage is a key reason why flyback converters are commonly preferred in various industrial applications. The simplicity of the flyback topology, requiring fewer components and offering straightforward implementation, contributes to its cost-effectiveness. This economic advantage makes flyback converters a widely adopted and practical solution in the industry for low power applications

A comprehensive evaluation has been conducted to compare the flyback-based converter [45] with the FB-based converter across various crucial parameters such as total voltage stress on primary switches, component count, volume, size, power density, full load efficiency, and cost. The detailed findings are summarized in Table 4, providing an insightful overview of the performance characteristics of the two converters. Fig. 10 further elucidates the comparison by presenting the specifications of the Flyback-based and FB-based prototypes. Upon careful examination of both the Table 5 and the graphical representation in Fig. 10, it becomes evident
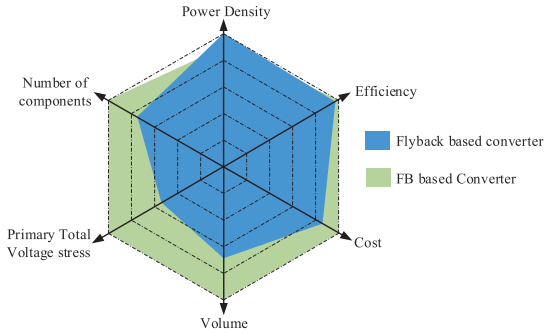
FIGURE. 10. The specification of the comparison between the Flyback based and FB based prototypes.

TABLE 5. Specification of the Two Converter Comparison

Topologies	Flyback based converter	FB Based Converter
Power Density	1.97 kw/dm^3	1.78 kw/dm^3
Efficiency	92.3 %	94.89 %
Cost	91 €	105 €
Volume	188*111*28 mm^3	165*111*46 mm^3
Total Voltage stress of primary side	197 V	360 V
Number of main components	9	12

that the flyback-based converter exhibits superiority in several aspects when compared to the FB-based converter. Despite the high efficiency of the FB-based converter, it is noteworthy that it incurs elevated costs and experiences increased total voltage stress across the switches, unlike the flyback-based counterpart. Notably, the flyback-based converter demonstrates a favorable combination of high power density and a reduced number of components, contributing to an overall cost reduction in the converter assembly.

In a comparative analysis between the flyback based converter and the FB based converter, it is initially observed that the flyback converter imposes a higher voltage stress on a switch than the FB counterpart. However, considering the number of switches, the overall voltage stress of the full-bridge converter surpasses that of the flyback converter. Additionally, alternative flyback converters, such as the one presented in [47], demonstrate parity in voltage stress with the full-bridge converter for individual switches.

Based on comprehensive theoretical analysis and the practical results showcased for converters within the transformer and coupled inductor family, it is evident that several key parameters must be considered for the effective deployment of these converters in industrial applications. These crucial parameters include, but are not limited to, the number of elements, efficiency, and notably the cost. In the realm of industrial applications, the selection of an appropriate converter structure demands a precise evaluation, taking into account the complicated balance between these fundamental criteria. Efficiency, cost-effectiveness, and the specific requirements

of the intended application all play fundamental roles in determining the optimal choice. This consideration is superior in achieving not only optimal performance but also cost-efficient and sustainable solutions for different industrial applications.

V. CONCLUSION

This paper presented a comprehensive evaluation of isolated high step-up dc-dc converters, emphasizing their applicability in distributed generation systems powered by renewable energy sources. The overview of competitive solutions highlights the importance of power electronic structures in incorporating renewable energy into the power grid, emphasizing their widespread and rapidly expanding usage. Through a comparative analysis, key parameters such as voltage conversion ratio, semiconductor element voltage stress, component size, and conduction and switching losses are considered. The selected configurations are also assessed in terms of cost estimation and financial feasibility. The investigation aims to guide researchers in identifying suitable isolated topologies with wide input voltage ranges and galvanic isolation for future research directions.

The comparison methodology is provided as systematic approach, considering capacitor and magnetic sizes, primary side switch voltage stress, primary side semiconductor conduction losses, and switching losses. The experimental examples of isolated dc-dc converters, specifically the flyback-based and full-bridge-based converters, validate the methodology and showcase distinct performance characteristics between the two.

The efficiency curve, losses breakdown, thermal characteristics, and cost comparison provide a comprehensive understanding of the trade-offs between the flyback and FB converters. Despite the higher efficiency of the FB converter, the cost-effectiveness of the flyback converter, attributed to its simplicity and fewer components, demonstrates its practical appeal in various industrial applications.

In conclusion, based on the comparative analysis and experimental validation, the paper recommends considering specific application requirements when choosing isolated high step-up dc-dc converters. The findings emphasize the importance of balancing efficiency and cost-effectiveness for practical implementation in distributed generation systems using renewable energy sources.

REFERENCES

[1] M. Malinowski, J. I. Leon, and H. Abu-Rub, "Solar photovoltaic and thermal energy systems: Current technology and future trends," *Proc. IEEE*, vol. 105, no. 11, pp. 2132–2146, Nov. 2017.

[2] J. Zeng, X. Du, and Z. Yang, "A multiport bidirectional DC–DC converter for hybrid renewable energy system integration," *IEEE Trans. Power Electron.*, vol. 36, no. 11, pp. 12281–12291, Nov. 2021.

[3] S. Gopinathan, V. S. Rao, and K. Sundaramoorthy, "Family of non-isolated quadratic high gain DC–DC converters based on extended capacitor-diode network for renewable energy source integration," *IEEE J. Emerg. Sel. Topics Power Electron.*, vol. 10, no. 5, pp. 6218–6230, Oct. 2022.

[4] Y. Yang et al., *Adv. in Grid-Connected Photovolt. Power Convers. Syst.*, Woodhead Publishing, 2018.

[5] H. Shayeghi, S. Pourjafar, M. Maalandish, and S. Nouri, "Non-isolated DC–DC converter with a high-voltage conversion ratio," *IET Power Electron.*, vol. 13, no. 16, pp. 3797–3806, Dec. 2020.

[6] E. L. Carvalho, A. Blinov, A. Chub, P. Emiliani, G. de Carne, and D. Vinnikov, "Grid integration of DC buildings: Standards, requirements and power converter topologies," *IEEE Open J. Power Electron.*, vol. 3, pp. 798–823, Oct. 2022.

[7] S. Beheshtaein, R. M. Cuzner, M. Forouzesh, M. Savaghebi, and J. M. Guerrero, "DC Microgrid protection: A comprehensive review," *IEEE J. Emerg. Sel. Topics Power Electron.*, early access, Mar. 12, 2019, doi: 10.1109/JESTPE.2019.2904588

[8] L. Mackay, N. H. van der Blij, L. Ramirez-Elizondo, and P. Bauer, "Toward the universal DC distribution system," *Electric Power Compon. Syst.*, vol. 45, no. 10, pp. 1032–1042, 2017.

[9] O. Matiushkin, O. Husev, D. Vinnikov, and J. Kurnitski, "DC-Ready photovoltaic solar converter," in *Proc.IEEE Int. Exhib. Conf. Power Electron., Intell. Motion, Renewable Energy Energy Manage.*, Nuremberg, Germany, 2023, pp. 1–7.

[10] P. Mohseni, S. Rahimpour, M. Dezhbord, M. R. Islam, and K. M. Muttaqi, "An optimal structure for high step-up non-isolated DC–DC converters with soft-switching capability and zero input current ripple," *IEEE Trans. Ind. Electron.*, vol. 69, no. 5, pp. 4676–4686, May 2022.

[11] S. Pourjafar, H. Shayeghi, S. M. Hashemzadeh, F. Sedaghati, and M. Maalandish, "A non-isolated high step-up DC–DC converter using magnetic coupling and voltage multiplier circuit," *IET Power Electron.*, vol. 14, no. 9, pp. 1637–1655, Jul. 2021.

[12] P. Alavi, P. Mohseni, E. Babaei, and V. Marzang, "An ultra-high step-up DC–DC converter with extendable voltage gain and soft-switching capability," *IEEE Trans. Ind. Electron.*, vol. 14, no. 9, pp. 4676–4686, May 2022.

[13] P. K. Maroti, S. Padmanaban, J. B. Holm-Nielsen, M. Sagar Bhaskar, M. Meraj, and A. Iqbal, "A new structure of high voltage gain SEPIC converter for renewable energy applications," *IEEE Access*, vol. 7, pp. 89857–89868, 2019.

[14] Y. Liu, W. Zhang, Y. Sun, M. Su, G. Xu, and H. Dan, "Review and comparison of control strategies in active power decoupling," *IEEE Trans. Power Electron.*, vol. 36, no. 12, pp. 14436–14455, Dec. 2021.

[15] O. Matiushkin, O. Husev, H. Afshari, D. Vinnikov, and R. Strzelecki, "Cost-effective piggyback forward based DC-DC converter," in *Proc. IEEE Appl. Power Electron. Conf. Expo.*, 2024, pp. 2106–2111.

[16] J. Yuan, F. Blaabjerg, Y. Yang, A. Sangwongwanich, and Y. Shen, "An overview of photovoltaic microinverters: Topology, efficiency, and reliability," in *Proc. IEEE 13th Int. Conf. Compat., Power Electron. Power Eng.*, 2019, pp. 1–6.

[17] M. Forouzesh, Y. P. Siwakoti, S. A. Gorji, F. Blaabjerg, and B. Lehman, "Step-up DC–DC converters: A comprehensive review of voltage-boosting techniques, topologies, and applications," *IEEE Trans. Power Electron.*, vol. 32, no. 12, pp. 9143–9178, Dec. 2017.

[18] Y. Koç, Y. Birbir, and H. Bodur, "Non-isolated high step-up DC-DC converters–An overview," *Alexandria Eng. J.*, vol. 61, no. 2, pp. 1091–1132, Feb. 2022.

[19] O. Husev, L. Liivik, F. Blaabjerg, A. Chub, D. Vinnikov, and I. Roasto, "Galvanically isolated quasi-z-source DC–DC converter with a novel ZVS and ZCS technique," *IEEE Trans. Ind. Electron.*, vol. 62, no. 12, pp. 7547–7556, Dec. 2015.

[20] E. S. Oluwasogo and H. Cha, "A quadratic quasi-z-source full-bridge isolated DC–DC converter with high reliability for wide input applications," *IEEE Trans. Ind. Electron.*, vol. 69, no. 10, pp. 10090–10100, Oct. 2022.

[21] J. Lee, M. Kim, S. Kim, and S. Choi, "An isolated single-switch ZCS resonant converter with high step-up ratio," *IEEE Trans. Power Electron.*, vol. 36, no. 10, pp. 11555–11564, Oct. 2021.

[22] N. Hassanpour, A. Chub, A. Blinov, and D. Vinnikov, "Soft-switching bidirectional step-up/down partial power converter with reduced components stress," *IEEE Trans. Power Electron.*, vol. 38, no. 11, pp. 14166–14177, Nov. 2023.

[23] Z. Zhang et al., "High efficiency step-up DC–DC converter for grid-connected photovoltaic microinverter applications," *IET Renewable Power Gener.*, vol. 16, no. 6, pp. 1159–1169, Apr. 2022.

[24] N. Yang, J. Zeng, R. Hu, and J. Liu, "Analysis and design of an isolated high step-up converter without voltage-drop," *IEEE Trans. Power Electron.*, vol. 37, no. 6, pp. 6939–6950, Jun. 2022.

[25] R. Kosenko, O. Husev, and A. Chub, "Full soft-switching high step-up current-fed DC-DC converters with reduced conduction losses," in *Proc. IEEE 5th Int. Conf. Power Eng., Energy Elect. Drives*, Riga, Latvia, 2015, pp. 170–175.

[26] M.-K. Nguyen, Y.-C. Lim, J.-H. Choi, and G.-B. Cho, "Isolated high step-up DC–DC converter based on quasi-switched-boost network," *IEEE Trans. Ind. Electron.*, vol. 63, no. 12, pp. 7553–7562, Dec. 2016.

[27] D. Vinnikov, J. Zakis, O. Husev, and R. Strzelecki, "New high-gain step-up DC/DC converter with high-frequency isolation," in *Proc. IEEE 27th Annu. Appl. Power Electron. Conf. Expo.*, Orlando, FL, USA, 2012, pp. 1204–1209.

[28] D. Vinnikov, A. Chub, O. Huse, and J. Zakis, "Quasi-Z-source half-bridge DC-DC converter for photovoltaic applications," in *Proc. IEEE Int. Conf. Ind. Technol.*, Seville, Spain, 2015, pp. 2935–2940.

[29] A. Chub, O. Husev, and D. Vinnikov, "Input-parallel output-series connection of isolated quasi-Z-source DC-DC converters," in *Proc. IEEE Electric Power Qual. Supply Rel. Conf.*, Rakvere, Estonia, 2014, pp. 277–284.

[30] A. Chub, D. Vinnikov, F. Blaabjerg, and F. Z. Peng, "A review of galvanically isolated impedance-source DC–DC converters," *IEEE Trans. Power Electron.*, vol. 31, no. 4, pp. 2808–2828, Apr. 2016.

[31] Y. C. Huang, Y. C. Hsieh, C. Y. Lin, and C. S. Moo, "Light load analysis and topology morphing between full/half-bridge DC-to-DC converter," *Int. J. Electron.*, vol. 111, pp. 298–317, 2023, doi: 10.1080/00207217.2022.2164070.

[32] H. Mao, S. Deng, J. Abu-Qahouq, and I. Batarseh, "Active-clamp snubbers for isolated half-bridge DC-DC converters," *IEEE Trans. Power Electron.*, vol. 20, no. 6, pp. 1294–1302, Nov. 2005.

[33] Q. Wu, Q. Wang, J. Xu, and Z. Xu, "Active-clamped ZVS current-fed push–pull isolated DC-DC converter for renewable energy conversion applications," *IET Power Electron.*, vol. 11, no. 2, pp. 373–381, Feb. 2018.

[34] Q. Wu, Q. Wang, J. Xu, and L. Xiao, "A wide load range ZVS push–pull DC-DC converter with active clamped," *IEEE Trans. Power Electron.*, vol. 32, no. 4, pp. 2865–2875, Apr. 2017.

[35] H. Kim, C. Yoon, and S. Choi, "An improved current-fed ZVS isolated boost converter for fuel cell applications," *IEEE Trans. Power Electron.*, vol. 25, no. 9, pp. 2357–2364, Sep. 2010.

[36] K. Kanathipan, R. Emamalipour, and J. Lam, "A single-switch high-gain PV microconverter with low-switch-voltage-to-high-voltage-bus ratio," *IEEE Trans. Power Electron.*, vol. 35, no. 9, pp. 9530–9540, Sep. 2020.

[37] A. R. Paul, A. Bhattacharya, and K. Chatterjee, "A novel SEPIC-ĆUK-based high gain solar PV microinverter for grid integration," *IEEE Trans. Ind. Electron.*, vol. 70, no. 12, pp. 12365–12375, Dec. 2023.

[38] A. Shawky, T. Takeshita, and M. A. Sayed, "Analysis and performance evaluation of single-stage three-phase SEPIC differential inverter with continuous input current for PV grid-connected applications," in *Proc. IEEE Appl. Power Electron. Conf. Expo.*, Phoenix, AZ, USA, 2021, pp. 2719–2726.

[39] S. A. Ansari and J. S. Moghani, "A novel high voltage gain noncoupled inductor SEPIC converter," *IEEE Trans. Ind. Electron.*, vol. 66, no. 9, pp. 7099–7108, Sep. 2019.

[40] N. Falconar, D. S. Beyragh, and M. Pahlevani, "An adaptive sensorless control technique for a flyback-type solar tile microinverter," *IEEE Trans. Power Electron.*, vol. 35, no. 12, pp. 13554–13562, Dec. 2020.

[41] R. Za'im, J. Jamaludin, and N. A. Rahim, "Photovoltaic flyback microinverter with tertiary winding current sensing," *IEEE Trans. Power Electron.*, vol. 34, no. 8, pp. 7588–7602, Aug. 2019.

[42] F. Zhang, Y. Xie, Y. Hu, G. Chen, and X. Wang, "A hybrid boost–flyback/flyback microinverter for photovoltaic applications," *IEEE Trans. Ind. Electron.*, vol. 67, no. 1, pp. 308–318, Jan. 2020.

[43] R. Erickson, M. Madigan, and S. Singer, "Design of a simple high-power-factor rectifier based on the flyback converter," in *Proc. IEEE 5th Annu. Proc. Appl. Power Electron. Conf. Expo.*, Los Angeles, CA, USA, Mar. 1990, pp. 792-801.

[44] B. Tamyurek and B. Kirimer, "An interleaved high-power flyback inverter for photovoltaic applications," *IEEE Trans. Power Electron.*, vol. 30, no. 6, pp. 3228–3241, Jun. 2015.

[45] H. Afshari, O. Husev, D. Vinnikov, O. Matiushkin, and N. V. Kurdkandi, "Comparison of grid-connected flyback-based microinverter with primary and secondary side decoupling approach," in *Proc. IEEE 63th Int. Sci. Conf. Power Elect. Eng. Riga Tech. Univ. (RTUCON)*, Riga, Latvia, 2022, pp. 1–6.

[46] I. Alhurayyis, A. Elkhateb, and J. Morrow, "Isolated and non-isolated DC-to-DC converters for medium-voltage dc networks: A review," *IEEE J. Emerg. Sel. Topics Power Electron.*, vol. 9, no. 6, pp. 7486–7500, Dec. 2021.

[47] W. Li, J. Liu, J. Wu, and X. He, "Design and analysis of isolated ZVT boost converters for high-efficiency and high-step-up applications," *IEEE Trans. Power Electron.*, vol. 22, no. 6, pp. 2363–2374, Nov. 2007.

[48] J.-Y. Lin, S.-Y. Lee, C.-Y. Ting, and F.-C. Syu, "Active-clamp forward converter with lossless-snubber on secondary-side," *IEEE Trans. Power Electron.*, vol. 34, no. 8, pp. 7650–7661, Aug. 2019.

[49] H. Wu and Y. Xing, "A family of forward converters with inherent demagnetizing features based on basic forward cells," *IEEE Trans. Power Electron.*, vol. 25, no. 11, pp. 2828–2834, Nov. 2010.

[50] H. Wu and Y. Xing, "Families of forward converters suitable for wide input voltage range applications," *IEEE Trans. Power Electron.*, vol. 29, no. 11, pp. 6006–6017, Nov. 2014.

[51] A. Abramovitz, T. Cheng, and K. Smedley, "Analysis and design of forward converter with energy regenerative snubber," *IEEE Trans. Power Electron.*, vol. 25, no. 3, pp. 667–676, Mar. 2010.

[52] T. Qian and Q. Wu, "A boost type resonant forward converter with topology combination," *IEEE Trans. Circuits Syst. II: Exp. Briefs*, vol. 65, no. 12, pp. 2008–2011, Dec. 2018.

[53] H. Afshari, O. Husev, and D. Vinnikov, "A novel isolated buck-boost DC-DC converter with wide range of voltage regulations," in *Proc. IEEE 17th Int. Conf. Compat., Power Electron. Power Eng.*, Tallinn, Estonia, 2023, pp. 1–6.

[54] Q. Wu, Q. Wang, J. Xu, H. Li, and L. Xiao, "A high-efficiency step-up current-fed push–pull quasi-resonant converter with fewer components for fuel cell application," *IEEE Trans. Ind. Electron.*, vol. 64, no. 8, pp. 6639–6648, Aug. 2017.

[55] T. Meghdad, M. Jafar, and A. Bijan, "High step-up current-fed ZVS dual half-bridge DC–DC converter for high-voltage applications," *IET Power Electron.*, vol. 8, no. 2, pp. 309–318, Feb. 2015.

[56] H.-S. Lee and J.-J. Yun, "Quasi-resonant voltage doubler with snubber capacitor for boost half-bridge DC–DC converter in photovoltaic micro-inverter," *IEEE Trans. Power Electron.*, vol. 34, no. 9, pp. 8377–8388, Sep. 2019.

[57] Z. Yao and J. Xu, "An improved integrated boost full-bridge converter," in *Proc. IEEE Smart Energy Grid Eng.*, Oshawa, ON, Canada, 2016, pp. 191–195.

[58] S. Pourjafar, P. Mohseni, O. Husev, O. Matiushkin, and D. Vinnikov, "Novel isolated high step-up DC-DC converter with wide input voltage regulation range," in *Proc. IEEE 64th Int. Sci. Conf. Power Elect. Eng. Riga Tech. Univ.*, 2023, pp. 1–6.

[59] K. Akbariavaz, S. S. Fazel, and M. Khosravi, "Fully FPGA-based implementation of a modified control strategy for power electronic transformer in railway traction applications," *IET Renewable Power Gener*, vol. 17, pp. 1904–1919, Apr. 2021.

[60] S. Deshmukh Gore et al., "Review on classification of resonant converters for electric vehicle application," *Energy Rep.*, vol. 8, pp. 1091–1113, Nov. 2022.

[61] Z. Yasser Yousefi and F. Seyed Saeed, "Soft-switching buck/boost full-bridge three-port converter for DC-DC applications," *Eng. Sci. Technol., an Int. J.*, vol. 41, May 2023, Art. no. 101382.

[62] R. Takarli, M. Adib, A. Vahedi, and R. Beiranvand, "A bidirectional CLLC resonant converter for EV battery charger applications," in *Proc. 14th Power Electron., Drive Syst., Technol. Conf.*, Babol, Iran, Islamic Republic of, 2023, pp. 1–6.

[63] M. Rezayati, F. Tahami, J. L. Schanen, and B. Sarrazin, "Generalized state-plane analysis of bidirectional CLLC resonant converter," *IEEE Trans. Power Electron.*, vol. 37, no. 5, pp. 5773–5785, May 2022.

[64] P. He, A. Mallik, A. Sankar, and A. Khaligh, "Design of a 1-MHz high-efficiency high-power-density bidirectional GaN-based CLLC converter for electric vehicles," *IEEE Trans. Veh. Technol.*, vol. 68, no. 1, pp. 213–223, Jan. 2019.

[65] Y. Wei, Q. Luo, and H. A. Mantooth, "A resonant frequency tracking technique for LLC converter-based DC transformers," *IEEE J. Emerg. Sel. Topics Ind. Electron.*, vol. 2, no. 4, pp. 579–590, Oct. 2021.

[66] S. Tandon and A. K. Rathore, "Analysis and design of series LC resonance-pulse based zero-current-switching current-fed half-bridge DC–DC converter," *IEEE Trans. Ind. Electron.*, vol. 68, no. 8, pp. 6784–6793, Aug. 2021.

[67] H. Seok, B. Han, B.-H. Kwon, and M. Kim, "High step-up resonant DC–DC converter with ripple-free input current for renewable energy systems," *IEEE Trans. Ind. Electron.*, vol. 65, no. 11, pp. 8543–8552, Nov. 2018.

[68] D. Menzi, D. Bortis, and J. W. Kolar, "A new bidirectional three-phase phase-modular boost-buck AC/DC converter," in *Proc. IEEE Int. Power Electron. Application Conf. Expo.*, 2018, pp. 1–8.

[69] O. Husev, O. Matiushkin, T. Jalakas, D. Vinnikov, and N. V. Kurdkandi, "Comparative evaluation of dual-purpose converters suitable for application in DC and AC grids," *IEEE J. Emerg. Sel. Topics Power Electron.*, vol. 12, no. 2, pp. 1337–1347, Apr. 2024.

[70] O. Husev et al., "Comparison of impedance-source networks for two and multilevel buck–boost inverter applications," *IEEE Trans. Power Electron.*, vol. 31, no. 11, pp. 7564–7579, Nov. 2016.

[71] H. Tarzamni, H. S. Gohari, M. Sabahi, and J. Kyyrä, "Non-isolated high step-up DC–DC converters: Comparative review and metrics applicability," *IEEE Trans. Power Electron.*, vol. 39, no. 1, pp. 582–625, Jan. 2024.

[72] B. Andres, L. Romitti, F. H. Dupont, L. Roggia, and L. Schuch, "A high step-up isolated DC–DC converter based on voltage multiplier cell," *Int. J. Circuit Theory Appl.*, vol. 51, no. 2, pp. 557–578, Feb. 2023.

[73] D. Sha, X. Wang, and D. Chen, "High-efficiency current-fed dual active bridge DC–DC converter with ZVS achievement throughout full range of load using optimized switching patterns," *IEEE Trans. Power Electron.*, vol. 33, no. 2, pp. 1347–1357, Feb. 2018.

[74] M. A. Chewale, R. A.Wanjari, V. B.Savakhande, and P. R.Sonawane, "A review on isolated and non-isolated DC-DC converter for PV application," in *Proc. Int. Conf. Control, Power, Commun. Comput. Technol.*, Kannur, India, 2018, pp. 399–404.

SAEED POURJAFAR (Member, IEEE) was born in Ardabil, Iran. He received the B.Sc. degree in electrical engineering from Azerbaijan Shahid Madani University, Tabriz, Iran, in 2015, and the M.Sc. degree in power electronics and drives from the Faculty of Electrical and Computer Engineering, Sahand University of Technology, Tabriz, in 2017, and the Ph.D. degree in power electronics and drives with the Energy Management Research Center, University of Mohaghegh Ardabili, Ardabil, Iran, in 2021. He is currently a Postdoctoral researcher with the Tallinn University of Technology, Tallinn, Estonia, focusing on dc-dc converters and the application of power electronics in renewable systems.

HOSSEIN AFSHARI (Student Member, IEEE) received the master's degree in electrical engineering from the Iran University of Science & Technology, Tehran, Iran. He has worked in the area of Power Electronics especially on Power Electronic Converters, DC-DC converters, as well as switching power supplies and also microconverters. Since May 2022, he has been the researcher with the Tallinn University of Technology, Tallinn, Estonia.

PARHAM MOHSENI (Student Member, IEEE) received the M.Sc. degree in power electronics and electrical machines from the University of Tabriz, Tabriz, Iran, in 2017. He is currently working toward the Ph.D. degree in electrical power engineering and mechatronics with Tallinn University of Technology, Tallinn, Estonia. His research interests include high-step-up power electronic converters, soft-switching circuits, multiple-input/output converters, and onboard chargers.

OLEKSANDR HUSEV (Senior Member, IEEE) received the Ph.D. degree from the Institute of Electrodynamics, National Academy of Science of Ukraine, Kyiv, Ukraine, in 2012. He currently a Senior Researcher and project Leader with the Department of Electrical Power Engineering and Mechatronics, Tallinn University of Technology, Tallinn, Estonia. His research interests include power electronics systems, novel topology design, control systems employing various algorithms, modeling, simulation, and applied power converter.

NOMAN SHABBIR (Senior Member, IEEE) received the B.S. degree in computer engineering from COMSATS University, Lahore, Pakistan, the M.S. degree in electrical engineering from the Blekinge Institute of Technology, Karlskrona, Sweden, and the Ph.D. degree in electrical power engineering and mechatronics from TalTech Estonia, Tallinn, Estonia, in 2022. He is currently a Research Fellow with the FinEST Center for smart cities, Tallinn, Estonia. His research interests include renewable energy systems, energy management, energy flexibility, and AI applications in Energy systems.

OLEKSANDR MATIUSHKIN (Member, IEEE) received the B.Sc. and M.Sc. degrees in industrial electronics from the Chernihiv National University of Technology, Chernihiv, Ukraine, in 2016 and 2018, respectively, and the Ph.D. degree in power electronics from the Tallinn University of Technology, Tallinn, Estonia, in 2022. He is currently a researcher with the Department of Electrical Engineering, Tallinn University of Technology. His research interests include power electronics, new topology design, microcontroller and FPGA programming, modeling, filter calculations, and control techniques for power electronics converters.

PAPER V

O. Matiushkin, O. Husev, **H. Afshari**, E. Romero-Cadaval and C. Roncero-Clemente, "Forward-Based DC-DC Converter With Eliminated Leakage Inductance Problem," in *IEEE Trans. on Ind. Electron*., vol. 72, no. 2, pp. 1638–1648, Feb. 2025, doi: 10.1109/TIE.2024.3429626.

Forward-Based DC-DC Converter With Eliminated Leakage Inductance Problem

Oleksandr Matiushkin [ID], *Member, IEEE*, Oleksandr Husev [ID], *Senior Member, IEEE*, Hossein Afshari [ID], *Student Member, IEEE*, Enrique Romero-Cadaval [ID], *Senior Member, IEEE*, and Carlos Roncero-Clemente [ID], *Senior Member, IEEE*

Abstract—The novel forward-based converter for low-power solar applications is presented in this work. The proposed converter provides an efficient performance in a wide range of the input voltage with low component count. The proposed dc-dc topologies are advanced forward dc-dc converters with an additional clamped output capacitor. The idea of such a type of converter is to transfer magnetizing energy of transformer to the output side, instead of using an input clamp circuit. Two possible topologies are considered to cover this feature. The design guidelines of the passive component of the proposed solutions are discussed. The converter may work in continuous conduction mode and discontinuous conduction mode due to different levels of the input power. A comparison between proposed topologies is made and discussed. Experimental prototype of the proposed forward-based dc-dc converter along with experimental results of the dc grid connection system are presented. The parameters of commercial photovoltaic panels have been chosen to validate the maximum power point tracking based on Perturb and Observe algorithm. The efficiency of the proposed solution is studied and discussed.

Index Terms—Dc-dc, forward dc-dc, microinverter, power electronics.

I. INTRODUCTION

ENVIRONMENTAL pollution and the depletion of natural resources are well-known problems nowadays. The gas and oil are the main energy sources, and their use leads to their complete attrition. On the other hand, the energy demand makes a resource problem worse. Technical progress allows us to change and improve the situation. The solution is new green technologies such as electrical vehicles and safe storage technologies. Solar photovoltaic (PV) power, wind power, and other forms of renewable energy sources (RESs) are possible energy sources to replace gas and oil, as it is cheaper and sustainable. However, a lot of the RES creates additional problems for ac grid lines. Thus, the use of RES with a conventional ac grid seems to be inefficient and not cost effective. Low voltage dc (LVdc) is considered as a more efficient system. The relevance of LVdc distribution system is demonstrated by the dc nature of most RESs, battery energy storage systems, home appliances, and electric vehicles [1], [2]. PV panels, fuel cells, and batteries generate a dc voltage and current [Fig. 1(a)]. Lamps, laptops, phones, TVs, and other residential loads have a dc nature or require a dc voltage [3], [4]. This advantage leads to reduce power electronics stages, higher efficiency, cost reduction, space and weight savings, and flexible placement of electrical equipment [5]. It attracts attention to dc-dc converters as a solution for dc grid integration where cost optimization is the main priority. At the same time, there is no business model for investors because they do not see the available dc grid. Potential investors do not see the sizable market and business cases because of the absence of dc appliances. To eliminate this gap between ac and dc appliances the novel concept of dual-purpose converters (universal converter or dc-ready solution) is proposed, which could simplify transition from ac to dc grids, giving flexibility to the LVdc grid investors and dc customers [6], [7]. Such a converter with universal capability can be connected to both types of grids by the same terminals.

The most common solution for isolated dc-dc converter is a flyback dc-dc converter [8], [9]. The flyback dc-dc converter has a simple structure, a small number of components, and wide industry use [Fig. 1(b)]. Advanced or integrated flyback topologies are proposed with improved features and capability [10], [11], [12], [13].

A hybrid boost-flyback/flyback converter [14] includes the diode to transfer magnetizing energy of primary side to the output. Such a type of converter can generate the output voltage less than the input voltage. Another conventional solution is a
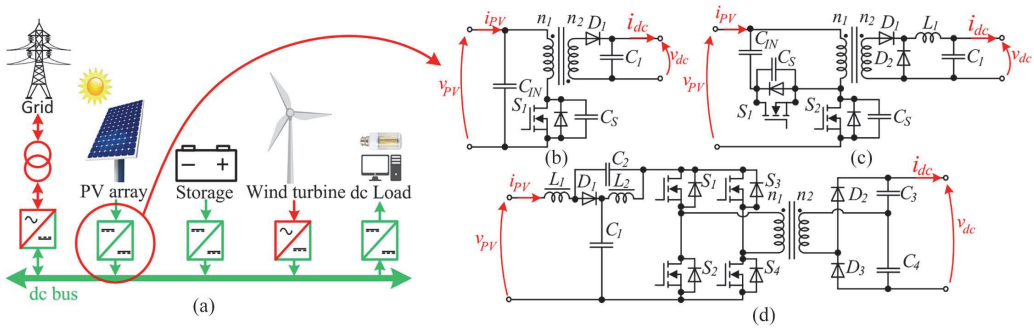
Fig. 1. (a) LVdc distribution system, possible isolated dc-dc topologies for PV converter. (b) Flyback dc-dc converter. (c) Forward dc-dc converter, and (d) QZS dc-dc converter.

forward dc-dc converter [15], which has an additional buck cell and a clamp circuit, as is shown in Fig. 1(c).

Instead of input clamp circuit, it is possible to transfer energy to another output, as it is shown in [17], [18]. This type of converter also has a boost solution with the same approach as a flyback case, as it was presented in [16]. Two works [19], [20] discuss families of forward-based dc-dc converters. Logically, interesting solutions are hybrid forward-flyback converters [21], [22], [23], [24] which combine two simple solutions and provide zero-voltage-switching performance with small input current ripple. The idea of the hybrid topology is to use a flyback cell instead of input clamp circuit of the forward converter, which allows to give energy to the output instead of saving in the input capacitor. Coupled inductor-based topology is a possible solution for PV applications. An overview of the dc-dc converters with a coupled inductors is discussed in [25]. Article [26] and [27] consider topologies with a charge pump and couple inductors. A charge pump is a function that can be implemented by adding a capacitor between primary and secondary sides of the transformer or couple of inductors. The charge pump capacitor saves energy from one winding and gives a charge to another winding. The quasi-Z-source converter [Fig. 1(d)] is one of the possible solutions for PV applications due to continuous input current [28]. The review article [29] considers different qZS-based galvanically isolated dc–dc converters. These converters are intended for applications with widely varying input voltage and stabilized output voltage. Comparative review of the different topologies and commercial solutions are investigated in [30], [31].

This article describes a novel nonisolated common-grounded forward-based dc–dc converter with a wide range of input voltage regulation. The initial idea is shown in [32]. Section II explains the details of the case study system: leakage inductance problem, operational modes, and calculation of the passive components. Comparative analysis of the proposed topologies is discussed in Section III and Section IV. Section V discusses the control system algorithm and Section VI shows the experimental results along with an efficiency study.

II. PROPOSED SOLUTIONS

The proposed dc-dc topologies are presented in Fig. 2. As isolation is not required in PV systems, it has direct ground
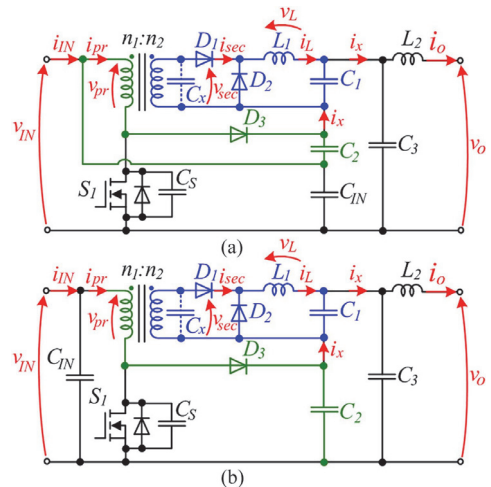
Fig. 2. Proposed forward-based dc-dc converter as a solution for solar application. (a) With 4 capacitors at the output side. (b) With 3 capacitors at the output side.

connection between the input and the output sides. So, proposed converters are common-grounded solutions, that do not have leakage current problem. Proposed solutions are forward based dc-dc topologies with the absence of an input clamping circuit. In contrast to the conventional forward dc-dc converter, an additional diode D_3 transfers magnetizing energy to the output side. Background of this idea is disclosed in [33]. The forward-based dc-dc converter is similar to a boost flyback converter, but it contains a forward dc-dc circuit. Considering the number of components, each proposed topology has four capacitors, two inductors, three diodes, a switch, and a step-up transformer. Inductor L_2 is considered as a filter for the output current. Proposed topologies can be connected to a single PV panel and fitted with dc grid. Each proposed converter has only one switch, which makes the control system easier, cheaper and simplifies auxiliary circuits. This section focuses on analytical analysis of the topology in Fig. 2(a). The same calculation approach was applied for the second topology [Fig. 2(b)].
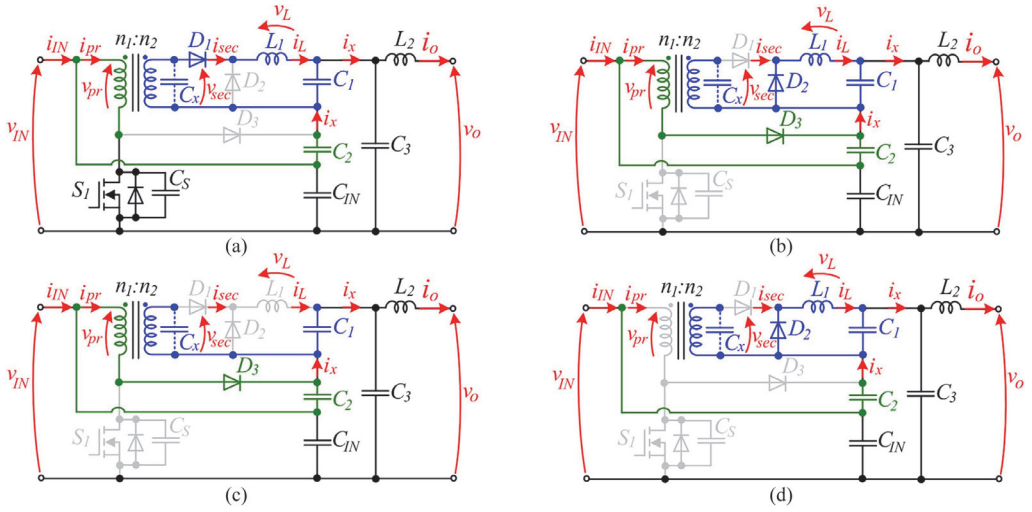
Fig. 3.   Equivalent circuits of the proposed forward-based dc-dc converter. (a) Active state. (b) Zero state. (c) DCM of inductor current. (d) DCM of the primary current.

A. Operational Modes of the Proposed Topology in Fig. 2(a)

The operational principle of the converter can be divided into several modes. The first mode corresponds to the linear continuous conduction mode (CCM). The CCM mode is accompanied by continuous currents of the inductors. Other modes are related to the discontinuous conduction mode (DCM) of the magnetizing inductor and the forward cell inductor L_1. The analysis of the operational modes is obtained by using the steady state analysis (SSA) [34]. The equivalent circuits of the proposed forward-based dc-dc converter are shown in Fig. 3. When the switch S_1 is turned ON the transformer gives energy to the forward cell and the magnetizing inductor starts to keep energy [Fig. 3(a)]. Diode D_1 also starts to conduct, but D_2 and D_3 are OFF. Capacitor C_1 is charging while capacitor C_2 is discharging. When switch S_1 is turning OFF, the current of the magnetizing inductor should flow with some path, therefore diode D_3 starts to conduct.

The forward-based converter goes to a zero state. The diode D_2 is conducting in the zero state, while D_1 is OFF. The capacitor C_1 is discharging and C_2 reversely is charging by the magnetizing current. It is possible to express the output voltage of the proposed solution by analyzing active and zero states and writing Kirchhoff equations. The average value of the output voltage depends on a transformer turns ratio, duty cycle, and the input voltage

$$V_O = \frac{v_{IN} \cdot (1 + N \cdot D \cdot (1 - D))}{1 - D} \tag{1}$$

where v_{IN} is the input voltage, N is the step-up ratio of the transformer (n_2/n_1), and D is the value of the duty cycle.

The average value of current of the inductor L_1 is an average value of the output current. The magnetizing current I_M can be derived considering the input and the output current values

$$I_{L1} = I_O, I_M = \frac{I_{IN} - I_O}{D} - N \cdot I_O \tag{2}$$

where I_O is the average output current and I_{IN} is the average value of the input current.

The output voltage consists of voltages across capacitor C_1, C_2 and the input voltage value. The SSA result showed that the average values of the capacitor voltages are different and depends on the input voltage, duty cycle and turns ratio of transformer

$$V_{C1} = V_{IN} \cdot N \cdot D, \quad V_{C2} = \frac{V_{IN} \cdot D}{1 - D}. \tag{3}$$

A value of the semiconductors stresses allows to choose transistor and diodes with necessary breakdown voltages. The semiconductors stresses are given in (4). However, the ripples of the capacitor voltages were not taken into account

$$V_{S1} = V_{D3} = V_{IN} + V_{C2}, \quad V_{D1} = V_{C2} \cdot N, \quad V_{D2} = V_{IN} \cdot N. \tag{4}$$

B. Selection of the Passive Components

The design of the passive components is a significant part of developing any power electronics converter. Choosing filters capacitors and inductance affects the stability and reliability of the converter. This section describes design guidelines for proposed forward-based dc-dc converter.

As the proposed dc-dc converter is transformer-based topology, the calculation may start from determining the magnetizing inductor. The value of the inductance depends on the transformer parameters: number of windings, absolute permeability, and core material parameters; the ripple of magnetizing inductor current can be determined using the T_{ON} interval and it depends on the input voltage, duty cycle, period, and the magnetizing inductance

$$L_M = \frac{\mu_{ef} \cdot \mu_0 \cdot n_1^2 \cdot A_{ef}}{L_{ef}}, \quad di_{L_M} = \frac{V_{IN}}{L_M} \cdot D \cdot T \tag{5}$$

where μ_{ef} is an effective relative permeability of the material, μ_0 is an absolute permeability of air or vacuum, n_1 is the winding

turns number of the primary side of the transformer, A_{ef} is an effective cross-section area of the magnetic core, L_{ef} is effective magnetic path length, T is a period of switching.

A nominal value of the forward inductance is possible to get considering time duration from 0 to DT, which corresponds to an active state. The choice of the inductor also depends on the mode in which the proposed converter should work. The inductance expression is shown as follows:

$$L_1 = \frac{V_{IN} \cdot N - V_{C1}}{di_{L1}} \cdot D \cdot T \qquad (6)$$

where di_{L1} is the current ripple in the forward cell inductor.

The capacitor definition is a more complicated process because of their connection to each other. It is possible to see from equivalent circuits, that the capacitors ripples depend on the current i_x [Fig. 3(a)] and on the output current

$$C_1 = \frac{I_O - i_x}{dv_{C1}} \cdot D \cdot T, \ \ C_3 = \frac{i_x - I_O}{dv_{C3}} \cdot D \cdot T, \ \ C_2 = \frac{-i_x}{dv_{C2}} \cdot D \cdot T. \qquad (7)$$

By solving (7) as a system of equations, it is possible to receive expressions of the capacitors depending on the voltage ripples of each capacitor. The capacitor C_2 could be zero or whatever value and capacitors C_1 and C_3 depend on C_2. The ripple of capacitor voltage C_2 always equals the sum of ripples of other capacitors

$$dv_{C2} = dv_{C1} + dv_O, \ \ K_{C1} = \frac{dv_{C1}}{V_{C1}}, \ \ K_O = \frac{dv_O}{V_O} \qquad (8)$$

where dv_{C1}, dv_{C2}, and dv_O are the ripples of the capacitors C_1, C_2, C_3 correspondingly. K_{C1} and K_O are ripple factors.

Another possible way to calculate capacitors values is converting triangle connection of C_1, C_2, C_3 to the star connection. The results of calculation should be reconverted back to triangle view, and after it is possible to obtain required capacitor values. The capacitor expressions are shown as follows:

$$C_1 = \frac{I_O \cdot D \cdot T + dv_{C1} C_2}{dv_{C1}}, \ \ C_3 = \frac{I_O \cdot D \cdot T - dv_{C1} C_2}{dv_O}, \ \ C_2 \in \forall. \qquad (9)$$

The output inductance is filtering the output current. The inductance proportional depends on the voltage ripple of the capacitor C_3. The obtained expression of the output inductance looks like as following:

$$\int_{DT/2}^{(1+D)T/2} v_{L2} \cdot dt = \int_{DT/2}^{(1+D)T/2} (v_{C3} - V_O) \cdot dt, \ \ L_2 = \frac{dv_O \cdot T}{8 \cdot di_O} \qquad (10)$$

where v_{L2} is a voltage across inductor L_2, v_{C3} is the voltage on the capacitor C_3 with ripples, di_O is the output current ripple.

C. Leakage Inductance Problem

The advantages of a forward dc-dc converter are a single switch solution, low cost, and high efficiency [35]. Despite the popularity of forward dc-dc converter, it has a significant disadvantage. it requires a core "reset" of the transformer. When the
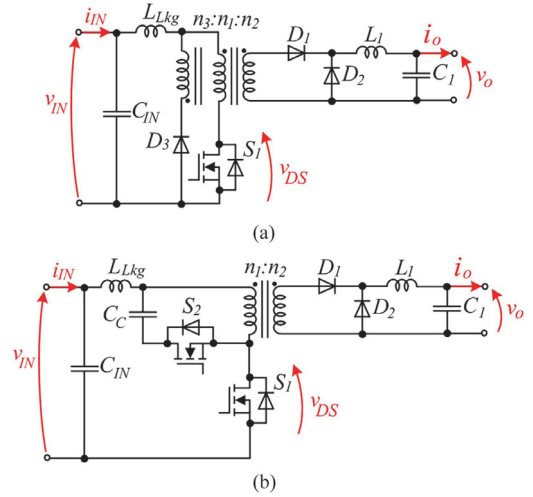
Fig. 4. Forward dc-dc converter. (a) Third winding. (b) Active clamp circuit.

switch is turning OFF, the storage energy in the transformer should be transferred somewhere, otherwise it causes a big voltage spike on the switch. On the other hand, if consider the parasitic parameters of the transformer, such as leakage inductance, the nonlinear processes appear during the operation of the converter. The stored energy in the leakage inductance is not recovered during OFF state of the switch. As a result, the drain-source voltage has a spike and high-frequency oscillation. Therefore, the switch with a higher drain-source breakdown voltage should be taken to reduce the risk of high-voltage spike.

One of the possible solutions for the core "reset" is tree winding transformer. The third winding can be added to fully reset the flux by the end of each switching cycle to prevent core saturation [Fig. 4(a)]. Other solutions exist to solve a spike problem across the switch, such as: adding an active clamp circuit [Fig. 4(b)]or another type of clamp circuit and using zero voltage switching.

However, article [36] showed the influence of the leakage inductance on the duty cycle. The duty cycle should be increased to reach the same output voltage with higher leakage inductance of the transformer. If the duty cycle reached maximum value, it means that the winding ratio of the transformer should be increased. All these issues should be considered for the transformer design along with ranges of the input voltage and the input power.

The proposed forward-based dc-dc topologies solve the "reset" core problem of the transformer. Instead of circulating the leakage inductance current in the primary side of the transformer, it flows to the output capacitor cascade and to the output through the diode D_3.

III. Comparison of the Proposed Topologies

The difference between proposed topologies in Fig. 2 is placement of the capacitor C_2. Based on the (9) the capacitor C_2

Fig. 5. Total capacitor energy of the two proposed topologies with different values of C_2 and versus the input voltage.

can be a zero as well, thus the topology in Fig. 2(a) can be transformed into the topology in Fig. 2(b).

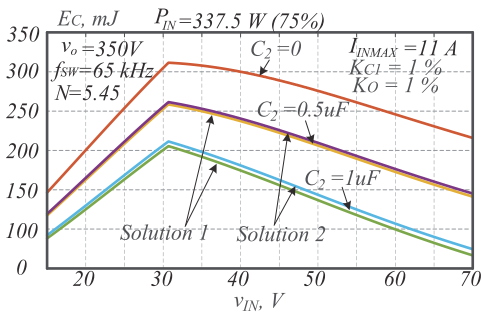However, the existence of capacitor C_2 allows to decrease other capacitors and as result decreases their cost and sizes. The capacitor C_2 helps to generate the input voltage on the output at the beginning [see topology in Fig. 2(a)], which speeds up the transient process on the output side. The voltage across capacitor C_2 is lower in the first topology due to additional connection with the input source. The comparison between two topologies was done using several criteria: overall capacitor energy (E_C), overall inductance energy (E_L), and semiconductor stresses (V_{STR}), and the conduction losses (P_{CL})

$$E_C = \sum_{j=1}^{3} \frac{C_j \cdot V_j^2}{2}, \quad E_L = \sum_{j=1}^{3} \frac{L_j \cdot I_j^2}{2}, \quad V_{STR} = V_{S1} + \sum_{j=1}^{3} V_{Dj}.$$
(11)

Fig. 5 shows the total energy of the capacitor with the same predefined ripple factors for both solutions. The input capacitor was neglected. These results showed that with increasing of capacitance C_2, the total energy of capacitors will be decreased. Due to lower voltage across capacitor C_2 the solution 1 [Fig. 2(a)] has lower capacitor energy. All other results of criteria are same in both cases, that is why only the first solution is considered for the further experimental validation.

IV. COMPARISON WITH CONVENTIONAL SOLUTION

The steady state analysis was applied for the flyback dc-dc converter [Fig. 1(b)]. The ripples of the passive components were chosen equaled for both cases. In the case of transformer design, the deviation and maximum value of the flux density should be the same. The turn ratio is chosen similarly to show the difference in the topology at the same parameters of the transformer. Table I contains expressions for both converters (passive elements, magnetizing current, and voltage stresses of the semiconductors). The comparison was done using four criteria. The criteria are the same as was mentioned in Chapter III. The first two criteria consider the total energy of the inductances and the total energy of capacitances. The third criterion is total conduction loss, and the last criterion is total semiconductor stress. The efficiency of the converters depends on the transistor

and diode models, that is why the values of the parameters of the semiconductors are chosen equally for both cases.

Fig. 6 depicts the comparison spider charts for both topologies under different input voltages and power. All the data is normalized for better presentation. The red areas of the diagrams correspond to the forward-based dc-dc converter, and the blue areas are related to the flyback dc-dc converter. Fig. 6(a) shows the comparison results in a case of 15 V of the input voltage and 10 A of the input current. The forward-based dc-dc converter is worth in this case, because of the higher semiconductor stress. All other criteria are approximately the same in this case. The situation is different in the case of 40 and 70 V of the input voltage [Fig. 6(b) and 6(c)]. The forward-based dc-dc converter has higher voltage stress on the semiconductors, but the total inductance energy is higher in the case of flyback dc-dc converter. It is due to the high magnetizing current of the flyback topology. As a result, the red and blue areas are the same in the second and third cases.

As the results, the proposed dc-dc converter has the next advantages:
1) The converter is a nonisolated common grounded solution, that leads to reduced cost and an elimination of the leakage current between grounds.
2) Despite a bigger number of semiconductors, it has only one active switch and the total conduction losses are the same as a conventional solution.
3) The total energy of the inductances is less than in conventional flyback solution.
4) Despite the additional capacitor cascade on the output side, the total energy of the capacitance is same as the conventional flyback solution.

The main disadvantage of the proposed dc-dc topology is high voltage stress on the switch and diodes

V. CONTROL SYSTEM DESCRIPTION

The simplified structure of the closed-loop system is shown in Fig. 6. The system consists of maximum power point tracking (MPPT) block and pulse-width modulation (PWM) block. The secondary side of transformer contains filters and diodes, that is why proposed converter can work only in unidirectional mode. The converter has an additional solid-state relay to avoid current spike during connecting to the dc grid. Dc-breaker is controlled separately by the microcontroller. The control system also contains software protection functions, which check all the measured values according to predefined limitations. If some of the measured parameters go over the limitation the converter stops to avoid faults and damage of the semiconductors and other components.

Perturb and Observe (P&O) method is selected as MPPT technique with a sample frequency 3.25 kHz. The MPPT block calculates changes in the input voltage and power. There are four zones depending on the incremental voltage and power. Zone 1 corresponds to the mode when the input power is increasing, and the input voltage is decreasing. The MPPT increases the duty cycle value in this case. When the input power and voltage are changing negatively the system identifies

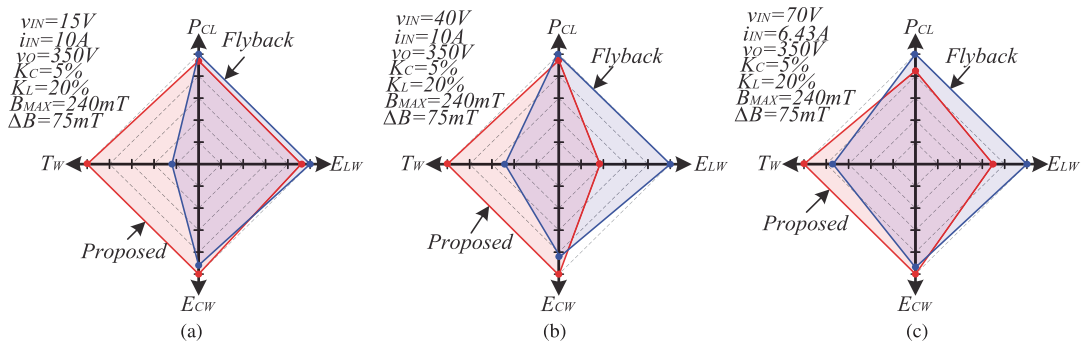| Parameter	Flyback dc-dc Converter	Proposed Forward-Based dc-dc Converter
Gain, $G = V_O/V_{IN}$	$N \cdot D/(1-D)$	$(1 + N \cdot D \cdot (1-D))/(1-D)$
Duty cycle, D	$V_O/(V_O + N \cdot V_{IN})$	$(N \cdot V_{IN} + V_O + \sqrt{4 \cdot N \cdot V_{IN}^2 + (N \cdot V_{IN} - V_O)^2})/(2 \cdot N \cdot V_{IN})$
Average magnetizing current, I_M	I_{IN}/D	$(I_{IN} - I_O(1 + N \cdot D))/D$
Capacitor, C_O	$I_O \cdot D \cdot T/(K_O \cdot V_O)$	$(I_O \cdot D \cdot T - (K_{C1} \cdot V_{C1} + K_O \cdot V_O) \cdot C_2)/(K_O \cdot V_O)$
Capacitor, C_1	$-$	$(I_O \cdot D \cdot T - (K_{C1} \cdot V_{C1} + K_O \cdot V_O) \cdot C_2)/(K_{C1} \cdot V_{C1})$
Inductance, L_1	$-$	$N \cdot V_{IN} \cdot (1-D) \cdot D \cdot T/(1-D)$
Inductance, L_M	$\mu_{ef} \cdot \mu_0 \cdot (V_{IN} \cdot D \cdot T)_{MAX}^2/(L_{ef} \cdot A_{ef} \cdot 4 \cdot \Delta B^2)$	
Voltage stress across switch S_1, v_{S1}	$(v_{IN} \cdot N + v_O)/N$	$v_{IN}/(1-D)$
Voltage stress across diode D_1, v_{D1}	$v_O + v_{IN} \cdot N$	$(v_{IN} \cdot N \cdot D)/(1-D)$
Voltage stress across diode D_2, v_{D2}	$-$	$v_{IN} \cdot N$
Voltage stress across diode D_3, v_{D3}	$-$	$v_{IN}/(1-D)$

Fig. 6. Spider charts for the comparison between flyback dc-dc converter and proposed forward-based dc-dc converter. (a) Input voltage is 15 V and input current is 10 A. (b) Input voltage is 40 V and input current is 10 A. (c) Input voltage is 70 V and input current is 6.43 A.
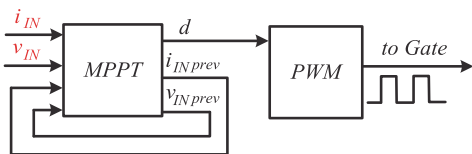
Fig. 7. Structure of the grid connected closed-loop control system.

it as a zone 2 and starts to decrease the duty cycle. Zone 3 corresponds to a case when the input power is decreasing, but input voltage is increasing. The duty cycle is increasing in this case. The last zone 4 relates to the mode when the input power and voltage are increasing. The MPPT block reduces the duty cycle value. As a result, the MPPT block acts as a main regulator in the closed-loop system and changes directly to the duty cycle without an intermediary stage.

VI. EXPERIMENTAL VERIFICATION

Fig. 7 shows the experimental prototype for proposed nonisolated common-grounded forward-based dc-dc converter. The volume of the experimental prototype is 157 mm × 112 mm × 47 mm. The proposed converter consists of auxiliary, power, control parts, dc breaker, electromagnetic interference (EMI) filter, additional output filter, Wi-Fi module, and hardware protection: fuse and varistor. Main parameters of experimental prototype are listed in Table II: values of passive components, electrical specifications of prototype and transformer parameters. The power part was designed according to the topology in Fig. 2(a). Input capacitance consists of a set of electrolytic capacitors, and all together equals 110 uF. All passive components were chosen according to the calculations in Section II. The control unit of the experimental prototype is ST microcontroller STM32H503CBT6, which is cheap and has enough advanced timers and ADC channels to satisfy current requirements of the converter. The input voltage range of the experimental prototype lies in a range from 15 V up to 70 V. The maximum input current is 11 A. The maximum output current is 1.3 A.

The maximum input power is 450 W and it is limited by input current as well. Fig. 8 shows a workplace where the setup was assembled and tested. The oscilloscope Tektronix MDO4034B-3 works with a high frequency and catches accurate power signals. The isolated voltage and current probes were used to measure important signals of the prototype. STLink is an intermediary device between MCU and laptop. It helps to debug program and detect problems if they occur.

<div style="text-align: center">

TABLE II
PARAMETERS OF PROPOSED CONVERTER

</div>

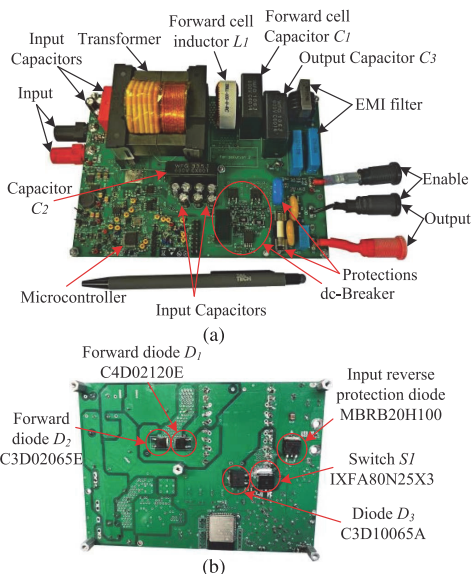| Parameter	Value
Input voltage range v_{IN}	15-70 V
Output voltage vo	350 V
Max input power P_{INMAX}	450 W
Max input current i_{INMAX}	11 A
Max output current i_{OMAX}	1.3 A
Switching frequency f_{SW}	65 kHz
Input capacitor C_{IN}	110 uF
Forward cell capacitor C_1	10 uF
Clamp capacitor C_2	3.3 uF
Output capacitor C_3	10 uF
Secondary side capacitor Cx	2.5 nF
Forward cell inductor L_1	1000 uH
Output inductor L_2	100 uH
Transformer core	ETD49
Core Material Grade	3C95
Magnetizing inductor (pr) L_m	212 uH
Leakage inductance of transformer (pr) L_k	27 uH
Number of turns (pr) n_1	18
Number of turns (sec) n_2	98
Core airgap	400 um

Fig. 8. Experimental prototype of the proposed forward-based dc-dc converter. (a) Top view. (b) Bottom view.

The core of the transformer is ETD49-3C95. The number of turns of the primary winding is 18 with a litzwire is 0.04 mm × 2000. The secondary winding turns are 98 and the litzwire is 0.1 mm × 45. The primary and secondary turns are wounded without layers overlapping to avoid parasitic capacitor between windings. Although the leakage inductance is increased, it does not significantly affect the semiconductor's stresses. The value of the magnetizing inductor at primary side is 212 uH, and at the secondary side is 6.36 mH.

Table III contains possible semiconductors parameters for the proposed converter. Several sets of semiconductors were selected for the experimental prototype. The cheapest

<div style="text-align: center">

TABLE III
POSSIBLE SEMICONDUCTORS FOR PROPOSED SOLUTION

</div>

Transistor/ Diode Model	Designator	I, A	V_{BR}, V	R_{ON} or V_F	Price, €	Eff., %
IXFA80N25X3	S_1	80	250	16	8.98	95.65
IXFT120N25X3	S_1	120	250	12	13.21	↑ 0.1
IXFT150N25X3	S_1	150	250	9.0	24.3	↑ 0.16
UJ3C065030B3	S_1	65	650	35	17.42	↑ 0.22
IDM02G120C5	D_1, D_2	14	1200	1.65	2.63	95.65
C4D02120E	D_1, D_2	10	1200	1.8	3.03	↓ 0.05
SBR20A300	D_3	20	300	0.92	1.66	95.65
C3D10065E	D_3	32	650	1.8	6.05	↓ 0.3
IPD95R450P7	dc-br.	14	950	0.45	2.27	95.65
IPD80R280P7	dc-br.	17	800	0.28	2.64	↑ 0.05
IPB95R130PFD7	dc-br.	36.5	950	0.13	6.10	↑ 0.1

Fig. 9. Experimental setup of the proposed dc-dc converter.

semiconductors were chosen in the first case. Si type transistor IXFA80N25X3 has 16 mOhms of drain-source resistor during conducting state and it is suitable for the switch S_1. The drain-source breakdown voltage of that transistor is 250 V. SiC Schottky diode IDM02G120C5 is a cheap option for diodes D_1 and D_2. Diode model SBR20A300 was chosen for the diode D_3. The dc-breaker is a four-quadrant switch where two transistors are connected in series. MOSFET IPD95R450P7 is cheap and satisfies the requirements for the dc-breaker. However, to increase efficiency the semiconductor with better characteristics but with a higher price can be selected. The column "Eff., %" in Table II contains efficiency measurement results with different semiconductors. The results showed how each semiconductor affects efficiency in comparison to cheaper semiconductor sets. The input voltage was 70 V, and the input current was 6 A.

In the second case, the semiconductors were chosen according to the following set: S_1-IXFT150N25X3HV, D_1, D_2-IDM02G120C5, D_3-SBR20A300, dc-breaker-IPB95R130PFD7 (two transistors).

Table IV contains commercial solar panels that were considered for the experimental validation of the proposed forward-based dc-dc converter. The solar panels have different voltages and currents, and they were selected to demonstrate a wide

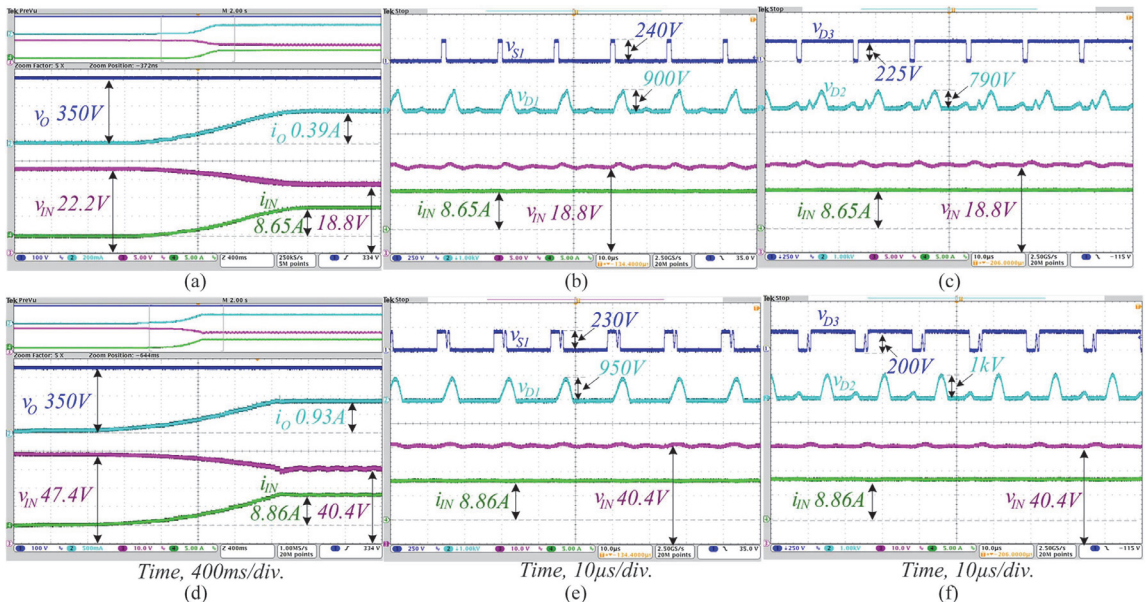| Solar Panel	Power, W	V_{OC}, V	V_{MPP}, V	I_{SC}, A	I_{MPP}, A	MPPT Efficiency Case 1, %	Converter Efficiency Case 1, %	Total Efficiency Case 1, %	MPPT Efficiency Case 2, %	Converter Efficiency Case 2, %	Total Efficiency Case 2, %
ED90-6P	90	22.6	17.8	5.36	5.06	99.84	90.24	90.1	99.84	90.17	90.03
ED160-6M	160	22.2	18.2	9.32	8.79	99.93	90.83	90.77	99.93	91.1	91.04
355R-AC	355	47.4	39.1	9.53	9.09	99.95	93.81	93.76	99.95	94.16	94.11
SPR-X22-370	370	69.5	59.1	6.66	6.26	99.48	93.96	94.47	99.48	95.05	94.55

Fig. 10. Experimental results of the proposed converter with different PV panels. PV and grid currents and voltages for. (a) Solar panel ED160-6M. (d) Solar panel 355R-AC, PV current and voltage and voltage stresses on switch S_1 and diode D_1. (b) Solar panel ED160-6M. (e) Solar panel 355R-AC; PV current and voltage and voltages across diodes D_2 and D_3. (c) Solar panel ED160-6M. (f) Solar panel 355R-AC.

voltage and power range of operation of the proposed converter. A programmable PV simulator Keysight E4360A emulates parameters of a real PV panel and acts as an input source for the proposed converter. The bidirectional power supply Itech IT6006-800-25 is used as an emulated grid side, where the voltage is 350 V. All the efficiency measurements were done by using precision power analyzer Yokogawa WT1800. Fig. 9 shows the experimental results of the proposed converter for a single panel ED160-6M and 355R-AC. ED160-6M panel has the MPP current is 8.79 A and the MPP voltage is 18.2 V. However, if set datasheet specifications for power supply, the PV simulator changes a little bit those parameters ($V_{MPP} = 18.6$ V, $I_{MPP} = 8.659$ A, $P_{MPP} = 161.06$ W). As a result, the MPPT algorithm has found the MPP current is 8.672 A and a MPP voltage is 18.56 V ($\varepsilon_{MPPT} = 99.93\%$). The total efficiency is 90.83% with cheap semiconductors set. The MPPT algorithm takes 1.8 s to find the MPP [Fig. 9(a)]. The semiconductors voltage stresses are shown in Fig. 9(b) and 9(c). The diodes D_1 and D_2 have high voltage stresses due to the transformer turns ratio and a fading-resonance process between primary

magnetizing inductor and parasitic capacitors. Additional capacitor C_x (Fig. 2) on the secondary side can decrease diodes voltage stress, but at the same time, it can increase voltage stress on the main switch and diode D_3. C_x value equaled 2.5 nF during the experimental tests.

The experimental results for the PV panel 355R-AC are shown in Fig. 9(d)–9(f). The PV simulator redefines real parameters as follows: $V_{MPP} = 40.034$, $I_{MPP} = 8.961$ A, $P_{MPP} = 358.75$ W. The control found a power point: $V_{MPP} = 39.94$, $I_{MPP} = 8.98$ A. The efficiency of MPPT is 99.95% and the total efficiency is 93.76% with cheap semiconductors. However, the total efficiency was increased in the second case by using an expensive set of semiconductors. Table II contains the total efficiency values for the second case. Despite the significant difference in price efficiency was increased by 0.35%, because the transistors have the same dynamic characteristics. It is more important for the proposed converter. According to the theoretical study, the diode D1 voltage stress reaches 1.4 kV at the high boost point. However, the experimental results showed another situation. The maximum voltage stress that was measured is 1.19 kV.
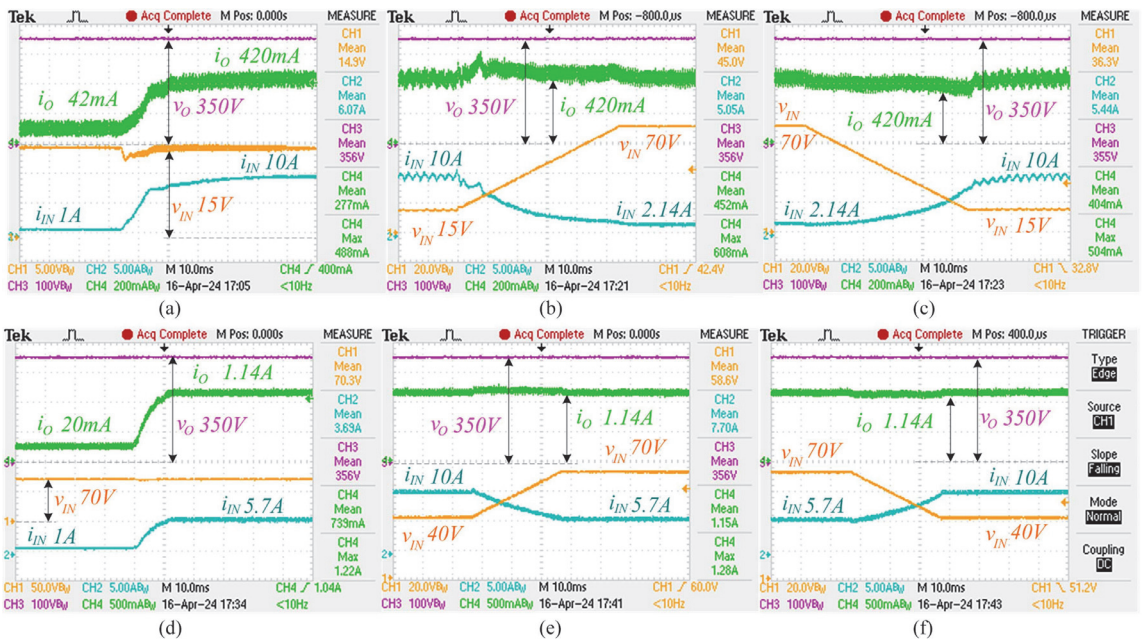
Fig. 11. Experimental results of the proposed dc-dc converter under different input voltage and current various. (a) Step change of the output current when the input voltage is 15 V. (b) Step change of the input voltage from 15 to 70 V. (c) Step change of the input voltage from 70 to 15 V. (d) Step change of the output current when the input voltage is 70 V. (e) Step change of the input voltage from 40 to 70 V. (f) Step change of the input voltage from 70 to 40 V.
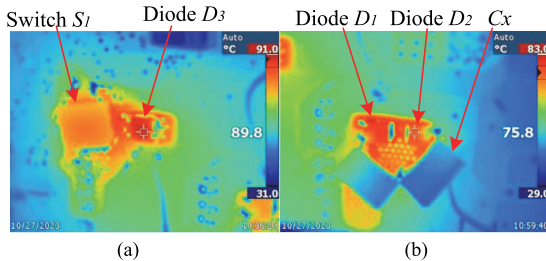

Fig. 12. Thermal pictures of the semiconductors using parameters of solar panel 355R-AC. (a) Switch S_1 and diode D_3. (b) Diodes D_1 and D_2.

The experimental results prove that the spike problem across the semiconductor does not exist for the proposed forward-based dc-dc converter. Fig. 10(d)–10(f) shows the experimental results in a case of 70 V of the input voltage. As a result, it can be claimed that the leakage inductance problem is solved in the proposed converter.

Regarding rapid change of the input or the output: usually they change quite slowly. The PV voltage and current can change in a case of shadowing, high temperature or low solar irradiance. Rapid load or voltage change can be seen during line interruption or short circuit faults. The control system has software and hardware protection: limitation of currents and voltages, reverse protected diode on the PV side, fuse and varistor, and dc-breaker. In a case of fault, the protection

system will stop the generating of the duty cycle, and the converter will be stopped.

As a result, the proposed converter was tested under the voltage and load step changes. The step of voltage and current were done by the dc power supply and the control system correspondently. Fig. 11 shows the experimental results under load and voltage step changes. Fig. 11(a) depicts the output current step change from 42 to 420 mA, when the input voltage is 15 V. As the input voltage is constant 15V the input current is also changing by step (1 A->10 A). Fig. 11(b) and 11(c) shows the input voltage step change from 15 to 70 V and vice versa. The output current is constant 420 mA. The output dc voltage is 350 V. Fig. 11(d)–11(f) shows experimental results when the input voltage is 70 V.

Fig. 12 shows thermal pictures of the semiconductors in a case of PV panel 355R-AC. The thermal picture was obtained by using the thermal camera Fluke Ti10. The switch and the diodes D_1, D_2 temperatures were around 80 degrees Celsius. The experimental results for the other 2 PV panels are not shown, but the efficiency value is collected in Table III.

Fig. 13 contains the efficiency curve versus the input current and under different variations of the input voltage. The efficiency of the dc-dc converter is lower under lower input voltages, because of the high input current and big duty cycle. The maximum point of efficiency in a case of 15 V is 90.55%. However, the efficiency increases as the input voltage increases. In the maximum point of the input voltage 70 V the efficiency reaches 95.85%. The auxiliary losses are included.
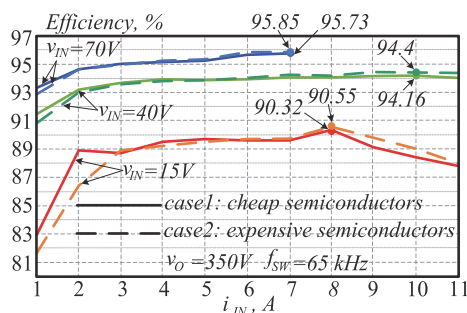
Fig. 13. Efficiency study versus input current under different input voltages and with different sets of semiconductors.

VII. CONCLUSION

Two topologies of a nonisolated common-grounded forward-based dc-dc converter were presented in this article. Design guidelines of the passive components were deeply investigated and presented in CCM. The second topology has a bigger capacitor energy, due to the higher voltage on capacitor C_2. The transformer turns ratio was chosen as a 5.8 to reach 350 V on the output side. The closed loop system with a grid connection is considered. The experimental prototype is presented with MPPT tests and an efficiency study. The proposed solution works in a wide range of input voltage with efficiency. The maximum achieved value of efficiency is 95.85% with higher prices semiconductors and 95.73% with cheap semiconductors. The proposed novel forward-based dc-dc converter can be considered a cost-effective solution and is recommended for industrial application.

REFERENCES

[1] L. Mackay, N. H. van der Blij, L. Ramirez-Elizondo, and P. Bauer, "Toward the universal DC distribution system," *Elect. Power Compon. Syst.*, vol. 45, no. 10, pp. 1032–1042, Jul. 2017.

[2] V. Fernão Pires, A. Cordeiro, C. Roncero-Clemente, S. Rivera, and T. Dragičević, "DC-DC converters for bipolar microgrid voltage balancing: A comprehensive review of architectures and topologies," *IEEE J. Emerg. Sel. Topics Power Electron.*, vol. 11, no. 2, pp. 981–998, Feb. 2023.

[3] T. Dragicevic, X. Lu, J. C. Vasquez, and J. M. Guerrero, "DC microgrids part I: A review of control strategies and stabilization techniques," *IEEE Trans. Power Electron.*, vol. 31, no. 7, pp. 4876–4891, Jul. 2016.

[4] T. Dragicevic, X. Lu, J. C. Vasquez, and J. M. Guerrero, "DC microgrids part II: A review of power architectures, applications, and standardization issues," *IEEE Trans. Power Electron.*, vol. 31, no. 5, pp. 3528–3549, May 2016.

[5] J. Arrillaga, Y. H. Liu, and N. R. Watson, *Flexible Power Transmission. The HVDC Options*, Hoboken, NJ, USA: Wiley, 2007.

[6] O. Husev, O. Matiushkin, D. Vinnikov, C. Roncero-Clemente, and S. Kouro, "Novel concept of solar converter with universal applicability for DC and AC microgrids," *IEEE Trans. Ind. Electron.*, vol. 69, no. 5, pp. 4329–4341, May 2022.

[7] O. Husev, D. Vinnikov, S. Kouro, F. Blaabjerg, and C. Roncero-Clemente, "Dual-purpose converters for dc or ac grid as energy transition solution: perspectives and challenges," *IEEE Ind. Electron. Mag.*, vol. 18, no. 1, pp. 46–57, Mar. 2024.

[8] R. Erickson, M. Madigan, and S. Singer, "Design of a simple high-power-factor rectifier based on the flyback converter," in *Proc. IEEE Fifth Annu. Proc. Appl. Power Electron. Conf. Expo. (APEC)*, Los Angeles, CA, USA: IEEE, Mar. 1990, pp. 792–801.

[9] B. Tamyurek and B. Kirimer, "An interleaved high-power flyback inverter for photovoltaic applications," *IEEE Trans. Power Electron.*, vol. 30, no. 6, pp. 3228–3241, Jun. 2015.

[10] T.-J. Liang, S.-M. Chen, L.-S. Yang, J.-F. Chen, and A. Ioinovici, "A single switch boost-flyback DC-DC converter integrated with switched-capacitor cell," in *Proc. IEEE 8th Int. Conf. Power Electron. (ECCE)*, Jeju, Korea (South), 2011, pp. 2782–2787.

[11] G. Spiazzi, P. Mattavelli, and A. Costabeber, "Effect of parasitic components in the integrated boost-flyback high step-up converter," in *Proc. IEEE 35th Annu. Conf. IEEE Ind. Electron.*, Porto, Portugal, 2009, pp. 420–425.

[12] G. Spiazzi, P. Mattavelli, J. R. Gazoli, R. Magalhaes, and G. Frattini, "Improved integrated boost-flyback high step-up converter," in *Proc. IEEE Int. Conf. Ind. Technol.*, Via del Mar, Chile, 2010, pp. 1169–1174.

[13] K. Luewisuthichat, P. Boonpraser, T. C. Ekkaravarodome, and A. Bilsalam, "Analysis and implement DC-DC integrated boost-flyback converter with LED street light stand-by application," in *Proc. Int. Conf. Power, Energy Innovations (ICPEI)*, Chiangmai, Thailand, Oct. 2020, pp. 197–200.

[14] F. Zhang, Y. Xie, Y. Hu, G. Chen, and X. Wang, "A hybrid boost–flyback/flyback microinverter for photovoltaic applications," *IEEE Trans. Ind. Electron.*, vol. 67, no. 1, pp. 308–318, Jan. 2020.

[15] S.-S. Lee, S.-W. Choi, and G.-W. Moon, "High-efficiency active-clamp forward converter with transient current build-up (TCB) ZVS technique," *IEEE Trans. Ind. Electron.*, vol. 54, no. 1, pp. 310–318, Feb. 2007.

[16] Z. Cao, Y. Gu, and D. Zhang, "A novel magnetic integrated boost-forward converter," in *Proc. IEEE/IAS Ind. Commercial Power System Asia (I&CPS)*, Chengdu, China, 2021, pp. 157–162.

[17] J.-E. Park, J.-K. Han, S.-H. Choi, and G.-W. Moon, "Two-switch forward converter with an integrated buck converter for high bus voltage in satellites," *IEEE Trans. Power Electron.*, vol. 38, no. 2, pp. 2041–2051, Aug. 2022.

[18] J. Cezar Giacomini, P. Fernando Soardi Costa, A. Manuel Santos Spencer Andrade, L. Schuch, and M. Lúcio da Silva Martins, "Desenvolvimento De Um Conversor CC-CC Boost-Forward Integrado Para Aplicações Com Elevado Ganho De Tensão," *Eletrônica de Potência*, vol. 22, no. 2, pp. 206–214, Jun. 2017.

[19] H. Wu and Y. Xing, "A family of forward converters with inherent demagnetizing features based on basic forward cells," *IEEE Trans. Power Electron.*, vol. 25, no. 11, pp. 2828–2834, Nov. 2010.

[20] H. Wu and Y. Xing, "Families of forward converters suitable for wide input voltage range applications," *IEEE Trans. Power Electron.*, vol. 29, no. 11, pp. 6006–6017, Nov. 2014.

[21] W. Li, L. Fan, Y. Zhao, X. He, D. Xu, and B. Wu, "High-step-up and high-efficiency fuel-cell power-generation system with active-clamp flyback–forward converter," *IEEE Trans. Ind. Electron.*, vol. 59, no. 1, pp. 599–610, Jan. 2012.

[22] F. Zhang and Y. Yan, "Novel forward–flyback hybrid bidirectional dc–dc converter," *IEEE Trans. Ind. Electron.*, vol. 56, no. 5, pp. 1578–1584, May 2009.

[23] R.-L. Lin and Y.-H. Huang, "Forward-flyback converter with snubber-feedback network for contactless power supply applications," in *Proc. IEEE Energy Convers. Congr. Expo.*, Atlanta, GA, USA, 2010, pp. 1422–1427.

[24] K.-C. Tseng, J.-Z. Chen, J.-T. Lin, C.-C. Huang, and T.-H. Yen, "High step-up interleaved forward-flyback boost converter with three-winding coupled inductors," *IEEE Trans. Power Electron.*, vol. 30, no. 9, pp. 4696–4703, Sep. 2015.

[25] H. Liu, H. Hu, H. Wu, Y. Xing, and I. Batarseh, "Overview of high-step-up coupled-inductor boost converters," *IEEE J. Emerg. Select. Topics Power Electron.*, vol. 4, no. 2, pp. 689–704, Jun. 2016.

[26] W. Yu et al., "High efficiency converter with charge pump and coupled inductor for wide input photovoltaic AC module applications," in *Proc. IEEE Energy Convers. Congr. Expo.*, San Jose, CA, USA, Sep. 2009, pp. 3895–3900.

[27] Y. Tang, D. Fu, J. Kan, and T. Wang, "Dual switches DC/DC converter with three-winding-coupled inductor and charge pump," *IEEE Trans. Power Electron.*, vol. 31, no. 1, pp. 461–469, Jan. 2016.

[28] D. Vinnikov and I. Roasto, "Quasi-Z-source-based isolated DC/DC converters for distributed power generation," *IEEE Trans. Ind. Electron.*, vol. 58, no. 1, pp. 192–201, Jan. 2011.

[29] A. Chub, D. Vinnikov, F. Blaabjerg, and F. Z. Peng, "A review of Galvanically isolated impedance-source dc–dc converters," *IEEE Trans. Power Electron.*, vol. 31, no. 4, pp. 2808–2828, Apr. 2016.

[30] K. Alluhaybi, I. Batarseh, and H. Hu, "Comprehensive review and comparison of single-phase grid-tied photovoltaic microinverters," *IEEE J. Emerg. Sel. Topics Power Electron.*, vol. 8, no. 2, pp. 1310–1329, Jun. 2020.

[31] J. Yuan, F. Blaabjerg, Y. Yang, A. Sangwongwanich, and Y. Shen, "An overview of photovoltaic microinverters: topology, efficiency, and reliability," in *Proc. IEEE 13th Int. Conf. Compat., Power Electron. Power Eng. (CPEPOWERENG)*, Sonderborg, Denmark, 2019, pp. 1–6.

[32] O. Matiushkin, O. Husev, H. Afshari, D. Vinnikov, and R. Strzelecki, "Cost-effective piggyback forward dc-dc converter," in *Proc. IEEE Appl. Power Electron. Conf. Expo. (APEC)*, Long Beach, CA, USA, 2024, pp. 2106–2111.

[33] S. Ben-Yaakov and Y. Amran, "Multiple output flyback converters: the role of output capacitors in shaping the currents of secondary windings," in *Proc. 21st Annu. IEEE Conf. Power Electron. Specialists*, San Antonio, TX, USA, 1990.

[34] R. W. Erickson and D. Maksimovic, *Fundamentals of Power Electronics*. New York, NY, USA: Kluwer/Plenum Publishers, 2001.

[35] C.-S. Leu, "Improved forward topologies for DC-DC applications with built-in input filter," Ph.D dissertation, Virginia Polytech. Inst. and State Univ., Blacksburg, VA, USA, 2006.

[36] R. Nur Hasanah, T. Taufik, and O. Setyawatia, "Impact of transformer's leakage inductance on duty cycle in isolated dc-dc converters," *Int. J. Smart Grid Clean Energy*, vol. 9, no. 1, pp. 61–68, Jan. 2020.

Oleksandr Matiushkin (Member, IEEE) received the B.Sc. and M.Sc. degrees in industrial electronics from Chernihiv National University of Technology, Chernihiv, Ukraine, in 2016 and 2018, respectively and the Ph.D. degree in power electronics from Tallinn University of Technology, Tallinn, Estonia, in 2022.

He is currently a Researcher with the Department of Electrical Engineering, Tallinn University of Technology. His research interests include power electronics, new topology design, microcontroller and field programmable gate array programming, modeling, filter calculations, and control techniques for power electronics converters.

Oleksandr Husev (Senior Member, IEEE) received the Ph.D. degree in industrial electronics from the Institute of Electrodynamics, National Academy of Science of Ukraine, Kyiv, Ukraine, in 2012.

He is currently a Senior Researcher and Project Leader with the Department of Electrical Power Engineering and Mechatronics, Tallinn University of Technology, Tallinn, Estonia, and an Associate Professor with the Department of Radiotechnic and Embedded Systems, Chernihiv Polytechnic National University, Chernihiv, Ukraine. His research interests include power electronics systems, novel topology design, control systems employing various algorithms, modeling, simulation, applied power converter and control system design, and stability investigation.

Hossein Afshari (Student Member, IEEE) was born in Zanjan, Iran, in 1997. He received the B.S. degree in electrical engineering from Semnan University, Semnan, Iran, in 2019, and the M.S. degree in electrical railway engineering from Iran University of Science and Technology, Tehran, Iran, in 2022. He is currently working toward the Ph.D. degree in power electronics with Tallinn University of Technology (Taltech), Tallinn, Estonia.

His research interests include modeling, control, and design of power electronic converters, power electronic transformer, grid-connected solar converters, and modular multilevel converters.

Mr. Afshari received the Best Paper Award at RTUCON Conference, in 2022.

Enrique Romero-Cadaval (Senior Member, IEEE) received the M.Sc. degree in industrial electronic engineering from the Universidad Pontificia de Comillas, Madrid, Spain, in 1992, and the Ph.D. degree in electrical and electronic engineering from the Universidad de Extremadura, Badajoz, Spain, in 2004.

He works as Power Electronics Full-Professor with the University of Extremadura, Badajoz, Spain and belongs to Power Electrical and Electronic Systems (PE&ES) R&D Group with the School of Industrial Engineering. He is currently President of Spanish Section of IEEE. His research interests include power electronics applied to power systems covering power quality, active power filters, electric vehicles, smart grids, energy storage, and renewable energy resources.

Carlos Roncero-Clemente (Senior Member, IEEE) received the international Ph.D. degree in electrical, electronic, and control engineering from the University of Extremadura, Badajoz, Spain, in 2016.

During the Ph.D. research, he was a Visiting Student with Tallinn University of Technology, Tallinn, Estonia, and Aalborg University, Aalborg, Denmark. He was a Postdoctoral Researcher with Nova University of Lisbon, Lisbon, Portugal, from 2016 to 2019. He is currently an Associate Professor in electrical engineering and Senior Researcher with the University of Extremadura. He is the author of more than 40 journal articles and 80 international conferences. His research interests include power electronic topologies and controls for renewable energy applications and smart grids.

PAPER VI

H. Afshari, O. Husev and D. Vinnikov, "A Novel Isolated Buck-Boost dc-dc Converter with Wide Range of Voltage Regulations," *2023 IEEE 17th International Conference on Compatibility, Power Electronics and Power Engineering (CPE-POWERENG)*, Tallinn, Estonia, 2023, pp. 1–6, doi: 10.1109/CPE-POWERENG58103.2023.10227443.

A Novel Isolated Buck-Boost dc-dc Converter with Wide Range of Voltage Regulations

Hossein Afshari
Department of Electrical Power
Engineering and Mechatronics *dept.*
Tallinn University of Technology
Tallinn, Estonia
hoafsh@taltech.ee

Oleksandr Husev
*Department of Electrical Power
Engineering and Mechatronics
Tallinn University of Technology*
Tallinn, Estonia
oleksandr.husev@taltech.ee

Dmitri Vinnikov
*Department of Electrical Power
Engineering and Mechatronics
Tallinn University of Technology*
Tallinn, Estonia
Dmitri.vinnikov@taltech.ee

Abstract—This paper proposed a novel isolated buck-boost dc-dc converter with wide range of voltage regulations. The proposed converter has significant features such as zero voltage switching operation, as well wide input voltage regulation range. This topology can be used in several application including Photovoltaic microconverter, when the voltage varies between 10 to 60 volts, and the output needs to be a constant dc voltage. The Buck, Buck-Boost, as well as Boost capabilities of proposed converter beside their switching states and equations of each switching states are presented. The steady state analysis is used to calculate the voltage gain for each mode. Finally, the simulation using PowerSim software is verifying the theoretical evaluation.

Keywords—DC-DC converter, isolated Buck-Boost, ZVS, Voltage regulation.

I. Introduction

Concerns caused by the emission of greenhouse gases and environmental pollution caused by fossil fuels on the one hand, and the increase in the price of fossil fuels and the fear of running out of this type of energy on the other hand, have prompted the countries of the world to use renewable energy sources such as wind energy, solar energy, and fuel cells as suitable alternative energy sources [1]. However, most renewable sources have a low output voltage level that is direct and variable with environmental conditions, and produces an unregulated voltage in their output, which does not have sufficient reliability [2]-[6]. The voltage of PV panels can vary significantly with changing conditions, while the output must be kept constant [7]. Also, some multi-purpose power supplies require a wide range of output voltage, while they are provided by a constant input source, and in these cases, step-up dc-dc converters with a wide range of voltage gain are the best choice [3].

The ability to increase and decrease the input voltage of step-up dc-dc converters makes them used in many other applications such as battery chargers, power supply systems, etc. Therefore, it is necessary to use interface transformers to achieve higher efficiency, increase and adjust the output voltage in renewable energy sources [8].

Minimizing size, cost and increasing efficiency of power electronics converters is a general goal during its design and optimization [9]. Several dc-dc converters are published in the literature to reach lower voltage stress across semiconductors as well as input current ripple, higher efficiency voltage

conversion ratio, as well as isolation [10], [12]. To overcome the challenges of safety, high voltage gain, galvanic isolation, and flexibility of system configuration, High-Frequency (HF) transformer isolated structures are introduced [13]. Current fed converters, which use an inductor are one of the significant topologies among isolated ones [14], [15].
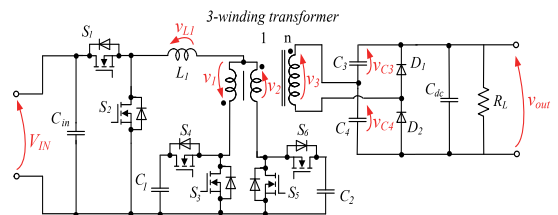

Fig. 1. Circuit topology of the proposed converter

A conventional current-fed push–pull converter [16] is potential topology, and has several benefits such as high voltage gain, low input current ripple, and low conduction loss of switches. However, the voltage spikes of switches resulting from leakage inductance of a transformer, high voltage stress and reverse-recovery issue, and low efficiency are important drawbacks of conventional converter. Also, since the duty ratio must be greater than 0.5, its input-voltage operating range is relatively narrow. In recent years, some improved current-fed converters have been published to solve the issues mentioned above. One of them is a zero-voltage-switching (ZVS) clamping-mode current-fed push–pull converters [17]-[22]. Its active-clamp circuit clamps a surge voltage of switches and recycles the energy stored in leakage inductance. Moreover, the converter operates at a duty ratio less than 0.5, so it can be suitable for wide input-voltage applications. However, although this converter is working under ZVS operation, ZVS does not improve the efficiency incredibly due to the small value of the energy stored in the output capacitances of switches in low input voltage. [18].

To improve existed solutions, the novel isolated buck-boost dc-dc converter is presented in this paper, which is shown in Fig. 1, and has multiple benefits including ZVS operation, isolation between input and output ports, wide voltage regulation range. Furthermore, the presented dc-dc converter can be operated in buck-boost, boost and buck modes with changing the gate signals, which will be mention in the following subsections.
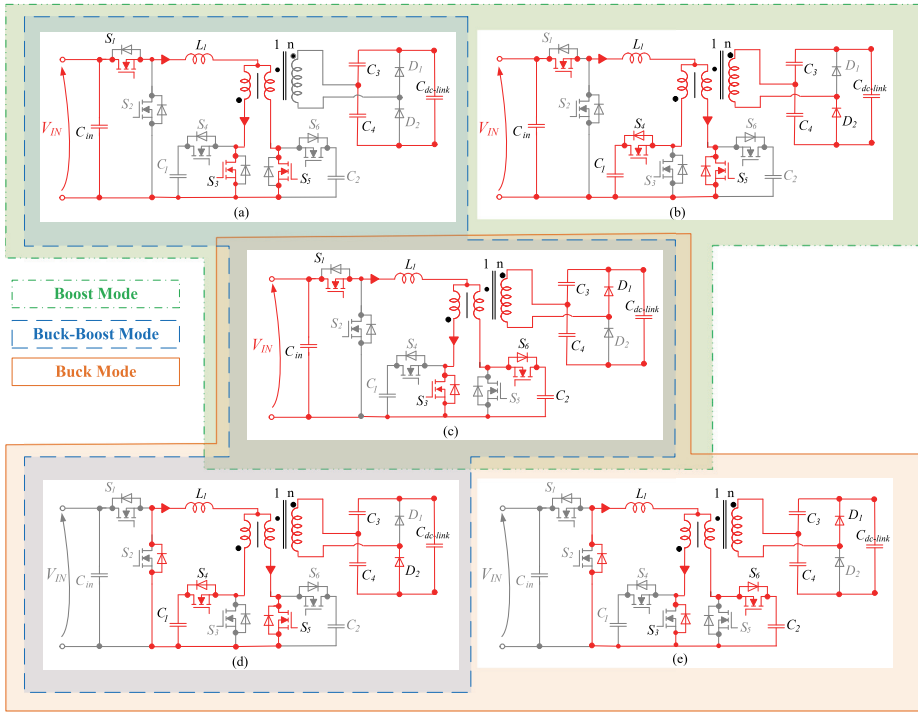
Fig. 2. Possible switching as well as operation modes states of proposed converter. (a) *S1*: ON, *S3*: ON, and *S5*: ON, (b) *S1*: ON, *S3*: ON, and *S5*: OFF, (C) *S1*: ON, *S3*: OFF, and *S5*: ON, (d) *S1*: OFF, *S3*: OFF, and *S5*: ON, and (e) *S1*: OFF, *S3*: ON, and *S5*: OFF

Section III is presented to the designing of passive components; the inductance is designed to work in CCM mode. Section IV denoted the simulation verification using software tool PowerSim. Finally, Section V is devoted to the conclusions of this article.

II. PROPOSED CONVERTER CONFIGURATION AND PRINCIPLE OF OPERATION

Fig. 1. shows the circuit configuration of the proposed converter. The structure is consisting of three winding transformer with the turn ratio of $n = N_1/N_3 = N_2/N_3$, six switches and three capacitors in primary side, as well as two diodes and three capacitors in secondary side of transformer. The inductance L_1 is adjusted to operate in Continuous Conduction Mode (CCM).

The possible operation modes are depending on the switching condition of S_1, S_3, and S_5, where switches S_1 and S_2, S_3 and S_4, as well as S_5 and S_6 switch in complimentary fashion. The appropriate operation of switches results in buck, buck-boost, as well as boost capabilities. Table.1 shows the switching table of the proposed converter beside Zero Voltage Switching (ZVS) condition feature. With this in mind that the converter works in Boost mode when we have an overlapping between the gate signals of switches S_3 and S_5, in all operation modes the ZVS operation is achieved.

The possible switching states of proposed converter beside the Buck, Buck-Boost, and Boost operation modes are illustrated in Fig. 2. To cover the possible switching conditions, we assumed that the shifted value between the gate signals of S_3 and S_4 are constant value, 180 degrees. Each mode is described in the following subsections.

State 1 [see Fig. 2(a)]

During this switching period, switches S_1, S_3, as well as S_5 are turned on and diode D_1 and D_2 are reverse biased. The voltage in the three-winding transformer is zero. Inductor L_1 is charged from the input source voltage. By applying Kirchhoff's current and voltage law in this state, the following equations are obtained.

TABLE I.   SWITCHING TABLE OF PROPOSED CONVERTER

Mode	S_1	S_2	S_3	S_4	S_5	S_6	state	ZVS
	ON	OFF	ON	OFF	OFF	ON	c	
Buck	OFF	ON	ON	OFF	OFF	ON	e	For D>0.5
	OFF	ON	OFF	ON	ON	OFF	d	
	ON	OFF	ON	OFF	OFF	ON	c	
Buck-Boost	ON	OFF	ON	OFF	ON	OFF	a	For D>0.5
	OFF	ON	OFF	ON	ON	OFF	d	
	ON	OFF	ON	OFF	ON	OFF	a	
Boost	ON	OFF	ON	OFF	OFF	ON	c	For 0<D<1
	ON	OFF	OFF	ON	ON	OFF	b	

$$v_{L_1} = V_{IN}, \tag{1}$$

$$i_{S_3} + i_{S_5} = i_{L_1}, \tag{2}$$

where, i_{S_5} and i_{S_3} are the currents across switch S_5 and S_3 respectively. v_{L_1} and i_{L_1} are the voltage and current of inductance L_1.

State 2 [see Fig. 2(b)]

During this switching state, switches S_1, S_5 are turned ON, and S_3 turned OFF. diode D_1 is reverse biased, and D_2 is conducting. With this mind, the capacitor C_4 is charged, and the territory voltage in three winding transformer is equal to v_{C_4}. Inductance L_1 is charged with slow slope same as mode 2. By applying Kirchhoff's law in this mode, the following equations are obtained.

$$v_{L_1} = V_{IN} - \frac{v_{C_4}}{n}, \tag{3}$$

$$i_{S_4} + i_{L_1} = i_{S_5}, \tag{4}$$

where, i_{S_4} and i_{S_6} are the currents across switches S_5 and S_3 respectively.

State 3 [see Fig. 2(c)]

In this state, switches S_1 and S_3 are turned on, and S_3 is off. Capacitor C_3 is charged since Diode D_1 is forward biased, and D_2 is reverse biased. Furthermore, Inductor L_1 is charged again. However, the charging speed of the inductance in this mode is lower than Mode 1 due to conduction of both switches S_3 and S_5. The following equations are derived from this state.

$$v_{L_1} = V_{IN} - \frac{v_{C_3}}{n}, \tag{5}$$

$$i_{S_6} + i_{L_1} = i_{S_3}, \tag{6}$$

$$v_3 = -v_{C_3}. \tag{7}$$

V_3 is the voltage of territory winding, and n is the turn ratio of three winding transformer. v_{C_3} is voltage across capacitor C_3.

The next two modes can be achieved assuming the fact that switch S_1 is conducted continuously during whole switching time (T_s).

State 4 [see Fig. 2(d)]

During this switching period, switches S_1 and S_5 are turned on, and S_3 is turn off. Diode D_2 is forward biased and capacitor C_4 is charged. Inductance L_1 is discharging through the body diode of switch S_2. In this state the voltage of inductance can be calculated according to (8).

$$v_{L_1} = \frac{-v_{C_4}}{n}. \tag{8}$$

State 5 [see Fig. 2(e)]

In this switching state, switches S_1 and S_2 are turned on, and switch S_5 is turned off. Capacitor C_3 is charged through Diode D_1, which is forward biased. Also, the Inductance L_1 is discharging and the voltage across this inductance is derived from the following.

$$v_{L_1} = \frac{-v_{C_4}}{n}. \tag{9}$$

Equations (10) and (11) can be derived from each mode. Equation (10) will use in calculation of voltage gain ($V_{dc-link}/V_{IN}$) in next subsections.

$$v_{C_3} + v_{C_4} = v_{dc-link}, \tag{10}$$

$$N_1 i_1 + N_2 i_2 = N_3 i_3. \tag{11}$$

where N_1, N_2, and N_3, are the turn ration of primary, secondary, as well as territory of three winding transformer.

Due to the wide range of operation, the proposed converter can be used in multiple applications such as grid-connected PV micro converter, when the input voltage is varied between zero to sixty volts, while the output of dc-dc converter is constant value 350 volts [7]. As mentioned before, the integration of states results in different operation modes including buck, buck-boost, and boost.

Fig. 3. depicts the operation range of proposed converter in buck, buck-boost, and boost modes. Assuming that the output is constant dc link, the operation mode is changed with increasing or reducing the input voltage. The normalized voltage gain G is defined as

$$G = \frac{n V_{IN}}{v_{out}}, \tag{12}$$

where n is the turns ratio of the transformer and $n = N_S/N_P$. The converter operates in the boost mode when $G < 1$, and operates in the buck mode when $G \geq 1$.

The key waveforms of all three possible operation modes are depicted in Fig. 4. The voltage gains of proposed converter beside their switching states are described one by one in the following.
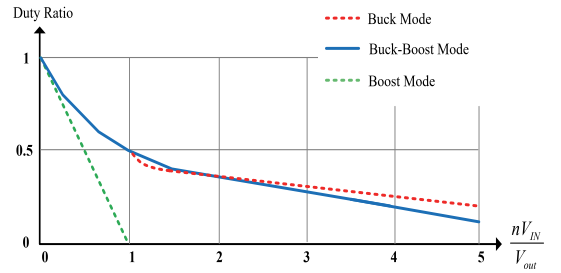

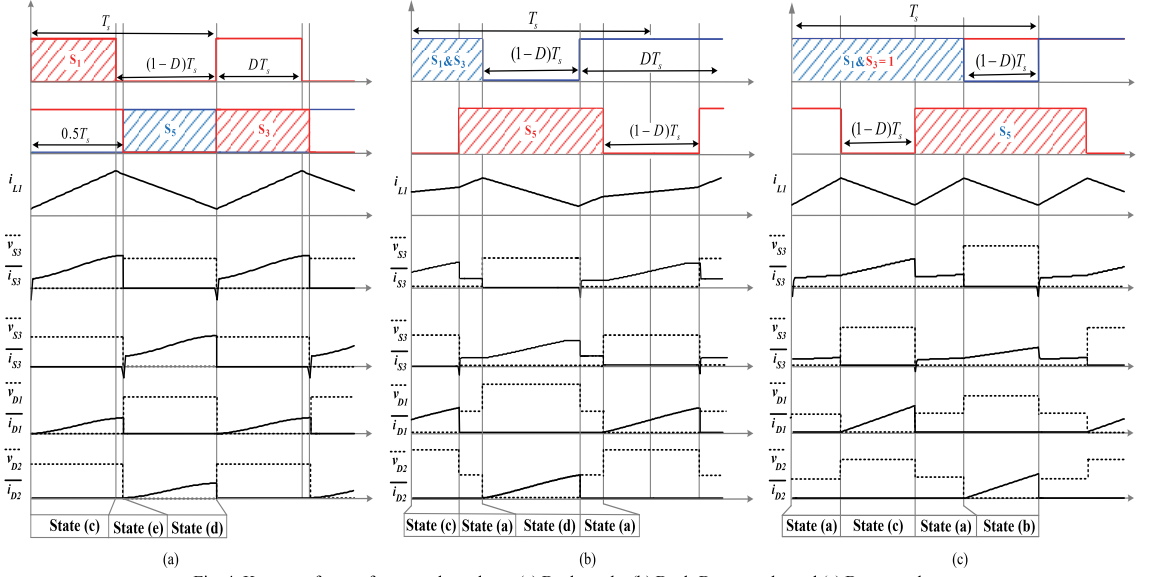Fig. 3. Operation range of proposed converter.

Fig. 4. Key waveforms of proposed topology; (a) Buck mode, (b) Buck-Boost mode, and (c) Boost mode.

A. Buck Mode

This mode is in result of switching states (c), (d), and (e) depicted in Fig.2. This mode is achieved when we don't have any overlapping between gate signals of switches S_3 and S_5- the gate signals shifted 180 degrees with duty cycles 0.5. According to the volt balance theory for inductance L_1, the voltage gain of proposed converter in buck mode is calculated according to the following equation.

$$D_{Buck} T_s (V_{IN} - \frac{v_{C3}}{n}) + \\ +(1-D_{Buck})T_s(-\frac{v_{C4}}{n}) \rightarrow \frac{V_{out}}{V_{IN}} = 2nD_{Buck}, \tag{13}$$

where n is turn ratio of three winding transformer, V_{IN} is the input voltage, V_{out} is output voltage, T_s is switching time, D is duty ratio of switch S_1, and v_{C3} as well as v_{C4} are capacitors C_3 and C_4 voltages respectively.

B. Boost Mode

In the boost mode, the switch S_1 is set to be the maximum value $D_{S1}=1$. Thus, the power flow is controlled by changing the duty ratio of switches S_3 and S_5, which assumed as same values. This mode consists of switching states (a), (c), and (d).

The voltage gain of proposed converter is derived from the volt balance theory for inductance L_1, where D_{Boost} is the duty ratio of switches S_3 and S_5.

$$(2D_{Boost}-1)T_s(V_{IN}) + (1-D_{Boost})T_s(V_{IN} - \frac{v_{C3}}{n}) + \\ +(1-D_{Boost})T_s(V_{IN} - \frac{v_{C4}}{n}) = 0 \rightarrow \frac{V_{out}}{V_{IN}} = \frac{n}{1-D_{Boost}}. \tag{14}$$

C. Buck-Boost Mode

This mode is in results of switching states (c), (a), and (d). To calculate the voltage gain it's assumed that duty cycle of all switches S_1, S_3, as well as S_5 are equal. D_{BB} is Buck-Boost mode duty cycle.

$$(1-D_{BB})T_s(V_{IN} - \frac{v_{C3}}{n}) + (2D_{BB}-1)T_s(V_{IN}) + \\ +(1-D_{BB})T_s(-\frac{v_{C4}}{n}) = 0 \rightarrow \frac{V_{out}}{V_{IN}} = \frac{nD_{BB}}{1-D_{BB}}. \tag{15}$$

II. COMPONENTS CALCULATION

Through shape of the inductance current i_{L1} in Fig. 4, and regarding calculated space for both the average and instant value of the inductance current, and time zone between zero to switching time. It can be derived that the operation mode is boundary for $\frac{\Delta i_{L1_{Max}}}{2} = I_{L1}$, and is CCM for $\frac{\Delta i_{L1_{Max}}}{2} < I_{L1}$.

According to the Fig. 3. the maximus value for $\Delta i_{L1_{Max}}$ is in switching state (c) for Buck mode, in state (a) for both Buck-Boost and Boost mode. The size of the inductance L_1 is calculated based on the equation derived from this switching state.

$$I_{L1} = \frac{P_{IN}}{V_{IN}}, \tag{16}$$

where P_{IN} is the input power and calculated based on the output power and the efficiency.
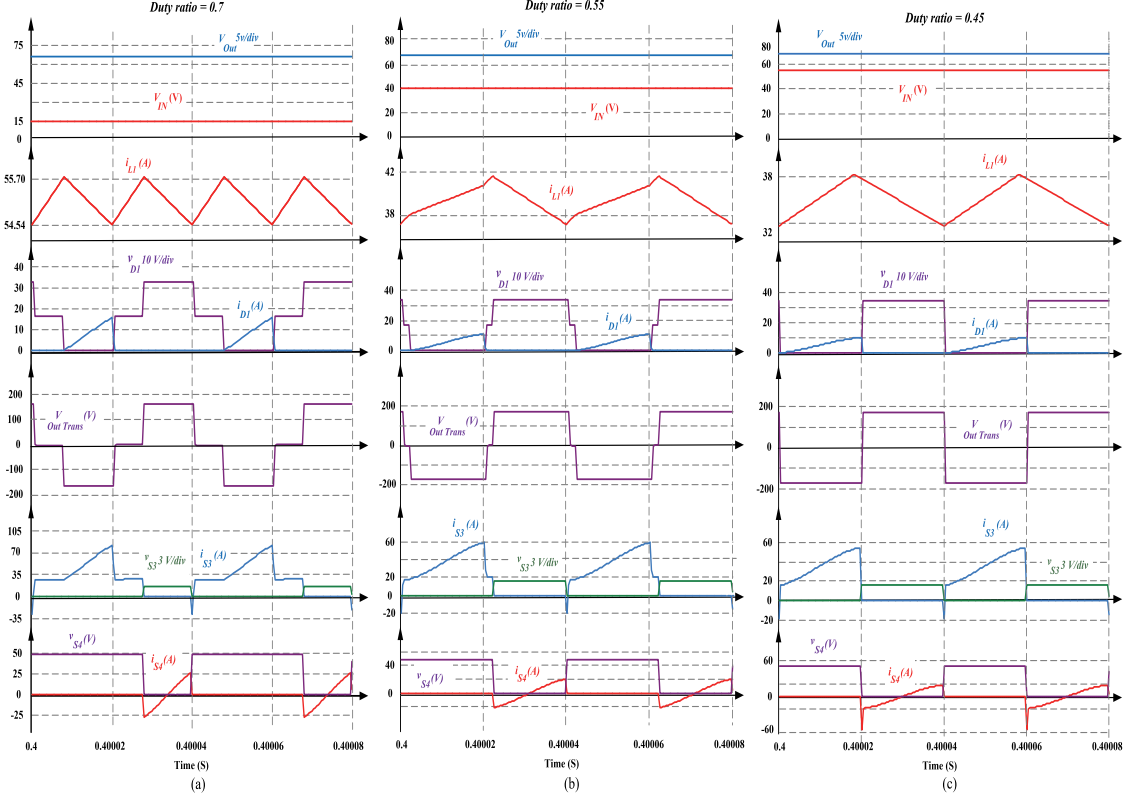
Fig. 5. Simulation results. (a) Boost mode. (b) Buck-Boost mode. (c) Buck mode.

Assuming CCM as an operation mode, and by replacing equation number (15) in $\dfrac{\Delta i_{L1_{Max}}}{2} < I_{L1}$.

$$\frac{V_{IN} \cdot v_{L_1} \cdot \Delta t}{2 \cdot P_{IN}} < L_1, \qquad (17)$$

where v_{L_1} and Δt are calculated according to equations (1) and (3) for states 3 and 1 respectively. With all in mind we have the following equations to calculate the inductance size in three operation modes.

$$\frac{V_{IN}^2}{2 \cdot P_{IN} \cdot f_s} < L_{1_{Boost}}, \qquad (18)$$

$$\frac{V_{IN}}{4 \cdot P_{IN} \cdot f_s}\left(V_{IN} - \frac{V_{out}}{2n}\right) < L_{1_{Buck \ or \ Buck\text{-}Boost}}. \qquad (19)$$

After calculating inductance based on the maximum value of above equations to operate appropriately in all three modes, we should have $\Delta i_{L1} < \%10 I_{L1}$.

The size of output capacitors-C_3, C_4, and $C_{dc\text{-}link}$, are obtained as follows.

$$\frac{V_{out} \cdot \Delta t}{R \cdot V_C \cdot 0.05} < C, \qquad (20)$$

where the voltage ripple of capacitor is assumed to be lower than 5 % of capacitor voltage, $\Delta V_C < 0.05 V_C$. Furthermore, Δt is calculated according to for states 3 and 1 respectively.

TABLE II.   CALCULATED PARAMETERS.

Parameter	Value
Input Voltage	V_{in}=10 V – 60 V
Output voltage	350 V
Transformer turn ratio (n)	7
Inductance	100 µH
Output capacitor	200 µF
Load	132.5 Ω
Switching frequency	25 kHz

III. SIMULATION RESULTS

The propounded converter circuit is simulated using PSIM software. The diodes and MOSFET chosen includes practical condition in the simulation. The calculated parameters of proposed converter are expressed in Table 2. The simulation results of novel isolated buck boost topology are presented in Fig.5. (a) Boost mode, (b) Buck-Boost mode, and (c) Buck mode.

To show the wide range of operation feature in this topology, the input voltage is various between 15 V, 40 V, and 55 V, while the output is constant dc voltage 350 Volts. To reach the required constant voltage, three duty cycles 0.7, 0.55, and 0.45 are considered in Boost, Buck-Boost, as well as Buck modes of proposed converter. As shown in Fig. 5. the output is constant voltage 350 volts for the different values of input voltages. Also, in each of the mentioned modes the current of inductance L_1 is validated by the CCM operation.

The Diodes D_1 and D_2, as well as Switches S_3, and S_5 all operate in ZVS condition. Furthermore, the shape of the voltage across territory side of three winding transformer is shown to validate the equation of each state, which are mentioned before.

IV. CONCLUSIONS

In this paper, the isolated Buck-Boost topology is presented. The topology consists of total six switching states. Integrating the three different switching states results in Buck, Buck-Boost, and Boost capabilities.

The simulation results verified the theoretical calculation especially CCM operation. The simulation validated the wide range of regulation feature for proposed converter, the output voltage is constant for different values of input voltages. Also, the current and voltage of switches as well as diodes shows the ZVS operation of the proposed converter in all three modes.

The main advantage of this topology is high voltage gain, ZVS operation, galvanic isolation, as well as wide range of operation appropriate for application such as photovoltaic microconverter, while input may vary in the very wide range while output has constant value.

REFERENCES

[1] N. Shabbir, L. Kütt, Hadi A. Raja, M. Jawad, Alo Allik, O. Husev. "Techno-economic analysis and energy forecasting study of domestic and commercial photovoltaic system installations in Estonia," *Energy* , Volume 253, 2022.

[2] F. Sedaghati, and S. Pourjafar, "Analysis and implementation of a boost DC–DC converter with high voltage gain and continuous input current," *IET Power Electronics*, vol. 13, no. 4, pp.798-807, 2019.

[3] H. Afshari, O. Husev, O. Matiushkin, and D. Vinnikov, "A Review of Hybrid Converter Topologies" in *Energies*, vol 15, no. 24, 2022.

[4] A. Chub, O. Husev and D. Vinnikov, "Input-parallel output-series connection of isolated quasi-Z-source DC-DC converters," *in proc. of 2014 Electric Power Quality and Supply Reliability Conference (PQ)*, Rakvere, Estonia, 2014, pp. 277-284.

[5] T. Nouri, N. V. Kurdkandi, O. Husev, "An Improved ZVS High Step-Up Converter Based On Coupled Inductor and Built-In

[6] P. Mohseni, S. Rahimpour, M. Dezhbord, M. R. Islam and K. M. Muttaqi, "An Optimal Structure for High Step-Up Nonisolated DC–DC Converters With Soft-Switching Capability and Zero Input Current Ripple," *IEEE Trans. on Ind. Electron.*, vol. 69, no. 5, pp. 4676-4686, May 2022.

[7] H. Afshari, O. Husev, D. Vinnikov, O. Matiushkin and N. V. Kurdkandi, "Comparison of Grid-Connected Flyback-based Microinverter with Primary and Secondary Side Decoupling Approach," *in proc. of IEEE 63th International Scientific Conference on Power and Electrical Engineering of Riga Technical University (RTUCON)*, Riga, Latvia, 2022, pp. 1-6.

[8] K. Akbariavaz, S.S .Fazel, and M. Khosravi, "Fully FPGA-based implementation of a modified control strategy for power electronic transformer in railway traction applications,". *IET Renewable Power Gener*, vol. 17, pp. 1904–1919, April 2021.

[9] O. Husev, D. Vinnikov, C. Roncero-Clemente, A. Chub and E. Romero-Cadaval, "Single-Phase String Solar qZS-based Inverter: Example of Multi-Objective Optimization Design," *IEEE Trans. on Ind. Applications*, vol. 57, no. 3, pp. 3120-3130, May-June 2021.

[10] V. Sidorov, A. Chub and D. Vinnikov, "Bidirectional Isolated Hexamode DC–DC Converter," *IEEE Trans. on Power Electron.*, vol. 37, no. 10, pp. 12264-12278, Oct. 2022.

[11] O. Husev, L. Liivik, F. Blaabjerg, A. Chub, D. Vinnikov and I. Roasto, "Galvanically Isolated Quasi-Z-Source DC–DC Converter With a Novel ZVS and ZCS Technique," *IEEE Trans. on Ind. Electron.*, vol. 62, no. 12, pp. 7547-7556, Dec. 2015.

[12] M. Azizi, O. Husev, D. Vinnikov and O. Veligorskyi, "Comparative Evaluation of Isolated dc-dc Converters for Low Power Applications," *in proc. of IEEE 20th International Power Electronics and Motion Control Conference*, Brasov, Romania, 2022, pp. 7-12.

[13] K. Khatun, V. R. Vakacharla, A. R. Kizhakkan and A. K. Rathore, "Small-Signal Analysis and Control of Snubberless Naturally Clamped Soft-Switching Current-Fed Push–Pull DC/DC Converter," *IEEE Trans. on Ind. Appl.*, vol. 56, no. 4, pp. 4299-4308, July-Aug. 2020.

[14] Y. H. Kim, S. C. Shin, J. H. Lee, Y. -C. Jung and C. -Y. Won, "Soft-Switching Current-Fed Push–Pull Converter for 250-W AC Module Applications," *IEEE Trans. on Power Electron.*, vol. 29, no. 2, pp. 863-872, Feb. 2014.

[15] Q. Wu, Q. Wang, J. Xu and L. Xiao, "Implementation of an Active-Clamped Current-Fed Push–Pull Converter Employing Parallel-Inductor to Extend ZVS Range for Fuel Cell Application," *IEEE Trans. on Ind. Electron.*, vol. 64, no. 10, pp. 7919-7929, Oct. 2017.

[16] A. L. Rabello, M. A. Co, D. S. L. Simonetti and J. L. F. Vieira, "An isolated DC-DC boost converter using two cascade control loops," *in proc. of ISIE*, Guimaraes, Portugal, 1997, pp. 452-456 vol.2.

[17] R. Kosenko, O. Husev and A. Chub, "Full soft-switching high step-up current-fed DC-DC converters with reduced conduction losses," *in proc. of 2015 IEEE 5th International Conference on Power Engineering, Energy and Electrical Drives (POWERENG)*, Riga, Latvia, 2015, pp. 170-175.

[18] J. M. Kwon, E. H. Kim, B. -H. Kwon and K. -H. Nam, "High-Efficiency Fuel Cell Power Conditioning System With Input Current Ripple Reduction," *IEEE Trans. on Ind. Electron.*, vol. 56, no. 3, pp. 826-834, March 2009.

[19] F. J. Nome and I. Barbi, "A ZVS clamping mode-current-fed push-pull DC-DC converter," *in proc. of IEEE International Symposium on Industrial Electronics. Proceedings. ISIE'98 (Cat. No.98TH8357)*, Pretoria, South Africa, 1998, pp. 617-621 vol.2.

[20] J. W. Lim, C. Bai, T. A. Wagaye, J. -H. Choi and M. Kim, "Highly Reliable Push–Pull Resonant DC/DC Converter for Medium-Power Applications," *IEEE Trans. on Ind. Electronics*, vol. 70, no. 2, pp. 1342-1355, Feb. 2023.

[21] Y. Li, Q. Li, B. Ji and S. Duan, "A ZVS Control Scheme for High Efficiency Buck-Boost Current-Fed Isolated DC-DC Converter," *IEEE Trans. on Transp. Electrification,* Early access, 2023.

[22] J. M. Kwon, E. H. Kim, B. H. Kwon and K. H. Nam, "High-Efficiency Fuel Cell Power Conditioning System With Input Current Ripple Reduction," *IEEE Trans. on Ind. Electron.*, vol. 56, no. 3, pp. 826-834, March 2009.

PAPER VII

H. Afshari, D. Vinnikov, O. Matiushkin, O. Husev, and M. Malinowski, "A Cost-Effective Non-Isolated Forward-Based Universal Microconverter for PV: Comparison with Interleaved Single-Stage Flyback Topology," *4th IEEE International Conference on Power Electronics Smart Grid and Renewable Energy, December,* 2025, IIT Dharwad, Hubli, Karnataka, India.

A Cost-Effective Non-Isolated Forward-Based Universal Microconverter for PV: Comparison with Interleaved Single-Stage Flyback Topology

Hossein Afshari, Dmitri Vinnikov, Oleksandr Matiushkin
Department of Electrical Power Engineering and Mechatronics
Tallinn University of Technology
Tallinn, Estonia
hossein.afshari@taltech.ee

Oleksandr Husev, Mariusz Malinowski
Department of Industrial Electronics
Warsaw University of Technology
Warsaw, Poland
oleksandr.husev@pw.edu.pl

Abstract—**This paper presents a novel dual-output forward non-isolated microconverter for photovoltaic systems, experimentally benchmarked against a conventional cost-effective flyback isolated topology. Both TRL4 microconverter prototypes were designed using identical components, except for their core topologies, to ensure a fair comparison. The proposed forward-based microinverter eliminates isolation components and integrates shared auxiliary circuits, enabling simultaneous DC and AC outputs while reducing the bill of materials costs by 28% for mass production. Cost savings are primarily attributed to simplified magnetics and the non-isolated architecture, making the proposed solution highly compatible with photovoltaic module applications where cost is a critical barrier. Theoretical calculations and experimental waveforms are presented to validate the approach, demonstrating the feasibility and cost-effectiveness of the forward-based topology for photovoltaic module applications.**

Keywords— *Cost Comparison, Flyback, Forward, Microconverter, Dual-purpose.*

I. INTRODUCTION

The global shift toward renewable energy systems is essential for combating climate change and reducing reliance on fossil fuels. Solar Photovoltaic (PV) technology has become a key driver of decarburization, fueled by declining module costs and supportive policy incentives [1]. However, achieving grid parity, where renewable energy becomes cost-competitive with fossil fuels without subsidies, requires further reductions in the costs of balance-of-system components, including inverters [2]. Microinverters, with their modular "plug-and-play" design, provide distinct advantages for decentralized solar systems, such as module-level Maximum Power Point Tracking (MPPT), improved safety through rapid shutdown capabilities, and enhanced performance under partial shading conditions [3]-[5]. Despite these benefits, microinverters are still more expensive than string and central inverters, largely due to redundant components like transformers and isolation circuits, as well as limited economies of scale. This cost disparity restricts their adoption primarily to residential markets, highlighting the need for innovative topologies that maintain modularity while significantly reducing Bill of Materials (BOM) costs.

This paper addresses this challenge by proposing a dual-purpose forward non-isolated microinverter [6]. In the flyback converter, interleaving is necessary to prevent core saturation at power levels above 200 W, making it a standard industry practice. However, the proposed forward-based topology inherently avoids saturation due to continuous energy transfer and transformer reset. Introducing interleaving in this case would increase component count, complexity, and cost without delivering significant performance gains. Therefore, for a fair and practical comparison, we benchmark the proposed simpler, non-interleaved forward-based converter against the commonly used single-stage interleaved flyback shown in Fig. 1a-b, respectively.
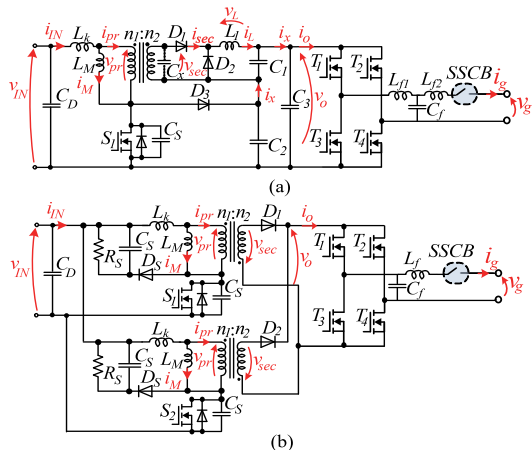

Fig. 1. A dual-purpose microconverter based on (a) proposed non-isolated forward converter. (b) conventional isolated single-stage flyback converter.

The microinverter market, as shown in Table I, includes key players like Enphase, AP Systems, Sungrow, Hoymiles, ZJ Beny, and Envertech, offering a range of products with varying power outputs, MPPT voltage ranges, and efficiencies [7]. Enphase leads with high-efficiency models (up to 98%), while other one provides cost-effective alternatives with slightly lower efficiency. This diversity highlights the trade-offs between efficiency, power output, and cost, underscoring the need for innovative solutions in microinverter research and commercialization. Efforts have primarily focused on flyback, interleaved flyback, and H-bridge-derived topologies. Flyback converters dominate the market (e.g., Enphase, APS Systems) due to their simplicity, galvanic isolation, and low component count [8]. However, their reliance on bulky transformers and isolation components raises costs, particularly for power levels exceeding 200 W [9], [10].

Interleaved flyback designs mitigate transformer size constraints but increase semiconductor counts, negating cost savings. H-bridge-based topologies (e.g., H5, HERIC) offer higher efficiency but require complex control and additional switches, raising BOM expenses [11], [12]. Recent research explores wide-band gap semiconductors to reduce losses, but these innovations often increase upfront costs [13]. Thus, a significant gap persists, one this paper aims to address through a non-isolated, dual-purpose microinverter architecture.

Manufacturer	Peak AC Power (VA / W)	MPPT Voltage (V)	Efficiency %		Cost
			Max	EU	
Enphase (IQ7 series)	250	27 - 37	98	97	$$$$
	295	27 - 45			
	320	53 - 67			
Enphase (IQ8 series)	240	27 - 37	98	97	$$$$
	290	29 - 45			
	325	33 - 45			
	349	36 - 45			
	380	38 - 45			
AP systems Dual Microinverter (DS3)	625 - 960	28 - 45	96.5	96	$$$
Sungrow (S450S)	450	16 - 60	96.2	95.4	$$$
Hoymiles (HMS series)	450	16 - 60	96.7	96	$$$
ZJ Beny (BYM series)	500-700	24 - 50	97.5	97	$$$
Envertech (EVT series)	360	22 - 48	96	95	$$$

The longstanding AC/DC debate, tracing back to Edison and Tesla's rivalry, has reemerged as DC-native technologies like PV and batteries transform energy systems. While AC grids remain dominant due to scalable voltage via transformers and existing infrastructure, DC systems offer key benefits: lower conversion losses, easier integration with renewables, and compatibility with modern technologies [14]. High-voltage DC excels in offshore wind integration, and low-voltage DC systems (e.g., 350–380 V) are increasingly used for local distribution [15]. However, DC adoption faces challenges like limited device availability and infrastructure constraints. Dual-purpose converters (Fig. 1) bridge this gap, enabling seamless AC/DC operation and reducing risks in transitional markets [16]. Developing nations can adopt DC-ready systems without losing AC compatibility, while existing grids can gradually integrate DC to boost capacity. This paper also applies this concept to microinverters, proposing a dual-output design that removes isolation costs while supporting hybrid PV-storage systems.

The proposed forward non-isolated microinverter challenges conventional single-stage flyback-based microinverter by eliminating isolation components (e.g., transformers, optocouplers) and integrating shared auxiliary circuits for simultaneous DC/AC operation. Unlike flyback designs, the topology leverages a simplified magnetic structure. To objectively evaluate the proposed design, two TRL4 universal prototypes were developed using identical components except for their core topologies. Cost savings arise from simplified magnetics and the elimination of isolation components in both the gate driver and sensor circuitry. As shown in Fig. 1a, the added inductance L_{fl} in the proposed forward-based converter, compared to the flyback design, is introduced to satisfy the zero-level requirement of the unipolar Pulse Width Modulation (PWM) scheme, rather than to improve total harmonic distortion. Without this inductance, the capacitor's instantaneous discharge path through the low-side bridge switches would result in a dangerously high di/dt and peak current, immediately burning out those switches.

II. THEORETICAL COMPARISON OF FLYBACK AND FORWARD-BASED NON-ISOLATED SOLUTIONS

Due to the single-stage configuration of power electronics converters, they produce a pulsating AC output, which is directly rectified. Steady-state analysis was carried out for both the proposed forward-based and flyback DC-DC converters, as shown in Fig. 1a-b. The ripple values for passive components were selected equally for both topologies to ensure a fair comparison. In the transformer design, the deviation and maximum flux density (240 mT) were kept identical. The turn ratio was also chosen similarly to highlight the differences between the topologies while maintaining consistent transformer parameters and maintained identical ripple factors for the capacitors ($K_c = 5\%$) and inductances ($K_L = 20\%$). Table II provides mathematical expressions for both converters, including passive elements, magnetizing current, and semiconductor voltage stresses. The comparison for both prototypes was evaluated using the parameters listed in Table III.

The first two criteria focus on the total energy stored in the inductances and capacitances. The third criterion evaluates total conduction losses, while the fourth assesses total semiconductor stress. Since the efficiency of the converters depends on the transistor and diode models, the semiconductor parameters were kept identical for both cases to ensure a fair comparison.

Fig. 2 presents charts comparing the two topologies under varying input voltages and power levels. The red areas represent the forward-based DC-DC converter, while the blue areas correspond to the flyback DC-DC converter. Fig. 2a shows the comparison results for an input voltage of 15 V and an input current of 10 A. In this case, the forward-based converter demonstrates higher semiconductor stress, while other criteria remain roughly equivalent. However, the scenario changes for input voltages of 40 V and 70 V (Fig. 2b-c). Although the forward-based converter exhibits higher semiconductor voltage stress, the flyback converter shows greater total Inductance energy due to its high magnetizing current. As a result, the red and blue areas are balanced in these cases. Fig. 2d shows the theoretical comparison of losses between Flyback and Forward based dc-dc converter. The proposed forward-based dc-dc converter works more efficiently with higher current, while the flyback dc-dc converter is better under lower current (less than 5-7 A).

The proposed forward-based DC-DC converter offers several advantages: it is a non-isolated, common-ground solution, which reduces costs and eliminates leakage current between grounds. Despite having more semiconductors, it features only one active switch, and its total conduction losses are comparable to those of conventional solutions. This makes it a viable and cost-effective alternative for certain applications.

TABLE II– Comparison table of the passive components and voltage stress across semiconductors.

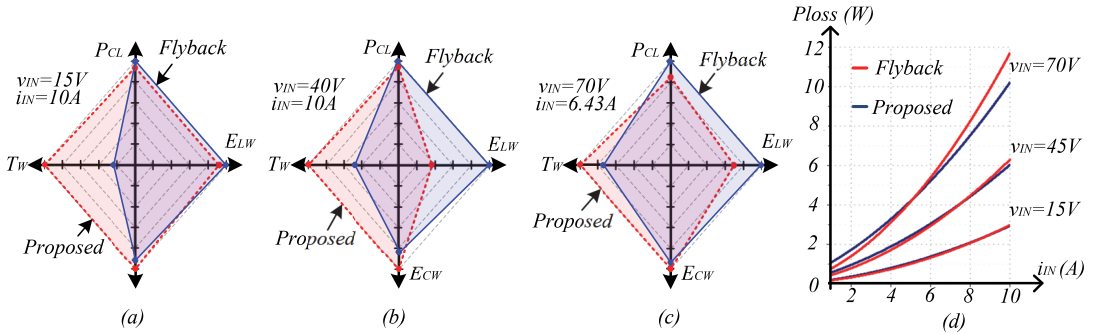| Parameter	Flyback dc-dc converter	Proposed Forward-based dc-dc converter
Gain, $G=V_O/V_{IN}$	$N \cdot D/(1-D)$	$\left(1 + N \cdot D \cdot (1-D)\right)/(1-D)$
Duty cycle, D	$V_O/(V_O + N \cdot V_{IN})$	$\left(N \cdot V_{IN} + V_O + \sqrt{4 \cdot N \cdot V_{IN}^2 + (N \cdot V_{IN} - V_O)^2}\right)/(2 \cdot N \cdot V_{IN})$
Average magnetizing current, I_M	I_{IN}/D	$\left(I_{IN} - I_O(1 + N \cdot D)\right)/D$
Capacitor, C_O	$I_O \cdot D \cdot T/(K_O \cdot V_O)$	$\left(I_O \cdot D \cdot T - (K_{C1} \cdot V_{C1} + K_O \cdot V_O) \cdot C_2\right)/(K_O \cdot V_O)$
Capacitor, C_1	–	$\left(I_O \cdot D \cdot T - (K_{C1} \cdot V_{C1} + K_O \cdot V_O) \cdot C_2\right)/(K_{C1} \cdot V_{C1})$
Inductance, L_1	–	$N \cdot V_{IN} \cdot (1-D) \cdot D \cdot T/(1-D)$
Inductance, L_M	$\mu_{ef} \cdot \mu_0 \cdot (V_{IN} \cdot D \cdot T)_{MAX}^2 / (L_{ef} \cdot A_{ef} \cdot 4 \cdot \Delta B^2)$	
Voltage stress across switch S_1, v_{S1}	$(v_{IN} \cdot N + v_O)/N$	$v_{IN}/(1-D)$
Voltage stress across diode D_1, v_{D1}	$v_O + v_{IN} \cdot N$	$(v_{IN} \cdot N \cdot D)/(1-D)$
Voltage stress across diode D_2, v_{D2}	–	$v_{IN} \cdot N$
Voltage stress across diode D_3, v_{D3}	–	$v_{IN}/(1-D)$

Fig. 2. The comparison between the flyback dc-dc converter and proposed forward-based dc-dc converter: (a) input voltage is 15 V and input current is 10 A, (b) input voltage is 40 V and input current is 10 A, (c) input voltage is 70 V and input current is 6.43 A. (d) Total power loss with input voltage variation

TABLE III. Design target parameters.

Input voltage (v_{in})	10 V to 75 V
MPPT voltage (V_{MPPT})	25 V to 60 V
Maximum input current (i_{in})	13 A
Maximum Input power	450 W
Switching frequency (f_s)	65 kHz
Resonance frequency (f_{RES})	20 kHz
DC load voltage	350 V
maximum flux density (B_{Max})	240 mT
AC load RMS voltage	230 V
AC Grid frequency (f_{grid})	50 Hz

III. TRL4-Validated Prototypes

A. Methodology of Control

As illustrated in Fig. 3, for DC load operation, both topologies employ similar control strategies utilizing a PI controller for controlling the injected power.

Ideally, for connection to an AC load, a single-stage operation is preferred to maximize efficiency and reduce complexity [6]. The conventional single-stage flyback-based microinverter (Fig. 4b) utilizes a simple control method, where a single loop regulates both MPPT and grid current

through controlling switch S1 and S2, while bridge switches T1 to T4 working as an unfolder circuit with zero crossing detection. This approach enables primary-side decoupling in combination with an unfolding circuit stage, achieving near-zero dynamic loss, which is an important efficiency advantage over dual-stage configurations.

However, in the proposed non-isolated forward-based topology, the presence of diode D1 necessitates a hybrid control strategy. A combination of high-frequency unipolar PWM at 65 kHz and low-frequency unfolding circuit operation at 100 Hz is proposed to retain the benefits of single-stage operation, as shown in Fig. 4a. The proposed converter cannot generate a full rectified sinusoidal waveform at the output that can be directly converted to a complete sine wave by the unfolding bridge. When the forward stage output closely follows the input voltage, the converter transitions into dual-stage operation, as it is depicted in Fig. 4c. The DC-DC stage handles MPPT, while the inverter stage manages power injection to the load.
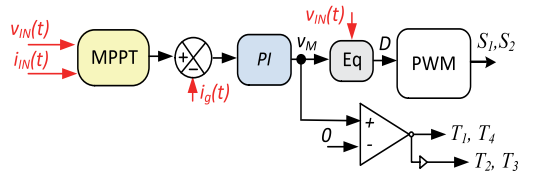

Fig. 3. The control methodology of dual-purpose proposed forward-based and flyback-based microconverters for connection to dc load.
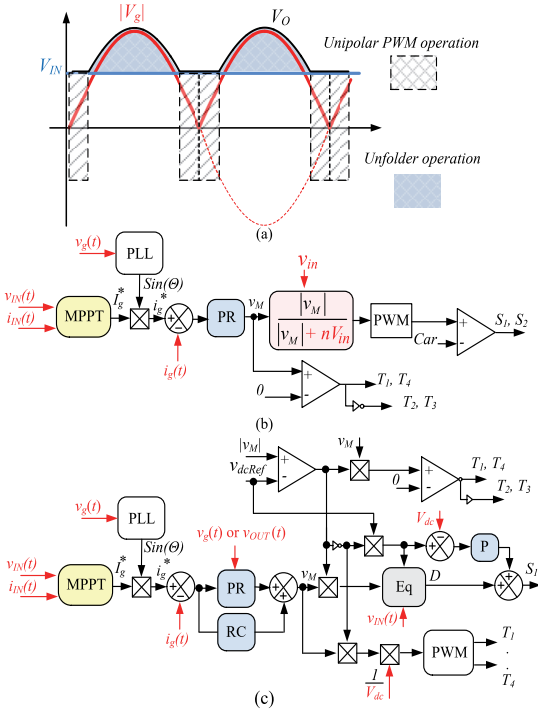
Fig. 4. (a) Active power control methodology of the proposed forward-based solution for an AC load. (b) single-stage control and (c) double-stage control methodology.

B. Prototypes Details

Fig. 5 shows the experimental setups of two dual-purpose microconverters: (a) a novel non-isolated forward-based design and (b) an isolated single-stage flyback-based design. The forward-based converter uses a common-ground, non-isolated structure, eliminating costly isolation components like transformers and optocouplers, simplifying the design. The flyback-based converter employs two ETD59 transformers for galvanic isolation, increasing complexity.

Both setups include PV side decoupling capacitors, an STM32 microcontroller, bridge MOSFETs, and EMI filters. Auxiliary supplies are powered by non-isolated linear IC regulators, and main switches use non-isolated drivers. In the flyback converter design, both high-side and low-side bridge switches require isolation, while the forward-based design only isolates the high-side switches, which is reducing costs. Bootstrap circuits are not feasible in dual-purpose solutions, emphasizing the forward-based design's cost and simplicity advantages for hybrid PV-storage systems.

Electrolyte capacitors are used as a passive decoupling approach due to active ones' cost barriers. Tables III-IV contain electrical specifications, the physical size of the prototypes and values of the passive components, as well as core materials and electrical details of the transformers used in the experimental setups. All passive components were chosen according to the calculations in [6], [14]. The control unit utilizes an STMicroelectronics STM32F334C6T6TR for the flyback-based converter and an STM32H503CBT6 for the forward-based solution. While both microcontrollers feature essential peripherals like high-resolution timers and analog-to-digital converters, the different selection was necessitated

by the flyback topology requiring a higher number of PWM channels than the forward-based design.

Table IV. ELECTRICAL SPECIFICATIONS

Parameter / Specification	Value / Type		
	Single-Stage Flyback Based Microconverter	Novel Forward Based Microconverter	
Converter volume (mm^3)	197.48*152.29*31.2	187.92*111.45*24.9	
Transformer Core	2*ETD59	ETD49	
Magnetic inductance (uH)	60	220	
Leakage inductance (uH)	0.370	28	
Decoupling capacitor (uF)	6 * 2200	6 * 2200	
Output filter inductance (*uF*)	*1*		
Output filter inductance (*uH*)	L_f =220	L_{f1} =680	L_{f2} =180
Secondary diode	IDM05G120C5XTMA1		
Microcontroller	STM32F334C6T6TR	STM32H503CBT6	
Main switch	IPB044N15N5ATMA1	IXFA80N25X3	
Bridge switches	STB28N65M2	C3M0120065J	
Snubber diode	MBR20H100CT	SBR20A300	
Snubber capacitor (uF)	0.100	3.3	
Snubber Resistor (kΩ)	2.35	-	
Dc circuit breaker	IPD95R450P7		

C. Experimental Results

The experimental results in Fig 5 compare the performance of a dual-purpose microconverter based on a proposed non-isolated forward topology and a conventional flyback-based topology under both AC and DC load conditions. The setups, shown in Fig 5a and 5d, illustrate the key components of each topology, including transformers, MOSFETs, filters, and control circuits. Subfigures (b) and (e) present the input voltage, current, and gate drive waveforms when connected to an AC load, while subfigures (c) and (f) show the corresponding results for a DC load.

The input voltage remains at 42V across all cases, with variations in current levels and gate drive voltages depending on the topology and load type. The measured waveforms reveal differences in electrical characteristics between the two configurations, offering insights into their behavior under different operating conditions. In the unfolding-based solution, the flyback converter initially produces a rectified sinusoidal waveform. The unfolding bridge then plays a crucial role in converting this signal into a sinusoidal waveform within the circuit.

Fig. 6 contains the efficiency curve versus different variations of the input voltage with 9 A constant input current, which is conducted using the Yokogawa WT1800E high-performance power analyzer. AC efficiency benefits from sinusoidal modulation under lighter loads. In forward based solution, beyond certain power, DC efficiency declines faster due to cumulative switching and conduction losses.
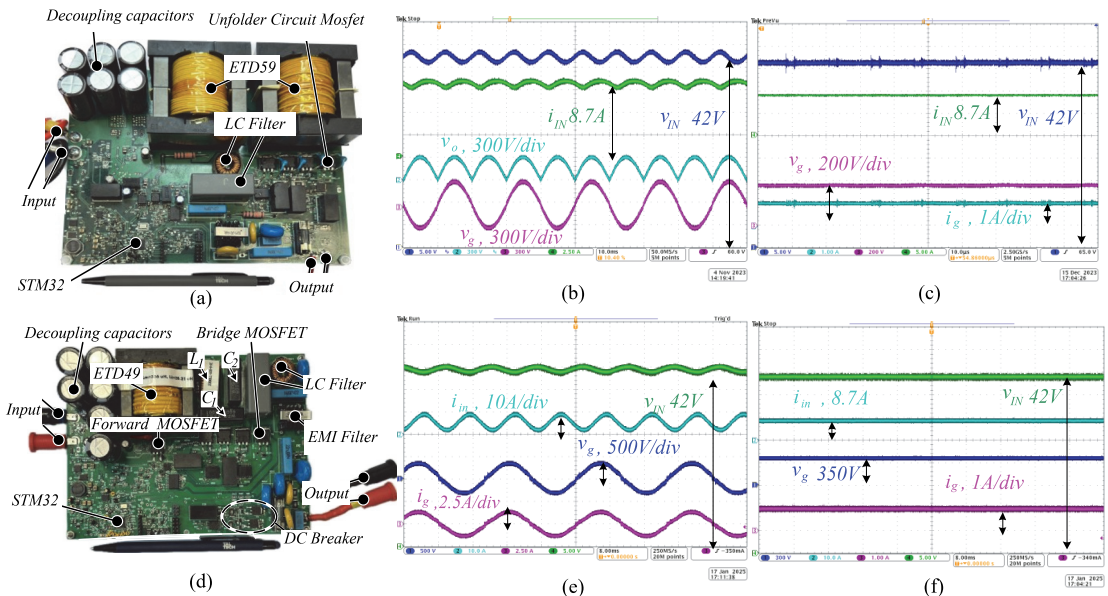
Fig. 5. Experimental setups and results of dual-purpose microconverters: Conventional interleaved isolated single-stage flyback-based dual-purpose microconverter (a)-(c). Proposed non-isolated forward converter; (d)-(f).
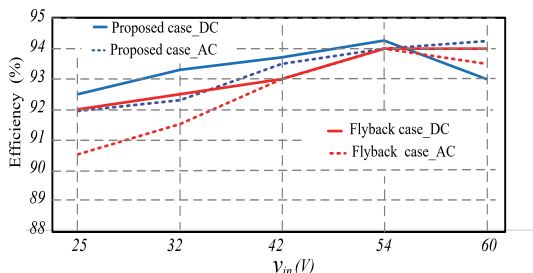

Fig. 6. Efficiency study versus different input voltages under input constant current.

IV. COST COMPARISON

The cost benchmarking analysis evaluates the proposed forward non-isolated microconverter vs the conventional single-stage flyback isolated microconverter, where costs are compared using current component prices in the market from the same component provider website, emphasizing the cost savings achieved through the proposed converter design comparing to single stage flyback based solution as a cost effective solution in industry for target power up to 450 watts.

As illustrated in Fig. 7, the forward-based topology demonstrates a 28.5% reduction in total costs based on the number of components required at different production levels (1, 10, 100, and 1000 units). The cost analysis is divided into several parts, such as the total cost of capacitors, semiconductors, Magnetics, Integrated Circuits (IC), resistors/varistors for protection, as well as printed circuit boards. In terms of semiconductors, PCB, resistors/protection, as well as capacitor costs, both topologies have almost similar costs. However, the cost of magnetics and ICs used for driver and sensors are higher in flyback-based solution compared to the proposed solution because of non-isolated inherent feature, which eliminates utilizing the isolated sensors and drivers and in general ICs.

A more detailed cost analysis, considering mass production scales, is presented in Table V. The power part, comprising magnetics, capacitors, and drivers, benefits from the removal of isolation components and the use of a non-isolated structure. These findings reinforce the economic advantage of the forward-based topology, particularly in large-scale manufacturing, where reducing isolated components and optimizing circuit integration translates to substantial cost savings. By demonstrating lower material costs and improved scalability, the forward-based microconverter presents a highly viable alternative for next-generation PV-storage applications.

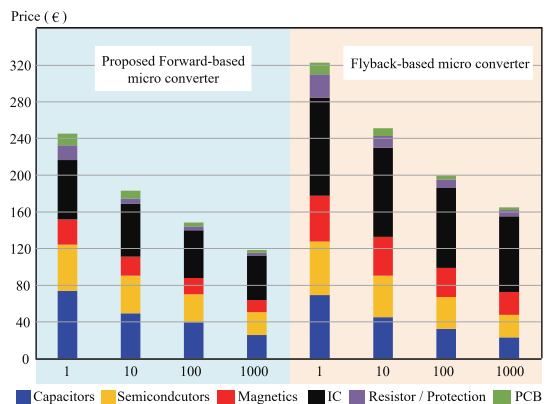
Fig. 7. Cost benchmarking of proposed non-isolated forward and interleaved flyback-based microconverters.

Meanwhile, the control part, which includes current and voltage sensors, control and communication circuits, and auxiliary supplies, shows substantial cost reductions due to the non-isolated architecture, which removes the need for expensive isolation components while streamlining the

design. These savings make the forward design particularly well-suited for mid-power (300–500 W) systems, ensuring both cost efficiency and compatibility with DC and AC grids.

Table V. Cost comparison of the control part and the power part, considering the current market price.

Topology	Control Part Cost (€) by Volume				Power Part Cost (€) by Volume			
	1 Unit	10 Unit	100 Unit	1000 Unit	1 Unit	10 Unit	100 Unit	1000 Unit
Proposed forward based	49	34	27	23	178	134	114	90
Flyback based	85	64	52	44	218	171	140	115

To further enhance cost efficiency, the adoption of Application-Specific Integrated Circuit (ASIC) technology can be considered. For large scale production ASIC-based design minimizes component count, reduces manufacturing costs, and improves performance. By integrating multiple control and sensing functions into a single chip, ASICs can further streamline circuit complexity, enhance reliability, and reduce overall production costs, making the forward-based topology even more competitive for PV module applications.

V. Conclusion

This paper presents a non-isolated forward-based microconverter challenging conventional single-stage non-isolated flyback-based microinverter topologies. Two TRL4 prototypes are designed and tested as dual-purpose microconverters for validation and comparison of the proposed forward-based solution with flyback ones.

The forward-based architecture not only reduces material costs but also maintains competitive performance, effectively addressing a key economic barrier in PV module adoption. Benchmarking against an equivalent flyback converter under identical conditions highlights its superior cost-effectiveness without compromising functionality. These findings underscore the potential of non-isolated topologies to drive down system costs in renewable energy applications while maintaining performance standards. The proposed architecture eliminates isolation components while integrating intelligent control schemes, achieving a 28% cost reduction (from 165€ to 119€) and dual-purpose DC/AC output performance capability.

The successful experimental realization of this prototype demonstrates the viability of cost-optimized, dual-output microconverters for residential and commercial PV systems. Further ASIC technology implementation will reduce component count and overall costs through system integration, and (2) optimizing efficiency and scalability. Usually, the ASIC approach integrates control logic, gate drivers, and protection circuits into a single chip, while power stage optimization could enhance performance in commercial-scale installations.

Acknowledgement

References

[1] Ali O M Maka, Jamal M Alabid, Solar energy technology and its roles in sustainable development, *Clean Energy*, Volume 6, Issue 3, June 2022, Pages 476–483.

[2] R. Burkart and J. W. Kolar, "Component cost models for multi-objective optimizations of switched-mode power converters," *2013 IEEE Energy Conversion Congress and Exposition*, Denver, CO, USA, 2013, pp. 2139-2146.

[3] A. K. Sahu, R. Patel and L. K. Sahu, "ANN Controlled Single-Phase Microinverter for Off-Grid Solar Application," in *IEEE Journal of Emerging and Selected Topics in Power Electronics*, vol. 13, no. 1, pp. 850-860, Feb. 2025.

[4] A. Chub, D. Vinnikov, O. Korkh, M. Malinowski and S. Kouro, "Ultrawide Voltage Gain Range Microconverter for Integration of Silicon and Thin-Film Photovoltaic Modules in DC Microgrids," in *IEEE Transactions on Power Electronics*, vol. 36, no. 12, pp. 13763-13778, Dec. 2021

[5] X. Xue, Z. Liu, W. Li and H. Su, "Design of a Single-Stage Dual Active Bridge Microinverter With Wide Load Adaptability Based on Loss Optimization," in *IEEE Transactions on Power Electronics*, vol. 40, no. 6, pp. 7919-7935, June 2025

[6] H. Afshari, O. Husev, O. Matiushkin, S. Pourjafar, N. V. Kurdkandi and D. Vinnikov, "Comprehensive Comparison of Grid-Connected Flyback-Based Microinverter With Primary and Secondary Side Decoupling Approach," in *IEEE Transactions on Industry Applications*, vol. 60, no. 6, pp. 9080-9089, Nov.-Dec. 2024.

[7] MicroInverter Comparison Chart 2024. Available online: https://www.cleanenergyreviews.info/microinverter-comparison (accessed on 24 March 2025).

[8] S. Pourjafar, H. Afshari, P. Mohseni, O. Husev, O. Matiushkin and N. Shabbir, "Comprehensive Comparison of Isolated High Step-up DC-DC Converters for Low Power Application," in *IEEE Open Journal of Power Electronics*, vol. 5, pp. 1149-1161, 2024.

[9] M. Forouzesh, Y. P. Siwakoti, S. A. Gorji, F. Blaabjerg and B. Lehman, "Step-Up DC–DC Converters: A Comprehensive Review of Voltage-Boosting Techniques, Topologies, and Applications," in *IEEE Transactions on Power Electronics*, vol. 32, no. 12, pp. 9143-9178, Dec. 2017.

[10] D. Carey, "Isolated Switch-Mode Power Supplies: How to Choose a Forward vs. a Flyback Converter," Analog Devices, 2024. Available online: https://www.analog.com/en/resources/technical%20articles/isolated-switch-mode-power-supplies-forward-vs%20flyback.html. (accessed on 24 March 2025).

[11] F. Sedaghati, and S. Pourjafar, "Analysis and implementation of a boost DC–DC converter with high voltage gain and continuous input current," *IET Power Electronics*, vol. 13, no. 4, pp.798-807, 2019.

[12] C. Deng, M. Chen, F. Zhang, R. Zheng and F. Jiang, "A Novel Analog Control Strategy With Simplified Implementation Scheme for Boundary Conduction Mode Flyback Microinverter," in IEEE Transactions on Power Electronics, vol. 40, no. 6, pp. 7967-7979, June 2025.

[13] Power Electronics Europe, "Gallium Nitride (GaN) based switches: Better Figure of Merit than Silicon or SiC," Available online: https://www.power-mag.com/pdf/feature_pdf/GaN_switches.pdf. (accessed on 24 March 2025).

[14] O. Matiushkin, O. Husev, H. Afshari, E. Romero-Cadaval and C. Roncero-Clemente, "Forward-Based DC-DC Converter With Eliminated Leakage Inductance Problem," in *IEEE Transactions on Industrial Electronics*, vol. 72, no. 2, pp. 1638-1648, Feb. 2025.

[15] E. Rodriguez-Diaz, M. Savaghebi, J. C. Vasquez and J. M. Guerrero, "An overview of low voltage DC distribution systems for residential applications," *2015 IEEE 5th International Conference on Consumer Electronics - Berlin (ICCE-Berlin)*, Berlin, Germany, 2015, pp. 318-322.

[16] O. Husev, D. Vinnikov, S. Kouro, F. Blaabjerg, C. Roncero-Clemente, "Dual-Purpose Converters for DC or AC Grid as Energy Transition Solution: Perspectives and Challenges," *IEEE Industrial Electron.* Magazine, Early access, 2023.

Curriculum vitae

Personal data

    Name: Hossein Afshari
    Date of birth: 18.06.1997
    Place of birth: Zanjan, Iran
    Citizenship: Iran

Contact data

    E-mail: Hossein.Afshari@taltech.ee

Education

2011–2015	Reza Rouzbeh State Model High school, Iran
2015–2019	Semnan University, Iran, BSC
2019–2022	Iran University of Science and Technology, Iran, MSC
2022–2025	Tallinn University of Technology, Estonia, PhD

Language competence

Persian	Native
English	Advanced
Estonian	Beginner
Azerbaijani	Native

Professional employment

17.01.2025–31.12.2025	Tallinn University of Technology, School of Engineering, Department of Electrical Power Engineering and Mechatronics, early-stage Researcher

Grants & projects

PRG675 "New Generation of High-Performance Power Electronic Converters Simultaneously Applicable for DC and AC Grids with Extended Functionalities" (1.01.2020–31.12.2024); Tallinn University of Technology, School of Engineering, Department of Electrical Power Engineering and Mechatronics.

EAG122 "Universal dc/ac battery storage interface (UniBSI)" (1.09.2021–31.08.2022); Tallinn University of Technology, School of Engineering, Department of Electrical Power Engineering and Mechatronics.

EAG234 "New Concept of Energy Router for Residential Application (SoftER)" (1.10.2023–31.10.2024); Tallinn University of Technology, School of Engineering, Department of Electrical Power Engineering and Mechatronics.

TK230U2 "Centre of Excellence in Energy Efficiency" (01.01.2024–31.12.2030); Tallinn University of Technology, School of Engineering, Department of Electrical Power Engineering and Mechatronics.

Infineon IPCEI "Infineon's PhD Booster program" (01.4.2023–31.12.2025); Infineon Technologies Austria AG.

Elulookirjeldus

Isikuandmed

Nimi: Hossein Afshari
Sünniaeg: 18.06.1997
Sünnikoht: Zanjan, Iraan
Kodakondsus: Iraani

Kontaktandmed

E-post: Hossein.Aafshari@taltech.ee

Hariduskäik

2011–2015 Rouzbehi Riigieelkool, Iraan
2015–2019 Semnani Ülikool, Iraan, BSC
2019–2022 Iraani Teaduse ja Tehnoloogia Ülikool, Iraan, MSC
2022–2025 Tallinna Tehnikaülikool, Eesti, PhD

Keelteoskus

Pärsia keel Kõrgtase
Inglise keel Edasijõudnud
Eesti keel Algtase
Aserbaidžaani keel Kõrgtase

Teenistuskäik

01.10.2018–31.12.2020 Tallinna Tehnikaülikool, Inseneriteaduskond, Elektroenergeetika ja mehhatroonika instituut, doktorant-nooremteadur

Toetused ja projektid

PRG675 "Laiendatud funktsionaalsusega alalisvoolu ja vahelduvvooluvõrkude jaoks üheaegselt rakendatavad suure jõudlusega elektrilised elektroonilised muundurid" (1.01.2020–31.12.2024); Tallinna Tehnikaülikool, Inseneriteaduskond, Elektroenergeetika ja mehhatroonika instituut.

EAG122 "Universaalne alalis/vahelduvvoolu muundur akusalvestitele" (1.09.2021–31.08.2022); Tallinna Tehnikaülikool, Inseneriteaduskond, Elektroenergeetika ja mehhatroonika instituut.

EAG234 "Elumajade jaoks mõeldud energiaruuteri uus kontseptsioon (SoftER)" (1.10.2023–31.10.2024); Tallinna Tehnikaülikool, Inseneriteaduskond, Elektroenergeetika ja mehhatroonika instituut.

TK230U2 "Energiatõhususe tippkeskus" (1.1.2024–31.12.2030); Tallinna Tehnikaülikool, Inseneriteaduskond, Elektroenergeetika ja mehhatroonika instituut.

Infineon IPCEI "Infineoni doktoriõppe kiirendiprogramm" (01.04.2023–31.12.2025); Infineon Technologies Austria AG.